Energy Harvesting from Human Motion for the Powering of Implantable, Wearable, and Peripheral Electronic Devices

Nathan Lowell Sharpes

Dissertation submitted to the faculty of the Virginia Polytechnic Institute and State University in partial fulfillment of the requirements for the degree of

Doctor of Philosophy
In
Mechanical Engineering

Shashank Priya, Chair
Dong S. Ha
Muhammad R. Hajj
Pablo A. Tarazaga
Christopher B. Williams

August 1st, 2016
Blacksburg, VA

Keywords: Energy Harvesting, Piezoelectric, Electromagnetic, Biomechanic, Occupancy Sensing, Implantables, Wearables, Self-Powered Devices, Smart Buildings

Energy Harvesting from Human Motion for the Powering of Implantable, Wearable, and Peripheral Electronic Devices

Nathan Lowell Sharpes

ABSTRACT

In the past two decades, the miniaturization of highly functional electronic devices has yielded the present condition where such devices are light enough, have a long enough battery life, are robust enough, and even stylish enough to be utilized for extended periods of time. Such devices can monitor activity and various bodily vital signs, and/or provide assistive actions. Due to the interrelationship between persons and assistive electronic devices, it is examined whether the actions (human motion) themselves can be used to power the electronic devices assisting those very actions. Such functionality results in a synergistic "win-win" interaction, rare in energy systems where trade-offs are pervasive. These interactions are studied in the context of the three types of solution spaces in implantable (inside the body), wearable (on the body), and peripheral (outside the body) devices. Specifically, it is studied whether heartbeats can power the pacemakers regulating the heartbeat; whether walking can power the portable communication equipment guiding the path; and whether movement within a smart building can power the occupancy measurement in automatic occupancy-drive lighting and climate control systems making the building habitable yet energy efficient. Novel energy harvesting solutions are developed for each category, with the impetus of harvesting sufficient energy to perform the desired function without encumbering the body.

ACKNOWLEDGEMENTS

I would like to thank the following funds, programs, and organizations for providing financial support toward my graduate research assistantship, both directly and indirectly funding the works described and not described in this dissertation:

- Samsung Research Program
- Office of Naval Research (ONR)
- National Aeronautics and Space Administration (NASA)
- National Science Foundation (NSF)
- Pratt & Whitney (P&W)
- Center for Energy Harvesting Materials and Systems (CEHMS)
- Boeing
- American Piezo Ceramics (APC)
- United States Army
- Rockwell Collins

I would also like to give my sincere thanks to those faculty and students who came before me, establishing a laboratory environment where I could prosper. Additionally, I would like to thank the many senior design students, undergraduate researchers, and high school students that I advised for their naive enthusiasm for the field of energy harvesting, pushing me to be good enough to be able to faithfully advise their pursuits.

My thanks are also extended to my friends and family who have supported me, loved me, and have been understanding of my absence while pursuing the works both discussed and not discussed in this dissertation. This is especially true of my wife, Caitlin.

Thank you all.

"After the knowledgement of, and obedience to, the will of God, the next aim must be to know something of His attributes of wisdom, power and goodness as evidenced by His handiwork…It is evident that an acquaintance with natural laws means no less than an acquaintance with the mind of God therein expressed."[1]

- James Joule

"…one thing is for sure: this farmers' son will successfully carry on his ancestors' tradition of a career in harvesting. Just a different kind of harvesting."[2]

- The CEHMS Chronicle
Student Profile: Nathan Sharpes

TABLE OF CONTENTS

LIST OF FIGURES

LIST OF TABLES

1 INTRODUCTION

In the past two decades, the miniaturization of highly functional electronic devices has yielded the present condition where such devices are light enough, have a long enough battery life, are robust enough, and even stylish enough to be utilized for extended periods of time. Such devices can monitor daily activity and various bodily vital signs, and/or provide assistive actions. Due to the interrelationship between an individual's actions and assistive electronic devices, it is examined whether the actions (human motion) themselves can be used to power the electronic devices assisting those very actions.

1.1 Definition of an Energy Harvester

In its simplest definition, an energy harvester is any mechanism, device, etc., that captures (harvests) wasted energy, to perform some useful work. This work could be performed immediately, or the harvested energy could be stored to be used at a later time. In the past two decades, with the growing prevalence of electronic devices, the focus of energy harvesting has been converting the source form of energy into electricity, for the recharging of batteries/capacitors or directly powering electronic devices. Today, the focus of research in the field of energy harvesting is almost exclusively concerned with the integration of adequate energy harvesting mechanisms/transducers with the intended platform (source of energy). Integration challenges dominate the implementation.

Energy harvesting may be thought of as a relatively new field, since it is only in the past few decades that circuit technology has allowed electronic devices to function at low levels of power, however the idea of capturing ambient energy is over a millennium old. By the definition provided in the previous paragraph, the first water wheels would be classified as energy harvesters, using the energy of flowing water, which typically goes unused, to perform the useful work of grinding grain into flour, cutting wood or stone, transporting loads, etc. Some centuries later, windmills were also realized to perform the same tasks. These examples of mechanical to mechanical energy harvesting have been practiced for a long time, along with other harvesting techniques not involving a conversion of energy from the source form. For example, the thermal to thermal harvesting, using underground temperature differentials with the surface, to heat/cool dwellings and preserve food. Since the discovery of electromagnetic induction, and ensuing

discoveries of piezoelectric, photovoltaic, thermoelectric, etc. materials, the focus of energy harvesting technology has been on converting available forms of waste energy into electricity.

In discussing the definition of an energy harvester is, it is also useful to talk about what an energy harvester is not. Any device which forces a system to perform more work than what would naturally occur, would constitute a deliberately powered device. Remember energy harvester capture waste energy. Such deliberately powered systems would certainly include those powered by fossil fuels, and even some typically considered "green" energy sources, such as biofuels and nuclear power. In the context of this work, devices like pedal powered or hand crank generators, which demand a person perform additional work for the sake of power production, are not considered energy harvesters. Though, if one were to use an exercise bicycle, where resistance is applied through electrical damping from a generator, that could be considered an energy harvester, since the goal is exercise and that energy is typically wasted.

1.2 Classification of Energy Harvesters

The preceding example brings to light the fact than an energy harvester is fundamentally coupled, by definition and by design, to its application. Indeed, the two are closely related, since an energy harvester cannot exist without an ambient energy source from which to derive its energy. Therefore, the application platform, or source of energy, is of the utmost importance in energy harvesting. Perhaps there is no application where this is more true than harvesting energy from humans. This is because we are particularly adept at sensing changes in our environment, with movements, both in terms of organ function, and gait, to minimize energy expenditure.

Being an especially sensitive system to harvest energy from, particular attention must be paid to the effect an energy harvester would have on the body. To understand the consequence of harvesting energy from the body, or more broadly the consequence of transferring energy from one system to another (in this case the body to the energy harvester), the theory of maximum power transfer is presented. This broad theory provides the groundwork for the levels of power and efficiency which can be expected when transferring energy from one system to another or converting energy from one form to another.[3] While the maximum power transfer theorem does not provide a total understanding of energy transfer and should not be explicitly taken as such,[4] it does provide a useful tool for explaining the effects of energy transfer on a source.

Maximum power transfer theorem is most easily explained in the context of an electrical system, using the equivalent circuit model shown on the left in Figure 1.1. Here, a voltage source with internal resistance is attached to a load resistance, to which it is transferring power. Here, this power transfer theorem is being described in terms of electricity, though it could also be described, thermally, chemically, or mechanically, where the electrical potential (voltage) could be considered as mechanical potential, and electrical resistance considered as mechanical damping. With respect to the given circuit model, the efficiency of power transfer, η, is the ratio of the input and output potentials, or,

$$\eta = \frac{V_L}{V_S} = \frac{R_L}{R_L + R_S} \quad , \tag{1.1}$$

where V_S and R_s are the source voltage and resistance, respectively, while R_L is the load resistance and V_L the resulting load potential. The power transferred to the load is then given as

$$P_L = \frac{V_L{}^2}{R_L} \quad . \tag{1.2}$$

Having defined power and efficiency, the resultant curves are plotted in Figure 1.1 as a function of the ratio of load to source resistance. The abscissa is presented as a ratio, because in energy harvesting the source characteristics (in this case resistance) are fixed, since only ambient energy is derived, and the load resistance is dictated by the design of the energy harvester device. Power is also presented as the ratio of instantaneous power to maximum power, because the level of power delivered to the load is dictated by the available source power, and so it can be easily compared to the level of efficiency, also on a zero to one scale.

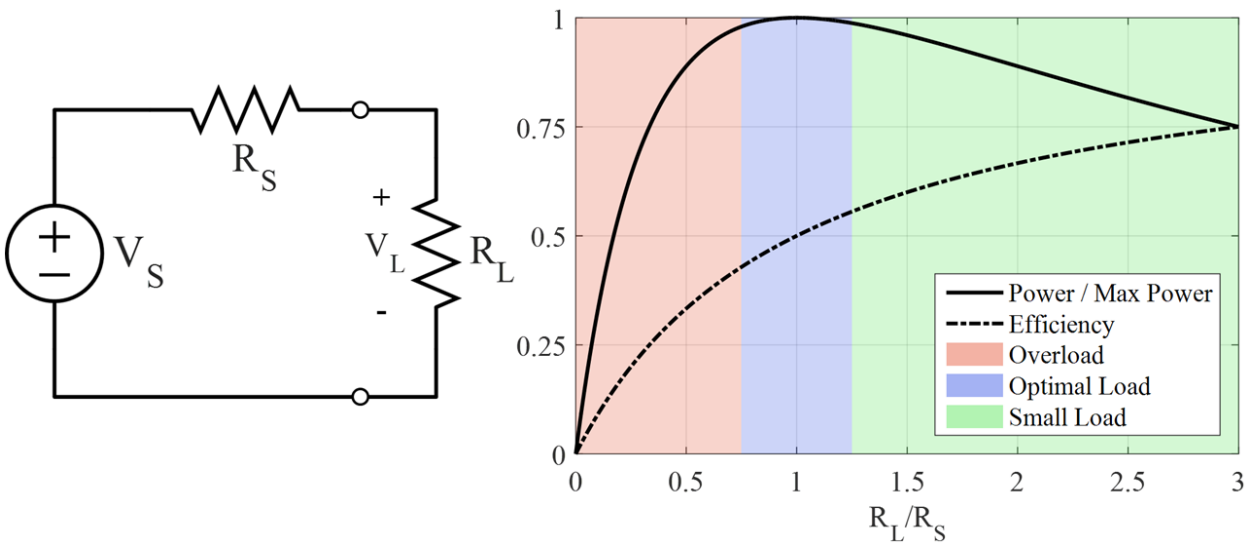

Figure 1.1 – (Left) Equivalent circuit model for power transfer between a source and a load. (Right) Graphical representation of maximum power transfer theorem with power and efficiency as a function of the ratio of source and load impedances.

From Figure 1.1 it can be seen that for load resistances much smaller than the source resistance, that neither an appreciable level of power transfer or efficiency is realized. In contrast, when the load resistance is much larger than the source resistance, power transfer is higher, though not optimal, but efficiency is much greater. It should be noted that a nominally larger value of load resistance corresponds to a smaller load (in terms of effect) on the source system, and vice versa. As load resistance increases to infinity (open-circuit), power transfer tends to zero, while efficiency tends to one (on a zero to one scale). In the region where load and source resistances are approximately the same, the maximal power is transferred and efficiency is around 50%. Here, the discussion is given in term of resistance for simplicity, though the discussion in terms of impedance (i.e. inclusion of inductance or capacitance, or mass and stiffness in mechanical terms), also holds. In interpreting Figure 1.1, three distinct regions present themselves as a function of applied load, in the form of Small Load, Optimal Load, and Overloaded systems, which are colored according to their region.

Small Load type energy harvesters are those which harvest much less energy than the source can output. Since the level of harvested energy is much less than the energy output of the source system, this type of harvester only has a small effect on the source. The efficiency of energy transfer is thus higher than other source to load impedance configurations. Since the load on the

system is so small, the harvester can be designed with few considerations for the source in mind, as the consideration of small power transfer is already made. Small Load type harvesters make up the bulk of energy harvesting devices.

Optimal Load type energy harvesters are those which harvest as much energy at any given instance as the source can sustain. Here, the influence of energy conversion rivals the power of the source system. The source is impeded somewhat, though not enough to compromise its functioning. Since the impedances are matched in an optimal load system, power transfer is the highest possible. This type of energy harvester is employed in commercial power generation systems, like hydroelectric power plants and windmills.

Overload type energy harvesters are those which attempt to harvest more energy than the source can sustain. This situation has a clamping effect on the system, which tends to slow the source system down. Therefore, the source cannot maintain its original power level (i.e. power level without the energy harvester), and subsequently there is less energy available to be harvested. Examples of this type of harvester include regenerative braking systems in cars, and door closer mechanisms (which prevent a door from slamming shut by dictating the rate of closing).

To give an illustration of how each type of system would look in a given application, the illustrations in Figure 1.2 were prepared to show the systems in the context of a wind turbine. The optimal load case is the situation which looks most familiar, as this is the form which has been optimized over time. The system could become overloaded if too many blades were used. In such a configuration, the turbine would act more like a wall, impeding airflow. In a small load configuration, the blades would be made too small, not capturing much of the airflow.

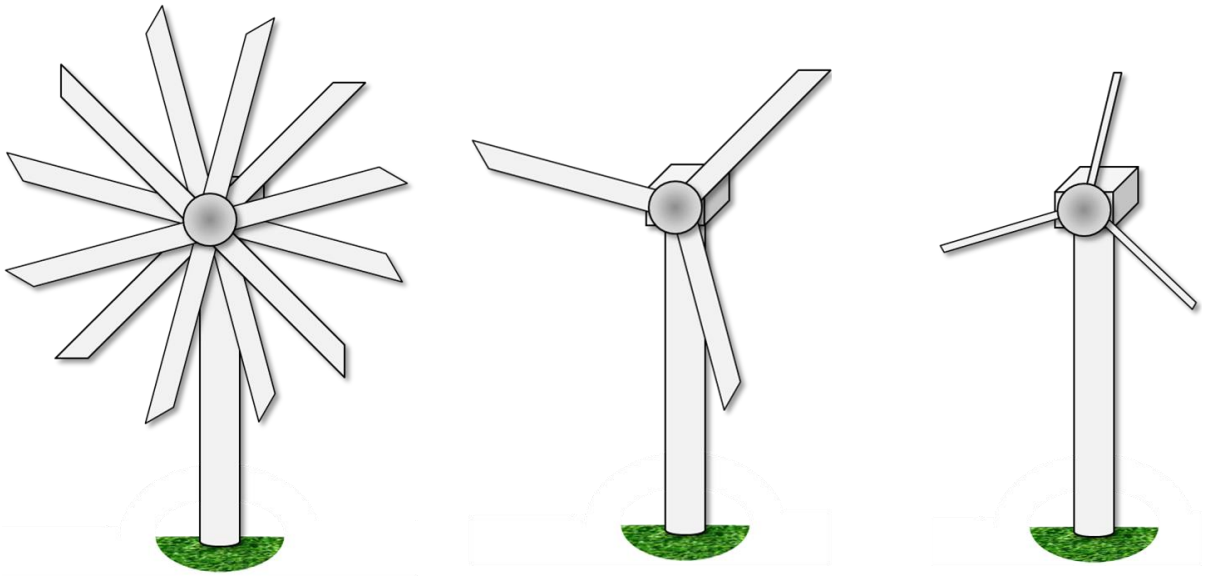

Figure 1.2 – Illustration of how each classification of energy harvester (by load placed on source) would look in the application of a wind turbine.

There is also a fourth classification of energy harvesters in the form of Decoupled systems. In these systems, energy is collected and stored in a medium of the same type of energy which was collected, before being converted into electricity. In this way, the source is decoupled from the energy conversion process, which tend to acts as a damper on the system. Collecting energy in the same form as the source of the energy acts as a force (like a spring in mechanical terms) on the source system, rather than a damper. At a later time, the stored energy is converted into electricity. Therefore, the harvesting and conversions can take place at different regions on the power transfer curves. In this way, the energy collection can be done such that it has the desired effect on the system, and the conversion (transduction) process can be performed ideally under optimal load conditions.

Examples of decoupled energy harvesters include the Solar One installation in the Mojave Desert, collecting the thermal energy of the sun from a mirror array, and storing the thermal energy in molten salt, the heat energy from which is later used to power a steam turbine-generator.[5] Here, the solar energy collection is a small load type, as it hardly has any effect on the sun. The conversion process is under optimal load condition. Another example is the SOLO-TREC ocean

thermal energy harvester, which utilizes a phase change material to gather energy from the thermal gradient in the ocean waters as it rises and sinks. The phase change material expands as it changes phase, increasing the pressure in an oil, which is released through a turbine-generator.[6] Here, energy is also stored in a thermal to thermal small load application (the SOLO-TREC does not affect the temperature of the ocean) while converting to electricity under optimal load conditions.

While decoupled type energy harvesters can be of great effectiveness, not all systems can be decoupled. Therefore, it is good to utilize decoupled systems wherever possible, though they must fit into niche applications.

The classification of energy harvesters according to their load on an energy source is summarized in Figure 1.3.

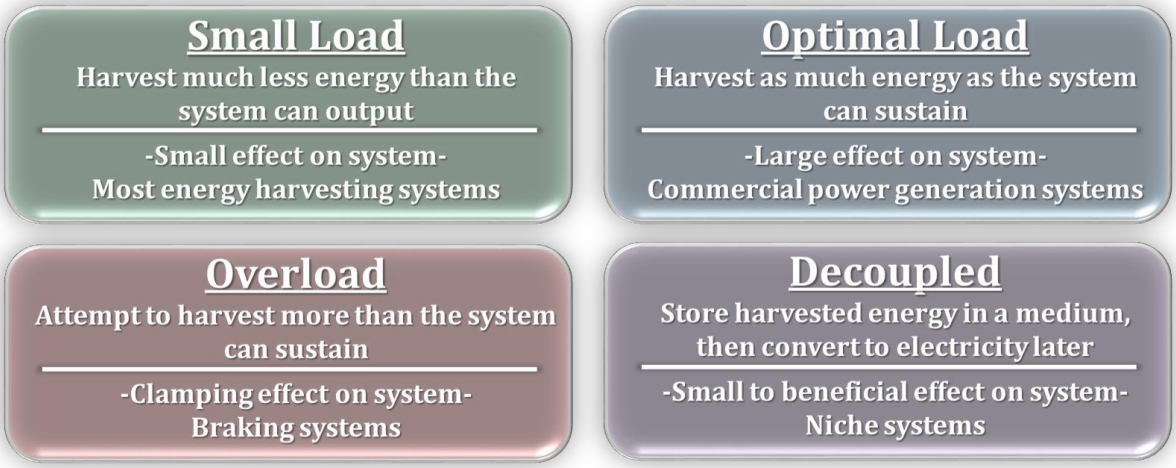

Figure 1.3 – Description of the possible types of energy harvester, classified by the load the energy harvester places on the source.

1.3 Overview of Energy Harvesting Transduction Techniques

There are many transduction techniques in energy harvesting, or ways of converting one type of energy into another. Most commonly this is a mechanical energy to electrical energy conversion. In this dissertation, two techniques, piezoelectric and electromagnetic induction, are employed in the forthcoming designs, and discussed in detail here, to convert the various types of mechanical motions in, on, or around the human body, into electricity. Other transduction

techniques, such as electrets, thermoelectrics, and photovoltaics, are mentioned in the forthcoming literature and technology overviews for each chapter, but not discussed in detail.

Piezoelectricity and electromagnetic induction are discussed in detail here to give the reader a basic understanding of the principle to be applied in each chapter. In this way, the content can be more easily followed, what are the intended consequences and progression of the research and subsequent proposed designs.

1.3.1 Piezoelectric

Piezoelectric materials are those which exhibit the behavior of generating electric fields in response to being strained. The reverse of this effect is also true. When an electric field is applied to the piezoelectric material, it will strain. This response is called the converse piezoelectric effect, which is used in actuator applications. In energy harvesting applications the direct piezoelectric effect is use to convert mechanical energy into electricity. The piezoelectric effect arises due to the asymmetric crystalline structure of the typically ceramic material (though there are types other materials exhibiting piezoelectricity) belonging to specific point groups. The crystal structure causes a spatial disparity in the centers of positive and negative charges, resulting in a dipole moment. If these moments are made to align in a single direction, through the application of a large DC electric field, then the material is considered to be “poled”. In this way, the charges created by each dipole can add across all domains to yield a significant voltage in response to applied strain.

An illustration of the piezoelectric effect is given in Figure 1.4. The representative material block in the neutral state has no charge across the material electrodes, with the charge centers in their neutral position. When the material either undergoes compression (Left) or tension (Right), it causes a deformation of the crystal domain, physically displacing the dipoles and inducing a potential. This potential creates an electric field and subsequent voltage across the material electrodes.

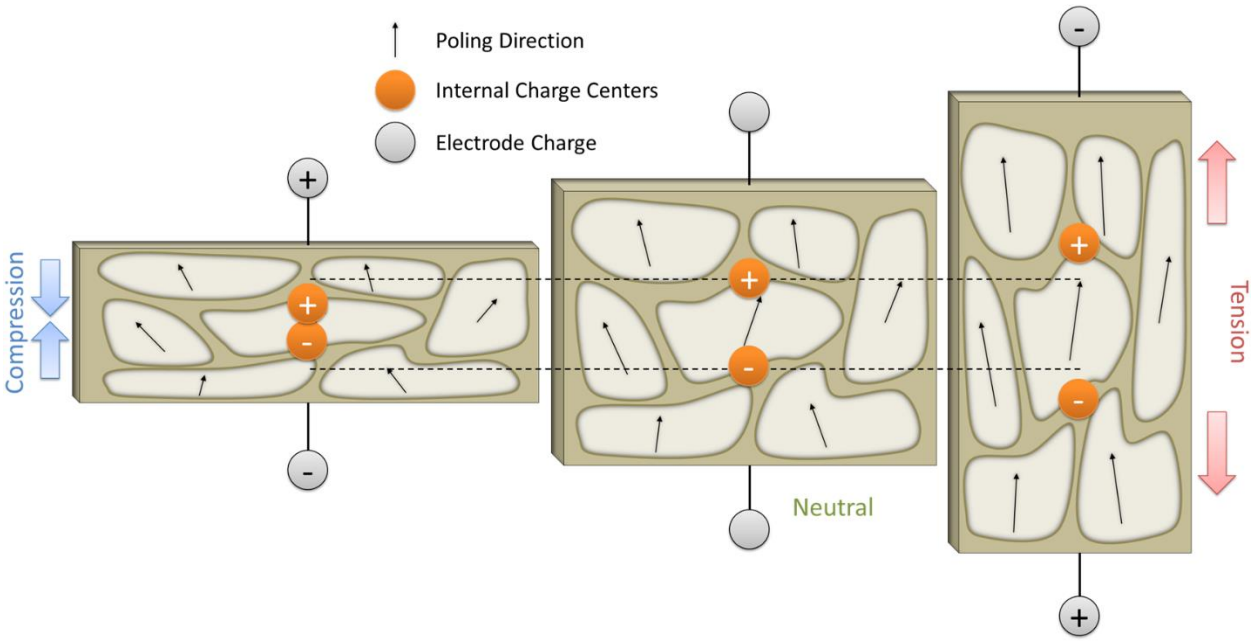

Figure 1.4 – Conceptual illustration of the piezoelectric effect, whereby the relative displacement of charge centers due to material deformation (exaggerated) generates a voltage across the electrodes of the material, driving current flow.

The voltage generated by the piezoelectric material is

$$v = gTt \quad , \tag{1.3}$$

where v is the static voltage produced in response to applied stress T, with g the piezoelectric voltage constant, and t the thickness of the material in the poling direction. Voltage produced is naturally dependent on the direction of the applied stress. As Figure 1.5 illustrates, if force is applied in the direction of poling, this is called the 33 mode. However, if force is applied perpendicular to the direction of poling, this is called the 31 mode. Piezoelectric properties are generally two to three times larger in the 33 mode than the 31 mode. This disparity in properties arises because of the Poisson's ratio of materials, or the thickness-wise contraction due to length-wise expansion. This is the reason that even though stress is applied perpendicular to the poling direction in the 31 mode, there results a proportionally smaller stress in the 33 direction, which still produces a voltage.

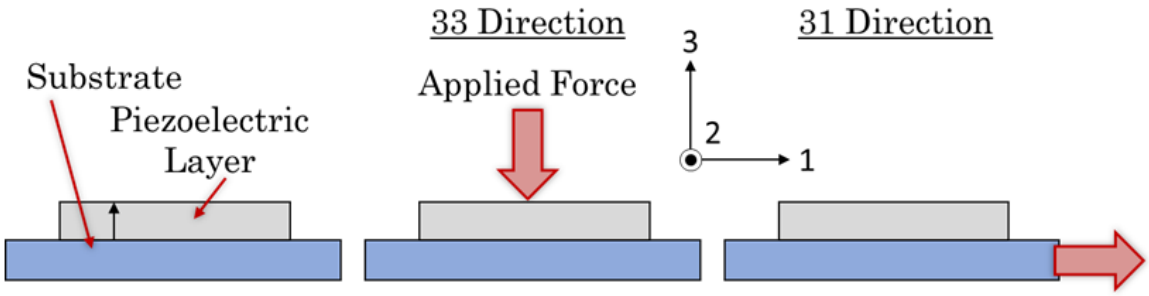

Figure 1.5 – Illustration of directionality convention whether force is applied in the poling direction (33 mode) or perpendicular to the poling direction (31 mode).

Despite lower properties, the 31 mode is often the chosen mode for energy harvesting, due it lending itself better to integrating with mechanical amplifiers, which can increase the energy density of the energy harvester due to the amplified stress in the piezoelectric layer. Direct application of stress on a piezoelectric material is not often practical and rarely effective. Therefore, a mechanical amplifier is most often used. Whereas, piezoelectric materials are applicable to many situations, the mechanical amplifier should be tailored to the energy harvesting source. Typically, these energy sources are either thought of as high-force-low-frequency (HFLF) or low-force-high-frequency (LFHF), and there are mechanical amplifiers advantageous for each. Low-force-low-frequency (LFLF) sources are not possessing enough energy to make a worthwhile energy harvesting application, and high-force-high-frequency (HFHF) sources push the mechanical limits of engineering materials, making energy harvesting often inaccessible. An example of a HFLF mechanical amplifier is shown in Figure 1.6(a-b) in a cymbal transducer. Cymbal transducers, like the one shown, amplify compressive vertical forces applied to the end caps (typically metal) before transferring it to the piezoelectric layer as tensile stress. This transducer has found applications in harvesting energy from human gait, a HFLF motion. An example of a LFHF mechanical amplifier is shown in Figure 1.6(c-d) in a cantilever beam transducer. Cantilever beam type transducers are attached to an energy source (base excitation) and utilize the inertia of a tip mass (at the free end) to bend the beam at resonance, stressing the piezoelectric layer near the fix end. This transducer has been well studied and has found many applications and variations, such as vibrations from machinery and buildings.

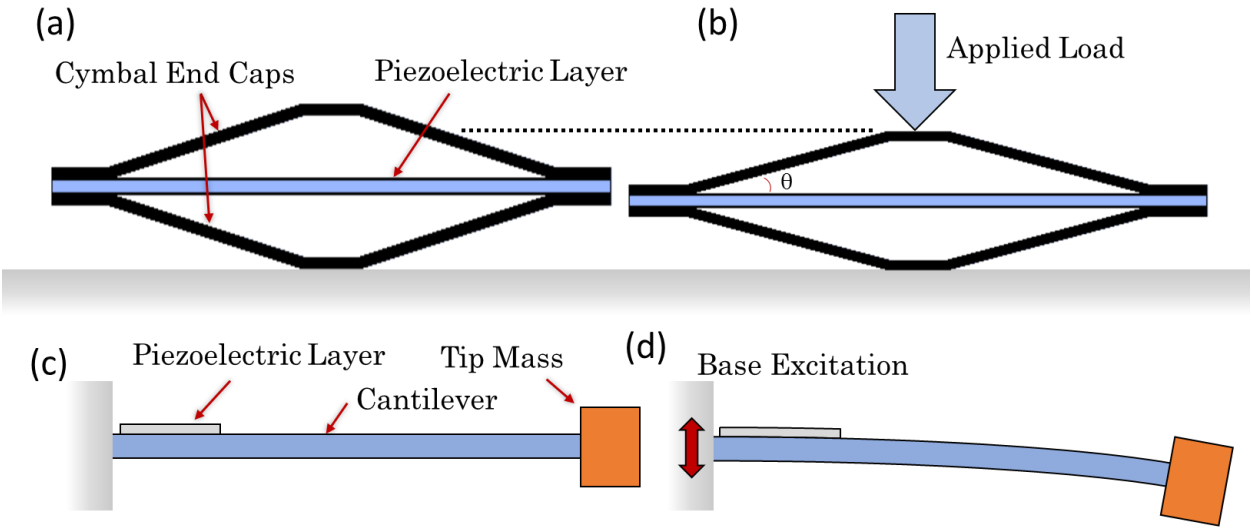

Figure 1.6 – (a) Cymbal transducer suitable for high-force-low-frequency, (b) loaded cymbal transducer converting vertical compressive forces into horizontal tensile stress in the piezoelectric layer, (c) cantilever transducer suitable for low-force-high-frequency, (d) bending response to base excitation (vibrations) shown with tensile stress in the piezoelectric layer. Both (b) and (d) utilize the piezoelectric in the 31 mode.

The current produced by a piezoelectric is given as

$$i = C\frac{dv}{dt} \quad , \tag{1.4}$$

where C is the capacitance of the piezoelectric material. It is no surprise that a piezoelectric material behaves as a capacitor, as the transduction mechanism requires displacement of separated charges. The fact that current is only produced when voltage is changing, means current is only produced when stress in the material is changing. This is a principal reason why piezoelectrics have found application in vibration energy harvesting. The capacitance of a piezoelectric is

$$C = \frac{K\epsilon_0 A}{t} \quad , \tag{1.5}$$

where K is the relative dielectric constant of the material, ϵ_0 is the permittivity of free space (8.85×10^{-12} F/m), A is the surface area of the piezoelectric material, and t is the thickness of the piezoelectric layer. Here it can be seen that a broad but thin piece of piezoelectric material yields the highest capacitance, which also lends well to vibration energy harvesting, as cantilever beams

are most often broad but thin beams. The bending stress in the cantilever beam, like the one shown in Figure 1.7, causes the length-wise expansion or contraction of the piezoelectric (31 mode).

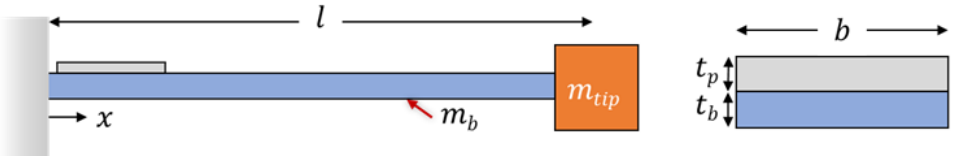

Figure 1.7 – Illustration of piezoelectric cantilever, with labeled parameters used in model.

In general, bending stress is calculated as

$$T = \frac{My}{I} \ , \tag{1.6}$$

where the stress, T, is a function of bending moment, M, distance from the neutral axis, y, and moment of inertia, I. The bending moment at a location along the beam, x, is given as

$$M_x = mg(l - x) \ , \tag{1.7}$$

where the equivalent mass, m, is

$$m = \frac{33}{144} m_b + m_{tip} \tag{1.8}$$

and g is the acceleration due to gravity (9.81 m/s^2). The distance from the neutral axis in the part of the beam without the piezoelectric layer is $t_b/2$. However, interest is in the part of the beam with the piezoelectric layer. Figure 1.8 illustrates how the neutral axis is found.

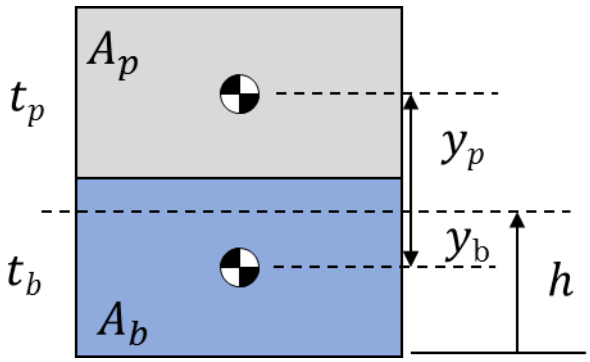

Figure 1.8 – Illustration of location neutral axis, h, and distances from the neutral axis to the center of area of each layer in the composite.

Assuming the piezoelectric layer is well bonded to the beam, the two share the same curvature when bending, meaning,

$$0 = E_b y_b A_b + E_p y_p A_p \quad . \tag{1.9}$$

Here, E is the Young's modulus and A is the cross-sectional area. To avoid charge cancelations due to opposing signs of stress, it must be the case that the neutral axis is in the beam. For this to be the case, h must be less than t_b, resulting in Equation (1.9) becoming

$$E_b \frac{t_b}{2} t_b b \geq E_p \frac{t_p}{2} t_p b \quad , \tag{1.10}$$

and simplifying to

$$E_b t_b^2 \geq E_p t_p^2 \quad . \tag{1.11}$$

Additionally,

$$h = \frac{t_b}{2} + y_b \quad , \quad h = t_b + \frac{t_p}{2} - y_p \quad . \tag{1.12}$$

Applying the Equations (1.12) into Equation (1.9) the neutral axis location is found from the expression:

$$E_b \left(h - \frac{t_b}{2}\right) t_b b = E_p \left(-h + t_b + \frac{t_p}{2}\right) t_p b \quad , \tag{1.13}$$

which simplifies to

$$h = \frac{E_b t_b^2 + 2E_p t_p t_b + E_p t_p^2}{2\left(E_b t_b + E_p t_p\right)} \quad . \tag{1.14}$$

Finally, the moment of inertia of the section of the beam without piezo is simply, $1/12 b t_b^3$. Similarly, the moment of inertia of the composite section of the beam can be found by parallel axis theorem,

$$I = \left[\frac{1}{12} b t_b^3 + t_b b y_b^2\right] + \left[\frac{1}{12} b t_p^3 + t_p b y_p^2\right] \tag{1.15}$$

From Equation (1.11), one can design the beam such that the piezoelectric layer is best used. Though, since such beams are most often used in vibration energy harvesting, the vibration performance must also be considered. The key characteristic of the vibration energy harvester is the resulting natural frequency. The natural frequency is given as, $\omega_n = \sqrt{k/m}$, where k is the stiffness of the beam. Thus,

$$\omega_n = \sqrt{\frac{3EI}{ml^3}} \quad . \tag{1.16}$$

From this analysis it's learned that the key parameters are the thicknesses of the beam and piezoelectric layers, as well as, the overall length of the beam. These terms are either squared or cubed in the stress or natural frequency calculations.

1.3.2 Electromagnetic Induction

In contrast to piezoelectric materials, where a change in strain field creates an electric field in the material, in electromagnetic induction a change in magnetic field creates an electric field in a closed circuit of conductive material. The result of both transduction mechanisms is that a voltage is induced and subsequently current is driven across a load. Just like piezoelectrics, the induction effect is inversible. One can provide an electric field to an inductor, creating a magnetic field, or one can give a changing magnetic field and generate an electric field. The latter effect is how nearly all electrical energy is generated in the world today.

The electromotive force produced by electromagnetic induction is described by Faraday's law of induction,

$$\mathcal{E} = -\frac{d\Phi_B}{dt} \quad , \tag{1.17}$$

where Φ_B is the magnetic flux through a conducting loop. The current produced is then

$$i = \frac{\mathcal{E}}{R} \quad , \tag{1.18}$$

where R is the electrical resistance of the conducting loop. The magnetic flux is the magnetic field (B) through an area (A),

$$\Phi_B = BA \quad . \tag{1.19}$$

To achieve a change in flux, either the magnetic field and/or the area of the conductor must be time variant, otherwise no voltage will be generated. There are several possibilities for varying both magnetic field strength and/or conductor area. Theoretically, the perimeter of the conductor could be deformed, thereby changing the area. However, typically the conductor loop is realized in a coil of wire wrapped around some form, making it impractical to deform. Magnetic field can become time variant if a permanent magnet is traversed through a coil, such as in a vibration energy harvester. Though, typically electromagnetic generators are realized in a rotating fashion.

The two most common implementations of a rotary induction generator are shown in Figure 1.9 below. Figure 1.9(a) illustrates a rotating conductor in a fixed magnetic field. Here, the normal vector to the magnetic field changes effective area of the conductor relative to the magnetic field, realizing the time variant behavior. While the magnetic flux is highest when the face normal is collinear with the magnetic field vector, voltage production is the time derivative of the flux. Thus voltage production is greatest when the conductor rotates orthogonal to the magnetic field lines. In (b) the same behavior is observed, though this time by rotating a permanent magnet in proximity to a stationary conductor. Here, field strength is greatest through the conductor when either the North or South poles point toward the face normal of the conductor. As the magnet rotates the magnetic field lines are no longer parallel to the face normal of the conductor, altering the magnetic flux. Note the voltage produced by either method is the same.

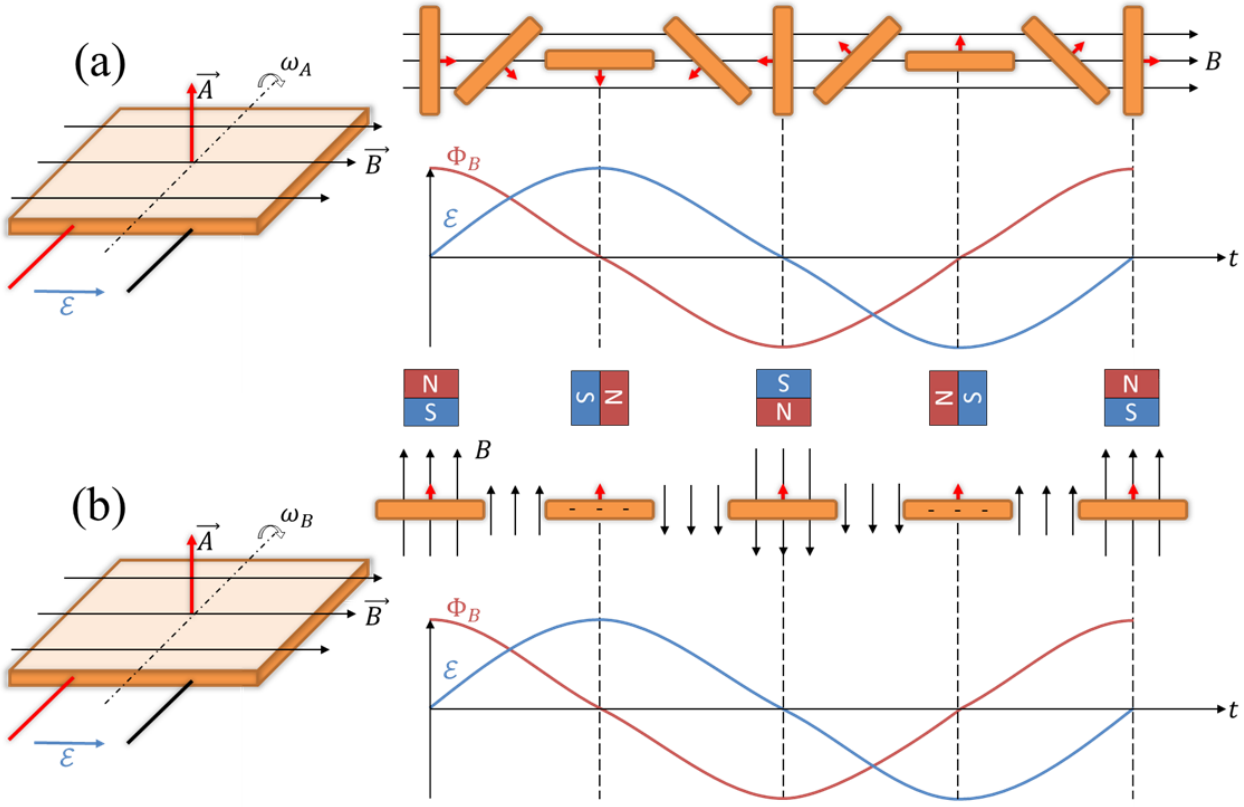

Figure 1.9 – Illustration of time varying magnetic flux and subsequent electromotive force produced by (a) alternating area of coils in a magnetic field, and (b) alternating magnetic field in a stationary coil.

For a rotating system where the magnetic flux is changing with time, like Figure 1.9(b), Equation (1.17) becomes

$$\mathcal{E} = -A\frac{dB}{dt} \quad . \tag{1.20}$$

Here,

$$B = B_{max}\cos(\omega t) \quad , \tag{1.21}$$

where B_{max} is the maximum value of magnetic field and ω is the rotation speed. This results in

$$\mathcal{E} = AB_{max}\omega\sin(\omega t) \quad . \tag{1.22}$$

1.4 Layout of Dissertation

Due to the interrelationship between individuals and assistive electronic devices, it is examined in this dissertation whether the actions (human motion) themselves can be used to power the electronic devices assisting those very actions. Such functionality results in a synergistic interaction, illustrated in the design synergy diagram of Figure 1.10, rare in energy systems, where trade-offs are pervasive. These interactions are studied in the context of the three types of solution spaces in implantable (inside the body), wearable (on the body), and peripheral (outside the body) devices, also illustrated in summary in Figure 1.10. Specifically, it is studied whether heartbeats can power the pacemakers regulating the heartbeat; whether walking can power the portable communication equipment guiding the path; and whether movement within a smart building can power the occupancy measurement in automatic occupancy-driven lighting and climate control systems making the building habitable yet energy efficient. Novel energy harvesting solutions are developed for each category, with the impetus on harvesting sufficient energy to perform the desired function without encumbering the body.

To not encumber the body, small load and decoupled systems are proposed, where little to even a beneficial effect on the human body is anticipated.

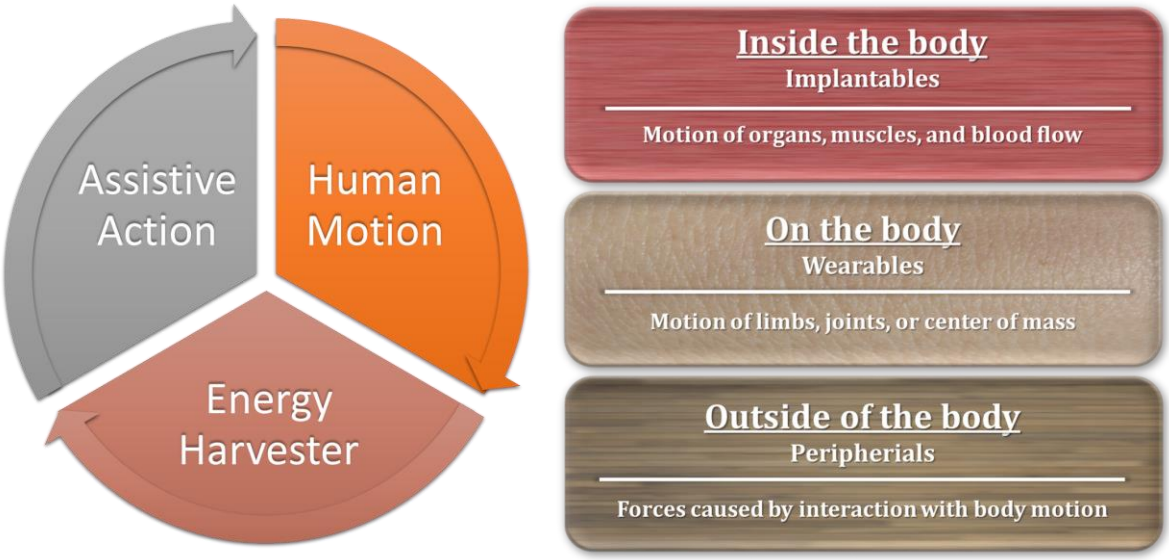

Figure 1.10 – (Left) Design synergy diagram, illustrating the dependence on each human motion, energy harvester, and assistive action. (Right) Overview of three solution spaces explored in this dissertations.

In each chapter, the topic application is introduced, followed by a review of the pertinent technology and literature. Next, the energy harvesting strategy is selected, before the novel research contributions achieved are chronicled. Results are sumarized in each chapter, as well as in the conclusions section.

2 POWERING IMPLANTED MEDICAL DEVICES: PACEMAKERS

2.1 Introduction

In recent decades, advances in medical technologies have resulted in an array of implantable devices to provide medical treatments and augmentations. Implantable medical devices are those which provide assistive function to the body, with all or part of the device being embedded inside the body. These assistive functions can range from restored or augmented sensing, in the case of cochlear and retinal implants; stimulation and regulation of body processes, in the case cardiac pacemakers, gastric stimulators, and muscle stimulators to address such conditions as dropped foot and Parkinson's; and medicine delivery systems, in the case of insulin pumps.[7]

Indeed, implanted medical devices provide increased longevity and quality of life. There are various hindrances, however, in the implementation of implantable devices, none-the-least of which is the addition of a foreign object to the body. There are limited materials available to package these implantable devices such that they will not be rejected by the body, which limits design freedom. This can lead to increased device size, which is an encumbrance to the patient receiving such an implanted medical device. The other key hindrance is the fact that since the device must be self-contained, for the sake of biocompatibility, necessitates that the power supply for the device must also be encapsulated with the rest of the electronics. There is subsequently an inherent lifetime associated with the device before it exhausts its stored energy.

It would therefore be quite advantageous if there was an approach by which energy could be derived from inside of the body by the device to power itself, preferably indefinitely. Any derivation of energy from inside the body, though, would need to be small so as to not disturb body functions. Consequently, any implanted device which would be sought to be powered by harvested energy would need to be a low power (small load type) device. Of the three classes of implantable devices; restored and augmented sensing, stimulation and regulation of body processes, and medicine delivery systems; sensing and/or stimulation devices inherently consume the least power.

Of all the implantable devices, the one where energy harvesting from inside the body could be of greatest direct use may be the cardiac pacemaker. A variety of conditions causing irregular heartbeat cycles are treated with a cardiac pacemaker. Over 700,000 new pacemakers are implanted in patients across the world each year, of which over 225,000 are in the United States

alone.[8] A pacemaker is an implanted device which delivers electronic pulses to stimulate the contraction of the heart to maintain a regular performance. The typical placement of the pacemaker relative to the heart, with typical dimensions and component layout is illustrated in Figure 2.1.

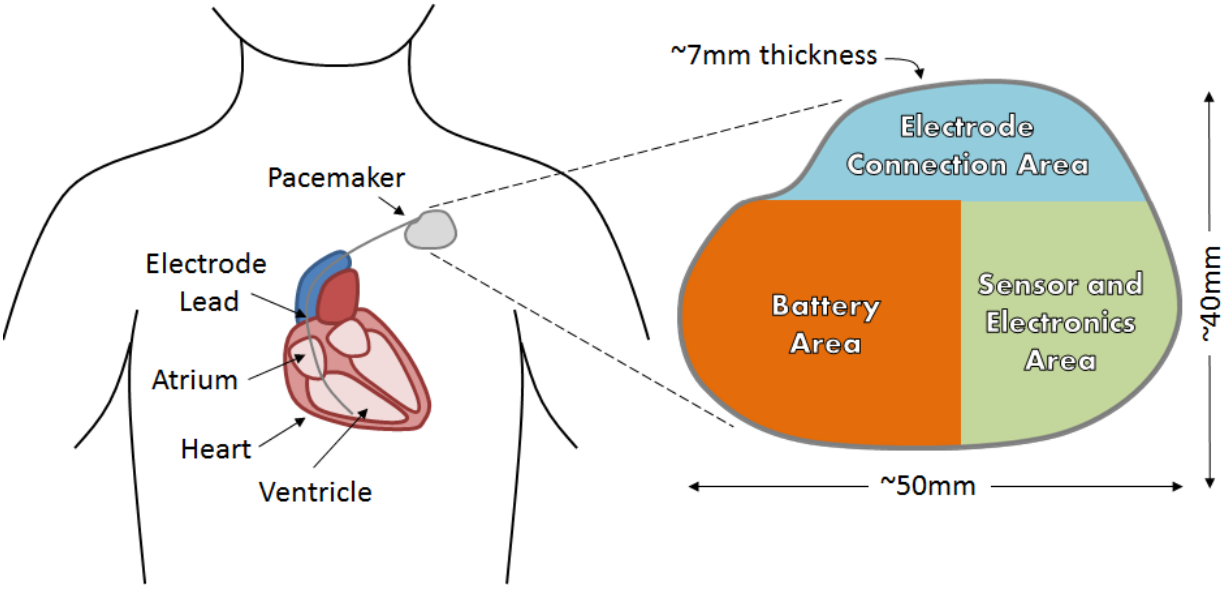

Figure 2.1 – Typical dimensions, installation location, and component schematic for a cardiac pacemaker.

As is evident in Figure 2.1 above, a large area (about half) of the typical pacemaker enclosure is occupied by the battery. Currently these batteries are lithium-based and can last from 5 to 10 years, with the entire device weighing between 12.5 to 15.5 grams.[9] The volume enclosed by the battery is approximately 26 mm × 26 mm × 6 mm. This volume will be taken to be the approximate size available for an energy harvester appropriate for implementation in a pacemaker. A harvester of this size would not displace any of the sensor and circuitry components which perform the pacing regulation, and would provide area for a small battery, which would be trickle charged by the energy harvester.

The basic design and size of the pacemaker has been largely unchanged since it was first put into practice decades ago, with incremental improvements in circuit design and battery life. Recently, however, a new class of leadless pacemakers has been researched and developed for direct implantation into the ventricle, rather than running in a wire lead. These 2.5 to 4 cm long cylindrical designs (approximately 6 mm diameter) include the Micra Transcatheter Pacing System

and Nanostim leadless cardiac pacemaker.[10] These designs have shown promising initial trials, but would significantly change the allowable size of associated energy harvesters in the future.

The goal of this chapter is to develop an energy harvesting solution which can be incorporated into the current pacemaker design, allowing it to operate indefinitely by deriving energy from the body. To this end, several key requirements have to be taken into consideration:

- To avoid biocompatibility issues, the harvester must be sealed within the pacemaker housing. Circuitry components and electrodes should not be displaced, so the harvester will occupy some of the battery area, with a smaller conformal battery around the harvester in the remaining area.
    - To fit within the housing the harvester must be smaller than approximately 27×27×5 mm.
- Sufficient power must be produced to justify removal of battery volume, ideally powering the pacemaker indefinitely.
    - Approximately 100 μW on average must be produced.

To ascertain what technologies could meet these requirements, a review of the current implantable energy harvester technology was conducted.

2.2 Review of Implantable Energy Harvesters

As mentioned earlier in this chapter, most implanted devices are battery powered, due to the simplicity and robustness batteries can offer, and the practical necessity of the inclusion of a power source in the implant. However, powering implantable devices with batteries imposes the need for periodic replacement of these batteries, which requires additional surgery for the patient. This replacement procedure can be anywhere from annoying, for otherwise healthy patients, to life threatening, for more elderly patients. To avoid the need to perform periodic additional surgeries on the patient, it is proposed that the implantable device can derive (harvest) energy from various sources to power its operation. In this way, the lifetime of the device has the potential to become indefinite, increasing the quality of life of the patient.

External energy sources that have been studied include kinetic energy from human movements, thermal energy from human body, solar energy from ambient lighting, or even ambient acoustic or electromagnetic waves. These external energies are harvested with an energy

harvester outside of human body, and then transmitted to the implanted device via electromagnetic, ultrasonic, infrared, etc. waves.

Other on-going research attempts to exploit available energy inside of human body. Most commonly studied is the feasibility to harvest energy from movements of cardiovascular system (e.g. the expansion and contraction of arteries). Chemical energy within human body could also be exploited via fuel cells. Due to high availability of glucose in body fluids, fuel cells that use glucose as a reactant have been extensively investigated. For implanted devices located at joints, kinetic energy from the forces in the joints are harvested to power the device directly.

The techniques mentioned are discussed individually and described in some detail in the following sections.

2.2.1 External Energy Sources

Many energy harvesting techniques have been employed to harvest energy present in the ambient of the human body. Depending upon the location, mechanical, thermal, acoustic, and electromagnetic radiation energies can all be available in the near of the human body. The work conducted by Niu et al. [11] provides an example of how a piezoelectric harvester could harvest mechanical energy from walking and transmit it to the implant devices within human body. In sections 2.2.1.1 and 2.2.1.2, primary methods for remote powering are discussed, including wireless electromagnetic energy transmission and ultrasonic energy transmission. The name "transantaneous energy transfer (TET)" is more commonly used in publications. In section 2.2.1.3, other ongoing research on remote powering are presented, including powering via infrared energy and low-frequency magnetic field coupling. In section 2.2.1.4, some direct-powering methods from ambient energy that have been developed for implanted devices are discussed.

2.2.1.1 Remote Powering from Electromagnetic Energy Sources

Electrical signals with frequency in the range of 10 kHz to 30 GHz are termed as Radio Frequency (RF) signals. Transmitting RF signals wirelessly as electromagnetic energy is a common method for remote powering of implanted devices. Based on the different attributes of the received electromagnetic wave, a link could be categorized as a near-field inductive link or a far-field antenna link. An illustration of an inductive link, with a power coil and receiver coil

embedded just under the skin to power implants is shown in Figure 2.2. Currently, for wireless device charging, there are ‘Qi’ and ‘A4WP’ standards.

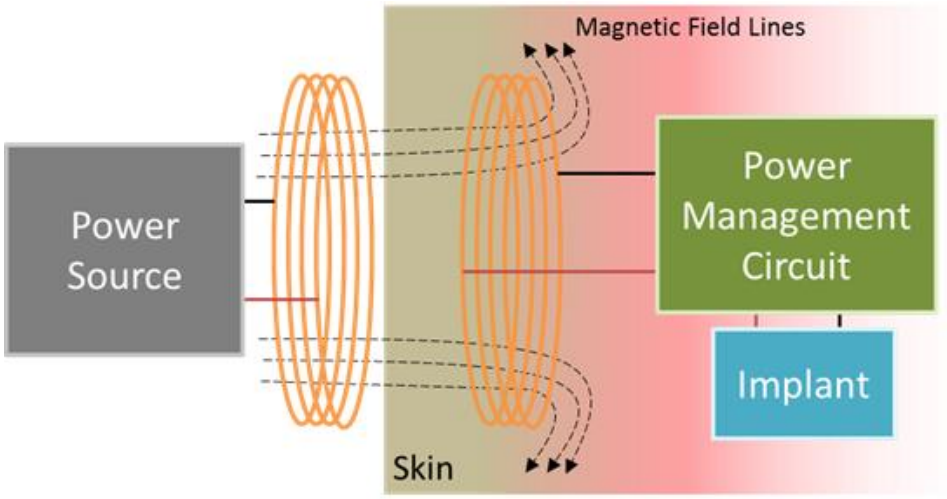

Figure 2.2 – Illustration block diagram of inductive link.

An energy harvester, a conventional generator, or mains power is the source of the energy to be transferred. This energy is used to generate high amplitude RF signal for transmission. Electromagnetic fields are generated by the RF signal at the primary coil inductor, and it is then coupled to the secondary coil inductor under the skin. An alternating current (AC) is generated at the secondary receiving coil inductor, which is rectified with power management circuit to convert it into direct current (DC) for powering the implanted device. The power management circuit also regulates the DC voltage in response to the changing load required by the implant device.

The inductive link between the two coils can be modeled as a transformer between two RLC circuits [12]. RLC circuits act as a band pass filter, transferring power efficiently only within a narrow frequency band around its resonant frequency. Therefore, the two sides of the inductive link must share a common resonance frequency, which must also be the excitation frequency, to transfer power effectively. The link can be classified as ‘Near Field’ or ‘Far Field’.

Near field inductive link typically works in a lower frequency range. Operating frequency of published devices range from 20 kHz [11] up to 500 MHz [13]. In order to design the system to have its resonance frequency in this range, and for efficient energy transfer, inductance should be relatively large, around several μH to tens of μH [11, 14, 15]. In consequence, the size of the

receiving inductor coil is often relatively large, around several centimeters in diameter [14, 15]. Naturally, for an implanted device, it is desirable to have device size minimized in order to also minimize the impact/encumbrance on the person. Nevertheless, near field inductive link is still a feasible design for powering artificial hearts [11], or within the stomach for esophageal impedance monitoring [14], but would, however, impose difficulties for clinical implementations like intraocular applications (inside the eye). The physiology of the eye limits antenna (inductor) size. Maximum size for implantation in the eye is determined by the size of the intraocular lens, which is approximately 10 × 6 mm [16].

Due to the aforementioned requirement of size, far field inductive links are advantageous for their smaller in sizes. Operation frequency is often higher, at ultra-high-frequency (UHF) in the range of 850MHz-950MHz [16], or up to 5.2GHz [17]. A most common form of antenna design is a quarter-wave monopole, in which the antenna is approximately $1/4^{th}$ of the wavelength of radio waves. With operation frequency of 5.2GHz and working intraocular with high permittivity, a monopole could be of the dimensions 1.5×3.2 mm^2 [17]. An electrically small antenna (length < $1/5^{th}$ of the wavelength) could also be carefully designed to resonate at a desired frequency [16]. However, far field antenna link has a disadvantage in terms of high transmission loss. The available power at the receiving antenna is given as,

$$P_{available} = P_t G_t \left(\frac{\lambda}{4\pi R}\right)^2 \tag{2.1}$$

where P_t is the transmitted RF signal power, G_t is the transmitting antenna gain, λ is the wavelength of transmitted signal, and R is the transmission distance between the transmitting antenna and the receiving antenna. From the Equation (2.1), a higher frequency signal (shorter wavelength) will observe higher transmission loss. Therefore, increasing operation frequency for smaller antenna is burdened by the operational power requirement.

Additionally, to power an implanted device, the power received must be processed to a DC form at a suitable voltage level. To this end, several methods of antenna design [17], signal rectification (in the forms of diode [18], passive MOS transistor [15], and active MOS transistor synchronous switch [19]), and voltage multiplier [13, 17, 19], have been discussed in the literature.

2.2.1.2 Remote Powering from Ultrasonic Energy Sources

RF link has the disadvantage of high attenuation per distance. Recently, a new type of energy transfer was suggested by Ozeri and Shmilovitz [20], based on the transmission of ultrasonic energy rather than electromagnetic energy. Ultrasonic Transcutaneous Energy Transfer (UTET) uses an external transmitting transducer attached to the skin surface facing an implanted receiving transducer. An electrical power source energizes the transmitter, which converts the electrical energy into travelling pressure waves (sound). The travelling pressure waves carry the energy through the tissue towards the implanted receiver positioned within the transmitter radiation lobe, as illustrated in Figure 2.3. The receiver uses a piezoelectric transducer, an electrostatic transducer, or an electromagnetic-harvester based system to convert the acoustic vibration back into electric energy to power the implant.

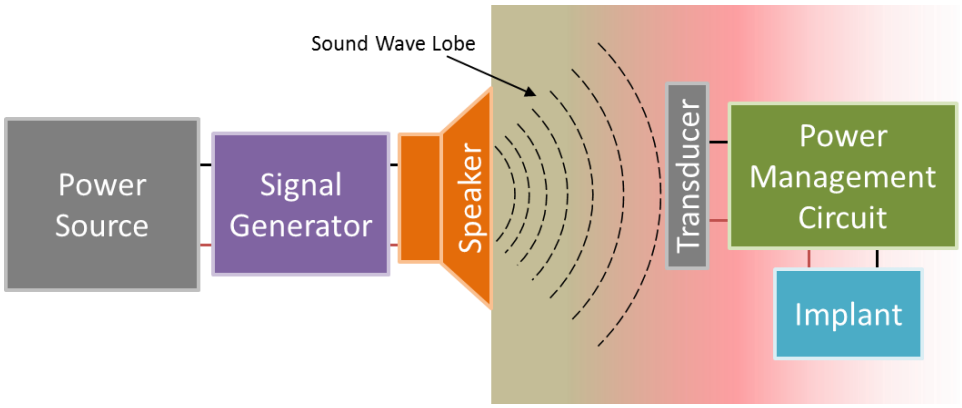

Figure 2.3 – Illustration block diagram of ultrasonic energy transfer.

A piezoelectric transducer could be used for converting acoustic energy back to electrical energy via the piezoelectric effect. A piezoelectric model includes a voltage source in series with a complex impedance network, in which the frequency-dependent reactance vanishes when the receiver operates exactly at the resonance frequency. If the receiver does not vibrate exactly at its resonance frequency, the frequency-dependent reactance can be either positive or negative, so the overall equivalent source impedance may be either inductive or capacitive [20]. The resonance frequency of piezoelectrics can be easily designed to be in the tens of kHz (the ultrasonic range) by varying the dimensions.

An electrostatic transducer is also one of the alternatives for a UTET link [21]. The structure proposed by Zhu et al. is a two degree-of-freedom (DOF) energy harvester which absorbs vibration energy in any in-plane direction. Electrostatic comb variable capacitors C_X and C_Y collect X and Y vibration contributions separately, and flow the currents into the external load. The capacitors are biased with a 100 V DC voltage.

Thirdly, an electromagnetic-based device could also be used to harvest the vibration energy caused by the ultrasonic sound waves of a UTET link. It is designed based upon Faraday's law of induction. By having a time varying magnetic flux pass through a coil of conductive wire, a current in the circuit is generated. The magnetic field that is required for the transducer can be provided by either integrated microfabricated magnet(s) or bulk magnet(s) [22]. The vibrations move the magnet(s), thus changing their relative position to the coil, varying the magnetic flux through coil.

In order to minimize the size of the three types of UTET based energy harvesters described above, they are often fabricated using microelectromechanical systems (MEMS) technology. An example of a MEMS electromagnetic energy harvesters, whose size is 2.7 × 2.2 mm, is presented in Ref. [22], while the electrostatic-based harvester has been described in Ref. [21] with fabricated dimensions of 2 × 2 mm. MEMS technology enables vibration harvesting devices to be integrated into implanted devices.

Ozeri and Shmilovitz recommend that an UTET link works best in the frequency range of 200 kHz–1.2 MHz for feasible deployment in implanted devices [20]. This recommendation takes into account the factors of signal transmission attenuation in soft tissue, the Rayleigh distance (area of natural focus at transition point between near and far field wave propagation), and transducer thickness. However, frequencies around 40 kHz are a common choice of operation frequency due to availability of off-the-shelf ultrasonic transmitters [21, 22]. Since an AC signal is received, the rectification and power management circuits for UTET link devices are be similar to a RF link.

Although the results presented in Ref. [20] show output power around tens of milli-watts with tens of volts of input signal, the other studies reported in literature show only nano-watts of output. This indicates that ultrasonic energy transmission is a promising field for development, but still need much improvement for actual implementation in implanted devices.

2.2.1.3 Other Remote Powering Methods

Apart from RF and UTET links, there are some other remote powering techniques including infrared radiation to photodiode array, low-frequency magnetic field to move implanted magnetic rotor, etc. [23].

A near-infrared power supply system has been proposed by Goto et al. [24]. Near-infrared light from a laser diode is received at the photodiode of the implanted device. It is then converted to electric power for charging and powering the device. The photodiode array consists of eight Silicon PIN photodiodes which occupy an area of 5.5 × 4.8 mm each, resulting in 28 × 20 × 3 mm total size. Power management circuit is not needed if the generated infrared is carefully controlled. The device was placed 0.8mm under the skin. It was claimed that after 17 minutes of charging time with 22 mW/cm^2 irradiation power, the power supplied was sufficient for a cardiac pacemaker to operate for 24 hours.

A method to power implanted device via low-frequency magnetic field has been proposed by Suzuki et al. [25]. A rotor outside of the body (rotor 1) couples together with an implanted rotor (rotor 2). Rotor 2 rotates synchronous to rotor 1, due to coupled alternating magnetic fields (like magnetic gearing), and thus electrical power is generated for an implanted device, due to coils being placed around rotor 2. The implanted device (rotor 2) was 10 cm^3 in size. By choosing the appropriate number of magnetic pole pairs for each rotor, the implanted rotor speed can be accelerated. Moreover, a single-phase and multi-polarized generator was applied to multiply the output voltage frequency. With a full-bridge rectifier implemented, the maximum output power could be reached up to 1.9 W for a 2 cm distance between the two rotors and a 70.5 Hz rotation speed of rotor 2. The measured efficiency of the power transfer link was 20%, which is the ratio of input and output power.

2.2.1.4 Self-powering from External Energy Sources

There are some specific devices that are implanted at locations open to ambient energy. Thus, no deliberate powering or power transfer scheme is necessary. Retina prosthesis are subjected to some amount of ambient lighting, and acoustic energy is available to cochlear implants. These devices could be designed to harvest energy directly from external energy source, which they are trying to measure, without the need of a deliberate energy transfer link.

Retina prosthesis consists of photodiodes fabricated in CMOS technology for energy harvesting [26]. In a typical semiconductor image sensor, a reverse biased PN junction diode (photodiode) is used to sense the incident light. Voltage (or current) signals on the photodiodes are read, processed, and digitized for reconstructing images falling on the focal plane of the photodiode array. On the other hand, if the photodiode in each pixel is forward biased, it could also work as a micro solar cell. One pixel of the implemented photodiode array is the energy harvesting and imaging (EHI) pixel. Transistors are used to switch the photodiodes between harvesting and sensing modes by alternating between forward or reverse bias. The incident lighting generates a current that could be transferred to the load or storage device. Upon switching, the received light information is then read out to the image processing circuit, powered by the harvested energy. At the maximum power point (MPP), the 54×50 EHI pixel array produces 380 mV and 8.75 μA, resulting in 3.35 μW of power delivered to the load for 60 klux illumination. Delivered power drops to 2.1 μW and 1.0 μW for 20 klux and 10 klux illuminations, respectively. Measured energy harvesting efficiency of the EHI pixel was around 9.4% for illuminations between 10 and 60 klux.

A cochlear implant that harvests acoustic energy has been proposed in [27]. Cochlear implants are used to restore hearing of those with hearing loss. Conventional cochlear implants include power hungry components such as microphone, sound processor, transmitter, and implant transducer. The concept was to implement an array of cantilever piezoelectric elements with different resonance frequencies within the human hearing band (~20 Hz - 20 kHz). When the cantilevers vibrate due to impinging acoustic sound, energy is generated to stimulate corresponding nerves via implanted electrodes. The proposed cantilevers were fabricated using MEMS technology. For the stimulation of the auditory nerve, it is important to generate required electrical potential from the vibrations of the eardrum. Therefore, bulk piezoceramic was chosen as a piezoelectric material due to its higher voltage output among other alternatives (such as sol-gel and screen-printed PZT). Measurement showed that with vibration of 0.1g (claimed typical vibration level of the eardrum), the cantilever could generate sufficient voltage to stimulate the auditory nerve.

2.2.2 Internal Energy Sources

Devices implanted into the body can be powered not only by external energy sources, but also energy sources internal to the body. An implanted electronic device can harvest energy within human body from sources including the expansion and contraction of muscles and arteries in the cardiovascular system, forces in joints and muscles, and chemical reactions. It is favorable to produce energy for implanted devices internal to the body, so that no deliberate actions need be taken on behalf of the patient. This is a similar strategy to self-powered devices, however, all energy is derived from sources internal to the body. The energy available in the body is large, however, an implanted device can only take advantage of a small portion of this energy, local to the device.

2.2.2.1 Cardiovascular System

Kinetic energy in the cardiovascular system arises via the displacements caused during the actuation of muscle tissue or pulsing of arteries by heartbeats. These types of energy are harvested by electromagnetic induction, and piezoelectric polymers or crystal based transducers.

In the case of induction, an oscillating mass, most commonly a permanent magnet, is driven through the displacements of muscles in the body, namely the heart. The oscillation of the mass comes by virtue of its inertia, as it tends to lag the motion of the heart. This phase lag creates relative motion between magnet (free to oscillate) and coils (fixed relative to the heart), thus inducing current flow via Faraday's law. Naturally, this relative motion is then frequency dependent and the dynamics of the harvester must match that of the heart, for highest performance. Piezoelectrics can also take advantage of this relative motion by using beams or membranes with piezoelectric elements, which are free to oscillate while their bases are fixed to the heart. Piezoelectrics can also be stressed directly (in phase) via pressure in expanding arteries.

Deterre et al. [28] reported a typical frequency spectrum of the heart. The acceleration spectrum of the heart can be derived by taking the Fourier transform of the time series of acceleration data at a point on the heart surface. The spectrum shows the greatest peak around 1-1.5 Hz with a magnitude of around 0.27 g (2.65 m/s^2). This is intuitive as this is the primary beat frequency of the heart. It is difficult for small energy harvesters to achieve such low frequencies. Though, the spectrum reveals a broadband plateau between 21-27 Hz of an amplitude around 0.1 g (0.98 m/s^2), that could be advantageous to target for an energy harvester. The peak at lower

frequency is regarded as too impractical to target, especially for MEMS devices as the volume and mass needed would be be too great for a small implantable device. Deterre et al. also noted the wide profile of the 21-27 Hz plateau making it ideal for a low quality factor or significantly damped energy harvesting system. It was then proposed by Deterre et al., although not fabricated or tested, a design whereby a linear transducer is used, which could power a pacemaker consuming 50 μJ per heart beat or around 100 μW. This performance is accomplished by utilizing a configuration that outputs 30 μW per gram of seismic mass, necessitating the use of a 3.5g tungsten mass. Tungsten was chosen so that the dimensions of the mass could remain small enough to fit in a 500 mm^3 harvester.

Zurbuchen et al. [29] characterized the motion of a sheep's heart as an analog to the human heart. They measured the motion of heart's surface in three-dimensions and used this information to find an energetically favorable spot to place a pendulum motion based energy harvester, consisting of the mechanism from a commercially available self-charging wrist watch. With the generator composed of a self-charging wristwatch mechanism, it was reported to provide an average power output of 16.7 μW or 11.1 μJ per heart beat when the generator was sewn in-vivo to a sheep's heart, which was beating at 90 beats per minute. Without any optimization of the device, it was claimed to be able to power the latest pacemaker, when not considering losses in the subsequent storage and control circuitry.

The longitudinal (in-plane) and radial (out-of-plane) displacements of the heart provide a solution space for many distinct mechanisms of inductive and piezoelectric energy harvesting, as reported by Khaligh et al. [30]. As the displacements on the surface of the heart are complex and three-dimensional in nature, both types of harvesters utilizing in-plane and out-of-plane motion are feasible for use in powering implantable devices.

For piezoelectric energy harvesting in the cardiovascular system, Polyvinylidene fluoride or PVDF is used due to its high piezoelectric properties and compliant nature [30-36]. In these applications the PVDF is wrapped around expanding/contracting arteries and muscles to harness the deformations or placed as a membrane adjacent to the blood flow to harness oscillating pressure differentials in veins as illustrated in Figure 2.4(a) and (b) respectively.

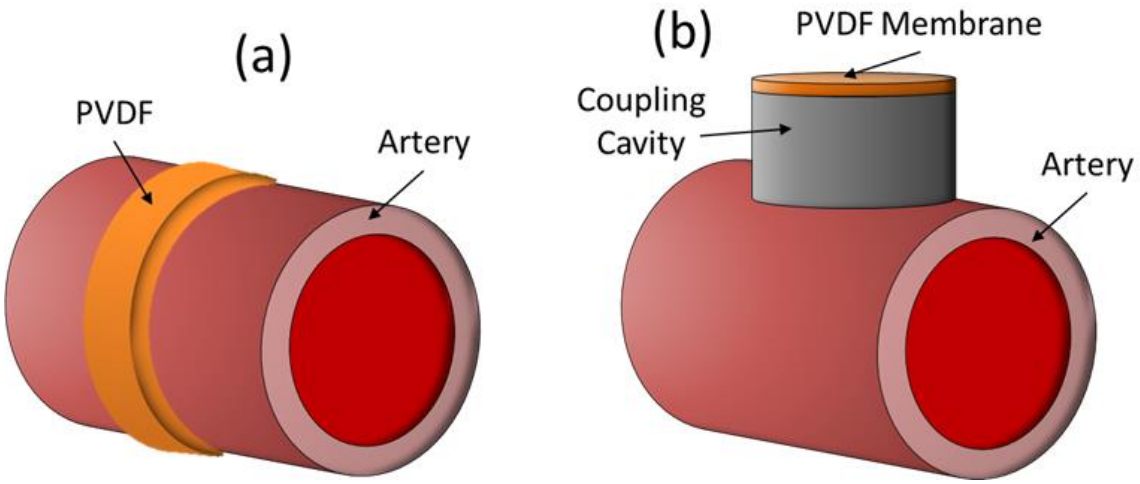

Figure 2.4 – Illustration of blood vessel (artery) (a) wrapped in PVDF film and (b) with attached PDVF membrane, for the harvesting of radial stresses and oscillating blood pressure, respectively, due to heart beats.

In the case where PVDF is wrapped around an artery, the pulsing blood flow and subsequent pulsing blood pressure causes the artery to expand and contract radially due to the compliance of the blood vessel. Both Potkay and Brooks [32], and Fadhil et al. [33], adopted similar designs. These designs involve embedding PVDF thin film inside a silicon cuff that is placed around the artery. Both studies demonstrated that power output can be increased by making PVDF cuff thinner, thus increasing the strain in the piezoelectric. The power can also be increased by increasing the length along the artery which the cuff runs. Experimentation was conducted by attaching the PVDF cuff around 12.7 mm Latex tubing and pulsing pressure through the tube. Potkay and Brooks achieved a power output of 16 nW across a 125 MΩ resistance with a 28 μm PVDF film. Fadhil et al. utilized the same method, however, thinning the piezoelectric down to 17 μm in thickness where they predicted a 30 nW of power per layer of PVDF across a 125 MΩ resistance. Blood pressure inside the artery reaches 120/80 mmHg during normal circumstances and can reach up to 250/150 mmHg while in hypertension. Naturally, the level of harvested power is directly proportional to the blood pressure and resulting strain at the arterial wall. Thus, the harvester maximizes energy output at higher blood pressures, however, one would not expect high blood pressure to be maintained indefinitely and power estimates for this type of device should be given at resting/normal pressure.

Deterre has also investigated the use of PVDF membrane actuated by blood pressure [34]. In this work, a PVDF membrane was located at the end of a branch of an artery, resembling a "T" connector. In this way the membrane does not impede blood flow and is actuated by changes in static pressure at the membrane. Detailed examination was conducted on the effects of various methods of energy extraction from the piezoelectric polymer. These methods are namely classical AC, classical DC, and active charge extraction method also known as synchronous switch harvesting on inductor.

Deterre et al. have reported on using the stagnation pressure of a diaphragm inside the heart as blood flow again the device [31, 35]. The proposed device would be placed within a cavity in the heart, utilizing the turbulent nature of the blood flow in the heart to rapidly oscillate the harvester. Fluctuations in pressure are transferred through a flexible diaphragm with corrugated micro-bellows and rigid shaft to a spiral spring with patterned electrodes and piezoelectric bimorph. Circuitry similar to that reported by Deterre et al. used in Ref. [29] converts the AC power produced by the oscillating piezoelectric in to DC power, with a small amount of energy lost due to deformation of the packaging (micro-bellows). The energy density of the fabricated device was reported to be 3 μJ/cm3/cycle, while for a concept design it was predicted to be 6 $\mu J/cm^3$/cycle.

Wang et al. have demonstrated Poly-dimethylsiloxane (PDMS) films that exhibit both piezoelectric and electret type properties, allowing for d_{33} charge coefficients much higher than that of PVDF films [36]. These cellular PDMS films have an elastic modulus up to 32% lower than solid PDMS. These materials could provide further opportunity to improve the performance of flexible harvesters.

2.2.2.2 Muscles and Joints

Kinetic movements of the body are among the most powerful sources of energy available for harvesting devices. There are a myriad of external kinetic energy harvesters, however, implantable devices are rarer. An interesting implantable energy harvester is the knee implant designed by Almouahed et al. [37]. In this work, multilayer piezoelectric stack elements are inserted into the base (tibial component) of an artificial knee implant and are stressed by an intermediate plate, which supports the femoral component and thus the weight of the body. With such a setup, forces ranging from 1000 to 2500 N were applied during the gait motion in

experimental trials. A model for predicting open circuit voltage output was provided which matched well with the experimental trials. The RMS power output from this implant was on the order of several milliwatts under optimal load resistance conditions.

Implanted bio-compatible material could generate energy from tension in the attachment of muscle tendon to the bone as proposed by Lewandowski et al. [38]. In this work, a piezoelectric generator is affixed between the bone of a rabbit and the attached tendon (Fig. 28). Apart from harvesting the energy from movement, the device also stores energy for use by other devices, but also uses some of the harvested power to stimulate the muscle. Lewandowski et al. demonstrated that sufficient energy is harvested to continue the process of stimulating the muscle and harvesting the movement, as the animal is adding work each time from its metabolism. A power output between 150 and 300 μW was observed depending upon the applied load (60-100 N), duration (0.25 s), and displacement (2-23 μm). As with the knee implant, a relatively high power is observed, due to the large forces involved. The power output from this work is unregulated and Lewandowski et al. highlight the need for additional regulatory circuitry to be able to ensure that the stimulation pulse given to the muscle is kept to the minimum necessary to produce the desired twitch force.

Using piezoelectric nanowires, it is also possible to harvest energy from small and delicate areas of the body. The expansion/contraction of the lungs in breathing is another kinetic motion which has been investigated by Li et al. [39]. The lungs of a rat were used to stress a single-wire generator (SWG), or a single strand of piezoelectric wire. It was found that on average 3mV and 30pA (90 fW) could be produced. Similarly, Falconi et al. examined the modeling and integration of piezoelectric nanowires throughout the body [40]. In this study it was also reported that the energy production is on the order of femto-joules. Power production is low in these cases due to the small capacitance of piezoelectric nanowires.

2.2.2.3 Chemical Energy Fuel Cells

Chemical energy could be directly harvested in the body by use of a fuel cell. Glucose fuels cells have shown promising results in energy harvesting from sugar in the body [41-43]. The glucose fuel cell operates by oxidizing glucose into gluconic acid, releasing two electrons. The released electrons then flow across a load resistance. The structure of a glucose fuel cell and chemical reaction are illustrated in Figure 2.5.

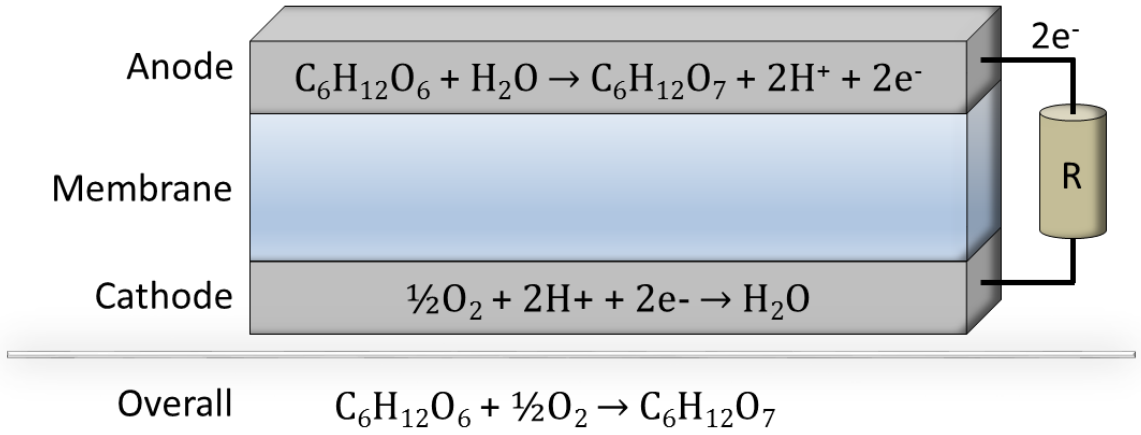

Figure 2.5 – Illustration of structure and chemical reactions of an abiotically catalyzed glucose fuel cell.

The concept requires that the fuel cell be placed in some proximity to blood flow, such that blood glucose could be reacted in the fuel cell. The power output from such fuel cell devices is reported to be in the range of microwatts per square centimeter. Kerzenmacher et al. also reported that after 50 days in a "physiological glucose solution" their device was still operating stably, indicating it is a good candidate for long term energy harvesting as compared to the short lifespan of devices based on enzymatic catalysts.[43] A glucose fuel cell was designed by Southcott et al. for the purpose of powering a pacemaker. Their fuel cell was 100 mm × 40 mm × 3 mm in dimension, so it would not fit in their pacemaker (Affinity DR 5330L, St. Jude Medical). The study demonstrated that fuel cell can, however, produce approximately 600µW which is enough to nominally power the pacemaker, t the dimensions are large.[44]

2.3 Selection of Energy Harvesting Strategy: Vibrations

While electromagnetic harvesters have shown that they can meet the size and power requirements for implantable pacemaker applications, there have yet to be studies available that include their interaction with existing pacemaker measurement and control circuitry. The question of whether the strong magnetic fields of the generator's permanent magnets or electromagnets will interfere with the functioning of the device needs to be addressed in future studies. After all, those

who received implanted cardiac pacemakers and instructed not to linger near high-voltage power lines or microwave ovens, which both radiate electromagnetic fields.

The human body is an excellent source of energy and there exist numerous approaches to harvest these energies to power implantable devices to increase quality of life. Solar energy and acoustic vibration can be harvested by retina prosthesis and cochlear implant, respectively. Knee prosthesis could harvest movements of knee joint. Remote powering of devices could be done by means of electromagnetic energy (including light energy) or ultrasonic vibration. Internally available energy could be obtained from cardiovascular system's movements or thru chemical reaction with body fluid.

It has been demonstrated that energy harvesting devices of various forms have the potential to derive appreciable amounts of energy. However, remote powering link loss or low output power is the main challenge of this particular application. As all implanted devices should remain small in size, advances in material selection, transducer design, and fabrication could be direction for future study. It remains to be seen whether energy harvesting can be done without significantly altering the performance of the body, or being noticeable by the wearer. Any device which causes the user to deviate from their normal activity will not be generally accepted.

There is the need for these devices to be tackled as a system design problem, since all parts (transducer, circuitry, sensors, human body, etc.) are all coupled and should not be considered alone. For example, if transducer interferes with sensor function, it is of little merit whether sufficient energy is produced, as the device will not function properly. This is true of energy harvesting devices in general, but is exceedingly important for implantable devices as the source of energy has feelings and is affected by the inclusion of harvester.

From the various forms of energy harvesting techniques presented here, it can be concluded that attempting to power pacemakers through the displacements (vibrations) caused by the beating of the heart would be the best option. This is largely due to their ability to fit within the size requirements of the pacemaker housing. Vibration harvesters are mostly higher aspect ratio and thin devices, the dimensions of which match well with the space available, as well as, being promising in their level of harvested power.

Like the review of implantable energy harvesters, a review of the state-of-the-art in vibration energy harvesters is now given.

2.4 Review of Vibration Energy Harvesters

Low frequency excitation sources, such as automobiles, the human body, industrial machines, electronic devices, and domestic appliances, are source of mechanical energy in the form of vibrations, that can be scavenged to power or recharge the low power devices such as cell phones, MEMS components [45, 46], pacemakers [47], cameras [48], wireless sensors and actuators [49, 50]. The demand for energy harvesters for battery charging or replacement exists in scenarios where maintenance is expensive and time consuming [51, 52]. Wasted mechanical energy can be converted into usable electrical energy through transduction mechanisms, such as electromagnetic [53], electrostatic [54], or piezoelectric [55-57]. It has been shown by Marin et al. that the piezoelectric transduction becomes relevant at the smaller size scales in the vicinity of 1 cm^3[58].

A significant impediment in the deployment of vibration-based piezoelectric energy harvesting devices has been the limitation that most of the low frequency transducers, usually in the form of unimorph or bimorph cantilever beams, extract energy in a very narrow bandwidth around the transducer's fundamental frequency. In such devices, slight deviation from the fundamental frequency causes a significant reduction in the level of harvested power, in some cases by orders of magnitudes. Because the ambient energy sources can include multiple and time varying frequencies, this impediment has directed the research in designing structures whose resonant frequency can be actively modulated to match the frequency of ambient vibrations.

Recent strategies for conforming the frequency response of an energy harvester to its vibration source are based on exploiting nonlinearities through harvester geometry, boundary and loading conditions to tune the resonance frequency and broaden the bandwidth. Ben Ayed et al. modeled the frequency response and power output of linear and quadratic geometrically tapered piezoelectric cantilevers [59]. Masana and Daqaq characterized the effect of axial loading of the natural frequency of pre-critical buckling load beams [60]. A study by Challa et al. determined the response of a cantilever beam with permanent magnet tip mass, to attractive and repulsive forces from external magnets by varying proximity to the beam [61]. In the study conducted by Mann and Sims, a low frequency system was designed using two fixed magnets to levitate a center oscillating magnet [62]. Investigations by Shahruz [63], and Sari et al. [64], show that wide bandwidth response can be achieved by creating arrays of geometrically varying cantilevers. Tang

et al. as well as Twiefel and Westermann have compiled reviews of other notable broadband vibration energy harvesting techniques [65, 66].

Vibration-based energy harvesters have recently received significant interest in order to operate low-power electronics and replace small batteries that require expensive and time consuming maintenance. Several investigations have been performed to design high power density energy harvesters from unused mechanical vibrations [48, 51, 52, 56, 67, 68]. These designs vary from simple beam and beam-mass systems [60, 68-71] to more complex structures including bending-torsion, zigzag, and spiral systems [72-74]. The objective of these diverse harvesters is to enable the harvesting of energy at specific frequencies from wasted mechanical energy in the given environment through various transduction mechanisms. Examples include electrostatic [56], electromagnetic [75], and piezoelectric [56, 68-70]. As mentioned earlier, the piezoelectric option has gained prominence at small-scale, especially when the dimensions are in the range of few cubic millimeters.

A piezoelectric cantilever beam, subjected to harmonic or random vibrations, is the most common concept used in the literature. For these types of energy harvesters, resonant responses are obtained when the excitation frequency matches the natural frequency of the harvester. These resonant motions result in maximum deflection of the structure, straining the piezoelectric material and producing electrical charge, which can be channeled as an alternating current across an electrical load resistance. Different strategies and techniques have been applied to design efficient, low-frequency, piezoelectric energy harvesters, such as considering different shape geometries [72-74, 76-79], developing bistable configurations [62, 80], and including magnetic coupling [68, 71]. As for shape geometries, simple and complex systems have been proposed in order to design energy harvesters that can operate effectively at an excitation frequency that matches their resonant frequency. In general, passive tunable harvesters have been designed by using cantilever, spiral, or zigzag configurations. However, a comparative analysis in terms of the efficiency of these simple and complex energy harvesting designs is missing.

Piezoelectric energy harvesting has long made use of the cantilever beam due to its ability to transfer a high amount of strain to the attached piezoelectric layers, frequency tunability, and ability to generate closed form analytical modeling.[81-85] However, the shortcomings of the cantilever structure, including narrow bandwidth and the need for large tip mass and/or impractically high aspect ratio to reach low resonance frequencies have been well established.

Surmounting these deficiencies in the one-dimensional cantilever-based vibration energy harvester has been a major focus in the literature, where techniques such as inducing nonlinearity using magnetic coupling configurations[47, 65, 68, 86], axial loading,[60, 65] and mechanical stoppers,[87, 88] varying cross-sectional geometry,[76, 77, 89] and employing two-dimensional geometries[47, 78, 79, 90-100] have been examined. In this study, a '1D' cantilever is defined as a structure that has constant cross-section, '1.5D' as a structure whose cross-section varies along a single axis, and a '2D' geometry as a structure where the cross-section curves or meanders in a plane. It has been shown that 2D beam shapes can outperform 1D beams in terms of power density and low resonance frequency for a given surface area.[99]

Vibration energy harvesters are designed most often to operate at resonance, where the resonant frequency of the energy harvester matches that of the dominant frequency of the vibration source. This matching of source and harvester mechanical impedances allows for the most efficient transfer of power from the source to the harvester. Therefore, having more power available to the harvester, more power can be transduced. The tragic consequence of such designs is that outside the narrow resonant frequency band, little power is converted. Addressing vibration energy harvester bandwidth, and increasing power output have been the major pursuits of researchers in this field for many years. To this point, several review and comparison articles have been written chronicling and categorizing the various strategies developed.[57, 65, 81-84, 101-104]

For any vibration energy harvester, it is paramount that the harvester's frequency response match that of the source. Figure 2.6 below shows the level of excitation (base acceleration) received by a pacemaker due to the beating of the heart, with data derived from the work of Deterre et al.[28] Here the largest acceleration is around 1-2 Hz, which is caused by the primary beating frequency of the heart. Additionally, there is a broader peak between 20-30 Hz. This peak is caused by soft tissue resonance (or ringing) around the heart in response to the width of the impulse of each beat.

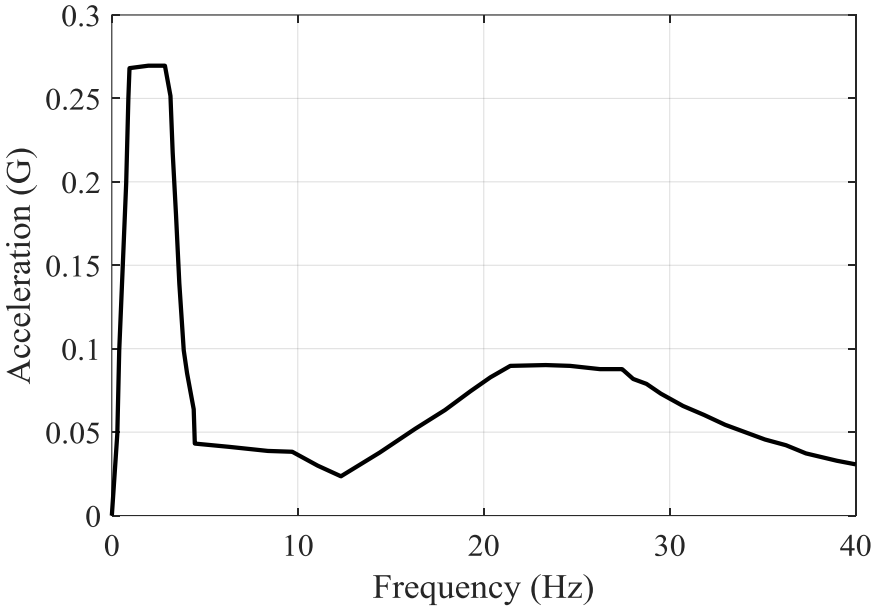

Figure 2.6 – Excitation level of vibrations received by a pacemaker as a function of frequency. Data derived from Ref. [28].

For a vibration energy harvester of the dimensions necessary to fit within the pacemaker housing, a 1-2 Hz resonance frequency would prove quite difficult to effectively achieve. Therefore, the broader 20-30 Hz peak will be targeted as a more realistic goal. Additionally, since the level of excitation at this broad beam is around 0.1 G, all studies on power output are conducted at this level of excitation.

From this review, it is evident that 2D vibration harvesters show promise, but have yet to be compared directly to their 1D or 1.5D counterparts in terms of output power and bandwidth. For this reason, the design of a vibration energy harvester suitable in terms of form factor, frequency response, and level of harvested power is first explored by comparing the merits of 1D and 2D vibration harvesters. To capture the broad resonance peak, a means of increasing the resonant bandwidth of vibration harvesters is then explored. Finally, studies on optimizing vibration harvester mode shapes for maximizing power output are conducted.

2.5 Comparative Analysis of One-Dimensional and Two-Dimensional Beam Shape Vibration Energy Harvesters

2.5.1 Introduction

In this section, focus is placed on comparing the performance between classical (one-dimensional) piezoelectric energy harvesters (beam-mass system) and complex (two-dimensional) piezoelectric energy harvesters (zigzag system). Experimental measurements are performed for these two types of piezoelectric energy harvesters with the same footprint (surface area) to quantify the power density and tunability. First the designs for each harvester are established, based on their most common configuration; the bimorph configuration for the cantilever harvester and the unimorph configuration for the zigzag piezoelectric energy harvester. The dimensions were chosen for each design, as shown in schematics in Figure 2.7, such that the zigzag would have 25.4 x 25.4 mm^2 area (approximately the area available in the pacemaker housing) and the cantilever would have approximately the same surface area. In this way, conclusions can be drawn about the performance of both of these structures and identify the regions where one has advantages over the other.

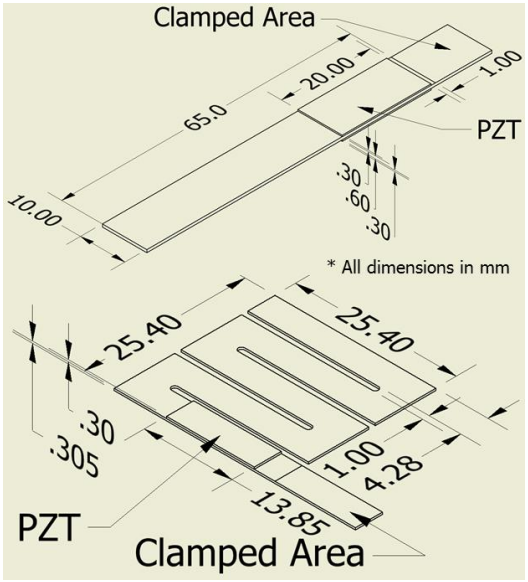

Figure 2.7 – (top) Schematic of a bimorph piezoelectric cantilever energy harvester (PZT on aluminum substrate), and (bottom) Schematic of unimorph piezoelectric zigzag energy harvester (PZT on steel substrate).

The same piezoelectric material was used in both configurations to allow for reasonable comparisons to be made between the output power density and overall magnitude of the power. The piezoelectric material utilized was APC 850 PZT with a $-d_{31}$ value of 175pC/N and a $-g_{31}$ value of 12.4×10^{-3}Vm/N.

2.5.2 Fabrication

The energy harvesting prototypes were constructed by first cutting the beam substrate shapes from larger sheets of material (Aluminum and Steel for the cantilever and zigzag configurations, respectively) via CNC machining. Different substrates were chosen for this comparison so that the frequency response characteristics of the two harvesters might be brought closer together, allowing for reasonable comparisons to be made. Since the zigzag structure is naturally more compliant than the classical cantilever, steel was chosen as the substrate making it stiffer. Thus, the two harvesters would have overlapping frequency regions when paired with appropriate tip mass, due to the relation to the natural frequency given in Equation (1.16). The piezoelectric elements were then bonded to the substrate at the areas of highest strain concentration in order to harvest the greatest amount of power without significantly increasing the stiffness and consequently the resonance frequency of the system. The bonding was accomplished using Loctite 120HP epoxy and allowing a cure of no less than 24 hours at room temperature before testing. The fabricated prototypes are shown in measurement setups in Figure 2.8.

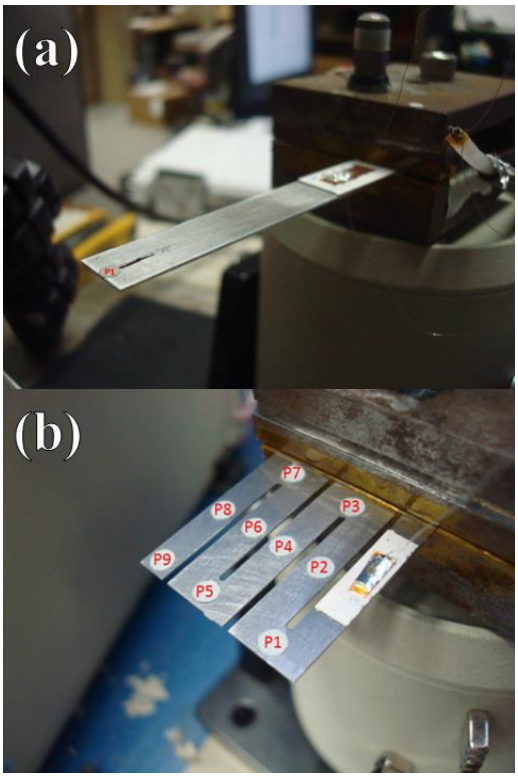

Figure 2.8 – Constructed (a) cantilever bimorph and (b) zigzag prototypes mounted in shaker clamp with labeled points of interest.

2.5.3 Experimental Setup

The constructed prototypes have reflective stickers (of negligible mass) placed in a pattern in the case of the zigzag configuration and at the beam tip in the case of the cantilever configuration to allow the use of a laser Doppler vibrometer to monitor the velocity at those points. Note that the point labels were overlaid on the picture for illustration purposes and were not present on the physical stickers, thus not altering their reflectivity. The experimental setup and specific measurement equipment are displayed in Figure 2.9.

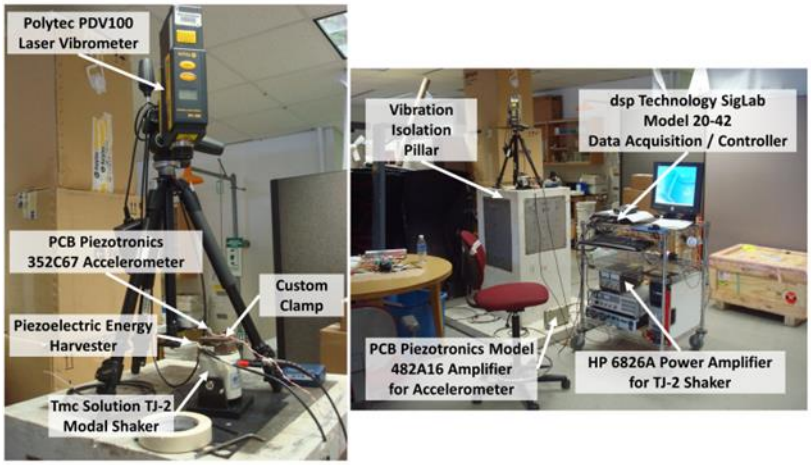

Figure 2.9 – Experimental setup for cantilever and zigzag piezoelectric energy harvester tests, with key components labeled.

The measurement system was controlled via desktop computer interfaced with the SigLab module. The SigLab produces a specified excitation voltage signal (sinusoidal wave in this case) at low current, which was then passed through the HP power amplifier, increasing the current of the signal, to power the TJ-2 shaker. The acceleration of the base of the energy harvesters (clamp) and velocity of the various points on the beam (Figure 2.8) were read by the SigLab from the PCB accelerometer and PDV100 vibrometer, respectively. The voltage output from the piezoelectric material was also recorded (across varying load resistances) by the SigLab. All measurements were done atop a vibration isolation pillar, which by virtue of its mass and location, was largely uninfluenced by the vibration of the surroundings (i.e. building, floor, persons walking, machinery, etc.). All cables used were BNC type, to provide shielding from any external electromagnetic noise sources. As can be seen in Figure 2.8, the BNC cable was not directly attached to the piezoelectric elements in each harvester rather it was attached via copper tape (~51μm thickness) and thin (44 gauge) wire. This approach was implemented for several reasons. Thin wire was used so that the attachment of wire(s) will not add any significant mass or stiffness to the piezoelectric energy harvesters and thus not alter their dynamics. The wires were first soldered to the copper tape and then adhered to the piezoelectric surface. In this way, one can avoid exposing the piezoceramic to high local temperatures associated with the direct application of molten solder. The poling directions and wire attachments used are shown in Figure 2.10.

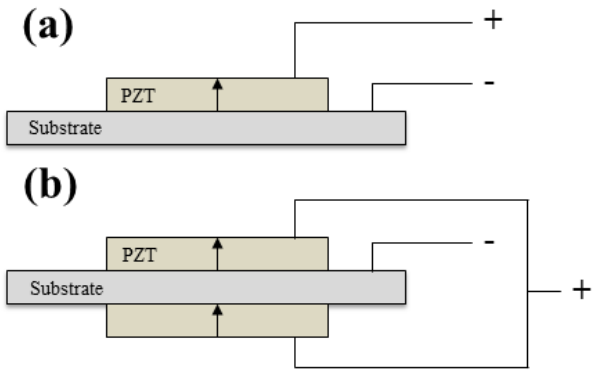

Figure 2.10 – Poling direction and wire connection diagram for (a) zigzag unimorph harvester, and (b) cantilever bimorph harvester with piezoelectric elements were wired in parallel.

2.5.4 Experimental Analysis & Results

Analysis is begun by examining the frequency response dynamics of both the systems. This is accomplished by applying a uniform white noise vibration input to each system and examining the Fourier transform of the cross-correlation between the base acceleration and beam tip velocity. In this way, all frequencies are subjected to the same spectral energy and the curves in Figure 2.11 can be regarded as the transfer functions of their respective systems. These measurements are taken for both connecting the piezoelectric elements in short-circuit and open-circuit configurations. One would expect, as is evident in Figure 2.11, that connecting the piezoelectric in short circuit-configuration allows the most charge to flow, effectively reducing the natural frequency by increased damping. For the zigzag case, a smaller volume of piezoelectric material is utilized than in the cantilever bimorph case and thus no measureable difference in frequency response between open- and short–circuit configurations is observed. For this reason, only the open circuit cases for the zigzag configuration are plotted.

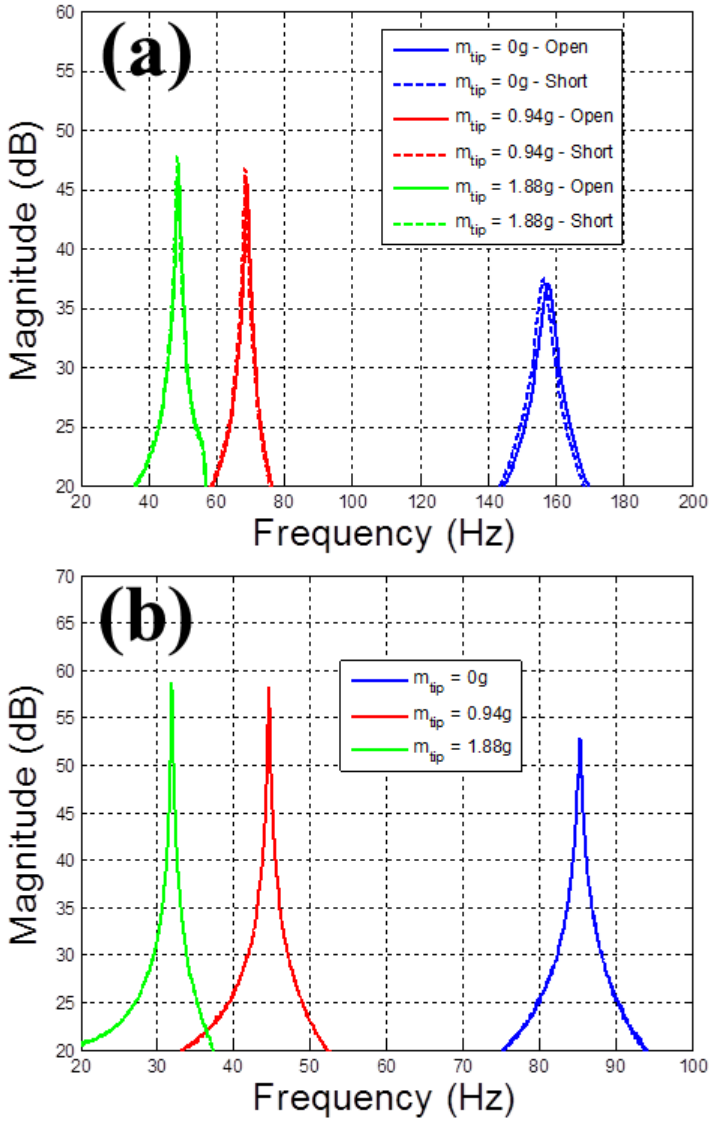

Figure 2.11 – Frequency response of (a) cantilever and (b) zigzag piezoelectric energy harvester for varying tip mass and electrical connection. There is no measureable difference between open and short circuit response for the zigzag harvester, thus only the open circuit response is shown.

In addition, tip masses of 0 g, 0.94 g and 1.88 g are employed to examine their effects on the natural frequency of the harvesters. It should be noted that increasing the tip mass for both the systems results in a decrease in the natural frequency and an increase in the amplitude of harvester's vibration. A plot of the variation of the fundamental frequency as a function of the tip mass is presented in Figure 2.12 where for all tip mass cases the zigzag configuration has a lower

fundamental frequency. The difference between the two systems is exceedingly evident at 0 g tip mass, when the harvester's shape was mostly responsible for its frequency response characteristics.

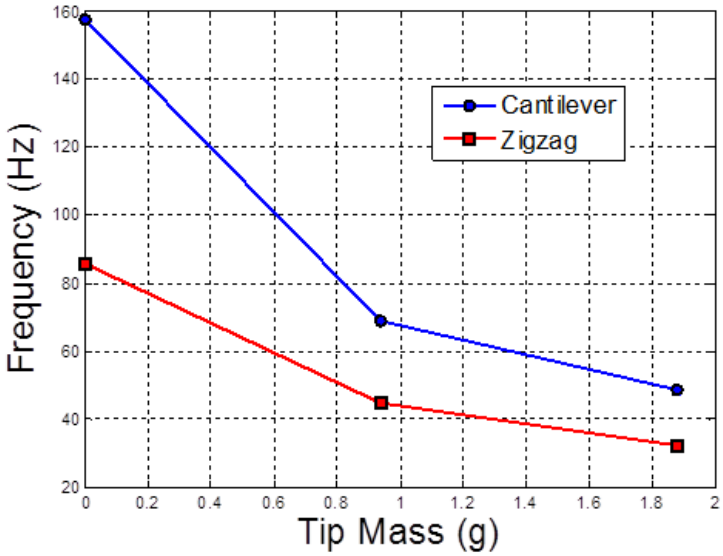

Figure 2.12 – Variation of harvester's fundamental frequency as a function of tip mass for cantilever and zigzag systems.

A comparison between the deflections of the two configurations at their respective first natural frequencies is performed for the case of zero tip mass. Note that all further tests are conducted at 0.1 G base acceleration (where 1 G = 9.81 m/s^2). In Figure 2.13, it is observed that the deflections of the two systems at their respective natural frequencies are similar, with the cantilever system exhibiting a greater deflection at resonance. The displacement plots in Figure 2.13 show the relative displacement of the respective positions labeled in Figure 2.8 and are realized by integrating the laser vibrometer velocity data at each point and averaging over several (at least 10) periods. The base displacement, which is integrated from the base acceleration, is then subtracted, leaving only the relative deflection of the respective points. Finite Element Analysis illustrations of the first natural frequency for each shape are also shown in Figure 2.13 in order to clarify the shape of each of the beams when excited at their respective fundamental frequencies.

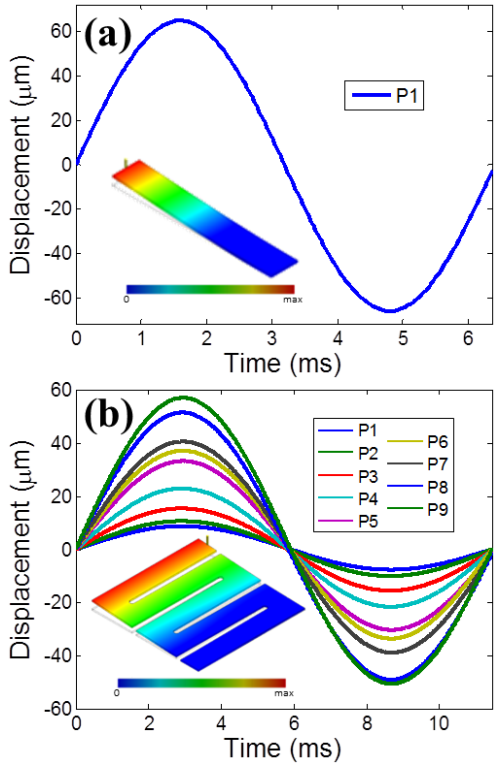

Figure 2.13 – Deflections of the point(s) shown in Figure 2.8 at the first bending frequency of the (a) cantilever and (b) zigzag piezoelectric energy harvesters at a base acceleration of 0.1G. Cantilever frequency is ~156Hz, with max deflection ~66μm, and zigzag frequency is ~86Hz, with a maximum deflection of ~57μm. Insets show FEA results for fundamental mode shape for clarity.

Next, the effects of the electrical load resistance on the performance of the harvesters were identified as shown in Figure 2.14. Here, the electrical load resistance is varied while exciting the system at a fixed frequency and for a given tip mass. The frequency was varied across a range near that of the measured fundamental frequency of each system. It is shown that a similar power output is obtained from both systems, despite their different form factors. In addition, an increase in the tip mass is accompanied by an increase in the harvested power for both systems. However, the more tip mass is increased, the less effective it becomes in lowering the fundamental frequency and increasing the harvested power.

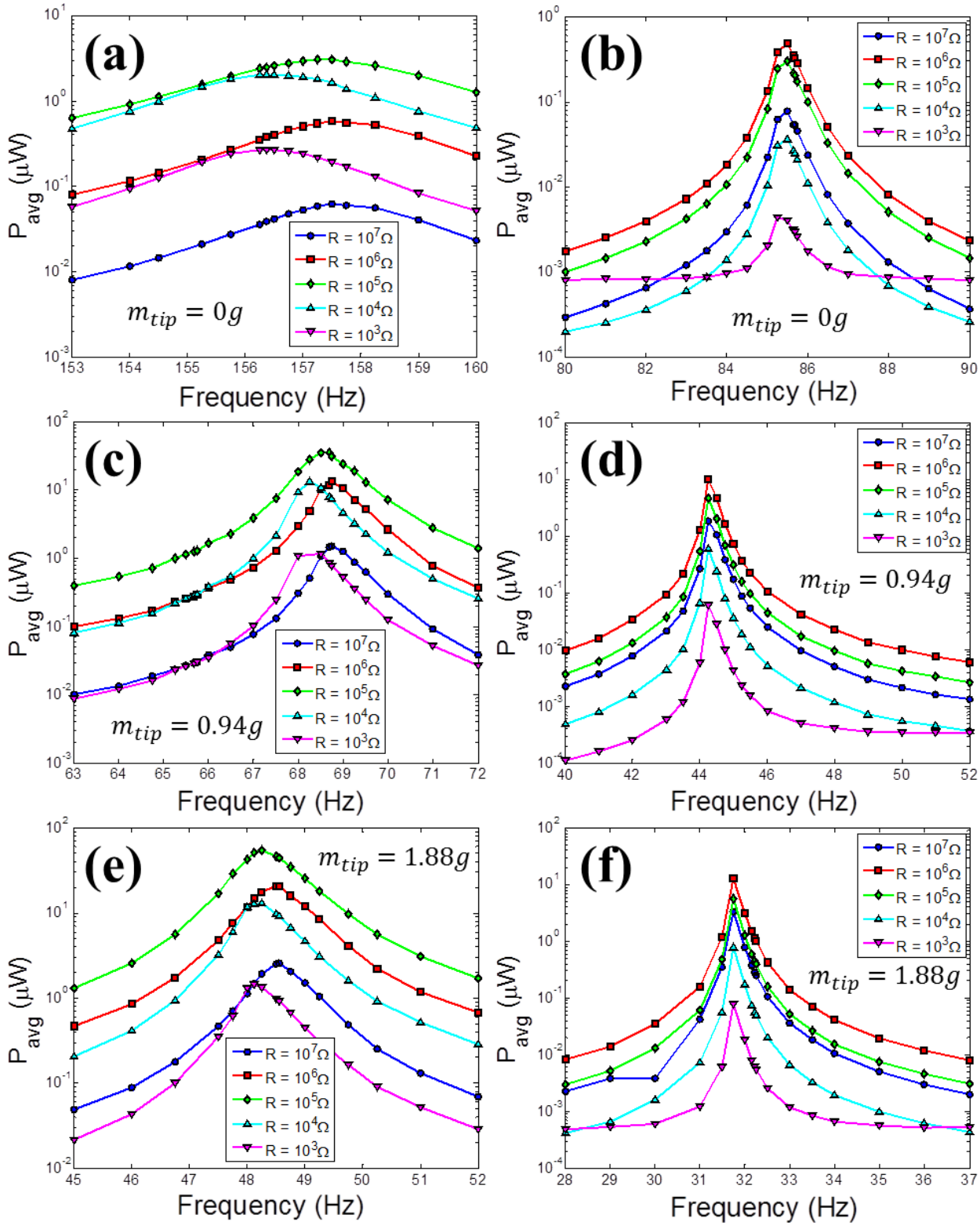

Figure 2.14 – Average power output as a function of frequency, electrical load resistance, and tip mass for (a)(c)(e) cantilever and (b)(d)(f) zigzag harvesters, at a base acceleration of 0.1G.

From Figure 2.14, it is clear that the dynamics of the system changes for different electrical load resistances. In fact, there is a shift in the peak frequency to the right when increasing the load resistance. At higher load resistances, current is reduced and higher values of the generated voltage are obtained. Furthermore, varying the electrical load resistance impacts the amplitude of the average harvested power indicating that some optimum electrical load resistance must exist, whereby the most power can be derived from the piezoelectric element(s). To determine this optimal electrical load resistance, the excitation frequency is fixed to either the short- or open-circuit fundamental frequency for the cantilever configuration or simply the open circuit case for the zigzag configuration and the electrical load resistance varied, as shown in Figure 2.15.

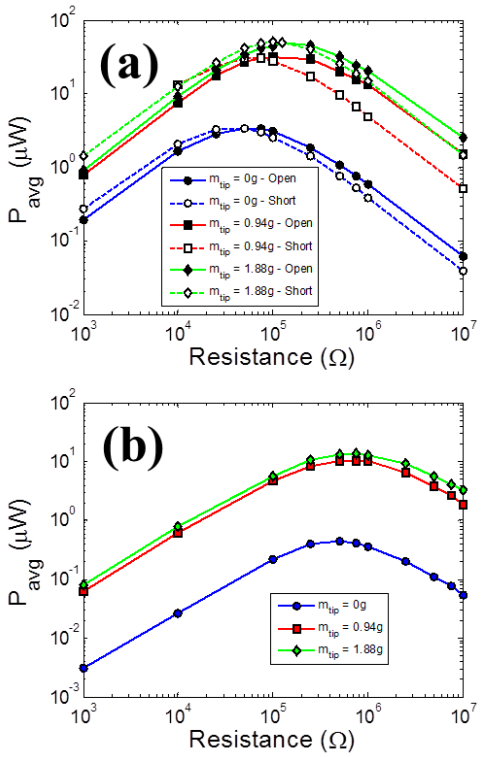

Figure 2.15 – Average harvested power as a function of the electrical load resistance and tip mass at a base acceleration of 0.1G, where for (a) the excitation frequency of the cantilever harvester is equal to the short- or open-circuit frequency, and for (b) the excitation frequency of the zigzag harvester is equal to the open-circuit frequency. These frequencies were found from the FRF's in Figure 2.11.

Figure 2.15 illustrates that the optimum electrical load resistance for the cantilever system is in the range of 50-100 kΩ, depending on the tip mass value, and in the 500-700kΩ range for the zigzag system. The high optimum load resistance of the zigzag configuration is why there is no observable difference between open and short circuit conditions, as the optimum condition is already very near open circuit. The difference in optimal load resistance values between the cantilever and zigzag results from the size of the piezoelectric layer(s) and the considered connection between these layers. These two main factors determine, along with material properties, the capacitance of each harvester. The optimal load resistance can be approximated by the complex impedance of the piezoelectric, or $1/(\omega C)$, where C is the capacitance of the piezoelectric layer(s) and ω is the excitation frequency in rad/s. Here, it can be seen how a larger capacitance for the cantilever piezoelectric energy harvester with parallel connection and its higher natural frequency for different tip masses result in a smaller optimum load resistance values for all considered cases.

With the information gathered, a final comparison of power density or power per unit volume is presented in Table 2.1. The volume of the cantilever harvester is 0.51 cm^3 and the volume of the zigzag harvester is 0.195 cm^3. Table 2.1 summarizes the first bending frequencies and power densities of the cantilever bimorph and zigzag piezoelectric vibration energy harvesters for different tip masses. Clearly, depending upon the available excitation frequency, the zigzag harvester is always significantly better in terms of low natural frequency and power density.

Table 2.1 – Summary of 1D cantilever bimorph and 2D zigzag unimorph piezoelectric energy harvesters power density as function of excitation frequency and tip mass at 0.1G base acceleration.

Shape	Tip Mass (g)	Natural Frequency (Hz)	Power Density ($\mu W/cm^3$)
Cantilever	0.00	157.50	0.73
	0.94	69.00	6.67
	1.88	48.75	10.60
Zigzag	0.00	85.78	2.13
	0.94	44.84	31.31
	1.88	32.34	65.08

2.5.5 Summary

In summary, two piezoelectric energy harvesters (bimorph cantilever and unimorph zigzag shape) were developed (surface <7 cm^2). The results showed that tuned energy harvesters can be designed to harvest energy at low frequency excitation (<100 Hz) and levels of harvested power was on the order of micro-Watts from different configurations with an input acceleration of 0.1 G. Depending upon the available excitation frequency, the tip mass and load resistance can be changed to harvest maximal amounts of power. It was demonstrated that the zigzag piezoelectric energy harvester can be a means of increasing power density for a given harvester area (footprint).

2.6 Increasing Bandwidth Using Preloaded Freeplay Boundary Condition

2.6.1 Introduction

In order to design the low-frequency and broadband energy harvesters a drastically different approach was investigated. This approach was established by inducing a second degree-of-freedom (termed here as preloaded freeplay), which has a resonant frequency near the natural frequency of the harvester, the interaction between which creates a broader resonant plateau rather than a sharp peak. In order to verify this approach, the concept was implemented on two different structures. Firstly, a unimorph zigzag piezoelectric energy harvester was designed that consisted of steel substrate and piezoelectric layer. Secondly, a conventional bimorph cantilever energy harvester consisting of aluminum and piezoelectric layers was utilized. These harvesters were subjected to direct vibration excitations and measurements were performed to determine the effects of tip mass and electrical load resistance on the performance of these harvesters with and without the preloaded freeplay effects, using the experimental setup and experimental methods of section 2.5.

For vibrating systems, besides the physical structure of the system, the condition of the boundaries plays the greatest role in the dynamics of the system. In general, more free boundaries yield lower frequency behavior, and more fixed boundary conditions yield higher frequency behavior. This performance comes about because of the boundary condition's effect on the stiffness of the vibrating system. Since most ambient vibration sources are relatively low frequency, in energy harvesting applications one of the boundary conditions is almost always a

free condition. Typically the free end is considered to be the tip of vibrating beam and is where mass is placed to alter resonant frequencies and amplitude of vibrations.

The other end of the beam, the base, typically has some form of clamping or fixation. For vibrations occurring in one dimensional translation, beams can have both translational and/or rotational degrees-of-freedom. Thus, for each degree-of-freedom there can be various levels of clamping or freedom. Illustration of the three most common types of vibration boundary conditions are shown in Figure 2.16. Pendulums allow free rotation but do not allow for (or clamp) translation. Pendulums offer very low frequency performance thanks to the freedom at the boundary, since the only restoring force is gravity. Clamped beams, or cantilevers, do not allow rotation or translation of the beam at the boundary. Cantilevers have relatively higher frequency performance due to the fixed boundary, with the stress in the beam providing a restoring force. The hybrid between Pendulums and Clamped boundaries is the Freeplay boundary condition. In freeplay, translation is free, however, rotation is fixed. The vibration response due to such a boundary condition can be nonlinear and chaotic.

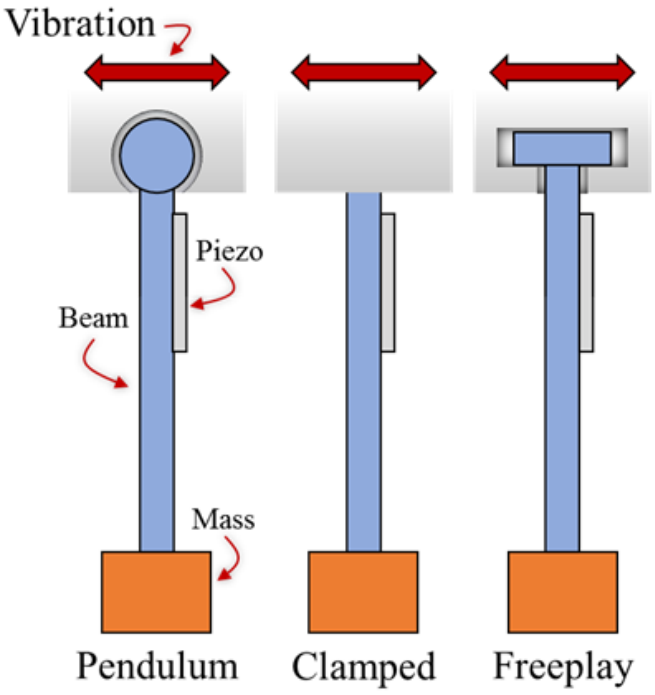

Figure 2.16 – Illustration of the three most common types of vibration boundary conditions in Pendulum (free rotation, clamped translation), Clamped (clamped rotation, clamped translation), and Freeplay (clamped rotation, free but bounded translation).

Pendulums do not lend themselves well to piezoelectric energy harvesting since the beam is not stressed. Indeed, since rotation is free, there is nothing to cause bending stresses to be transduced by the piezoelectric layer. Rather, they find application in electromagnetic harvesters, not discussed here. Due to this reality, clamped cantilevers are nearly exclusively employed in piezoelectric vibration energy harvesting applications. Freeplay boundaries can allow some relative motion between the beam and vibration source. When the beam translates against the bounds of the freeplay, an amplified bending occurs since the base of the beam has an initial velocity condition. This dynamic can aid in energy harvesting and harvester bandwidth, but is inherently chaotic.

Combining the clamped and freeplay boundary conditions, into the so-named "preloaded freeplay" boundary condition was shown to significantly increase the harvester bandwidth without creating chaotic vibration behavior.[105]

2.6.2 Concept Description

The characterization of freeplay has been studied in the context of aeroelastic vibrations, where it is considered a negative effect, since it can create instabilities and make it difficult to control aircraft [106]. However, in this section, I propose to utilize freeplay as a positive effect in energy harvesting.

We start by proposing a clamp which is connected to the vibration source (shaker) by a screw with threads that are slightly mismatched with those on the shaker adapter. Through this modification, the screw is still able to be tightened and secure the clamp to the shaker as shown in Figure 2.17(a). However, there is a larger than normal air gap between the external threads of the clamp screw and internal threads of the shaker adapter as shown in Figure 2.17(b). The preloaded (tightened) screw with the clamp acts as a spring-mass system as shown in Figure 2.17(c). When this spring-mass system resonates, there is enough force to overcome the applied force due to the preload condition. This phenomenon causes a freeplay to occur between the clamp-screw and shaker adapter, creating a second degree-of-freedom. Therefore, there is a degree-of-freedom caused by the stiffness of the PEH (k_{beam}) and another degree-of-freedom between the clamp and the vibration source (k_{screw}). It is important to note, that this freeplay condition and subsequent second degree-of-freedom only exists in the frequency band where the clamp-screw system resonates and at all other times it can be considered as a single degree-of-freedom system. By

tuning the natural frequency of the clamp-screw system near the natural frequency of the PEH system, a broadband frequency response is created. Hence, the electrical performance of the device was maintained at the optimum level across a larger range of frequencies. This principle will be demonstrated on two different structures and use the results to discuss the physical basis behind the enhancement.

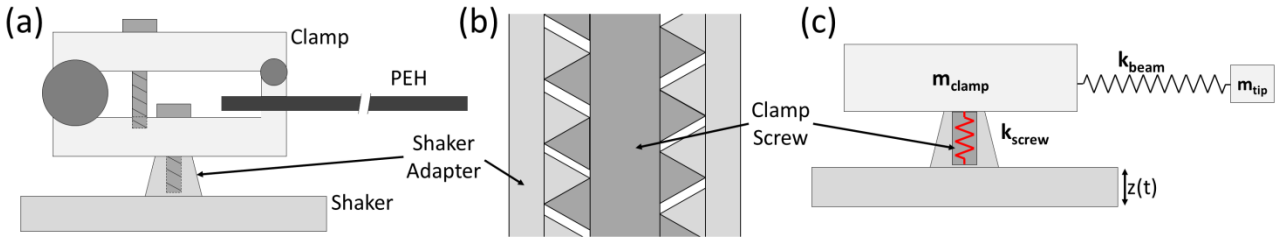

Figure 2.17 – Representations of the preloaded freeplay phenomenon: (a) a physical representation of the piezoelectric energy harvester (PEH), clamp, and shaker system, in which the clamp and shaker are held together by (b) a preloaded (tightened) screw with slightly mismatched threads allowing a larger than normal air gap between threads. When the excitation frequency is at the fundamental frequency of the clamp-screw system, (c) the response is enough to overcome the preload force and induce a second degree-of-freedom, with one degree due to the stiffness of the PEH (k_{beam}) and one due to the proposed preloaded freeplay (k_{screw}).

The effect of the proposed preloaded freeplay boundary condition on energy harvesting capabilities was investigated for one-dimensional (1D) cantilever (Figure 2.18(a)) and two-dimensional (2D) zigzag (Figure 2.18(c)) PEHs. These two structures were chosen, as it has been shown that 1D and 2D beam shapes can have advantages over one another in certain situations, and it was sought to examine the different effects, if any, freeplay would have on these PEH beam shapes [99, 107]. The dimensions were chosen for each design, as shown in the schematics in Figure 2.18(a) and (c), such that the zigzag would have 25.4mm x 25.4mm in cross-sectional area and the cantilever will also have same surface area. In this way, a comparative analysis can be performed independent of the area of the harvester. These are the same beams used in the experiments of Section 2.5. The piezoelectric material and the base excitation (0.1 G (9.81 m/s^2)) were kept at the same level in all cases to allow for the reasonable comparisons to be made between

the power outputs of the two harvester structures. The properties of the piezoelectric material are listed in Table 2.2.

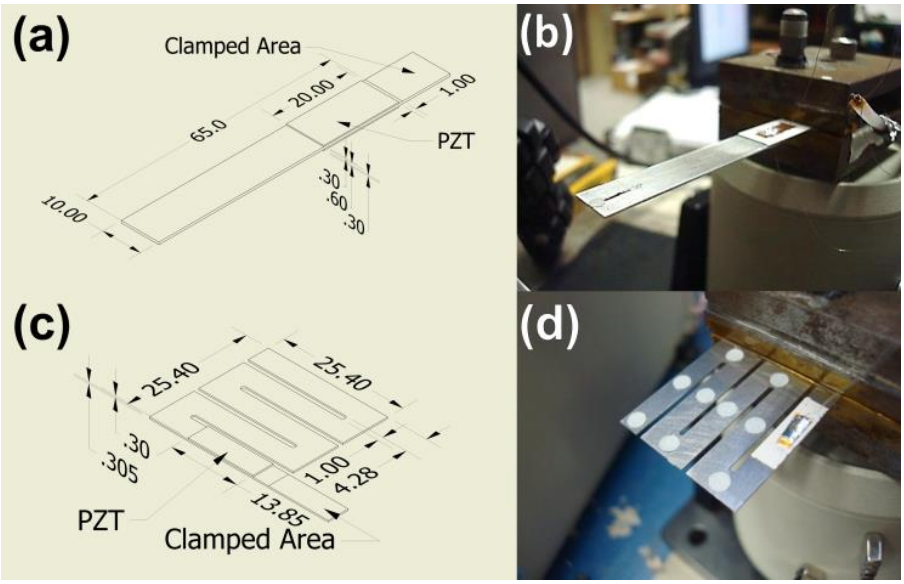

Figure 2.18 – Schematic (dimensions in millimeters) and constructed prototypes mounted in a test clamp attached to shaker, for cantilever (a) and (b), and zigzag in (c) and (d). Note that both the configurations have a surface area of approximately 645mm^2.

Table 2.2 – List of piezoelectric material properties.

Supplier	American Piezoceramics
Material	APC 850 (PZT)
-d31 (pC/N)	175
-g31 (mVm/N)	12.4

2.6.3 Experimental Results

We start our analysis by comparing the deflections of the two configurations. Deflection of the beam tips were measured at their respective first resonant frequencies by integrating laser vibrometer data with respect to time. A detailed description of experimental procedure and equipment information is provided in the supplementary document. It was found that the tip deflections of the two configurations were quite similar, with the cantilever and zigzag

piezoelectric energy harvesters having maximum deflections of approximately 66μm and 57μm respectively, at 0.1G base acceleration and 0g tip mass.

In Figure 2.19, it is shown that the deflections of the two systems shown in Figure 2.18 at their respective natural frequencies were similar, with the cantilever system exhibiting a slightly greater deflection at resonance. The displacement plots in Figure 2.19 show the relative displacement of the respective beam tips, and were obtained by integrating the laser vibrometer velocity data at each point over several periods, and averaging them together into one period. The base displacement, integrated from the base acceleration, was then subtracted leaving only the relative deflection of the respective points.

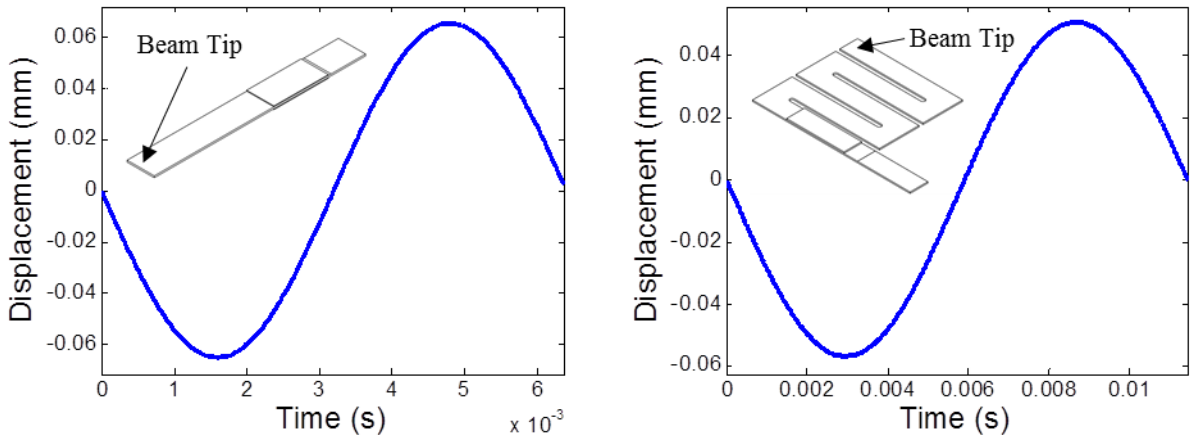

Figure 2.19 – (Left) Deflection of beam tip at the first bending frequency of the cantilever piezoelectric energy harvester (~156 Hz) at a base acceleration of 0.1 G. Max deflection ~66 μm. (Right) Deflection of beam tip at the first natural frequency of the Zigzag piezoelectric energy harvester (~86 Hz) at a base acceleration of 0.1 G. Max deflection ~57 μm.

Next, tip masses of 0 g, 0.47 g, 0.94 g, 1.42 g and 1.88 g were employed to examine their influence on the frequency response. It is observed that for both systems increasing the tip mass results in a decrease in natural frequency and increase in the amplitude of vibration. Figure 2.20(a) shows the variation of the fundamental frequency as a function of the tip mass. Clearly, for all tip mass cases, it can be noted that the zigzag harvester has the lower fundamental frequency. The difference between the two systems is exceedingly evident at 0 g tip mass, where the harvester's shape was mostly responsible for its frequency response characteristics. The natural frequency of

the clamp-screw, designated as the spring frequency, is not a function of the tip mass. For each tip mass case, a frequency response function was generated. As Figure 2.20(b) and (c) show, whenever the natural frequency of the PEH is near the spring frequency, a broadband effect was observed as the resonant peaks of the harvester and spring frequencies combined, maintaining an elevated level of beam deflection across a wider band of frequencies. It is important to note that for the other cases, where the natural frequency of the PEH is tuned to a frequency not near the spring frequency, the system behaves as a simple single degree-of-freedom system.

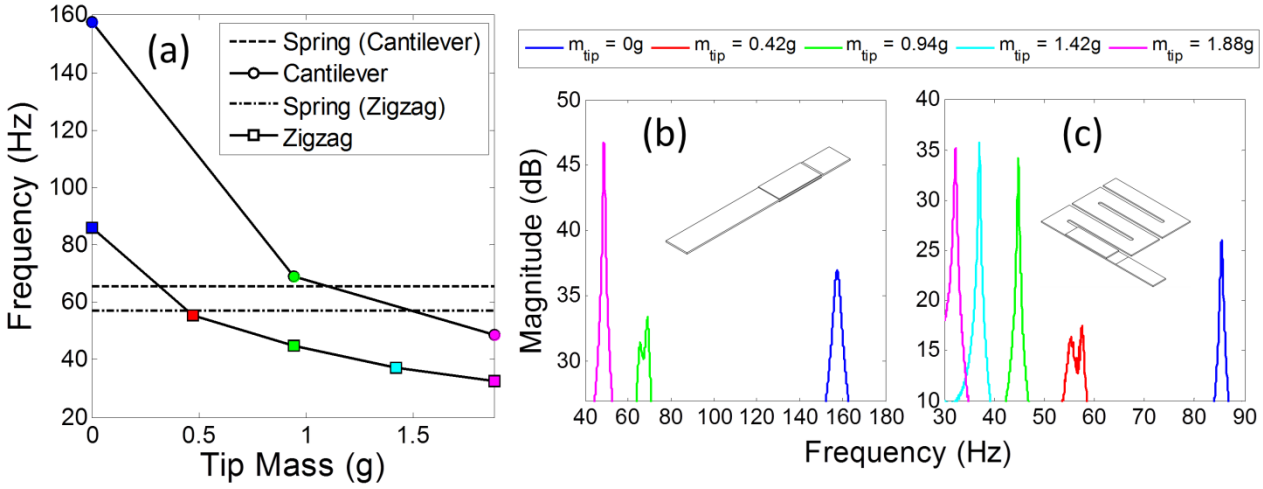

Figure 2.20 – Dynamics of systems subjected to preloaded freeplay effects. (a) Dependency of "Spring" (preloaded freeplay) frequency, cantilever and zigzag natural frequencies on tip mass. Note the natural frequency of the piezoelectric energy harvesters (PEH) is inversely proportional to the tip mass, while the spring frequency is largely independent of the tip mass. Frequency response functions for cantilever (b) and zigzag (c) for each point in (a), measured in arbitrary decibel units, showing the induced broadband effects due to the interaction of the two degrees of freedom as the fundamental frequency of the PEH approaches the spring frequency.

After finding the frequency regions where the broadband effect was observed, sweeps of frequency and electrical load resistance were conducted to locate the maximum power point. In Figure 2.21, it can be seen that the regions where the beam dynamics are broadband (Figure 2.20) are also resulting in a larger frequency region whereby power output was maintained at a high level (dashed lines), as compared to a fix boundary condition single degree-of-freedom system (solid lines). What is interesting is that for the normal case, the average power output has a higher

peak than the spring case for the range of 55.2 Hz and 56.2 Hz (around 1 Hz difference). On the other hand, including the spring effect is very beneficial for all frequencies outside the resonant range (55.2 Hz - 56.2 Hz). In the approximate range of frequencies between 54 Hz and 58 Hz, a broadband response of the harvester takes place. In fact, any variation in this range yields almost the same level of average harvested power. This result is the same for all electrical load resistances.

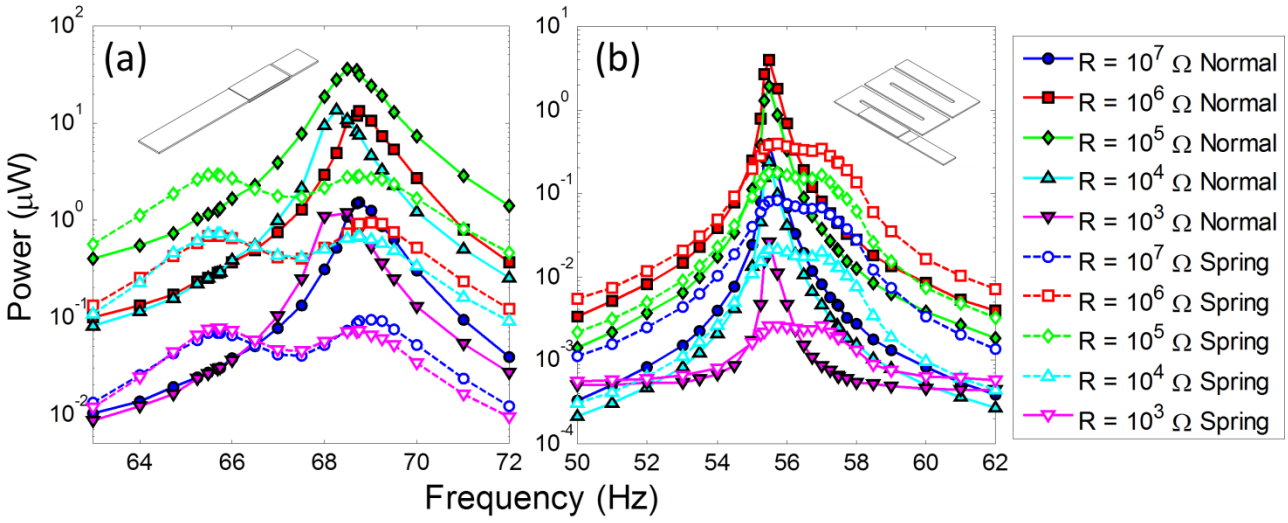

Figure 2.21 – Power output as a function of frequency and electrical load resistance in the broadband interaction range for cantilever (a) and zigzag (b) systems, with the solid lines with filled points corresponding to the "normal" (clamped) boundary condition and the dashed lines with non-filled points corresponding to the "spring" (preloaded freeplay) boundary condition.

Similar to the zigzag geometry, for the normal case of the cantilever piezoelectric energy harvester, the average power output has a higher peak than the spring case. On the other hand, including the spring effect is beneficial only for certain frequencies outside the resonant range. In the range of frequencies between 64 Hz and 71 Hz, a broadband response of the harvester takes place. Unlike the zigzag energy harvester, the classical cantilever beam case is better than the two degree-of-freedom ("Spring") case when the excitation frequency is larger than 66.5Hz. For lower values of excitation frequency, maximum harvested power is obtained when including the spring effect.

We can conclude that if the available excitation frequency is in the resonant frequency range, the energy harvesters with fixed boundary condition are better than the harvesters with preloaded freeplay boundary condition. Outside the resonant range, including the spring effect

results in higher values of the power output, as shown in Figure 2.22(c,d). The preloaded freeplay clamp spring broadband effect was shown to be very beneficial for the zigzag system but less effective for the cantilever bimorph system because of the greater compliance of the zigzag structure, making it more sensitive to the induced second degree-of-freedom. This is evident in Figure 2.22(a,b) where the increase in half-power bandwidth is larger for the zigzag structure than the cantilever bimorph. Additionally, from Figure 2.22, it is shown that PEH half-power bandwidth is largely unaffected by load resistance, and power output displays the normal parabolic trend (when plotted on log-log scale) with or without the preloaded freeplay effect.

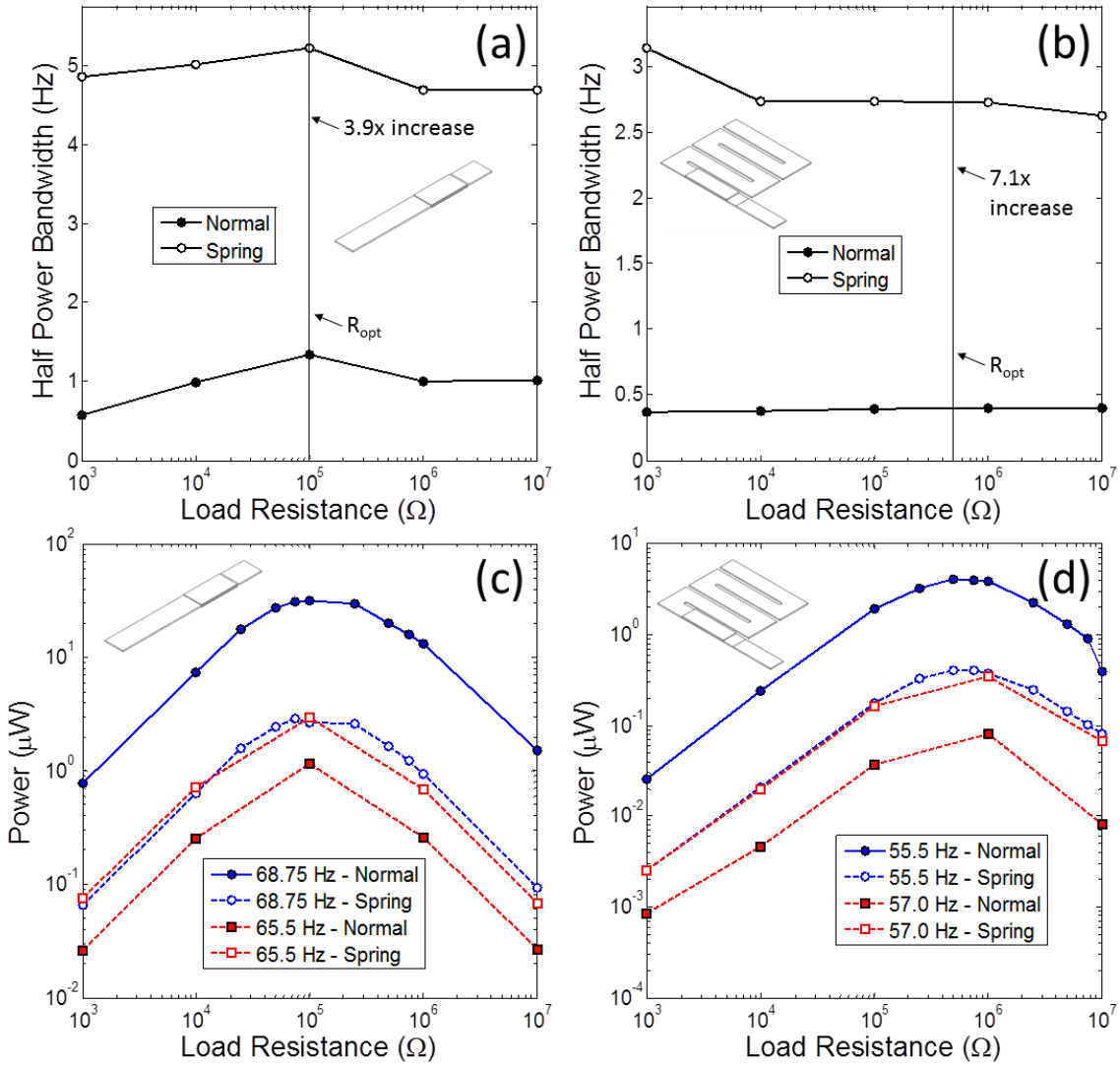

Figure 2.22 – Half-power bandwidth and power output at as function of electrical load resistance for cantilever (a,c) and zigzag (b,d) systems.

2.6.4 Tuning the Preloaded Freeplay Effect

Tuning the frequency and amplitude at which the preloaded freeplay phenomenon occurs is accomplished by controlling the mass of the clamp and tightness of the connection (preload). As Figure 2.23(a) demonstrates, adding mass to the clamp both lowers the spring frequency and causes an increase in amplitude. Here, the "Normal" case is taken to mean when the freeplay effect is not introduced. The "Screw" case is when the freeplay (spring) effect is introduced and the "Screw + Mass" case is adding approximately 35g of additional mass to the 400g clamp. In addition, tightening the connection between the clamp and vibration source has little effect on spring frequency (Figure 2.23(c)), but proves to reduce the amplitude of freeplay effect, as preload is increased. Here, "Snug" refers to a preload whereby the clamp and vibration source are securely connected and "Fully Tightened" refers to a preload whereby the screw cannot be tightened any further by hand with a 5cm hex wrench. Figure 2.23(b) and (d) show a qualitative illustration of the effects seen in Figure 2.23(a) and (c) respectively. The shaded regions below the "Preload Line" represent the area where the response of the clamp is not large enough to overcome the preload of the tightened screw and the system remains a single degree-of-freedom system. Above this region the response is large enough to overcome the preload and induce a second degree-of-freedom. A combination of adjustments in clamp mass and tightening of the clamp screw can move the effects of the freeplay condition to a frequency range which are near to the harvester dynamics. This tuning capability is demonstrated for the 0.42 g tip mass case of the zigzag harvester and 0.94 g tip mass case of the cantilever harvester, where the spring frequency was adjusted to approximately 65.5 Hz and 57 Hz respectively, to broaden the existing peaks of the harvester response.

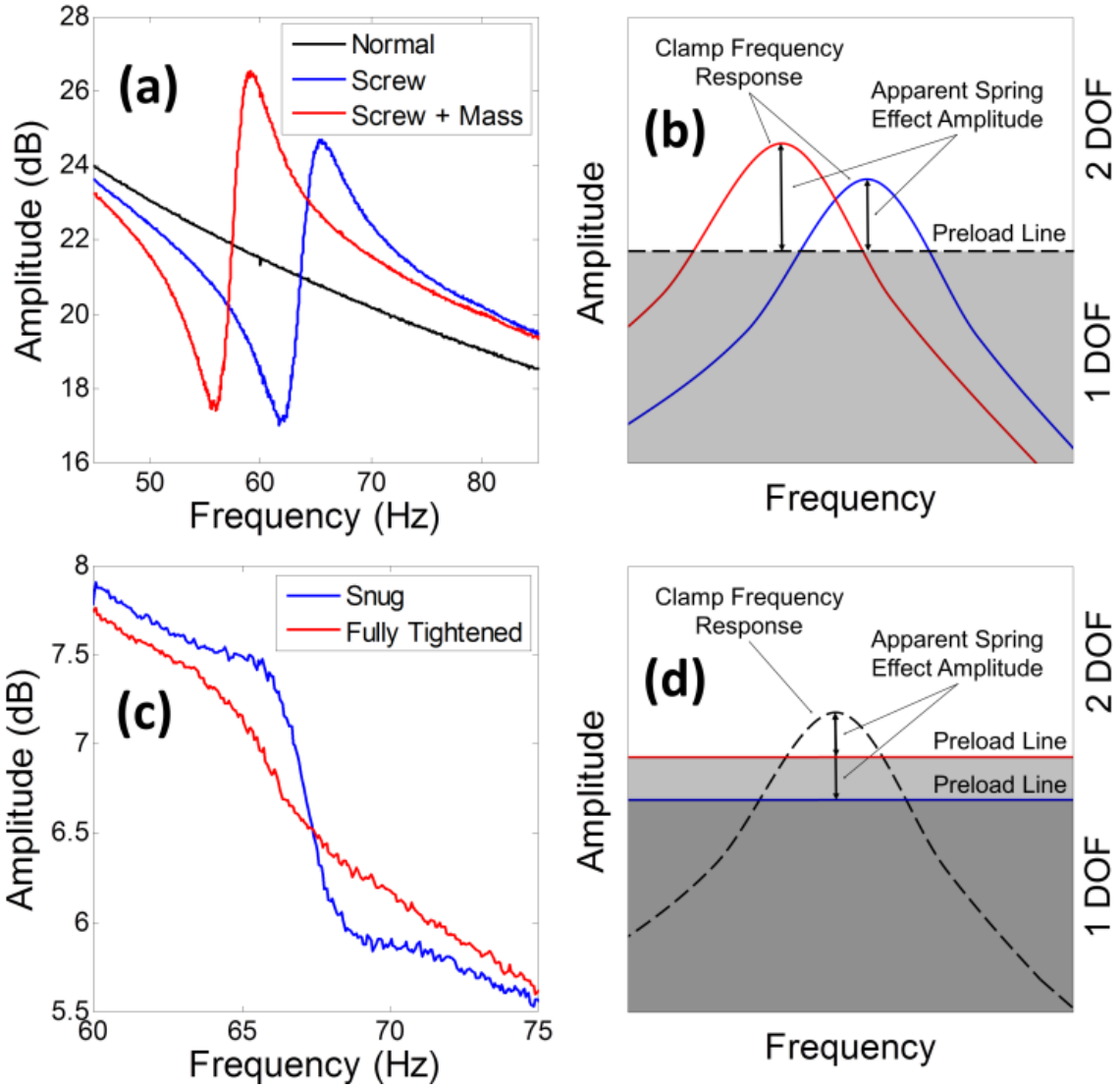

Figure 2.23 – Effect of clamp mass (a) and screw tightness (c) on frequency and amplitude of preloaded freeplay effect. Illustrations (b) and (d) offer a qualitative depiction of the effects seen in (a) and (c) respectively and when one degree-of-freedom (DOF) or two are present.

2.6.5 Summary

In conclusion, a two degrees-of-freedom piezoelectric energy harvester was proposed based on the modification of the beam's boundary conditions described as "preloaded freeplay" condition, rather than fixed. The results showed that tuned broadband energy harvesters can be designed using a preloaded freeplay clamp spring for a spring-bending coupling effect, combining the bandwidth of the two degrees-of-freedom. Depending upon the available excitation frequency,

the tip mass and spring frequency can be designed to induce broadband effects. A comparative analysis was performed between both cantilever bimorph and zigzag unimorph harvesters to deterministically establish the advantages of the preloaded freeplay boundary condition. While both harvesters benefited, in terms of broadband response, the effects of preloaded freeplay were greater on the zigzag harvester due to it being more compliant than the cantilever bimorph. Using this approach, it was demonstrated that the coupled degree-of-freedom dynamics results in an approximately 4-7 times increase in PEH half-power bandwidth, over the fixed boundary condition case, as shown in Figure 2.22.

This increased frequency range comes with the compromise of peak harvested power, as can be seen in Figure 2.21. Indeed, no spectral energy (integrated area under the curves) is gained via the preloaded approach. Rather, it is spread out over a much larger range instead of concentrated in a narrow band. Though, some energy is even lost through the freeplay. Nevertheless, this technique is best suited for, and provides advantages in, applications where excitation frequency is broad, such as in impact/impulse loading (ex. human gait, heart beats) and noisy environments (ex. structural vibration), or where excitation frequency is time varying, such as in rotating machinery which do not maintain a constant operating rotation speed.

2.7 Increasing Power Generation Using Two-Dimensional Concentrated Stress Structures

2.7.1 Introduction

In this section, a more optimized 2D beam shape was pursued, with the goal of increasing electrical power production, while confining the harvesters to a $25.4\times25.4mm^2$ area. This form factor allows for applications in implantable technologies (ex. pacemakers) and mobile electronics (ex. laptop computers, and cell phones).

Previous studies have focused on using 2D beam shapes to lower the resonance frequency to match the low frequency sources, using zigzag/meandering,[79, 92, 93, 96-100], spiral,[94, 95, 108] and circular arc[78, 90, 91] shapes. These geometries are effective at lowering the vibration resonance frequencies by reducing the stiffness of the 2D cantilever structure. However, in the pursuit of low natural frequency, it has been overlooked that lowering beam stiffness is being

accomplished by distributing stress throughout the structure, which reduces the beam's ability to stress the piezoelectric element(s), and subsequently decreases the electrical harvested power. Situations may demand this compromise in order to match the harvester's dynamics to the source dynamics, nonetheless, in many other scenarios power density needs to be improved. Here it is sought to improve the electrical response using the proposed 2D beam shapes while simultaneously seeking to maintain the low frequency dynamics.

2.7.2 Concept Generation

Upon reflection of the results of the experiments of Section 2.5, it became apparent that, for 2D beam shapes, the resonance frequency itself does not tell the whole story for a particular shape in terms of output power. For this reason, many new beam shapes were designed that could be made in the same 1 in^2 area. Table 2.3 through Table 2.7 tabulate simulation results for several new beam shapes. For all simulations, 6061 Aluminum was used as the constituent material. For the fundamental mode shape simulations, arrows indicate the proposed location(s) of tip masses, however a tip mass of zero was used in simulation of mode shapes. The coloration is on a scale of displacement and all figures are of the same scale. For the stress analysis, a unit tip mass was used in each simulation. This means that for shapes that required two tip masses to be symmetrically loaded, the two tip masses summed to the mass used for the shapes where only one tip mass location was used. In this way, all systems retained the same total mass. All stress analysis figures are on the same arbitrary stress scale.

It is also important to note that all of these simulations are for the beam only and do not take into account the additional piezo ceramic that will be bonded to the beams. The piezo will affect the dynamic characteristics of each beam in its own way and is something that will need to be analyzed more carefully on a case by case basis. The stress analysis is for a static load, which is sufficient for describing the fundamental mode shape.

The beams share a standard span width of 4.28mm and spacing of 1mm, which was to be used as standard dimensions for all subsequent designs. Interestingly, the Zigzag and Spiral showed the same fundamental resonance frequency. As is evident from the stress distribution of these two shapes, the Spiral has lower stress, making it more susceptible to stiffness changes brought about by the additional of piezo segments. It was then examined, the effect of rotating the Zigzag pattern along with making a revered spiral. These designs are shown in Table 2.3.

Table 2.3 – Beam shapes of interest (Zigzag and Spiral)

Name	Schematic	Fundamental Mode Shape	Stress Analysis
Zigzag	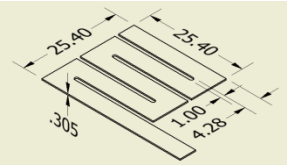	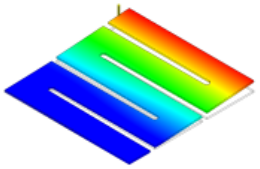 $f_{n_1} = 82\ Hz$	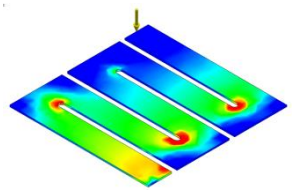
Spiral	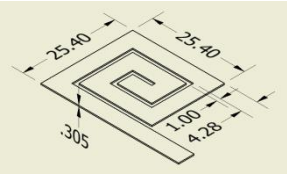	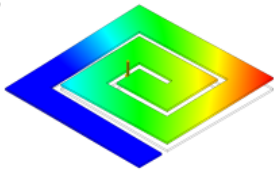 $f_{n_1} = 82\ Hz$	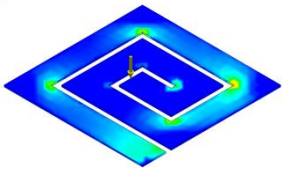
Rotated Zigzag	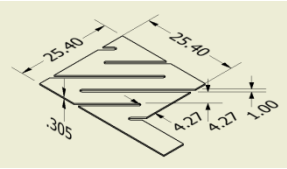	 $f_{n_1} = 99\ Hz$	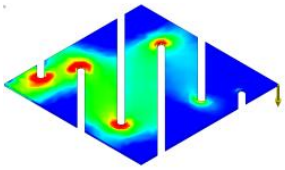
Spiral Revert	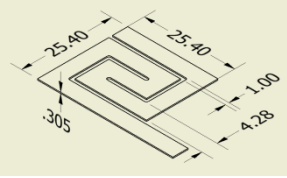	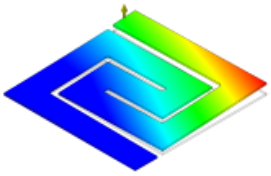 $f_{n_1} = 89\ Hz$	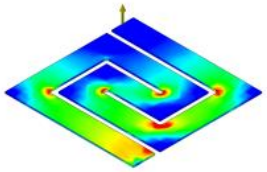

Next the effect of combining the Zigzag and Spiral designs was investigated with the goal to combine the favorable properties of both. These efforts resulted in the Sidewinder and Sidecart designs, shown in Table 2.4.

Table 2.4 – Beam shapes of interest (Combination Spiral-Zigzag)

Name	Schematic	Fundamental Mode Shape	Stress Analysis
Sidewinder	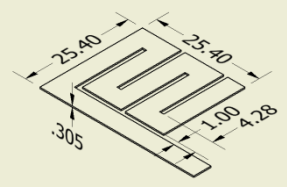	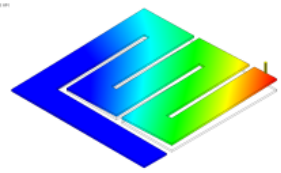 $f_{n_1} = 82\ Hz$	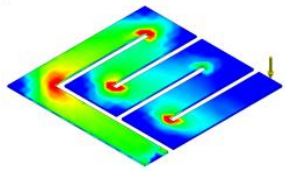
Sidecart	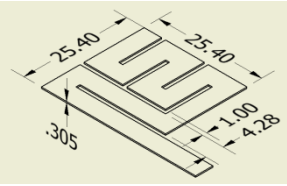	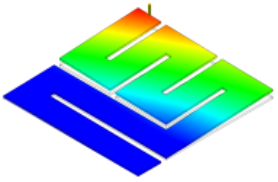 $f_{n_1} = 82\ Hz$	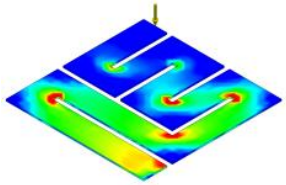

After reviewing the designs presented in Table 2.3 and Table 2.4, it became evident that the Zigzag and Spiral based designs always distributed the stress across the structure. In this way, lower natural frequencies are achievable, however, since the stress is distributed so much, one runs into the conflict of percentage of piezo covering the structure to harvest energy and negatively affecting the dynamics. A design was then pursued that would effectively concentrate the stress in the structure to a particular span. In this way, a small area covered by a piezoelectric layer would be more fully stressed and the dynamics of the beam less affected by its presence. The results of these efforts brought about the Elephant, Curl, Flex and Twist designs, shown in Table 2.5. One will notice that the resonance frequency for these designs are higher than the Zigzag and Spiral designs. This is because the stress is concentrated instead of distributed, resulting in higher resonance frequency. However, as mentioned previously, this does not tell the whole story because, for this design, less piezo can be used to achieve the same result in power.

Table 2.5 – Beam shapes of interest (Stress concentration)

Name	Schematic	Fundamental Mode Shape	Stress Analysis
Elephant	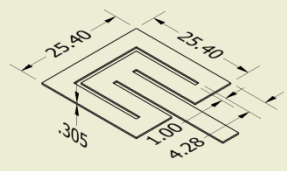	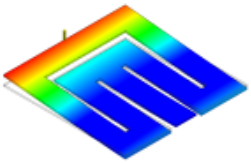 $f_{n_1} = 139\ Hz$	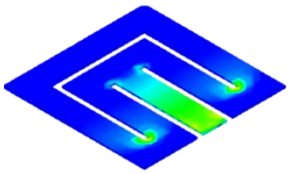
Curl	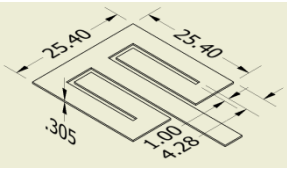	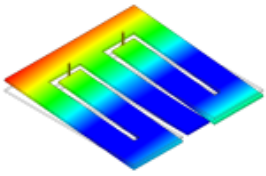 $f_{n_1} = 165\ Hz$	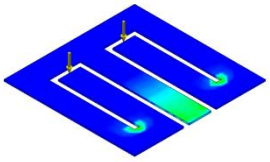
Flex	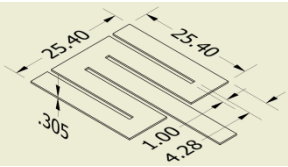	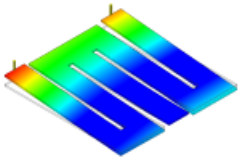 $f_{n_1} = 158\ Hz$	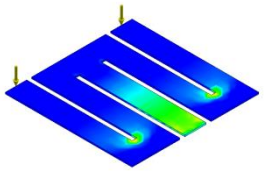
Twist	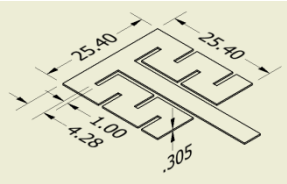	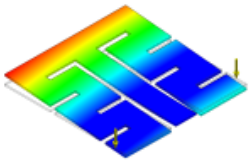 $f_{n_1} = 165\ Hz$	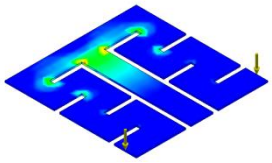

In a further attempt to stress a particular span of the beam, designs that maximized the length of the span coming from the clamped end to the first turn of the beam were conceived, resulting in the Spartan, Leia and Mopar designs, available in Table 2.6. These designs yield interesting results, with resonances in between the previous groups and unique stress distributions and concentrations.

Table 2.6 – Beam shapes of interest (Longest initial span)

Name	Schematic	Fundamental Mode Shape	Stress Analysis
Spartan	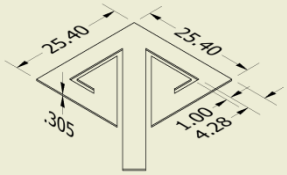	 $f_{n_1} = 130\ Hz$	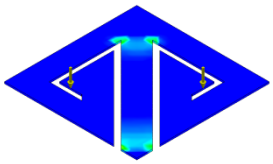
Leia	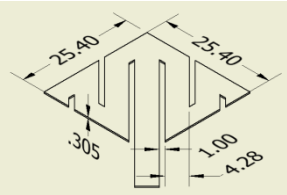	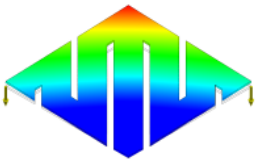 $f_{n_1} = 130\ Hz$	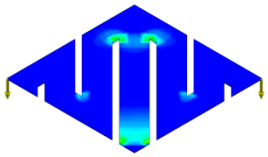
Mopar	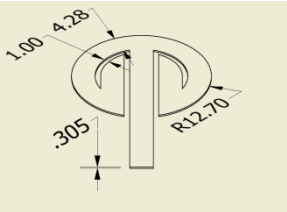	 $f_{n_1} = 155\ Hz$	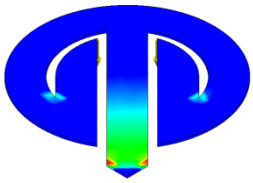

A simple cantilever beam of length and width standard to the other designs presented earlier is shown in Table 2.7 for the sake of comparison. It should be noted that all of the 2D beam shapes show between a 2-4 fold decrease in fundamental frequency.

Table 2.7– Comparison to equivalent size cantilever beam

Name	Schematic	Fundamental Mode Shape	Stress Analysis
Simple Cantilever	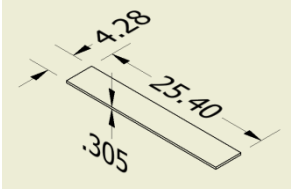	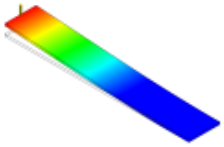 $f_{n_1} = 402\ Hz$	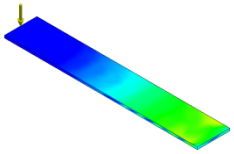

The designs with 180 degree turns prove more favorable than those which incorporate 90 degree turns. This is due the fact that right angle turns in the beam creates a moment arm on the previous beam span, inducing torsion. This torsion leaches from the desired bending stresses, since the cross-section of the beam is a wide, flat rectangle, which resists torsion. This is another reason why the Zigzag design tends to outperform the Spiral design as the 180 degree turns minimized these torsion inducing moment arms.

2.7.3 Concept Evaluation

In order to validate the simulations shown in the previous section, four of the more promising beam shapes were manufactured. The designs chosen for manufacturing were the Zigzag, Spiral Revert, Elephant and Flex designs. For each design, a beam was fabricated without a piezoelectric layer, to validate the vibration model simulation, and a beam with a piezoelectric layer, to observe the effect of adding stiffness to the structure. The fabricated test specimens are shown below in Figure 2.24. All specimens were cut (CNC mill) from the same sheet of 0.305" thick mild steel. Identical pieces of piezo (APC 850) were also cut to custom fit the dimensions of the beam's spans, and bonded to the beam. Fabrication steps follow those of section 2.5.2.

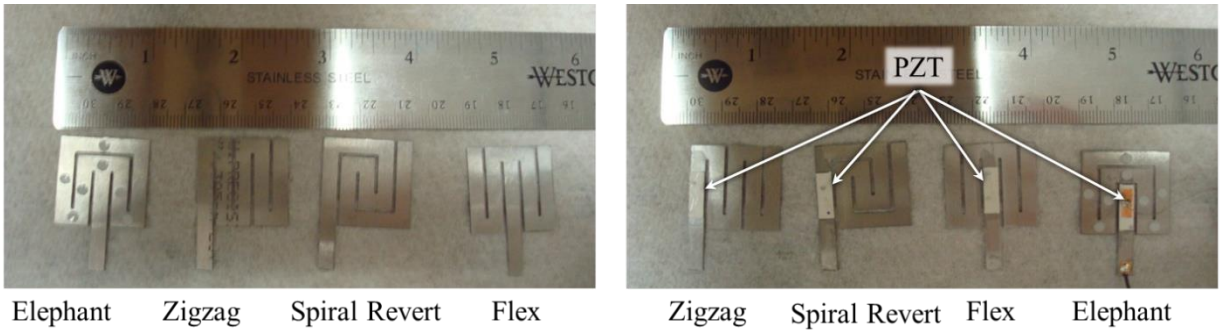

Figure 2.24 – (Left) Beam specimens without piezoelectric layer. (Right) Beam specimens with piezoelectric layer.

The first beam to undergo testing was the Elephant design (without piezoelectric layer). The test specimen was first subjected to random base excitation frequencies ranging from 0-500 Hz (using the same experimental setup described in section 2.5.3). The laser vibrometer measured the velocity of key positions on the beam, shown as P1-P8 in Figure 2.25. The silver

circles at each measurement position are dots of reflective tape of negligible mass, which improves the resolution of the vibrometer data by reflecting the laser directly back to the vibrometer instead of having it scattered by the dull metal surface of the beam. The Fourier transform of the cross-correlation of the vibrometer measurement and the base acceleration (accelerometer mounted to clamp) was then used to establish a frequency response for the beam, also shown in Figure 2.25.

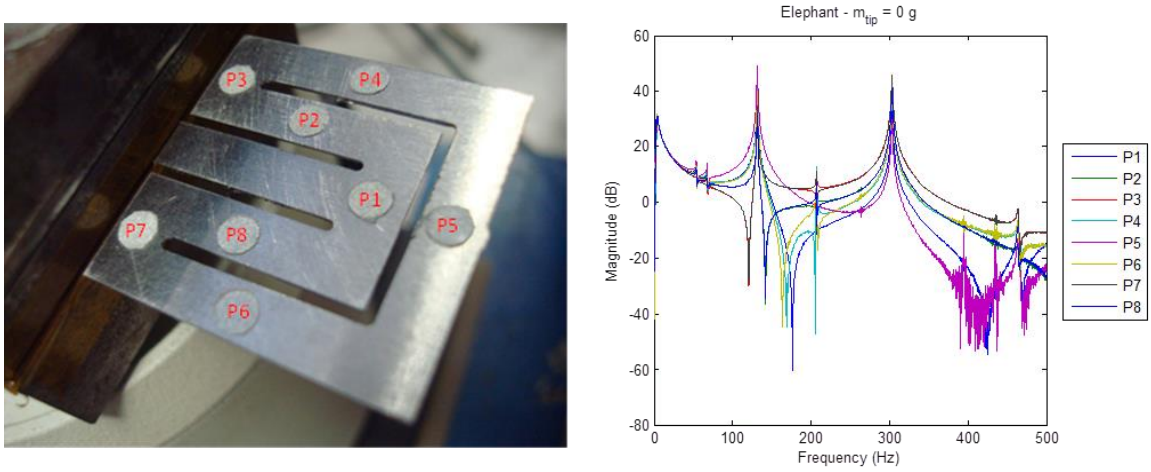

Figure 2.25 – (Left) Measurement positions on the beam with (Right) corresponding frequency response functions.

As is evident in Figure 2.25, regardless of the location of the vibrometer measurement, the measured resonance frequencies were the same and were $f_{n_1} = 131.5\,Hz$ and $f_{n_2} = 303.1\,Hz$. Since all points yielded the same frequency peaks, all subsequent measurements for frequency response were taken at P5, where the response for the first natural frequency was the largest. Tip masses were then placed on the outermost span of the beam in increasing amounts, as shown in Figure 2.26.

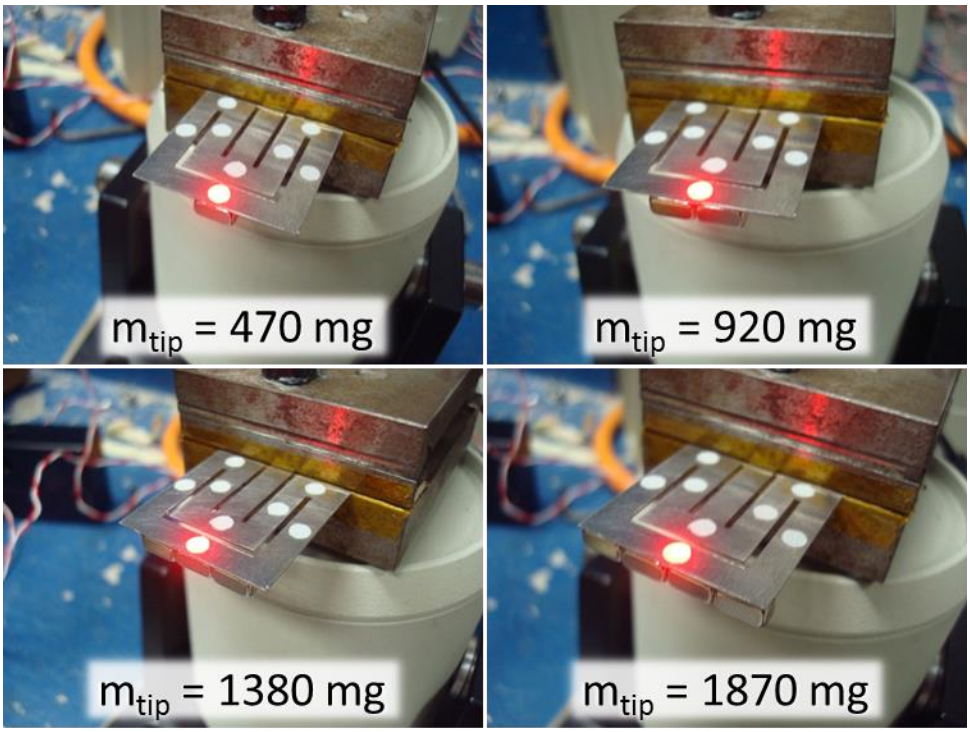

Figure 2.26 – Pictures of how tip masses were added to the beam during testing.

The resulting frequency responses are shown in Figure 2.27, and first two resonance frequencies in Table 2.8.

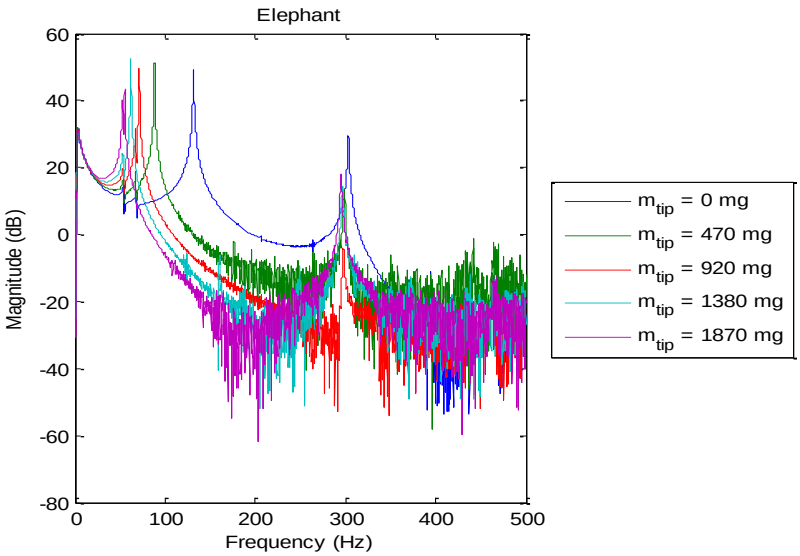

Figure 2.27 – Frequency response for increasing tip masses.

Table 2.8 – First and second resonance frequencies as a function of increasing tip mass, for beam without piezo

$m_{tip} = 0$	$m_{tip} = 470$ mg	$m_{tip} = 920$ mg	$m_{tip} = 1380$ mg	$m_{tip} = 1870$ mg
$f_{n_1} = 131.5\ Hz$	$f_{n_1} = 88.3\ Hz$	$f_{n_1} = 71.25\ Hz$	$f_{n_1} = 61.9\ Hz$	$f_{n_1} = 54.5\ Hz$
$f_{n_2} = 303.1\ Hz$	$f_{n_2} = 298.8\ Hz$	$f_{n_2} = 297.3\ Hz$	$f_{n_2} = 296.6\ Hz$	$f_{n_2} = 295.2\ Hz$

One will notice that the fundamental frequency predicted in Table 2.5 was 139 Hz, and the experimentally measured fundamental frequency was 131.5 Hz. This is in good agreement with the model and the lower measured frequency can be explained by the fact that the model had the structure clamped right on the border of the one inch square, where in reality a small amount of space is given between the edge of the square and the clamp, so that they do not come in contact while vibrating. This effectively lengthens the center span of the Elephant, resulting in the lower frequency. It is also worth noting that the second resonance frequency is largely unaffected by the lowering of the fundamental frequency with this tip mass configuration. This phenomena is further explored in Section 2.8.

Integrating the velocity data, obtained by the vibrometer, at each point P1-P8, the mode shape of the beam can be verified. Figure 2.28a shows the averaged displacement of the measurement points across one period and corresponding schematic of measurement positions (Figure 2.28b). These two were then overlaid to create an animation of the beam vibration, of which the maximum deflection is shown in Figure 2.28c and compared to simulation (Figure 2.28d). The measured experimental first mode shape matches well with the predicted simulation first mode shape.

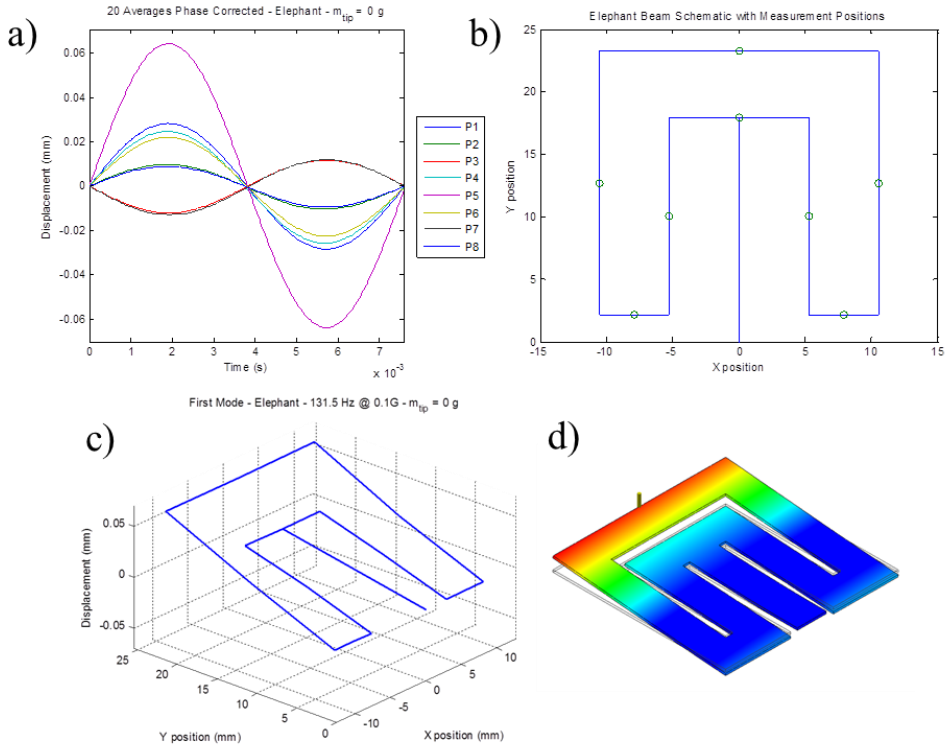

Figure 2.28 – a) Averaged measured displacements for one period. b) Schematic of measurement locations. c) Measured first mode shape isometric view. d) FEA simulated first mode shape isometric view.

2.7.4 Effect of Piezoelectric Layer

The same experimental steps were followed as in the previous case to examine the effect of adding the piezoelectric layer to the beam. Figure 2.29 shows frequency response for the Elephant beam with PZT for increasing tip masses, while Table 2.9 summarizes the measured natural frequencies as a function of tip mass.

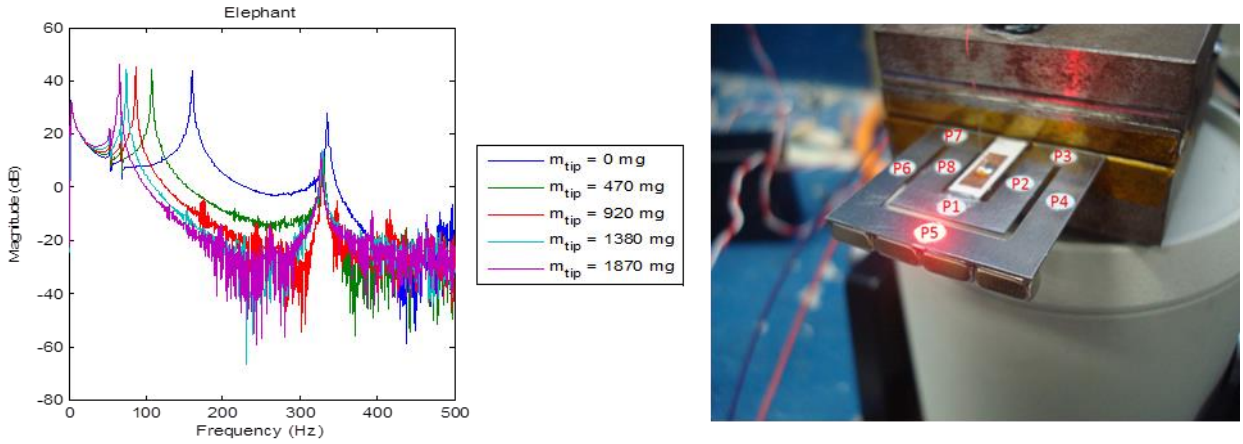

Figure 2.29 – (Left) Frequency response function for increasing tip mass. (Right) Measurement point for the Elephant beam with piezoelectric layer.

Table 2.9 – First and second resonance frequencies as a function of increasing tip mass, for beam with piezoelectric layer

$m_{tip} = 0$	$m_{tip} = 470$ mg	$m_{tip} = 920$ mg	$m_{tip} = 1380$ mg	$m_{tip} = 1870$ mg
$f_{n_1} = 160.3\ Hz$	$f_{n_1} = 108.0\ Hz$	$f_{n_1} = 86.37\ Hz$	$f_{n_1} = 75.0\ Hz$	$f_{n_1} = 65.5\ Hz$
$f_{n_2} = 335.9\ Hz$	$f_{n_2} = 330.5\ Hz$	$f_{n_2} = 328.9\ Hz$	$f_{n_2} = 328.6\ Hz$	$f_{n_2} = 326.7\ Hz$

The addition of piezo, as expected, increased the resonance frequencies as stiffness was added to the system. This effect is not dramatic, however, and the addition of a small tip mass quickly brings resonance below 100 Hz. As before the displacement was integrated from the velocity measurements and used to illustrate the fundamental mode shape, as shown in Figure 2.30.

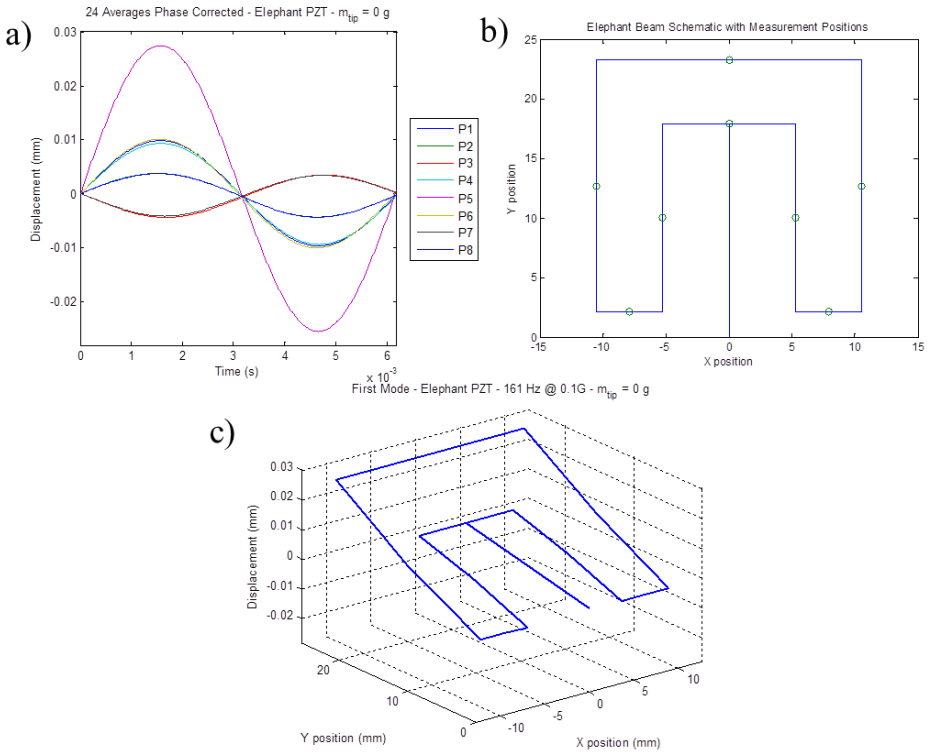

Figure 2.30 – a) Averaged measured displacement for one period. b) Schematic of measurement locations. c) Measured first mode shape of Elephant beam with PZT isometric view.

The overall shape of the first mode is largely unaffected by the addition of the piezo, however, the amplitudes of the displacements are approximately halved, due to the increased stiffness. With the knowledge that simulations do not differ significantly between simulating with or without the piezoelectric layer, the other fabricated beam shapes were evaluated for what is ultimately the most important parameter, the power output.

2.7.5 Further Explanation of Design and Predicted Performance Increase

I begin by examining the current standard for 2D beam shapes, the Zigzag beam shape shown in the schematic drawing of Figure 2.31(a). Since stress transfer from the beam to the piezoelectric material is of principal importance, a finite element stress analysis of the Zigzag beam shape was conducted, as presented in Figure 2.31(b), for the first bending mode, found in Figure 2.31(c). Figure 2.31(b) shows the distributed nature of the stresses in the undeformed Zigzag shape, colored with stress magnitudes resulting from first bending mode vibrations, where warm colors represent tension, cold colors represent compression, with green representing zero stress.

Simulations are done in the Stress Analysis environment of Autodesk Inventor Professional 2013. The simulations takes into account the forces of gravity and of the tip mass. The tip masses are treated as point force for simplicity. This is a valid approach as the tip masses only add a constant force to the end of the beam, and since the beams undergo small deflections. Simply assuming beam stresses by adding point forces to the tip is not sufficient to describe the distributed mass of the beam, which is why gravitational forces are also considered in the simulations, which take into account the distributed mass of the beam in stress calculations.

Distributing stress makes for a more compliant (i.e. less stiff) beam, with low natural frequency. However, this creates a problem when determining where to place the piezoelectric layer(s). If the piezoelectric material is placed throughout the beam, it must be separated and poled in opposition to adjacent segments, as discussed by Berdy et al.,[79] due to the alternating sign of stress, as shown in Figure 2.31(b). Furthermore, the closer one gets to the free-end of the beam, the lower the magnitude of stress. This results in the situation where each successive segment of piezoelectric becomes less effective and connecting like-poled segments in parallel leads to detrimental charge redistribution and loss of efficiency[109, 110]. For this reason, it was chosen to place the piezoelectric material only on the first segment of the Zigzag harvester, where stress is the highest.

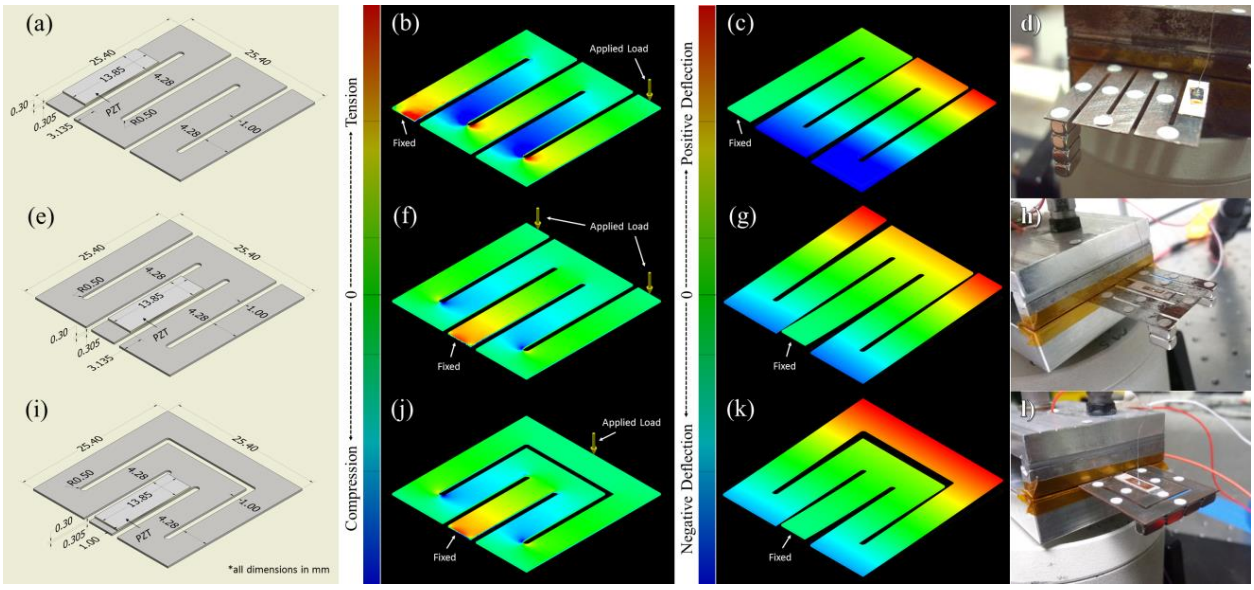

Figure 2.31 – Dimensioned drawing, finite element stress analysis for first bending mode, first mode shape, and picture of the fabricated device in test setup for Zigzag (a-d), Flex (e-h), and

Elephant (i-l) beam shapes, respectively. Coloring of (b,f,j) are all with respect to the same arbitrary stress scale, and coloring of (c,g,k) are all with respect to the same arbitrary modal displacement scale.

In order to solve the problem of distributed stress in 2D beam shapes, it is next sought to create a structure whereby stress is focused onto a single beam segment, upon which the piezoelectric material may be most effectively placed. Another problem to consider is the presence of torsional forces in the Zigzag design. Torsional stresses are not readily harvestable by the flat rectangular profile of these planar 2D beam shapes, due to the resulting orthogonality of electric field to the material polarization and electrodes, and are therefore undesirable [97, 111]. Harvester performance should increase if these forces are removed or ideally transformed into bending forces. Torsional forces are also present in spiral and arc-segment based designs [78, 90, 91, 94, 95, 108]. Berdy et al.,[79] have addressed this problem by connecting two Zigzag beam shapes at their free-ends, creating a fixed-fixed configuration. Exploiting symmetry to reduce the onset of torsional forces is valuable; however, a cantilever configuration is a better performing option to a fixed-fixed configuration. Therefore, the symmetric zigzag cantilever, termed 'Flex', is introduced and presented in Figure 2.31(e). It can be noted that the stress in this design is more concentrated in the first segment near the fixed end, as shown in Figure 2.31(f). This is due to the decrease in torsional forces by symmetry, allowing for a more pure bending motion to occur. In this case, rather than placing a unit force on the tip of the beam, as in Figure 2.31(b), a half unit force is placed on both terminating free ends of the Flex beam shape. The bending motion is also reflected in the mode shape of Figure 2.31(g).

With the Flex design, torsional forces are still present due to the two ends being free (i.e. unsupported). It does seem counterintuitive; the merit of the cantilever is the fixed-free configuration, however, in the 2D case, the presence of the free-end not being collinear with the fixed-end, creates undesirable torsional effects. It is in the spirit of eliminating free-ends, but somehow maintaining a cantilever-like configuration, the closed-circuit symmetric meandering configuration, termed 'Elephant', displayed in Figure 2.31(i), was developed. In Figure 2.31(j), a high concentration of stress can be observed in the first beam segment, due to the optimally pure bending motion of the mode shape, rendered in Figure 2.31(k). This is accomplished by joining

the meanders on either side of the plane of symmetry at the top of the beam, forming a closed-circuit, whereby torsional effects are forced to cancel out.

2.7.6 Experimental Setup

To validate the findings of the finite element analysis and quantify the merits of the given concentrated stress structures, experimental investigations were conducted on a series of fabricated test specimens. These test specimens were constructed, according to the dimensions given in Figure 2.31(a,e,i), with the substrate being mild steel and the piezoelectric layer being American Piezoceramics APC850 PZT. Attached to each harvester were also 1.88g tip masses, consisting of four 6.35×3.175×3.175mm neodymium magnets, chosen for their ease of installation and reconfigurability. The fabricated test specimens are shown in Figure 2.31(d,h,l), while the experimental setup is pictured in Figure 2.32.

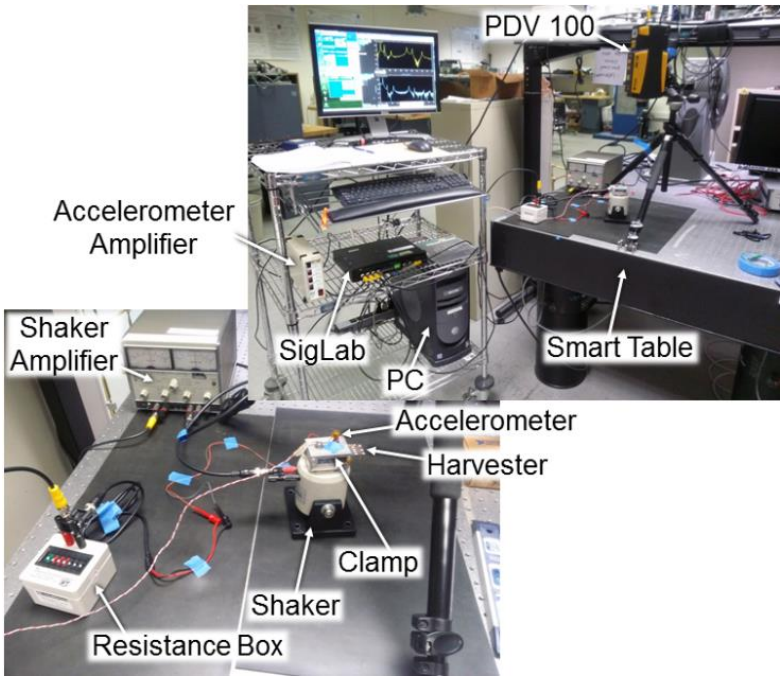

Figure 2.32 – Experimental setup for characterizing the harvesters fabricated in this section.

Individual harvesters were then placed into a custom clamp and attached to a TMC Solution TJ-2 modal shaker, which was placed upon a Newport ST series Smart Table vibration isolation table, as picture in Figure 2.31(d,h,l). Reflective dot stickers (of negligible mass and stiffness) were applied to various spots on the beams to provide points to shine a Polytec PDV 100 laser

Doppler vibrometer onto, so that beam vibrations and mode shapes may be measured. Using an alignment shim, the edge of the harvesters were made parallel to the clamping face with an offset of approximately 300μm, so that the beams would not rub the clamp during vibration. To measure base excitation, a PCB Piezotronics model 352C67 accelerometer was adhered to the clamp, using adhesive wax, with output conditioned through a PCB Piezotronics model 482A165 amplifier. Electrical load resistance across the piezoelectric layer was varied using an IET Labs RS-201 resistance substituter. Data acquisition was accomplished using DSP Technology SigLab Model 20-42, and National Instruments 9234 and 9929 cDAQ cards. It is important to note that any voltage measurement takes place across some internal resistance (typically 1MΩ). Therefore, the true load experienced by the harvester is the combination (usually in parallel) of the given resistance and the internal resistance of the measurement equipment. This fact seems to be overlooked in some of the literature, which can significantly impact the reported optimal load value. This error would not change the level of reported power, as the actual resistance given to the system is what it is, though the value given is not what is reported.

2.7.7 Experimental Results

The designed harvesters were subjected to varying frequency input (base excitation) and load resistances. Base excitation was held constant at 0.1g acceleration across all frequencies. Both frequency and resistance were varied manually until maximum values were located. The predicted mode shapes were experimentally validated. Mode shapes are measured by mapping magnitude and phase information from transfer function taken at each point (reflective dots in Figure 2.31(d,h,l)), referenced to the accelerometer at the base, to its corresponding physical location in space. The amplitude in arbitrary modal units is the magnitude of the transfer function, divided by the maximum value of the transfer functions of all the considered points. The amplitude is then multiplied by the sine of the phase angle to obtain the sign of the amplitude. Figure 2.33 shows the experimentally measured mode shapes compared against the predicted mode shapes from the Finite Element Analysis.

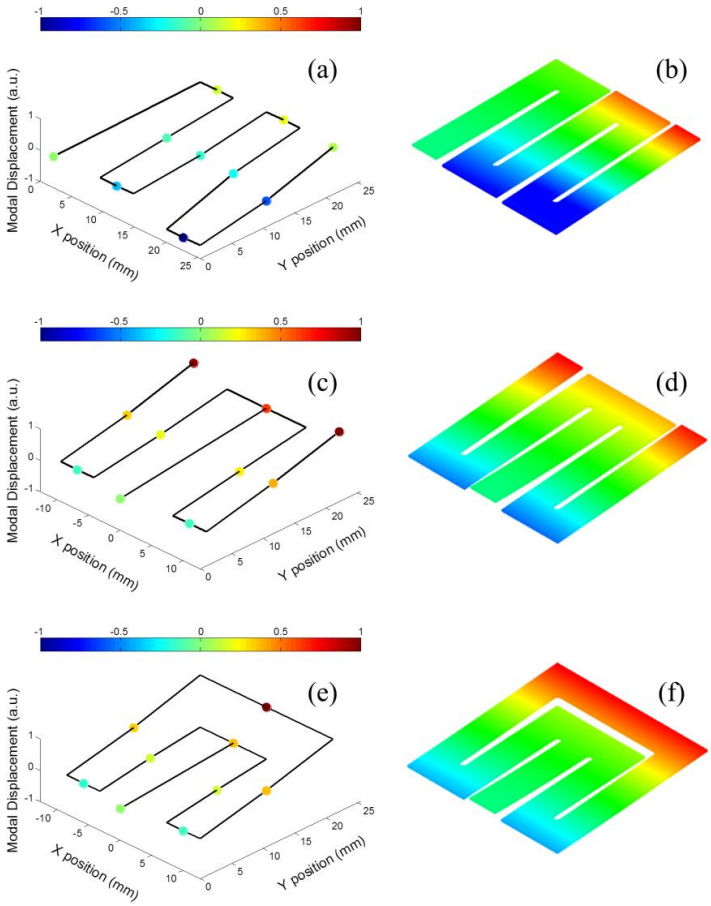

Figure 2.33 – Experimentally measured mode shapes (a,c,e) compared against their predicted shapes (b,d,f) for the (a,b) Zigzag, (c,d) Flex, and (e,f) Elephant beam shapes.

Figure 2.34(a-c) show the experimental results for each of the three 2D beam shapes, excited at their first bending frequency, and maximum power/load resistance. It follows from Figure 2.34(a) that the Zigzag harvester is capable of producing 2.93 μW across 0.75 MΩ at 65.6 Hz. Inspecting Figure 2.34(b), the Flex harvester produced 32.2 μW across 1 MΩ at 62.0 Hz base excitation frequency. In both designs, the electromechanical coupling is quite small, as no frequency shift was observable between the short-circuit (R_L≈103 Ω) and open-circuit (R_L≈107 Ω) frequencies. However, for the Elephant harvester, it's noted a substantial shift between short-circuit and open-circuit frequencies, as well as, a large power output of 81.3 μW across 1 MΩ at 68.125 Hz, as shown in Figure 2.34(c). From these findings, the merits of the Elephant design, and how it is beneficial towards efficient low-frequency piezoelectric energy harvesting are clear.

It should be noted that while the dimensions of the piezoelectric elements for all three designs are identical, the Elephant has a shorter fixed-end segment, so piezoelectric element is mounted slightly closer to the clamped boundary as compared to the other two designs, giving it access to slightly higher stresses. This bias does not alter the superiority of the Elephant design. Rather, the relative performance of the Zigzag and Flex designs may be marginally closer to that of the Elephant design, had the piezoelectric elements been bonded closer to the clamped boundary.

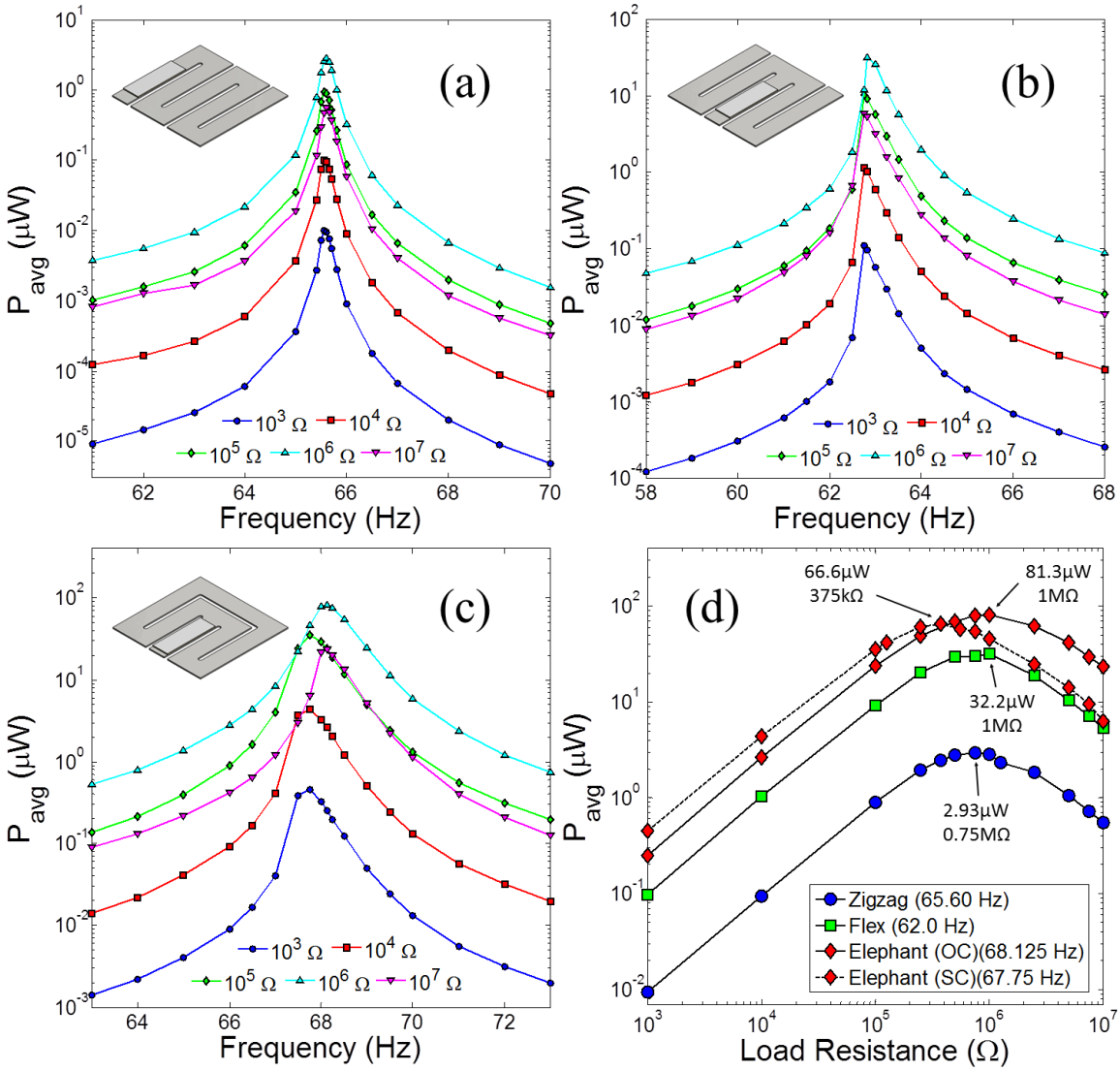

Figure 2.34 – Experimental results for average power production as a function of frequency and electrical load resistance for (a) Zigzag, (b) Flex, and (c) Elephant configurations, with (d) average

power as a function of electrical load resistance at each harvester's respective resonance frequency. All input vibrations were at 0.1g base acceleration.

2.7.8 Modeling

In addition to the numerical and experimental analyses, a single-degree-of-freedom model is applied to all considered harvesters in order to gain additional understanding of the phenomena involved in their performance. To this end, further testing was conducted, including determining the damping ratio, ζ, and short-/open-circuit frequencies, ω_{nsc} and ω_{noc} respectively.

Damping ratios were found by imposing an initial displacement to the tip of each beam by making a plucking motion at the beam tip with the broad side of a small flat head screwdriver and recording the amplitude of vibration (via vibrometer) as it decayed, while the piezoelectric layer was in short-circuit configuration (to null electromechanical effects). The damping ratios were calculated using the method of logarithmic decrement by averaging calculations from several different peaks in each decay, and then averaged across five redundant trials, yielding a range of ratios that could be used in the model.

To find the difference in short-circuit versus open-circuit frequencies, that could not be readily observed when varying frequency manually, the harvesters were subjected to random base excitation in both short-circuit (wire leads connected) and open-circuit (wire leads apart) configurations, while monitoring beam tip vibrations (via vibrometer). The transfer function between base acceleration and tip vibration was then examined to find the disparity in short-circuit and open-circuit resonant peaks. Finding such subtle changes in peak frequency required measuring for around 300 seconds and employing 4-5 averages, yielding a frequency resolution of approximately 0.012-0.015 Hz; where the resolution of a discrete transfer function is the number of averages divided by the measurement period. With this fine frequency resolution, the frequency shifts for all proposed harvesters were determined.

For a digital transfer function, the frequency resolution is the number of averages taken divided by the measurement period. Thus, dividing 4 or 5 by approximately 300 seconds is where the 0.012-0.015 Hz resolution comes from. The exact measurement period varied slightly between harvesters due to the measurement being manually started, and stopped when it was observed the

desired time was passed. 4 or 5 averages were used depending on the signal quality for each of the experiments.

Values used in the model can be found in Table 2.10, where M_b and M_{tip} are the mass of the beam and mass of tip mass respectively (via A&D EJ-300 scale), C_p is the capacitance of the piezoelectric layer (via Fluke 179 Multimeter), Θ is the electromechanical coupling factor (calculated), and a the base excitation acceleration.

Table 2.10 – Analytical model parameters.

Parameter	unit	Zigzag	Flex	Elephant
M_b	g	1.51	1.51	1.51
M_{tip}	g	1.88	1.88	1.88
C_p	nF	3.1	3.1	3.1
ζ		0.00611	0.00365	0.00374
ω_{noc}	rad/s	2π(65.6000)	2π(62.8467)	2π(68.1250)
ω_{nsc}	rad/s	2π(65.5888)	2π(62.7976)	2π(67.7705)
Θ	μC/m	20.0515	41.0868	114.8154
a	m/s^2	0.981	0.981	0.981

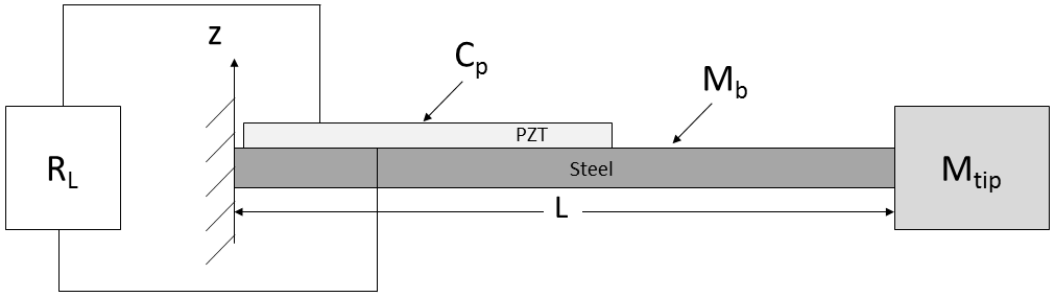

Figure 2.35 – Representation of single-degree-of-freedom model used in analytical modeling.

The governing equations of a single-degree-of-freedom piezoelectric vibration energy harvester, shown in Figure 2.35, are given by:

$$M_{eq}\ddot{w}(L,t) + C_{eff}\dot{w}(L,t) + K_{eff}w(L,t) + \Theta V(t) = -M_{eq}\ddot{w}_b(t) = M_{eq}\mathrm{a}\cos(\Omega t) \quad (2.2)$$

and

$$\frac{V(t)}{R_L} + C_p\dot{V}(t) - \Theta\dot{w}(L,t) = 0 \quad . \quad (2.3)$$

where w is the relative displacement of the beam, with $w(L,t)$ being the relative displacement of the beam tip, and $w_b(t) = w_0\cos(\Omega t)$ is the base displacement. Ω is the base excitation frequency, w_0 is the amplitude of the base displacement, and $a = w_0\Omega^2$ is the base acceleration. K_{eff} is the effective stiffness of the 2D beam shape (as if it were a linear spring) which is defined as:

$$K_{eff} = \omega_n^2 M_{eq} \quad , \quad (2.4)$$

where ω_n is the natural frequency of the beam, and M_{eq} is the equivalent mass (as if all mass were considered at the tip), defined as,

$$M_{eq} = \frac{33}{140}M_b + M_{tip} \quad , \quad (2.5)$$

where M_b is the mass of the beam, and M_{tip} denotes the mass of the tip mass. Furthermore, the effective damping is described by,

$$C_{eff} = 2\zeta\omega_n M_{eq} \quad , \quad (2.6)$$

where ζ is the damping ratio. Furthermore, R_L is the load resistance across the piezoelectric layer, with $V(t)$ representing the generated voltage across R_L, while C_p is the capacitance of the piezoelectric layer. Finally, the electromechanical coupling factor can be calculated using the relation,

$$\Theta = \sqrt{M_{eq}C_p\left(\omega_{n_{oc}}^2 - \omega_{n_{sc}}^2\right)} \quad , \quad (2.7)$$

where $\omega_{n_{oc}}$ and $\omega_{n_{sc}}$ are, respectively, the open- and short-circuit resonant frequencies. Next, a state vector, X, is defined as,

$$\mathrm{X} = \begin{Bmatrix} X_1 \\ X_2 \\ X_3 \end{Bmatrix} = \begin{Bmatrix} w(L,t) \\ \dot{w}(L,t) \\ V(t) \end{Bmatrix} , \quad (2.8)$$

and the governing Equations (2.2) and (2.3) are written in state space form as,

$$\dot{\mathrm{X}} = \begin{Bmatrix} w(L,t) \\ \dot{w}(L,t) \\ \dot{V}(t) \end{Bmatrix} = \begin{bmatrix} 0 & 1 & 0 \\ -\omega_n^2 & -2\zeta\omega_n & -\dfrac{\Theta}{M_{eq}} \\ 0 & \dfrac{\Theta}{C_p} & -\dfrac{1}{R_L C_p} \end{bmatrix} \begin{Bmatrix} X_1 \\ X_2 \\ X_3 \end{Bmatrix} + \begin{Bmatrix} 0 \\ a\cos(\Omega t) \\ 0 \end{Bmatrix}. \quad (2.9)$$

Equation (2.9) can be analytically solved through a closed-form solution analysis or numerically. The average power output is then defined as,

$$\mathrm{P_{avg}} = \frac{V_{rms}^2}{R_L} \ , \quad (2.10)$$

where V_{rms} denotes the root mean square of the generated voltage.

It should be mentioned that the electromechanical coupling coefficient exhibited by the Elephant harvester is larger than its counterparts. This results in a strong increase in the level of the harvested power. Also noteworthy is the large observed damping ratio of the Zigzag design. This in part is responsible for the lower observed power, and comes from the higher number of segments distant from the fix end, causing more sign changes of the stress, observed in Figure 2.31(b). The Zigzag design has four segments away from the fixed end while the Flex and Elephant have two, resulting in approximately twice as much damping.

Figure 2.36 shows the comparisons between the results of the analytical model and the experimental measurements for the three beam geometries when R_L=$10^6\Omega$. Looking at the coefficient of determination, R^2, there is an excellent fit for the Elephant geometry, a good fit for the Flex geometry, and a poor fit for the Zigzag geometry. This is because the model is suited for describing bending. The influence of torsional effects is not captured in the model, which is the major cause of discrepancy between the model and measurement results. These results further prove how the proposed Elephant 2D beam shape eliminates torsional effects, increasing harvester performance by giving an optimally pure bending motion.

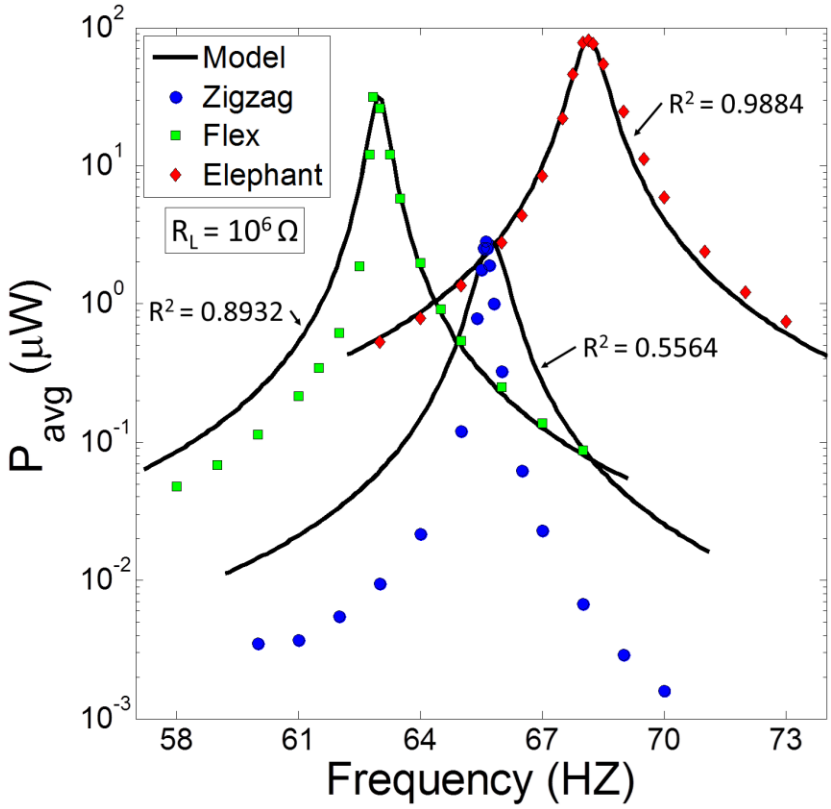

Figure 2.36 – Comparison of analytical single-degree-of-freedom bending model and experimental results for the case of $10^6\Omega$ load resistance.

Of additional note is the fact that above in Figure 2.36, the black curves representing the model are above the experimental results. If one were to argue that a model does not attribute some energy to a system, then one would expect the model predicted power to be less than the experimental results, which naturally include all influences. This would perhaps indicate that the presence of torsion not only does not contribute to energy harvesting, but may also hinder it in some way. While the effects of torsion on two-dimensional beams may be more confounding than what is explained here, the fact remains that optimizing a harvester for bending yields dramatically better power production.

2.7.9 Relative Non-dimensional Harvester Performance Figure of Merit

To compare the harvesters proposed in this work to those in the literature, a methodology of comparison is proposed. As the applications and design strategies of piezoelectric energy harvesters are vast, it necessitates a dimensionless parameter comparison. Indeed, those modeling

vibration energy harvesters frequently examine their designs with dimensionless parameters; however, this strategy has escaped the comparison of experimental studies. With this impetus, I present the Relative Non-dimensional Harvester Performance Figure of Merit, $\mathcal{S}$, defined as,

$$\mathcal{S} = \mathrm{S_P} s_P \mathrm{S_M} s_M S_{BW} s_{BW} S_V s_V \quad . \tag{2.11}$$

where the upper-case letters indicate relative dimensionless parameters, with lower-case letters being weighting coefficients, where the sum of the weighting coefficients equals to unity. The individual dimensionless Figures of Merit are defined as,

$$\mathrm{S_P} = \frac{P_{avg}\omega_n}{M_{eq}a^2} \ , \qquad S_M = \frac{\sqrt{s_{11}^E \epsilon^T}}{d_{31}} \ , \qquad S_{BW} = \frac{\Delta_{3dB}}{\omega_n} \ , \qquad S_V = \frac{LW}{T^2} \tag{2.12}$$

where S_P is the dimensionless power, S_M represents the dimensionless material, S_{BW} denotes the dimensionless band-width, and S_V is the dimensionless volume Figure of Merit, respectively. s_{11}^E is the compliance of the piezoelectric material, or $1/Y_{11}^E$, where Y_{11}^E is the Young's Modulus. ϵ^T is the permittivity of the material, or $K^T\epsilon_0$, where K^T is the relative dielectric constant and ϵ_0 is the permittivity of free space (8.85×10^{-12} F/m). Δ_{3dB} is the half-power bandwidth of the average power versus frequency curve. Finally, L, W, and T are the length, width, and thickness of the harvester, respectively (including all tip masses, materials, circuitry, etc.), as if the harvester was encased in a cuboid. Each dimensionless parameter is made relative (and normalized to unity) by dividing the calculated parameter value for each harvester by the maximum value of each parameter set . Additional dimensionless parameters may be suggested and weighting coefficients adjusted according to individual application needs. For example, if the harvester were to be placed on a large machine vibrating at an unvarying frequency, the weighting coefficients s_{BW} and s_V could be made small. It is also suggested that $s_P = s_M$, since the two are coupled. Compared to the cited experimental works, it is noted, in Figure 2.37, that the relative performance of the proposed Elephant harvester is the highest one, where all parameters are given equal weighting, which shows the effectiveness of the designed 2D concentrated stress structures.

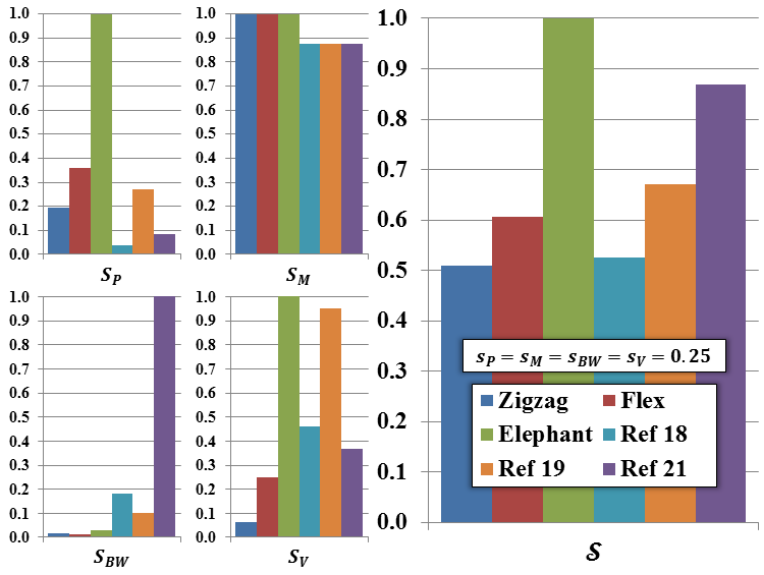

Figure 2.37 – Relative Non-dimensional Harvester Performance Figure of Merit with equal weighting to all constituent non-dimensional parameters, comparing proposed harvester designs to several literature references.

2.7.10 Summary

In summary, it has been shown how the current strategy of using highly compliant 2D beam shapes to harvest energy from low frequency vibrations creates performance reducing torsion. A characteristic Zigzag shaped beam was created to compare against the two proposed 2D beam shapes. The proposed 2D beam shapes, termed as 'Flex' and 'Elephant', were created with the goals of realizing a concentrated stress structure, whereby stress in the beam is concentrated in a small area where a piezoelectric layer may be placed, rather than distributed throughout the beam, while also maintaining a low resonance frequency. Through analytical and finite element modeling, and experimental measurements, it has been shown that the Elephant harvester was able to provide a significant increase in power production with only a minimal change in resonance frequency, compared to the Zigzag harvester. Moreover, the Elephant harvester has a large effective beam tip whereby large tip mass may be placed while retaining a low-profile, resulting in a low volume harvester, and subsequently large power density. Finally, a strategy for comparing piezoelectric energy harvesters using relative non-dimensional parameters was introduced, where

the performance of the Elephant harvester was observed to be higher than that of the considered literature references.

2.8 Mode Shape Combination of Elephant Beam Shape

Vibration energy harvesters are most often designed to operate at resonance, where the resonant frequency of the energy harvester matches that of the dominant frequency of the vibration source. This matching of source and harvester mechanical impedances allows for the most efficient transfer of power from the source to the harvester. Availability of more power to the harvester thus results in higher transduction. The drawback of such designs is that outside the narrow resonant frequency band, little mechanical power is transduced. Addressing vibration energy harvester bandwidth and increasing power output have been the major focus areas of research. Several review and research articles have addressed the strategies towards achieving higher power density and broad bandwidth.[57, 65, 81-84, 101-104]

A promising area with respect to vibration energy harvester design that has received less attention is the mode shapes of the considered dynamic systems. The vast majority of harvester designs employ some variation/modification of a single-degree-of-freedom one-dimensional cantilever beam, and the mode shapes of such beams are well known. This is especially true for the first bending mode, which is almost exclusively the chosen vibration mode for harvesting. Here, the term ‘one-dimensional’ implies emphasis on a specific dimension, typically the length, along which the only variations in geometry, materials, mass, etc. occur. One-dimensional designs are not conducive towards mode-shape optimization. Thus, two-dimensional beam shapes (those that curve, meander, spiral, etc. in a plane) have gained research interest as they offer the ability to modify the vibration characteristics, in order to achieve the desired performance.

Wu et al. have proposed a two-degree-of-freedom design, by folding a two mass cantilever back on itself, thereby creating a ‘cutout cantilever’.[112] This design improves on the continuous cantilever with two masses by effectively altering the stiffness matrix, which was demonstrated through a lumped parameter model. This architecture allowed bringing two bending modes closer to each other resulting in a broadband response. One promising design for enhancing the performance of vibration-based energy harvesters, by using a two-dimensional beam shape, was recently proposed.[113] This shape, termed ‘closed-circuit symmetric meandering configuration’,

or ‘Elephant’, showed improved power generation (over an order of magnitude) compared to a ‘Zigzag’ shaped beam by engineering the beam shape for an optimized first bending mode and stress concentration in the piezoelectric section.

2.8.1 Theorized Combined Mode Shape

In the prior section, the Elephant beam shape was examined only in its first bending mode. With further examination, it was found that the second bending mode of the Elephant configuration possesses an intriguing mode shape relative to the first bending mode. For the harvester geometry shown in Figure 2.38(a), the first and second bending modes are rendered in Figure 2.38(b) and (c), respectively. Inspection of these mode shapes indicates that they are nearly opposite of each other. In the first bending mode, the section of greatest deflection is furthest from the clamped section in the y-direction, while small deflection is observed in the sections closest to the clamped section in the y-direction. In contrast, the highest deflection in the second bending mode is observed in the sections closest to the clamped section in the y-direction, and very little deflection is observed in the section furthest from the clamped section in the y-direction.

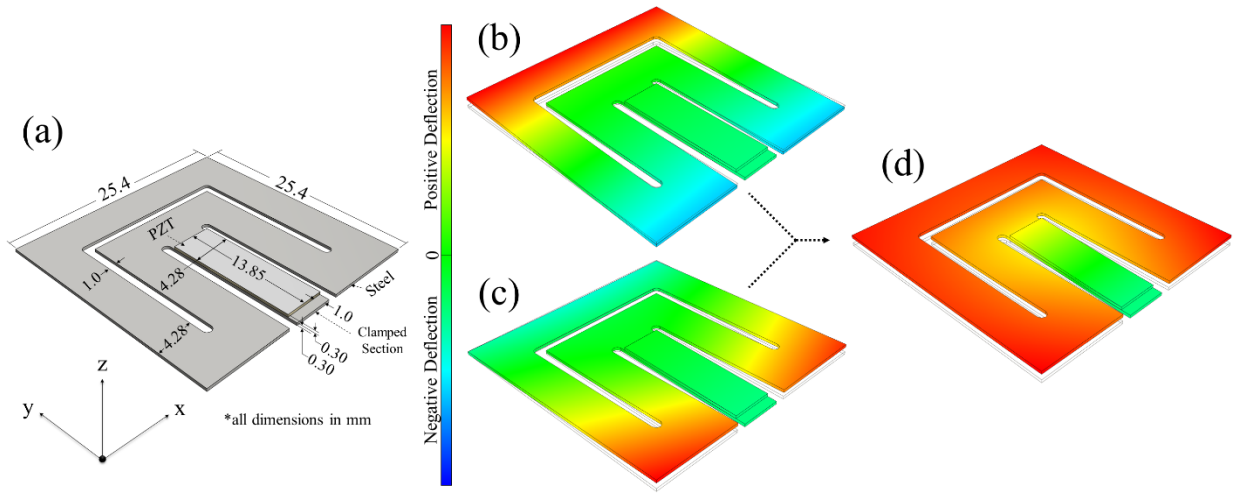

Figure 2.38 - (a) Dimensioned schematic of ‘Elephant’ two-dimensional vibration energy harvester, (b) 1st bending mode of Elephant, (c) 2nd bending mode of Elephant, and (d) proposed combined mode shape.

The fact that the first two mode shapes do not share areas of common deflection, at least to a significant degree, implies that they are nearly orthogonal to each other. It follows then, that the modal frequencies of each shape could be adjusted independently, namely through mass loading structural modification. This theory was inspired by observation of Figure 2.29, were it can be seen that when 'tip mass' was added, the first modal frequency decreases, however, the second modal frequency remained nearly unchanged. This is an unusual observation, because typically the addition of mass to a simple vibrating system lower all modal frequencies.

Modifying the beam structure through mass loading has the effect of lowering the natural frequency associated with each mode, as $\omega_i = \sqrt{k_i/m_i}$, where k_i and m_i are the equivalent stiffness and mass associated with each mode, resulting in modal frequency ω_i. In a single-degree-of-freedom system, this mass loading takes the form of 'tip mass' or 'proof mass', and is used to tune the harvester dynamics to that of the source dynamics for the most efficient power transfer. As a secondary effect, power output is also increased as kinetic energy is increased due to the presence of more moving mass in the system.

It is then hypothesized, that there must exist a modified structure, whereby mass is added at the points of highest deflection of each mode (to have the greatest effect), resulting (by virtue of near orthogonality) in the shifting of second bending modal frequency near enough to that of the first bending modal frequency to create the combined mode shape depicted in Figure 2.38(d). Combining these opposite modes would result in the entire beam vibrating in phase. This mode shape is desirable for energy harvesting because the entire mass of the structure is in motion and moves in phase, thereby increasing kinetic energy, and subsequently stress in the piezoelectric layer. Based upon this hypothesis, it is proposed that this combined mode shape would yield higher power output.

The simulations in Figure 2.38(b) and (c) were generated using the Modal Analysis tool in the Stress Analysis environment of Autodesk Inventor 2016. Figure 2.38(d) was generated using the Static Analysis tool in the Stress Analysis environment of Autodesk Inventor 2016. Therefore, this 'combined' mode shape was not revealed via FEA, but rather prescribed through the point forces throughout the beam and distributed load to yield the mode shape hypothesized in this study, as shown in Figure 2.39.

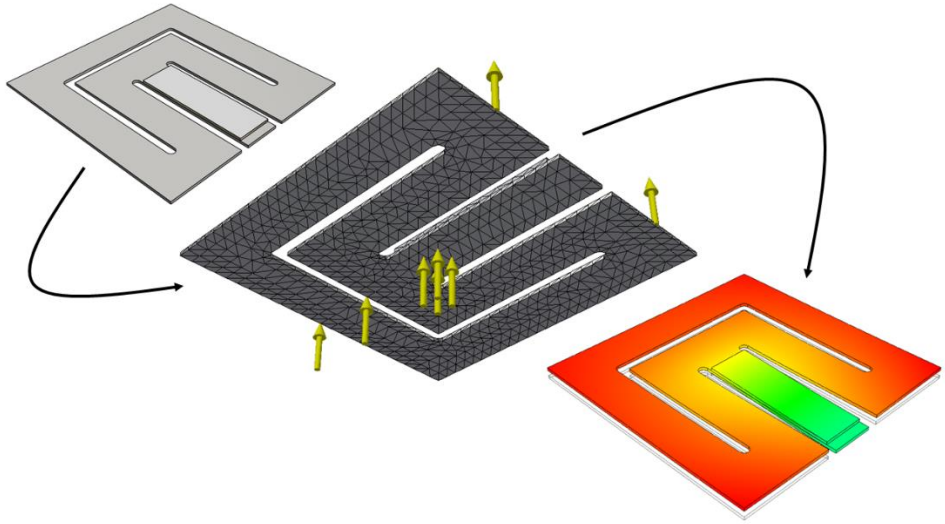

Figure 2.39 – Creation of Figure 2.38(d) by prescribing point and distributed loads in the Static Analysis tool in the Stress Analysis environment of Autodesk Inventor 2016.

Further information about the FEA simulations is provided in Figure 2.40. Here, it is also predicted from the modal analysis the presence of a torsion mode, shown in Figure 2.40(d), occurring between the first and second bending modes. This mode is not useful for energy harvesting, but influences the other modes, as is discussed later.

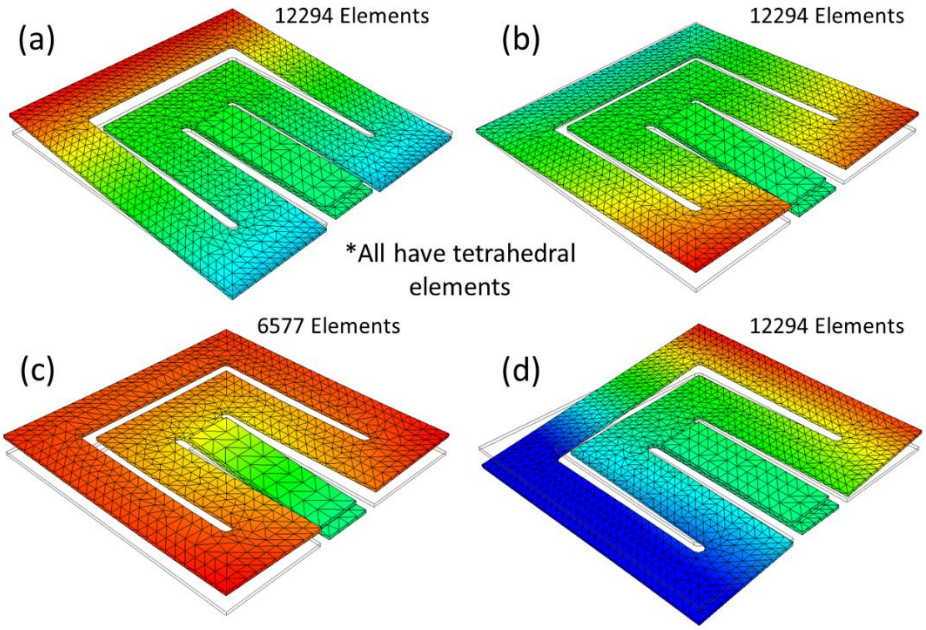

Figure 2.40 – Additional information on FEA simulations. (a), (b), and (d) are predicted modes using Modal Analysis, while (c) is prescribed, as Figure 2.39 shows, using Static Analysis, both in the Stress Analysis environment of Autodesk Inventor 2016.

2.8.2 Effect of Mass Loading on Modal Frequencies

To observe the conditions where this mode combination could occur, masses were added to the points on the beam corresponding to the highest deflection in the first and second bending modes, labeled as ‘Mass Mode 1’ and ‘Mass Mode 2’ in inset of Figure 2.41. The subsequent transfer functions generated from each configuration were observed to find the modal frequencies plotted in Figure 2.41.

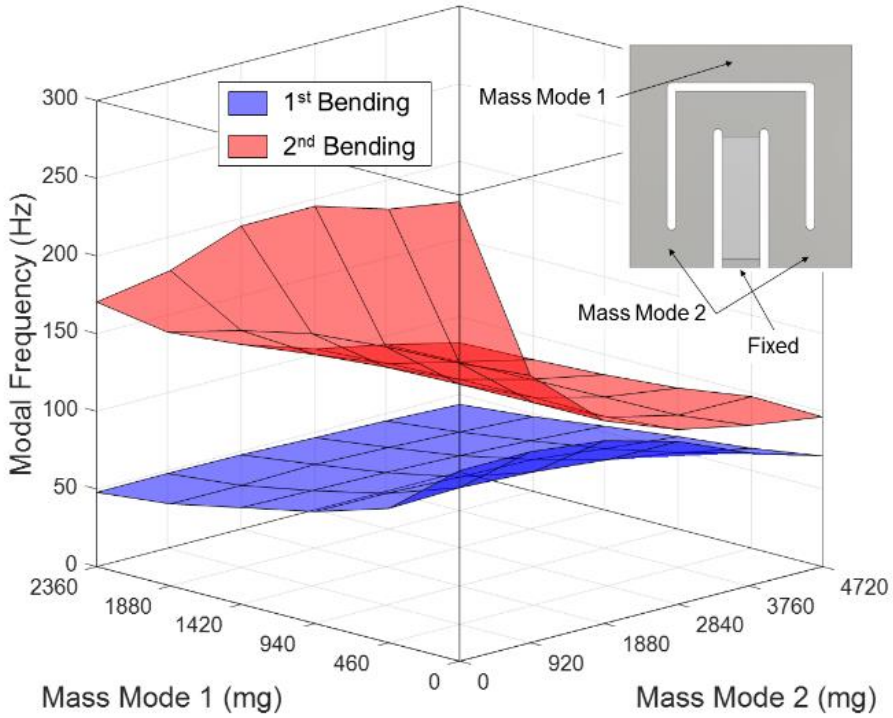

Figure 2.41 – 1st and 2nd bending modal frequencies as functions of mass loading on the areas of highest deflection for each respective mode shape, with inset showing mass placement location(s).

From Figure 2.41, it can be seen how the two modes are largely independent of one another. By keeping mass constant at one location and increasing mass at the other location, the mode associated with the mass being kept constant does not significantly change modal frequency. It is at the same time observed, the expected inversely proportional decay in modal frequency of the mode upon which mass is being increased. The exception to this observation is the case when there is no added mass on 'Mode 1' (the first bending mode) and mass is added to 'Mode 2' (the second bending mode). Here, the curves are drawn near to each other, as if they would cross, but then diverge. Indeed, the curves cannot cross (i.e. the second bending mode becomes the first) for this system, due to the presence of an anti-resonance between these two modes. As the curves diverge, it can be said that sufficient mass has been added, such that a new system is created. Because the curves of Figure 2.41 are nearest when there is no mass at the area of highest deflection of the first bending mode while mass is added to the area of highest deflection of the second bending mode, in all subsequent experiments, mass will only be added to the area of highest deflection of the second bending mode.

To further clarify the experiments associated with Figure 2.41; the planes depicted are the peaks of transfer functions generated while sequentially adding mass to the specified locations. Transfer functions are the crossed power spectral density from the base acceleration signal to the voltage output of the piezoelectric layer, while subjected to white noise excitation for approximately 100 seconds and sampling at 2000 Hz. Mass placements are depicted in Figure 2.42, with subsequent transfer functions given in Figure 2.43.

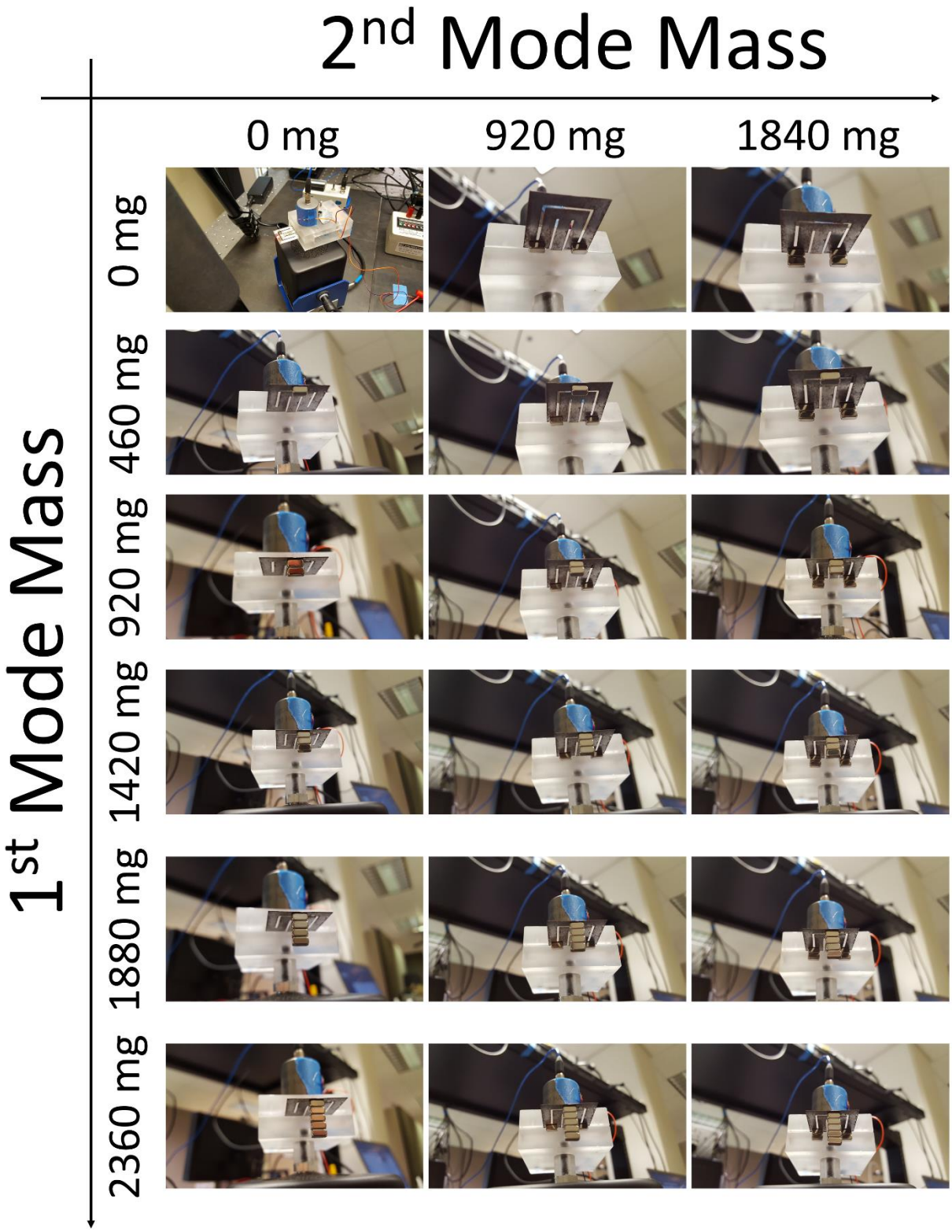

Figure 2.42 – Mass placement for the experiment in Figure 2.41.

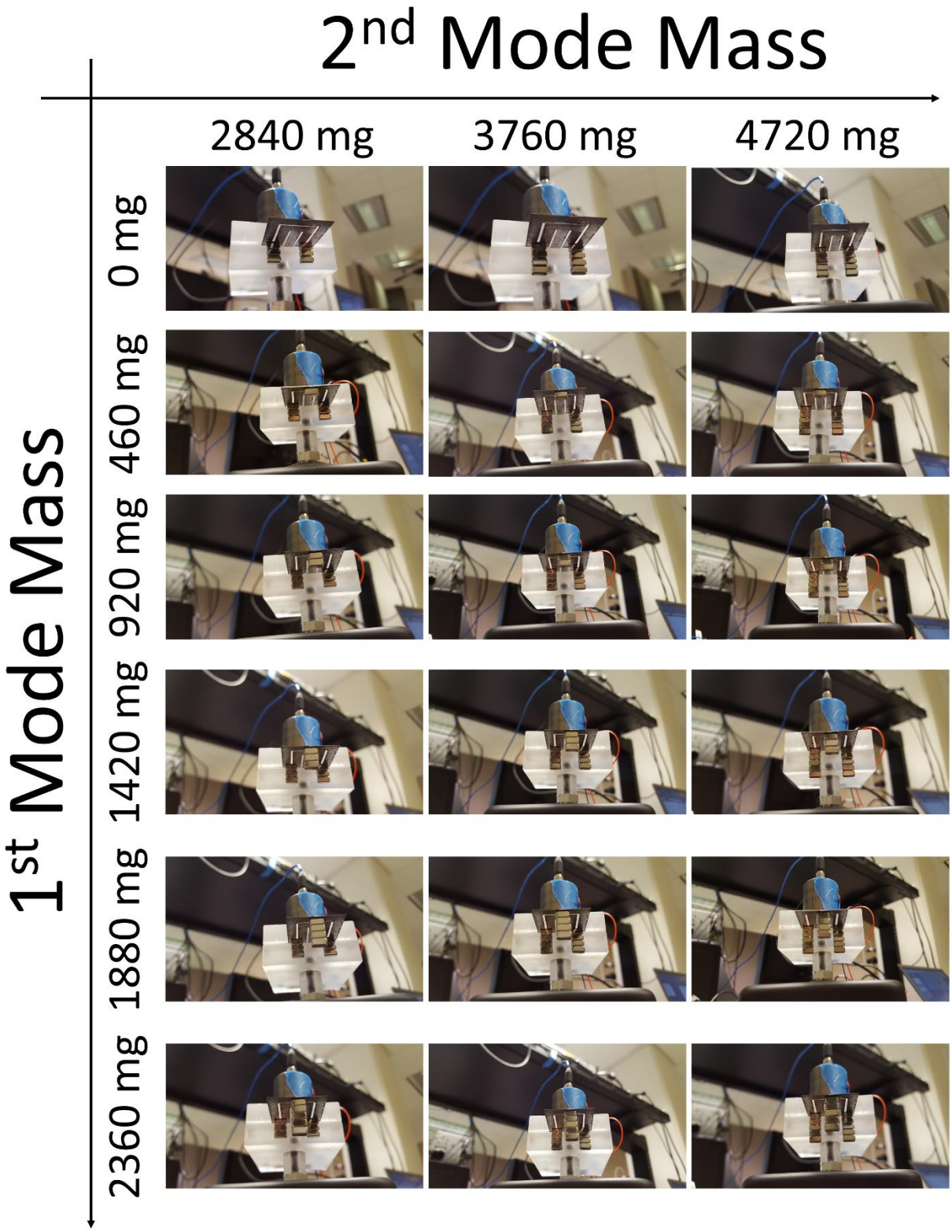

Figure 2.42 – Mass placement for the experiment in Figure 2.41 (Continued…)

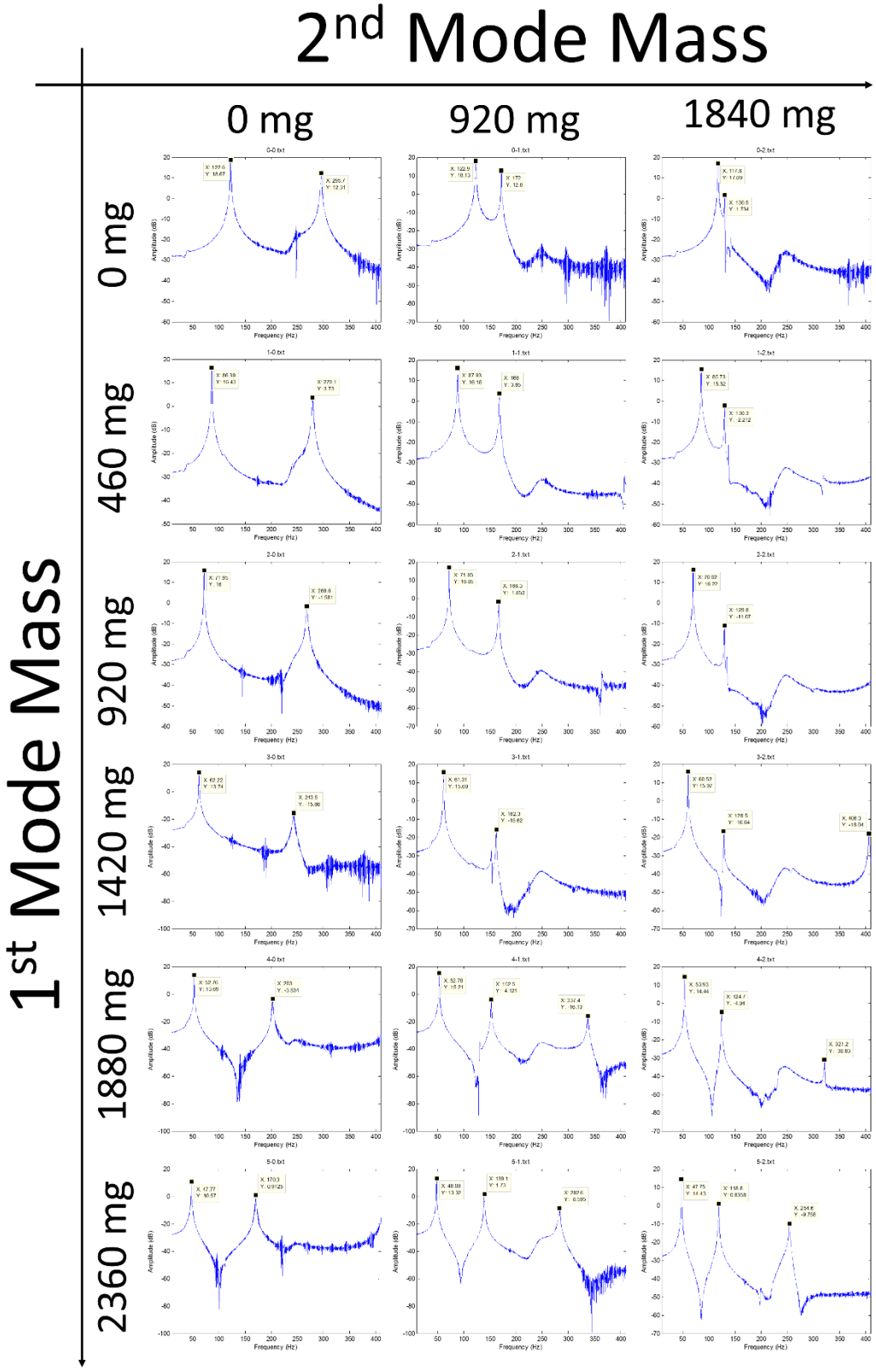

Figure 2.43 – Transfer functions for the experiment in Figure 2.41.

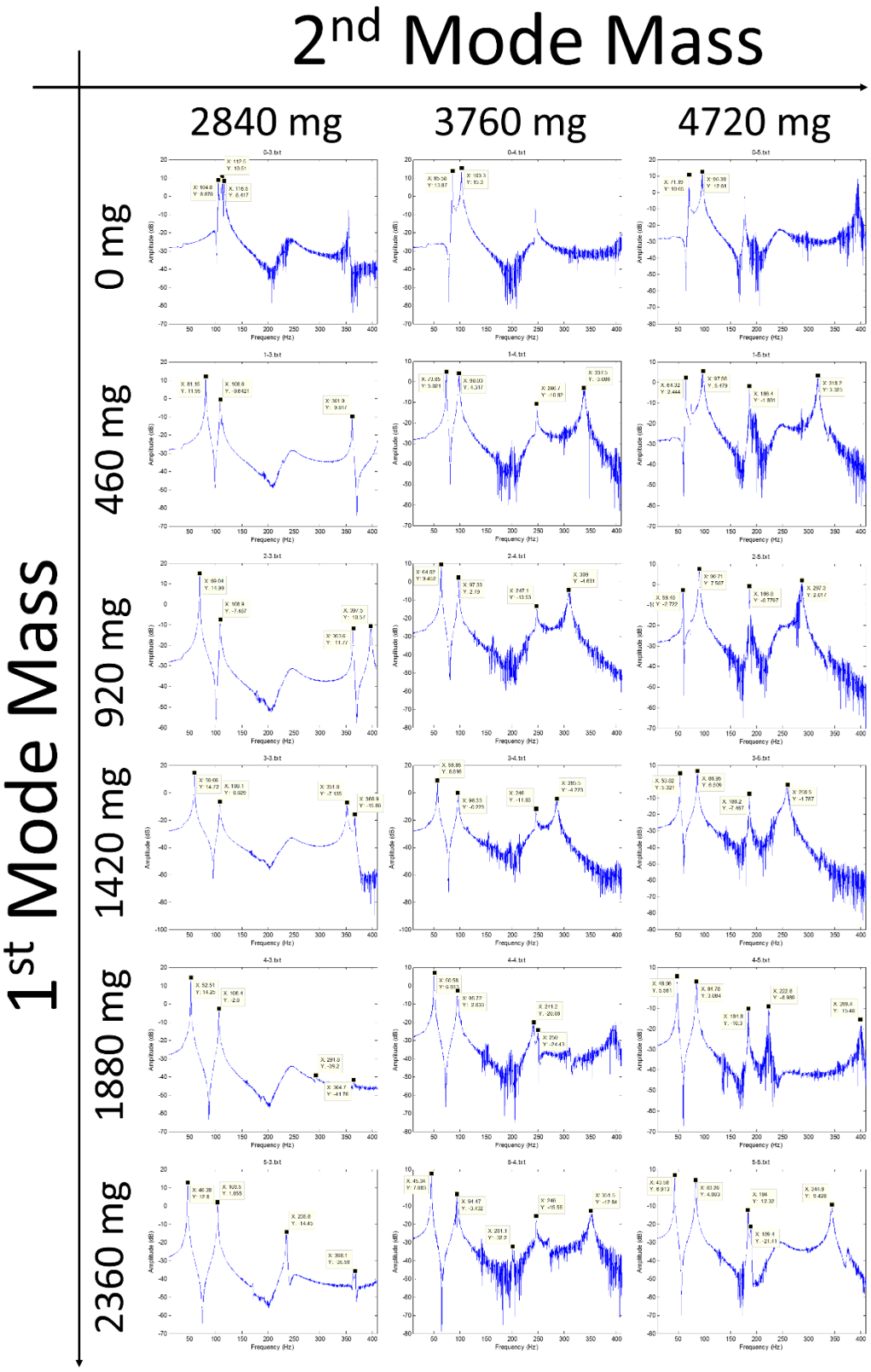

Figure 2.43 – Transfer functions for the experiment in Figure 2.41 (Continued…)

2.8.3 Effect of Mass Loading on Mode Shapes

Next, the mode shapes of the first two bending modes are surveyed, in order to identify the evolution of a combined mode shape. Mass was sequentially loaded on the second bending mode and the beam scanned manually with a Polytec PDV100 laser vibrometer, as in Section 2.8.3.1, and automatically Polytec PSV 500 scanning laser vibrometer, as in Section 2.8.3.2, while subjected to white noise vibration. To increase the resolution of mode shape and modal frequency measurements, 26 mass values were used, rather than 6 as in the previous experiment of Figure 2.41. The mass types and placements are shown in Figure 2.44 below.

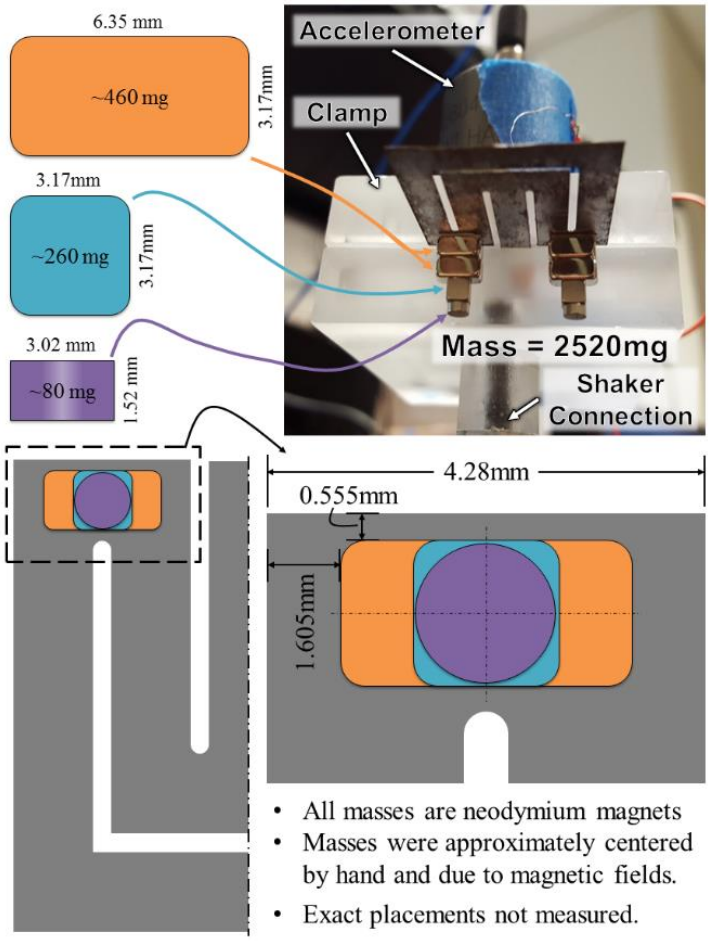

Figure 2.44 – Mass configuration placements for experiments shown in the following sections.

2.8.3.1 Single Point Laser Vibrometer Measurements of Mode Shapes

The mode shapes of the Elephant beam were first measured using a single point vibrometer. This is accomplished by exciting the beam with white noise and shining the laser vibrometer at different points on the beam. These points are labeled as P1, P3, P5, and P7 in Figure 2.45(a). At each point, a transfer function between the vibrometer signal and the base acceleration is calculated, generating the Bode plot in Figure 2.45(b). The peaks of the transfer functions are taken to be the modal frequencies (highlighted with dashed black lines in Figure 2.45(b)). The magnitude of the peaks are multiplied by the sine of their phase angle, normalized to unity, and then plotted in the z-axis at their physical location in the x-y plane, in Figure 2.45(c). Points are then connected by lines to illustrate the mode shape.

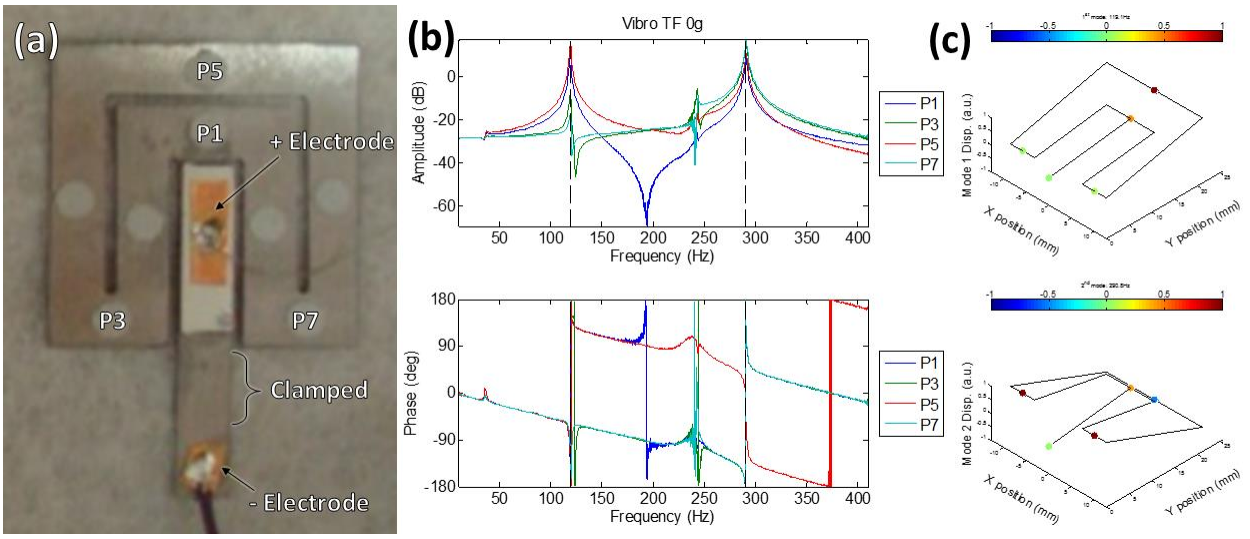

Figure 2.45 – (a) Point nomenclature and picture of beam out of clamp. (b) Bode plots of transfer functions at different beam points. (c) Resultant mode shape plots.

The mode shapes were initially measured this way before employing a scanning laser vibrometer. The mode shapes for the measured masses (not all the masses used in the scanning laser experiment were used here) are shown in Figure 2.46. The mode shapes match well with the ones measured with the scanning laser discussed later. The 'Piezo TF' are the transfer functions of the piezoelectric layer voltage and the base acceleration. The peaks of these transfer functions are used along with additional mass and PSV 500 measurements to create Figure 2.50(b).

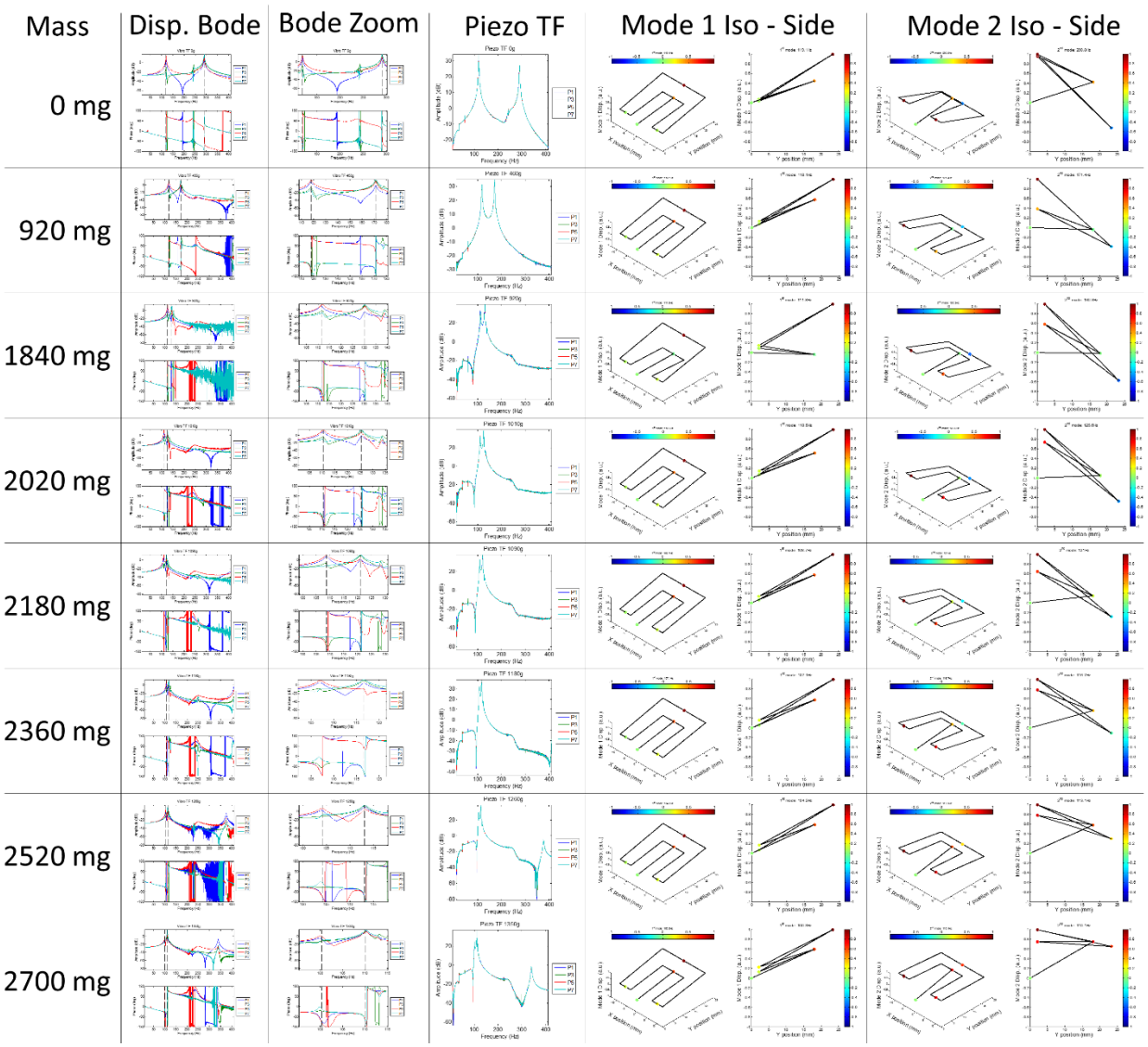

Figure 2.46 – Experimental mode shapes measured using a single point laser vibrometer.

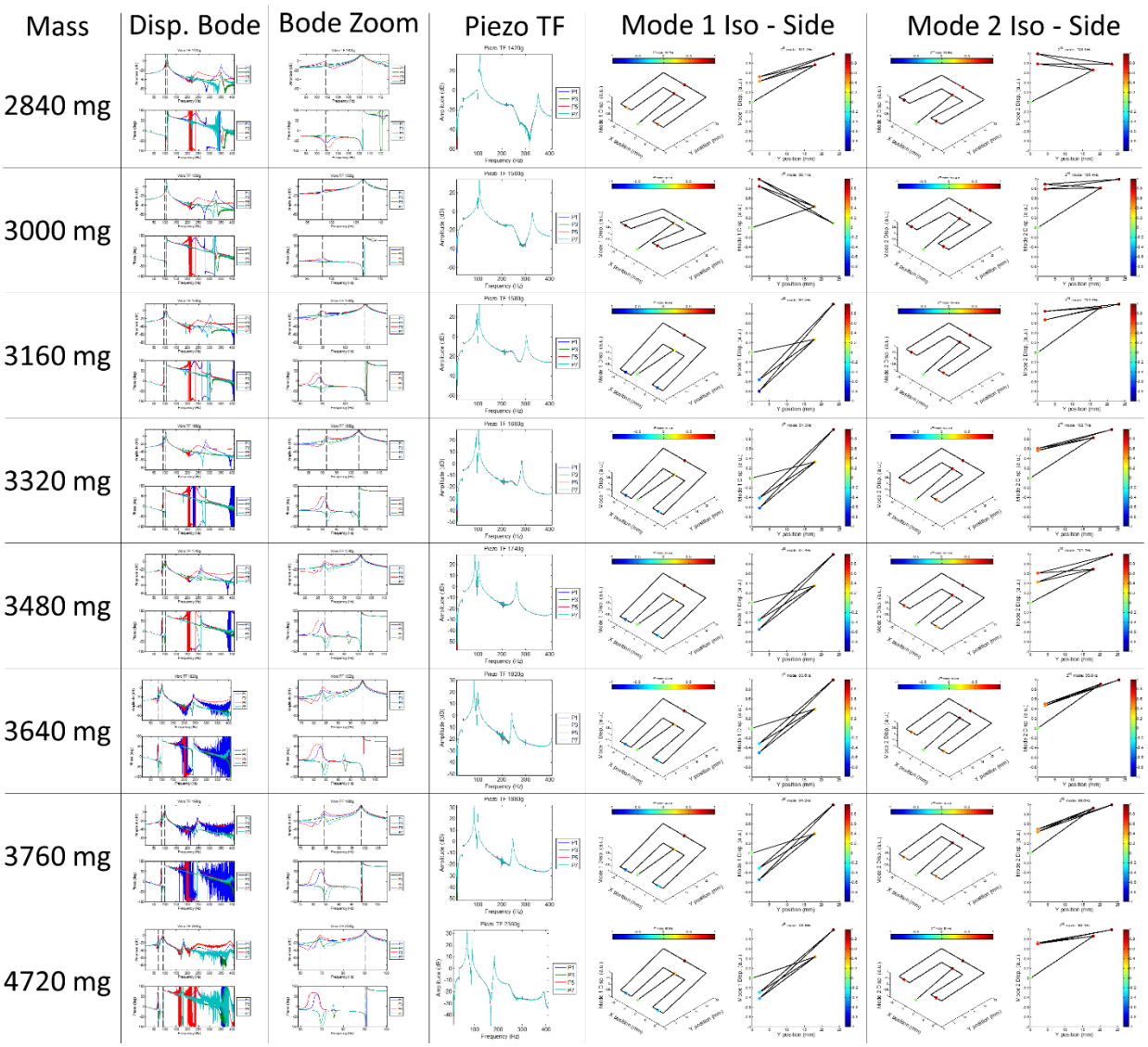

Figure 2.46 – Continued…

2.8.3.2 Scanning Laser Vibrometer Measurements of Mode Shapes

During the measurement of the mode shapes, the use of a Polytec PSV 500 scanning laser vibrometer became available, allowing for fully detailed mode shape measurement to be taken. The experimental setup is pictured in Figure 2.47(b), while the laser scanning pattern is shown in Figure 2.47(c). All data acquisition and signal generation for this study was handled by the PSV 500's system.

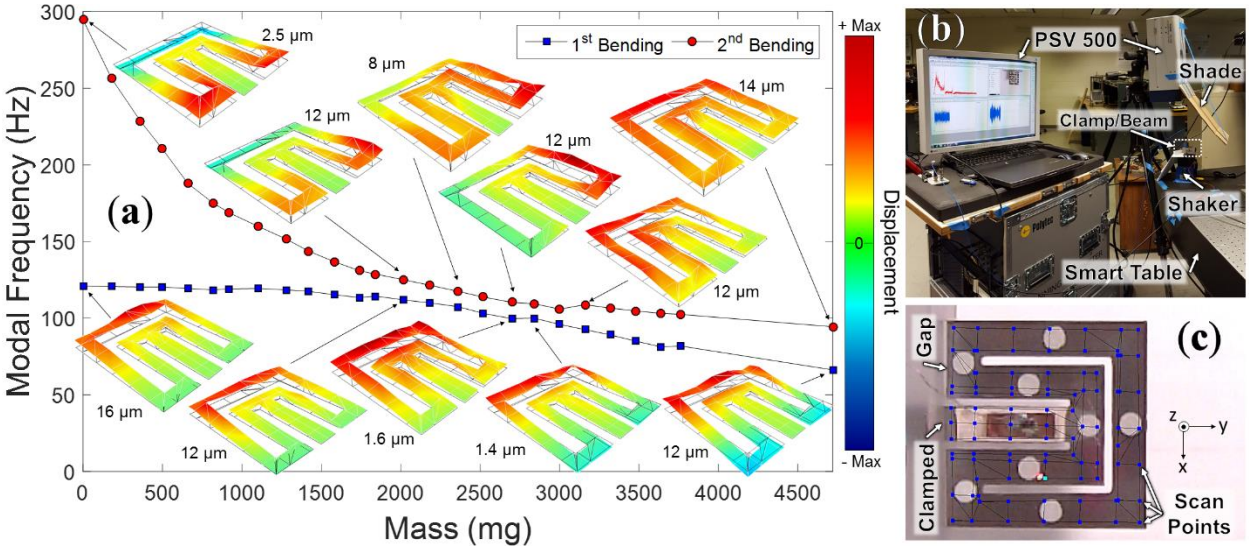

Figure 2.47 – (a) Selected scanning laser vibrometer measured mode shapes for the 1st and 2nd bending modes of the Elephant beam as a function of mass loading, (b) experimental setup, (c) scanning pattern over the beam, and detailed view of the clamped beam.

Starting from the zero added mass case, in Figure 2.47(a), it is clear that the mode shapes predicted by the finite element modal analysis (Figure 2.38(b-c)) are validated. By adding mass, the first bending mode is largely unchanged in shape, frequency, and amplitude all the way up to 2020 mg. For the second bending mode, however, while the mode shape remains the same, the amplitude of vibration increases. At 2360 mg, a change in the mode shapes is observed as the curves approach one another. In both the first and second bending modes, the entire beam vibrates in phase. The first mode shape appears to pivot about the clamped end, while the second mode transforms into the combined mode shape hypothesized in Figure 2.38(d). Around 2700-3000 mg of added mass, the mode shapes begin to vary significantly. Above 3000 mg of added mass, sufficient mass is added to constitute a new system. Clearly, the modal frequency of the first bending mode is no longer roughly constant, but decreases with mass. The first mode shape of this new system appears to pivot about the middle (on the y-axis) of the beam, while second mode shape looks again like the combined mode shape and vibrates in phase.

2.8.3.2.1 Influence of Torsional Mode

It can be noticed that some of the second bending mode shapes in Figure 2.47(a) are not symmetric about the center of the beam (in the x-axis). This phenomena is not due to asymmetry

in mass placement, rather, these apparent twists in the second bending mode shape are caused by the coupling of the first torsion mode with the second bending mode. The first torsion mode does not contribute to energy harvesting, so it is not readily observable in the transfer function between the base excitation and the voltage output, as is evident in Figure 2.46 in the Piezo TF. It is, however, evident in the transfer function between base excitation and vibrometer reading, as is evident in Figure 2.46 in the Bode plots. The effect of the torsion mode can also be seen in the mode shapes measured by single laser vibrometer, given in Figure 2.46. The torsion mode shapes as a function of added mass are plotted in Figure 2.48 below along with several additional measured mode shapes of the second bending mode, where it most strongly interacts with the torsion mode.

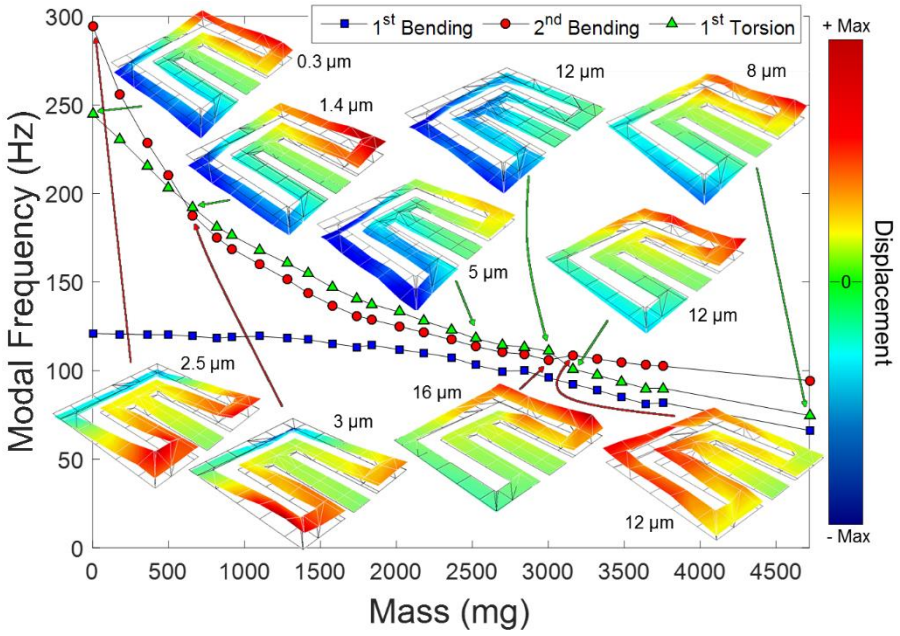

Figure 2.48 – Selected scanning laser vibrometer measured mode shapes for the 2nd bending and 1st torsion modes of the Elephant beam as a function of mass loading.

2.8.4 Resulting Effects on Energy Harvesting Performance

After confirming the hypothesis of the existence of a combined mode shape, it was examined if this mode shape can transduce more power. Power production is typically measured in response to broadband excitation (white noise/random), or at a particular frequency or set of

discrete frequencies (sine sweep). In this study, both types of measurements were taken using the experimental setup pictured in Figure 2.50(a). This setup was also used to collect the data in Figure 2.41, and this shaker/clamp/beam/accelerometer arrangement is the same as in Figure 2.47(b).

In this setup, base excitation is provided to the harvester by a TMS K2007E01 modal shaker, through a custom acrylic clamp, upon which a PCB Piezotronics 393B04 accelerometer is fastened. Since the magnetic masses would be placed close to the clamp, a custom plastic clamp was machined out of acrylic, to avoid any induced damping that would be caused by the vibrating magnets moving near a metal clamp. The accelerometer signal is fed through a Kistler Piezotron Coupler 5112 before it is read by a NI9234 DAQ card. The signal from the Polytec PDV100 laser vibrometer is also read by this card. Voltage output of the harvester is read across an IET Labs RS-201 precision resistance substituter by a NI9229 DAQ card. The input signal to the shaker is also read by this card. This signal is produced by a NI9269 card and is wired directly to the shaker, since the shaker used has an integrated charge amplifier. These NI DAQ cards are housed in a cDAQ-9174 chassis and connected to a laptop running several LabVIEW VI's programmed for the different measurement tasks. For clarity, the above described setup is shown in schematic form in Figure 2.49 below.

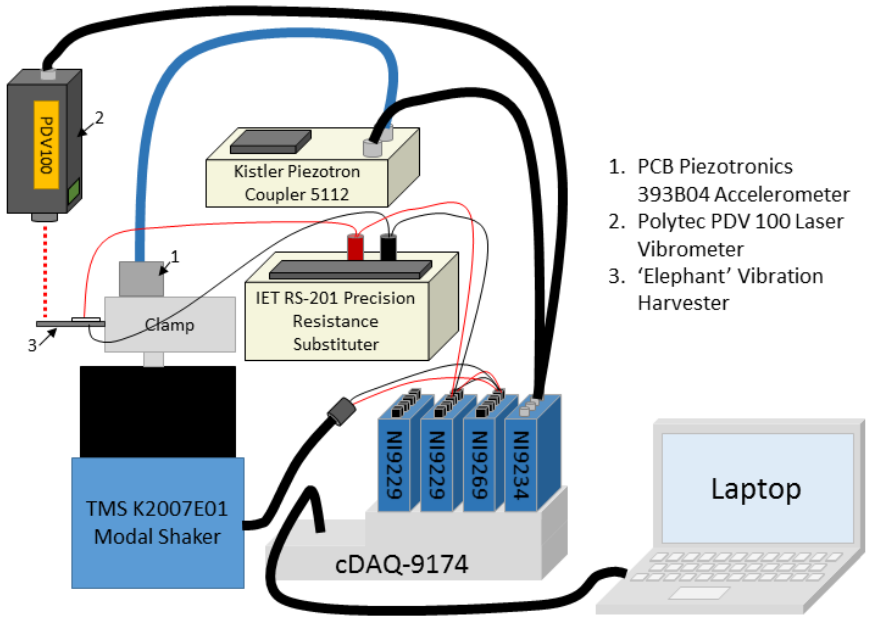

Figure 2.49 – Schematic diagram of experimental setup, pictured in FIG. 6(a).

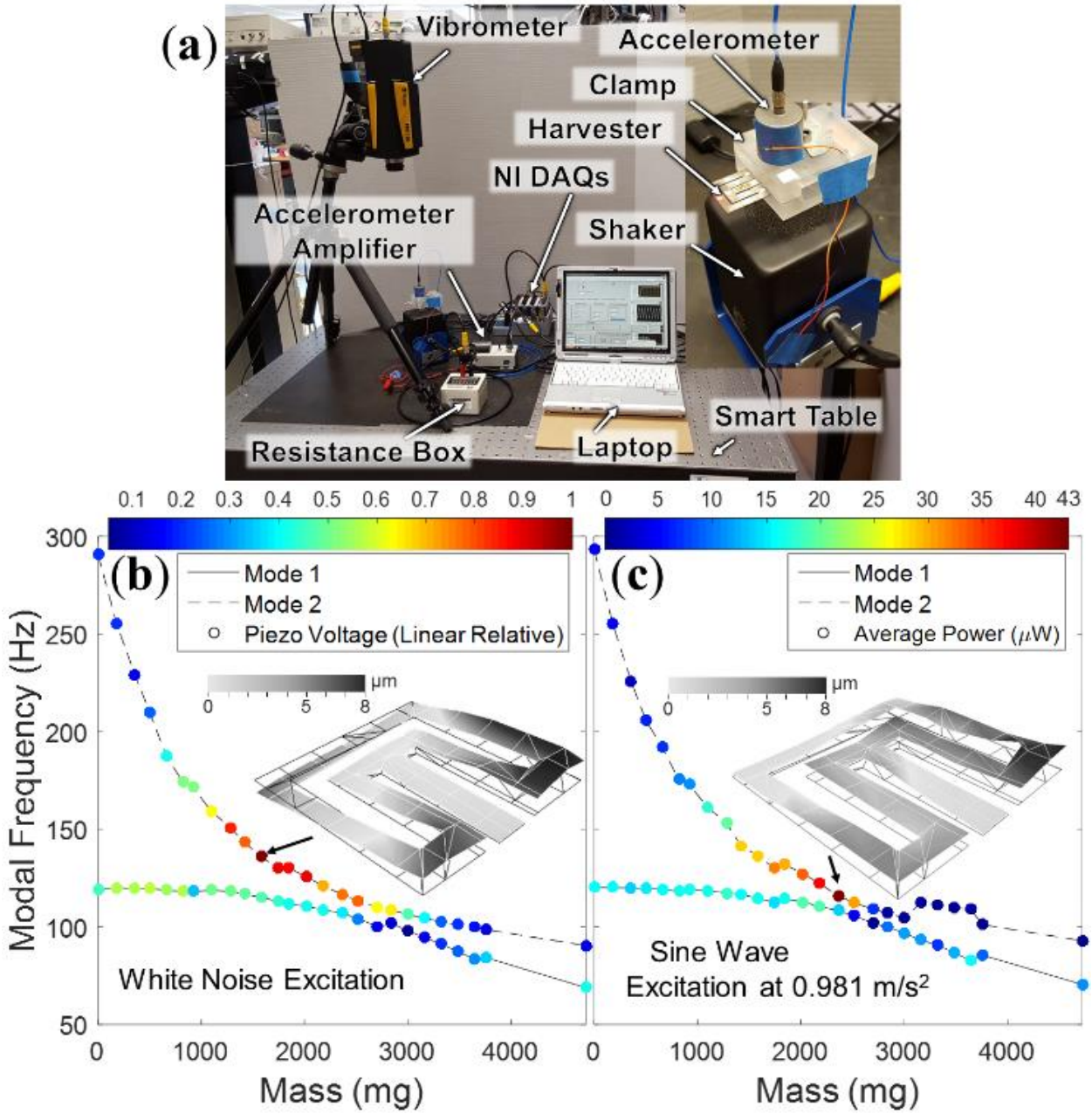

Figure 2.50 – (a) Experimental setup with close up of shaker/clamp/harvester, (b) linear relative open circuit voltage and modal frequency as a function of loaded mass when subjected to white noise excitation, (c) average optimum power and modal frequency as a function of loaded mass when subjected to sine wave excitation.

The results of the harvester's performance when subjected to white noise excitation are shown in Figure 2.50(b). Simply looking at the generated voltage in the time history would only

yield the aggregate performance of the harvester across all frequencies. However, it is desired to compare the performance contributions of the first and second bending modes. Thus, the peaks of the transfer function between harvester's voltage output and accelerometer signal (base excitation) are taken as the performance metric. Consequently, since the transfer function is inherently a ratio, the absolute level of voltage output of the harvester is lost and can only be compared in relative means across the mass loading configurations. Therefore, 'Piezo Voltage' is given in Figure 2.50(b) as a linear relative measure, normalized such that the maximum value is unity. Here it is seen the best performance occurs at 1580 mg of added mass, in the second bending mode ('Mode 2'). The associated mode shape is shown in the inset. The highest level of performance results from the optimal region of enough added mass that increases the kinetic energy but is not enough to cause excessive mechanical impedance. This concept is important in the random excitation case, because for this type of excitation the harvester cannot take advantage of resonance.

The Elephant harvester performance under single frequency sine wave excitation at an amplitude of 0.981m/s^2 ±1% is shown in Figure 2.50(c). The maximum power produced was measured to be 43 μW at 2360 mg of added mass in the second bending mode. The inset picture on the plot shows the mode shape which produced the highest power. This mode shape corresponds with the mode shape hypothesized in Figure 2.38(d).

Here, each point was measured by scanning across a frequency range in which the modal frequency would occur (by stepping through a discrete number of frequencies, with 0.1 Hz steps), calculating power, and obtaining the maximum value. As the input signal frequencies were iteratively stepped though the selected range, a closed loop PID controller ensured that the level of base acceleration remained constant. Since a wide range of frequencies were involved in this measurement, the electrical load resistance was changed for each measurement according to the theoretical approximate optimum load resistance, $R_{opt} = 1/\omega C$, where the capacitance of the piezoelectric layer, C, was measured to be 3.1 nF.

Figure 2.51 summarizes the values used in the experiment shown in Figure 2.50(c). Load resistances used are the approximate theoretical optimum values, and the frequencies ranges swept were ±5 Hz of the modal frequencies measured in Figure 2.47. Since the NI DAQ's measures across a resistance of 1 MΩ, a variable resistor must be placed in series or parallel with the DAQ to vary the electrical load resistance. In this case, since all optimum resistances are less than the native resistance of the DAQ, the variable resistor is placed in parallel. Thus, the resistance the

variable resistor is set to must add in parallel with the DAQ resistance, in order to achieve the optimal load. This is why Rset (the value the variable resistor was set to) is different from Ropt (the optimal load).

C	f1	ω1	f2	ω2	Ropt1	Ropt2	Rdaq	Configuration		Rset1	Rset2	fset1			fset2		
3.10E-09	120.9375	759.8727	294.6875	1851.576	4.25E+05	1.74E+05	1.00E+06	1	0	7.38E+05	2.11E+05	116	121	126	290	295	300
	120.6250	757.9092	256.2500	1610.066	4.26E+05	2.00E+05		2	90	7.41E+05	2.51E+05	116	121	126	251	256	261
	120.3125	755.9457	228.7500	1437.279	4.27E+05	2.24E+05		3	180	7.44E+05	2.89E+05	115	120	125	224	229	234
	120.3125	755.9457	210.3125	1321.432	4.27E+05	2.44E+05		4	250	7.44E+05	3.23E+05	115	120	125	205	210	215
	119.3750	750.0552	187.8125	1180.061	4.30E+05	2.73E+05		5	330	7.55E+05	3.76E+05	114	119	124	183	188	193
	118.4375	744.1648	175.0000	1099.557	4.33E+05	2.93E+05		6	410	7.65E+05	4.15E+05	113	118	123	170	175	180
	119.0625	748.0918	168.7500	1060.288	4.31E+05	3.04E+05		7	460	7.58E+05	4.37E+05	114	119	124	164	169	174
	119.3750	750.0552	160.0000	1005.31	4.30E+05	3.21E+05		8	550	7.55E+05	4.72E+05	114	119	124	155	160	165
	118.4375	744.1648	151.5625	952.2953	4.33E+05	3.39E+05		9	640	7.65E+05	5.12E+05	113	118	123	147	152	157
	117.5000	738.2743	143.7500	903.2079	4.37E+05	3.57E+05		10	710	7.76E+05	5.56E+05	113	118	123	139	144	149
	115.3125	724.5298	136.8750	860.011	4.45E+05	3.75E+05		11	790	8.03E+05	6.00E+05	110	115	120	132	137	142
	113.4375	712.7488	130.9375	822.7046	4.53E+05	3.92E+05		12	870	8.27E+05	6.45E+05	108	113	118	126	131	136
	114.3750	718.6393	128.7500	808.9601	4.49E+05	3.99E+05		13	920	8.14E+05	6.63E+05	109	114	119	124	129	134
	111.8750	702.9314	125.0000	785.3982	4.59E+05	4.11E+05		14	1010	8.48E+05	6.97E+05	107	112	117	120	125	130
	110.0000	691.1504	121.5625	763.7997	4.67E+05	4.22E+05		15	1090	8.75E+05	7.31E+05	105	110	115	117	122	127
	107.5000	675.4424	117.5000	738.2743	4.78E+05	4.37E+05		16	1180	9.14E+05	7.76E+05	103	108	113	113	118	123
	103.1250	647.9535	113.7500	714.7123	4.98E+05	4.51E+05		17	1260	9.91E+05	8.23E+05	98	103	108	109	114	119
	99.6875	626.355	110.3125	693.1139	5.15E+05	4.65E+05		18	1350	1.06E+06	8.71E+05	95	100	105	105	110	115
	100.0000	628.3185	109.3750	687.2234	5.13E+05	4.69E+05		19	1420	1.06E+06	8.85E+05	95	100	105	104	109	114
	95.9375	602.7931	105.9375	665.6249	5.35E+05	4.85E+05		20	1500	1.15E+06	9.40E+05	91	96	101	101	106	111
	92.5000	581.1946	108.7500	683.2964	5.55E+05	4.72E+05		21	1580	1.25E+06	8.94E+05	88	93	98	104	109	114
	89.0625	559.5962	106.5625	669.5519	5.76E+05	4.82E+05		22	1660	1.36E+06	9.30E+05	84	89	94	102	107	112
	85.0000	534.0708	104.6875	657.771	6.04E+05	4.90E+05		23	1740	1.53E+06	9.62E+05	80	85	90	100	105	110
	81.2500	510.5088	103.1250	647.9535	6.32E+05	4.98E+05		24	1820	1.72E+06	9.91E+05	76	81	86	98	103	108
	81.8750	514.4358	102.5000	644.0265	6.27E+05	5.01E+05		25	1880	1.68E+06	1.00E+06	77	82	87	98	103	108
	66.2500	416.261	94.3750	592.9756	7.75E+05	5.44E+05		26	2360	3.44E+06	1.19E+06	61	66	71	89	94	99

Figure 2.51 – Summary of values used in the experiment represented in Figure 2.50(c).

Using the values given in Figure 2.51, voltage output from the piezoelectric was measured across all mass and frequency ranges by discretely stepping through frequencies in 0.1 Hz steps. After the measurement, the power was calculated along with half-power bandwidth. If the half power occurred between two measurement points, the value was linearly interpolated between the points. This data is presented in Figure 2.52 and Figure 2.53 for the first and second bending modes respectively. Here, in the plot titles C#F#, means configuration (what mass configuration 1-26, see Figure 2.51 for associated masses) and frequency (1-2, meaning first or second bending mode).

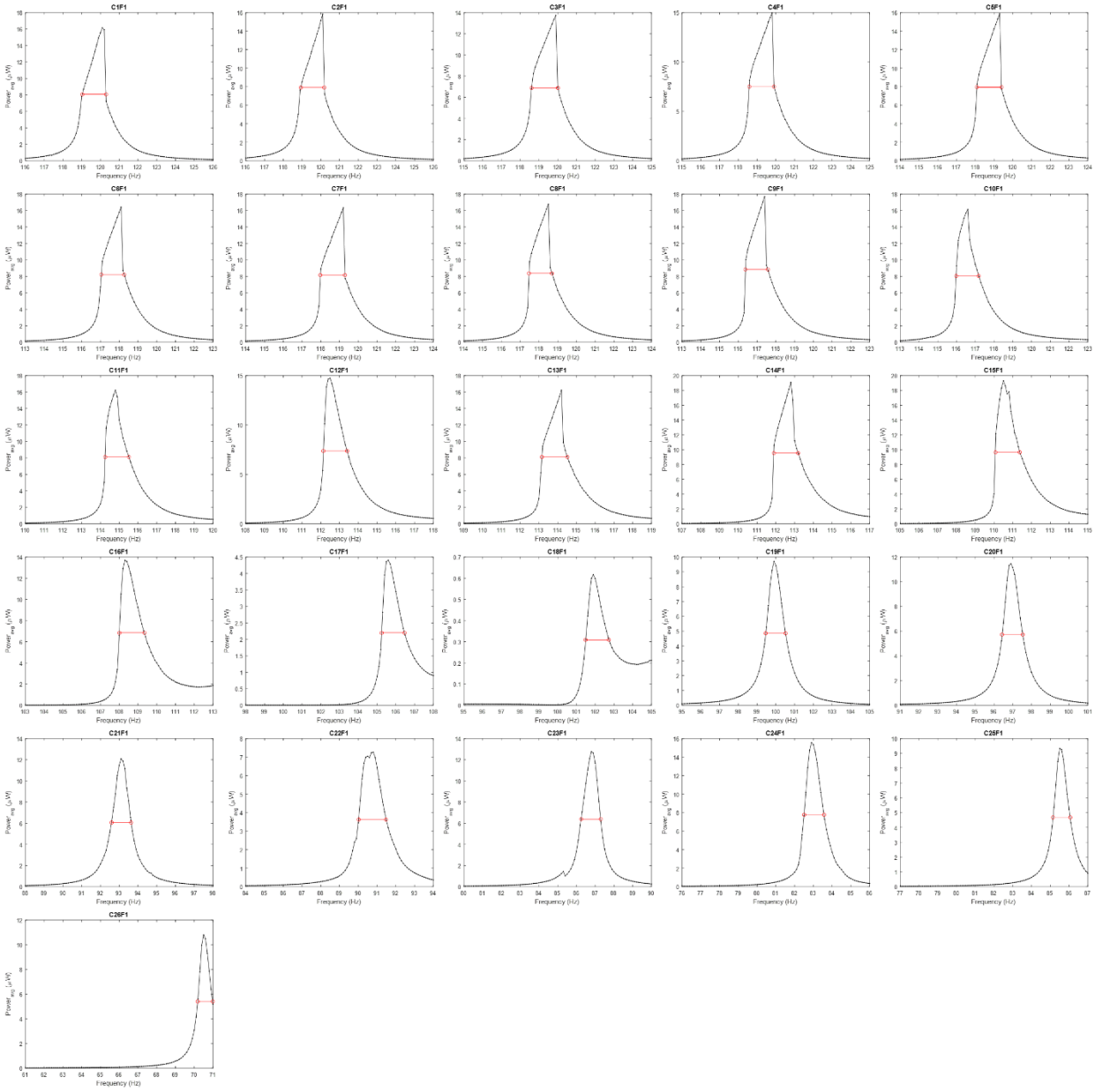

Figure 2.52 – Power plots for the first bending mode.

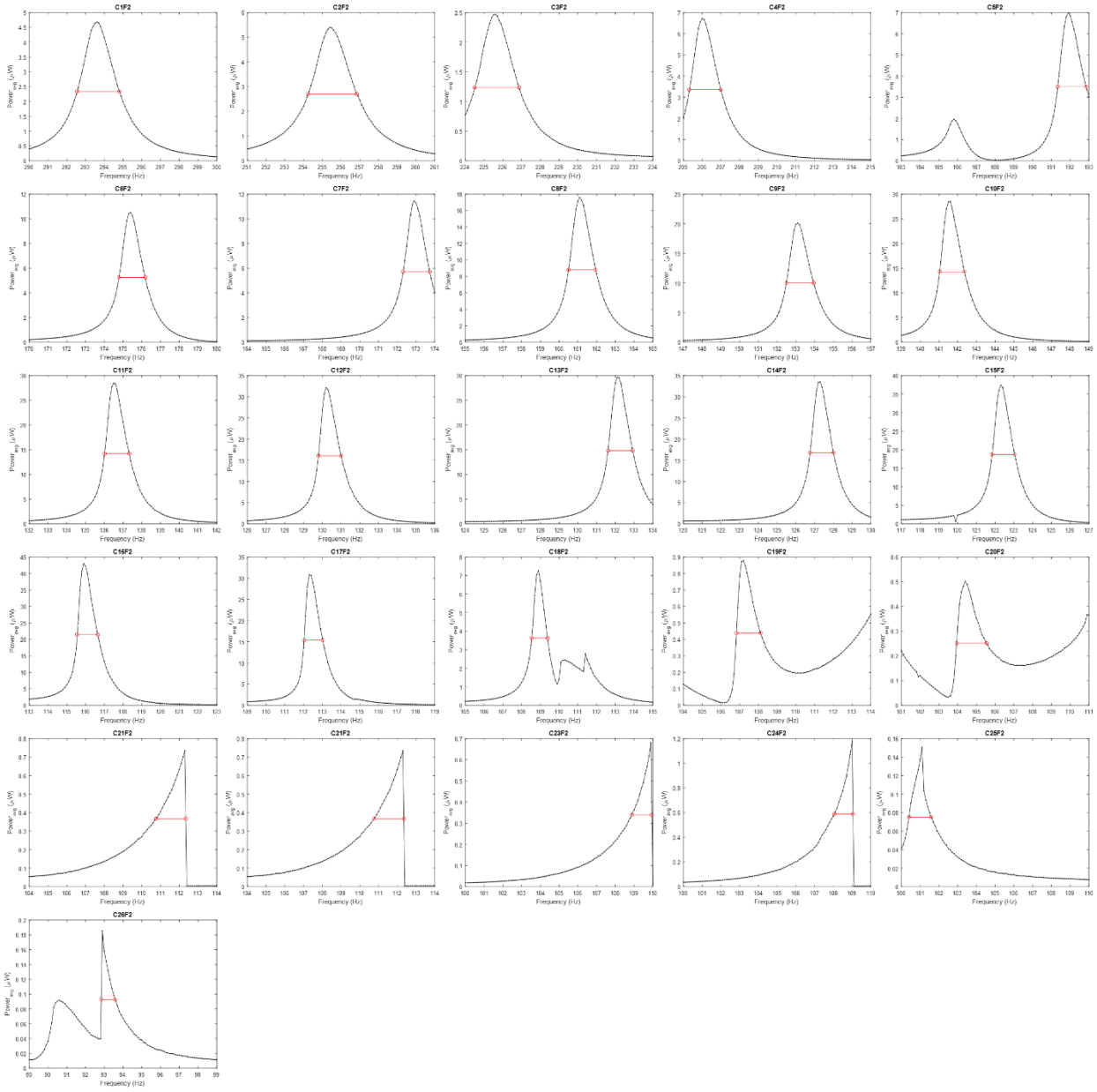

Figure 2.53 – Power plots for the second bending mode.

The half-power bandwidth of the harvester is given in Figure 2.54. This data comes from the curves of Figure 2.52 and Figure 2.53. Bandwidth is largely independent of added mass. Bandwidth does appear to spike around 3000 mg added mass, however from Figure 2.50, it is evident that the power output is very low at this point. The resonant peak is broad and short, then, giving the appearance of increased broadband performance, though performance as a whole is low at this point.

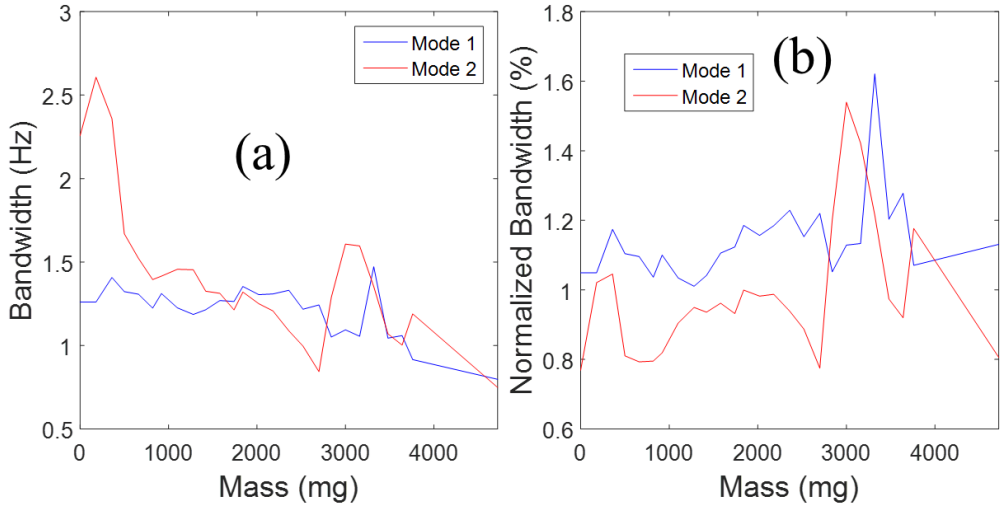

Figure 2.54 – (a) Half power bandwidth as a function of added mass. (b) Bandwidth normalized by center frequency.

2.8.5 Summary

In summary, a combined mode shape (combination of first and second bending modes) of the 'Elephant' two-dimensional vibration harvester was found to occur under specific mass loading structural modification conditions. This mode shape was shown to produce the highest level of power under single frequency sine wave excitation, compared to all other mode shapes and mass configurations, due to the extra kinetic energy in the system and extra stress in the piezoelectric layer provided by the entire beam moving in phase.

2.9 Conclusions

In the pursuit of powering implantable devices, a device must be chosen which performs a critical enough task to warrant additional research effort to increase its functionality and longevity of operation, while at the same time consume low enough power to be able to be power by an accompanying energy harvesting device. In this chapter the argument was made that cardiac pacemakers would be most fitting for the integration of an implanted energy harvester. Hundreds of thousands of pacemakers are implanted worldwide each year, performing the critical task of heartbeat regulation. The size of current pacemakers gives suitable space for an energy harvester

to integrate into the pacemaker's housing, by sacrificing some of the space currently occupied by the battery (slightly more than half of the housing). To this end, the form factors of approximately 26 mm × 26 mm × 6 mm was chosen to be a reasonable size the energy harvester could occupy, still allowing ample for some battery space and not modifying the space available for the sensors and circuitry performing the pacing control.

With the available volume of the harvester established, the implanted harvester transduction strategy was evaluated. There exist many methods of both imparting energy into the body, and also deriving energy from body processes. It was reasoned that it was more attractive to derive energy from inside the body, so the implant patient would ideally never have to intentionally charge their implant. Of the methods for deriving energy from inside the body, using a piezoelectric vibration energy harvester to transduce mechanical vibration from the heartbeat, was determined to be the method of greatest promise and where the greatest contribution could be made.

First, the geometry of the piezoelectric vibration energy harvester was optimized, as the size of the harvester is the main constraint, as it must fit in the pacemaker housing. Typically cantilever beams are used in vibration energy harvesters. These beams, to vibrate at low frequencies, most often have a high aspect ratio, up to 10:1. Since the space available is a square, high aspect ratio is not favorable, as it is a poor use of space and would lower the energy density of the harvester. Therefore, it was first studied the benefits of using a two-dimensional beam vs a one-dimensional cantilever. A Zigzag type meandering 2D piezoelectric vibration energy harvester was fabricated and compared against a 1D vibration energy harvester of the same surface area (footprint). It was found that the 2D vibration harvester was able to achieve up to 6.5 times higher power density than its 1D counterpart.

Power output is only half of the story. The other half is the vibration harvesters bandwidth, or the frequency range over which the harvester still produces appreciable power. For this reason, a novel technique for increasing harvester bandwidth was developed, coined ‘Preloaded Freeplay’. This technique utilized a clamped fixture attached to a vibration source with mismatch treads. The system behaved as a single-degree-of-freedom system, until the ‘spring frequency’ was reached, whereby the preload on the screw was overcome and due to the mismatched screw threads had a freeplay condition, inducing a second degree-of-freedom near the harvesters natural frequency, producing a large bandwidth through their interaction in the frequency domain. While this

technique does not harvest any more energy, energy is harvested over a larger range of frequencies, which is favorable for vibration sources which change their operation frequency over time. This makes for an excellent match for harvesting the vibration of heartbeats, as the heart changes its beat frequency in response physical activity and other stimuli. Both 1D and 2D energy harvester designs were tested with the preloaded freeplay effect where it was found the 2D Zigzag should a 7.1 times increase in bandwidth, compared to 3.9 times increase for the 1D cantilever. This further showed the advantages of a 2D vibration harvester.

With the merits of a two-dimensional design, both in terms of power density and ability have larger bandwidth, a design study was conducted to find the optimal 2D vibration harvester beam shape. Of the many proposed designs, it was found that the ones which eliminated torsion moments, producing a pure bending motion, and concentrating stress in the piezoelectric layer. It was shown that the beam shape termed 'Elephant' showed the greatest power output, over 27 times more than the previous state-of-the-art Zigzag design.

From the previous study, it was obvious that the mode shapes of 2D vibration harvesters can play a large role in harvester performance. Examining further the Elephant vibration energy harvester, it was found the first and second bending modes shared a unique relationship in that they were opposite of each other, not sharing areas of common deflections. It was found that by adding mass to strategic locations of the beam, the first and second bending modes could combine into a hybrid mode shape whereby the entire beam vibrated in phase at the same amplitude. This caused more mass to be in motion, and thus provide more kinetic energy to be transduced by the piezoelectric layer experiencing more stress from this extra mass in motion.

While the extra mass in motion does produce more power in comparison to all the considered configurations in that study, the fact that there is more mass to be moved by the constant level of base excitation, implies that the amplitude of the displacement of this mode shape is reduced. This is why approximately 43 μW (at 0.981 m/s2, 115.9 Hz, 2360 mg, 437 kΩ) is produced in this study, but approximately 81 μW (at 0.981m/s2, 68.125 Hz, 1880 mg, 1 MΩ) was produced in the prior work, where harvesting was done using only the first bending mode. It is also considered that since the same harvester was used in Section 2.8 as Section 2.7, that some fatigue effects may have also contributed to the lower power output. Also, due to the large number of configurations to be measured, performing a resistance sweep for each configuration, to find the optimal electrical load resistance value was not feasible. Therefore, since the load resistance

was the theoretical approximate value, and perhaps not the true optimal value, this could also contribute to the observed lower power.

It is expected that this study will provide the vibration energy harvesting community direction towards exploiting mode shapes in the future design of two-dimensional beam shapes to better tailor harvester performance and increase both power production and bandwidth.

3 POWERING WEARABLE ASSISTIVE DEVICES: SOLDIER CARRIED DEVICES

3.1 Introduction

With the pervasive trend of computers becoming more powerful and smaller, portable electronic devices provide a level of functional enhancement, productivity, and convenience never before achievable. New guidance and communication equipment has made the modern soldier much more effective, though these systems consume power, which is supplied in the form of batteries. Should the soldier be away from base for an extended amount of time, sets of spare batteries must be carried to keep the portable electronic systems operational as the primary batteries are depleted. This battery weight can be around 7 kg (~16 pounds) of the 45 kg (~99 pounds) which soldiers carry on a 72 hours mission. [114-116] Having some 10% of their load consisting of batteries is significant. What's more, this is an abrupt change in the pack weight (carried load) of the modern soldier compared to historical carried load.

Figure 3.1 shows the carried load of soldiers across the past 2,700 years, with data derived from the work of Orr.[116] What can be seen is that historically, even in times before guns, through the American Revolution, American Civil War, WWI, WWII, and into the 1970's, soldiers carried a mean of 30 kg. From the 1980's onward, with the introduction of portable electronics and communications equipment, the soldier carries on average of 47 kg. A significant fraction of this abrupt change is due to battery weight associated with portable electronics. This weight does appear to have been somewhat constant over past few decades. In the 80's, the portable electronic systems were large, and few were carried. As the systems became smaller and lighter, they also became more powerful and useful, leading to the number of systems needed to be carried also increasing. Thus, the weight savings of making the systems smaller was offset by the growing number of electronic systems carried, and the reliance upon them.

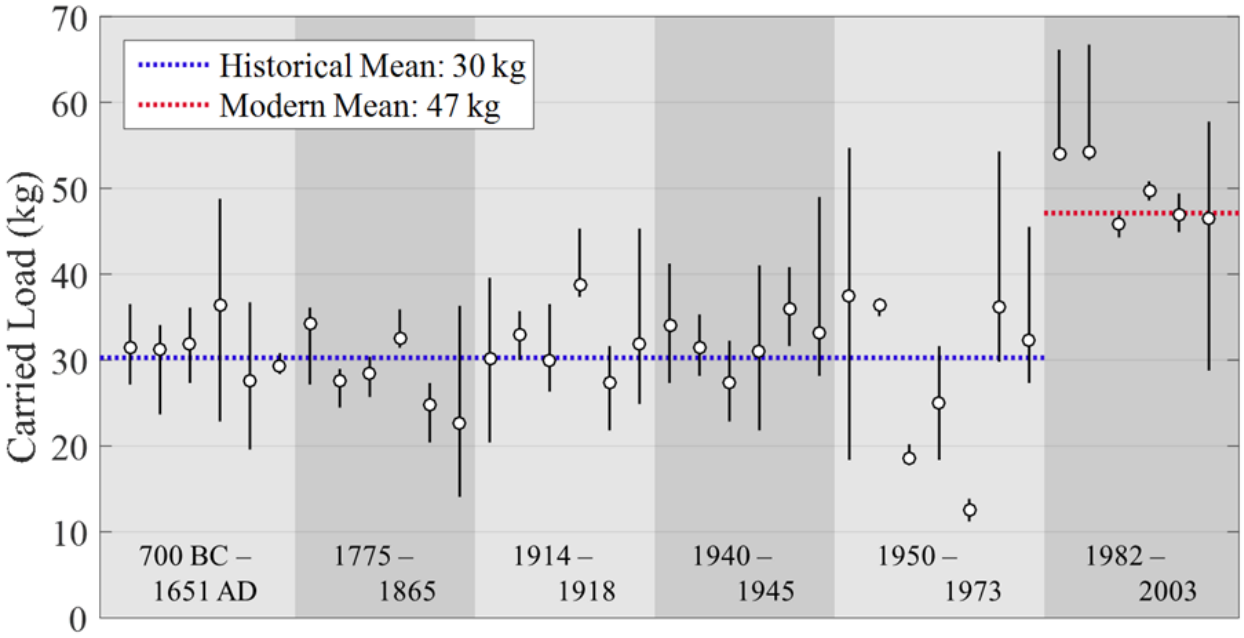

Figure 3.1 – Load carried by soldiers across time, with highlighted disparity between historical and modern mean carried load. Data derived from Ref. [116].

Inspired by the desire to reduce the burden of extraneous amounts of spare batteries carried by soldiers, in this chapter, a method of harvesting power from a soldier's motion is investigated. It is proposed that with the soldier generating power as they go, the number of spare batteries, and subsequently their weight burden, will be reduced. Reducing battery weight by recharging a primary battery pack, will allow the soldier to move with less fatigue and lower chance of injury.

With the goal of battery charging, a small load type of energy harvester will not be effective as it would take a prohibitively long time to charge a battery a significant amount. Since the goal is to reduce the burden on soldiers, an overload or optimal load type harvester would also be unacceptable. This leaves a decoupled type harvester as a design choice, which will be the type of harvester used in this chapter, where the strategy would be storing the forces of bodily motion briefly before converting to electricity, so the body is not damped. Here, I will define a significant charge rate of a battery as the rate of USB device slow charging, which is in the range of 0.5 to 3 W. Of course any amount of current delivered to a battery could be argued as "charging the battery", though one would expect at least slow charging to be satisfied with the rate of charging.

Additional constraints come in the form of appearance and noise generation. These are more subjective than the power output requirement, but are equally important. The harvester

cannot protrude from the body, as it may interfere with motion or become snagged on obstacles. The harvester cannot generate extraneous noise as it could compromise the soldier position to enemies. Unlike an implanted device, a wearable harvester can be taken off at a whim, and a wearable harvester not being worn produces no power and gives no functionality. Therefore, the subjective aspects of the harvester (i.e. how it looks, feels, sounds, etc.) are just as important as the power output.

With these considerations in mind, in this chapter I will begin by reviewing current wearable technology before selecting a harvester strategy, location, and type. Following this, a biomechanics analysis is conducted to give a baseline set of data to design from and compare to the final effects of the energy harvester mechanism. Finally the harvester mechanism is described in detail focusing on the holistic design philosophy and then the details of each section of the mechanism.

3.2 Review of Wearable Technologies

In the past two decades, the miniaturization of highly functional electronic devices has yielded the present condition where such devices are light enough, have a long enough battery life, are robust enough, and even stylish and trendy enough to be worn for extended periods of time. Such systems can monitor activity and various bodily vital signs, and/or provide assistive actions. In this section, assistive wearable devices will be surveyed with greater focus given to exoskeleton type designs. Health monitors are also briefly surveyed as they are currently the most popular and well known type of wearable technology.

3.2.1 Health Monitors

There are a myriad of reasons why wearable health monitors have gained popularity in recent times. They can provide security and peace of mind for the elderly in the case of panic buttons and fall sensors. They can provide additional information for doctors with long term measurement to monitor blood oxygen levels with pulse oximetry sensors and heart rate with blood pressure sensors, and can help diagnose the onset of diseases like sleep apnea, which previously required laboratory sleep studies.[117-119]

Besides the quality of life and medical benefits of wearable health monitors prescribed by physicians, wearable health monitors have also gained popularity in personal recreation and entertainment.[120] Indeed these types of wearables have risen up alongside smart phones, giving users the ability to process and view their fitness data, in some cases in real time. Intercommunication between such wireless devices can form a symbiotic relationship, especially as the sales of devices increases.

With the continued shrinking of electronic components, these wearable monitors have begun being incorporated into other technologies. The recent introduction of smart watches with health monitoring features has blurred the lines between dedicated wearable health monitors and multifunctional portable electronic devices. Even smart phones have begun giving the user the ability to collect simple biometric data, such as steps walked, by analyzing accelerometer data in the phone. This user feedback, or digital health interventions, has been shown to aid in cardiac health and even weight loss.[121]

Even with the reduction in component size of health monitors some still regard them as too intrusive. For this reason, there is continued interest in wearable electrochemical sensors.[122] These sensors, working off of chemical reactions in saliva, tears, and sweat, are fabricated on anything from cotton and PET plastic film to temporary tattoos and dentures. In these sensors, basic data readings are transmitted over thin film antenna. The non-intrusive nature of these sensors makes them ideal for long term monitoring, where comfort is paramount. These sensors are also beneficial for measuring specific chemicals in or on the body, like cortisol and calcium levels, but also in pathogen detection.

3.2.2 Exoskeletons

It has the pursuit of man throughout the generations to constantly improve the capabilities and quality of living of humanity. To accomplish such advancements, we have turned to tools and machines to give us capabilities we cannot readily perform on our own. However, tools and machines are often specialized for one specific task, and lack the deft, robustness, and beauty of the human body. It is then a natural motivation to attempt to combine the power of a machine with the acumen of a human. The resulting field of study is known as assistive human exoskeletons, and concerns itself with the development of robotic suits that may be worn by a human to enhance the capabilities already exhibited by the body. Such technology is aimed at either augmenting

strength, reducing fatigue, or rehabilitating lost function. Born in the most recent century, this field is currently at a precipice, whereby maturing technology is beginning to make its way out of laboratories and into an applied role in society. Such an exciting time warrants a review of the state-of-the-art and a look at the history at how we arrived at where we are today.

3.2.2.1 Timeline

While it is debated exactly when design of exoskeleton type devices began, dedicated scientific research and public interest in this field is largely attributed to the release of the science fiction novel *Starship Troopers* by Robert Heinlein in 1959. This novel featured futuristic soldiers equipped with powered suits of armor, enhancing their capabilities and allowing them to combat a threatening interstellar arachnoid species. A few years later in 1963, the character Ironman appeared in Marvel Comics, who was able to achieve strength rivaling that of super heroes by donning a powered exosuit. During this period, General Electric was working on the first practical powered exosuit. They debuted their work in 1965, calling it Hardiman. At this time it was apparent that the actuator technology, computer control, and energy storage technology was not at the point where a truly practical, untethered, exoskeleton could be produced, leading to a stagnation of any work of significance in the area of assistive exoskeletons.

The next noteworthy stride in exoskeleton technology came in the form of the Spring Walker Body Amplifier in 1991, which was a spring powered leveraging suit allowing wearers to adopt a bounding stride, combining bipedal running with a kangaroo like leg mechanic. Being that there was still a lack of cohesive effort in the research or industrial communities, progress remained slow. Interest by the public in exosuit technology, however, began to increase again in the mid to late 90's with the introduction of television shows like *Mighty Morphing Power Rangers* and *Mobile Suit Gundam Wing* premiering in the United States. While interest was increasing, it was mostly amongst children viewing these shows.

At the dawn of the new century, the perfection of Computer-Generated Imagery (CGI) allowed for live action movie actors to be shown possessing the super-human capabilities given to them from even more advanced exoskeleton suits. Movies such as *Iron Man* (2008), *G.I. Joe: The Rise of Cobra* (2009), *Avatar* (2009), *Elysium* (2013), and *Edge of Tomorrow* (2014) raised the interest in human exoskeletons. Somewhat fittingly, the same technological advances making CGI in movies possible also pushed the development of practical exosuits forward during this same

timeframe. The realization of small integrated sensors, compact but powerful computers, optimization of several actuator technologies, and increased power density of energy storage batteries, has fostered unprecedented progress in assistive human exoskeletons in the past decade.[123, 124]

3.2.2.2 Nomenclature

In this review, the terms ‘exoskeleton’ and ‘exosuit’ are used interchangeably. In literature, some authors prefer to coin designs with minimal rigid parts as ‘exosuits’, presumably to avoid any thoughts of a rigid, armor-like structure that may be thought of when reading ‘exoskeleton’. However, for all intents and purposes, they are synonymous. Furthermore, those piloting the exoskeleton suit will be termed as the ‘wearer’ or the ‘user’.

Exoskeletons differ from prosthetics in that they are meant to fit around the body, rather than attached to it. While prosthetics and exoskeletons can both be used to restore lost function to the body, exosuits are not meant to replace a lost limb, like a prosthetic. So while the two may share similar technologies and applications, in this review I will draw this subtle distinction between them, focusing only on types of assistive human exoskeleton. When most people think of human exoskeletons, images of large, powered, strength amplifying suits come to mind. However, such flavors of human exosuits are but a small fraction of research in this area. Indeed, there are three main types of exoskeletons: active, quasi-passive, and passive.

Active exoskeletons are defined by controlling all movements of the wearer. This means that the user cannot make any movements that are not caused by or without the assistance of the suit’s actuators. This implies that all of the user’s motion is amplified by the suit. This type of exoskeleton tends to be the largest and most powerful. However, it is the most power consuming design, leading to the reality that most active design are either tethered to a power source (mains, generator, hydraulic pump, etc.), or have a very short battery life.

Quasi-passive designs still make use of actuators, but allow the wearer to make some movement unassisted. In this way, certain movements are amplified, while others are either powered by the user, or the user’s force is simply matched by the exosuit. Therefore, quasi-passive designs tend to be slimmer and more human-like than active designs, and are more readily battery powered for mobile use.

Passive exosuits are characterized by a lack of powered actuators. With these designs, the user provides all effort for motion. The goal of passive designs is thus to improve the efficiency of movement, rather than augmenting user power. Efficiency is improved by not allowing the wearer to deviate from designed motion paths, and by collecting energy during certain movement when negative muscle work is done (rather than that work being done by the body) and releasing the stored energy back to the user when positive muscle work is done. Alternatively, the stored energy could be converted into electricity. Such a method is called an energy harvesting device.

Each main type of exosuit can be further classified as either quasi-anthropomorphic or anthropomorphic. Anthropomorphic means that the design mimics the human body in that joint types and locations match that of the body. This type of suit is most common in passive and quasi-passive architectures as the user's body is responsible for some or all of the motion, and the suit must not impede the body. Quasi-anthropomorphic architectures take the liberty of shifting joint locations, but typically maintain the same types of joints as the body. This is more common in active exoskeletons where it is difficult to capture all degrees of freedom of the body with actuators, so additional or different joints must be added. Non-anthropomorphic designs are not typically seen in the realm of human exoskeletons, since the exoskeleton is worn by a person and must at least in some way follow the form of the human body. While it is possible to interact with the body in a non-anthropomorphic way, it is often an intangible goal in exosuit design to maintain as human-like appearance as possible.

Additional distinction can be made for what parts of the body the exosuit interacts with. This classification is typically hand,[125] lower-body,[126] upper-body,[127] or total-body exoskeletons.

3.2.2.3 Actuation

For active and quasi-passive designs, a method of actuation is needed to augment or assists the user's motion. Actuation takes place around joints of the exosuit, through one of several conventional actuators or more recently artificial muscles.

There are many types of joints in the human body, but the ones mimicked by exoskeletons are almost exclusively synovial joints. The goal in engineering joints for exoskeletons is seldom to mimic the structure of the joint itself, but rather achieve its function. For example, bearings are used to reduce friction rather than cartilage atop a fluid membrane. The typical types of joints used

in exoskeleton design are ball and socket, and hinge joints. Taking inspiration from the natural arrangement of joints, exoskeleton joint design is often a decomposition of anatomy.

Analogous to the body, where actuation takes place around joints, exoskeleton actuators mimic the placement of muscles. The most common forms of actuation are termed 'conventional' actuators. These actuators are hydraulic cylinders, linear actuators, and various electronic motors (dc, servo, stepper, etc.).

Hydraulic cylinders exploit incompressibility of high pressure fluids to provide high forces over a small area. These forces cause the arm of the piston to push in and out of the cylinder. Linear actuators use a servo type motor attached to a ball screw through gearing. The ball screw mechanism acts like a nut and bolt, only instead of the threads interacting directly, force is transmitted across ball bearings. This allows for much smoother motion and control. Finally, various types of electronic motor can be used to achieve other types of actuation, or turn joints directly. An example of an alternative actuation is using a Bowden cable pulled as it is wound by an electric motor to move finger joints.

In recent times, mimicking of muscles more directly in operation has been investigated. Two leading designs will be presented here. Both designs employ the same basic actuation strategy illustrated in Figure 3.2, whereby a cylindrical volume undergoes a diametrical dilation, which in turn necessitates a lengthwise contraction of the cylinder in order to maintain a constant volume. This contraction in the length direction is what is used for actuation.

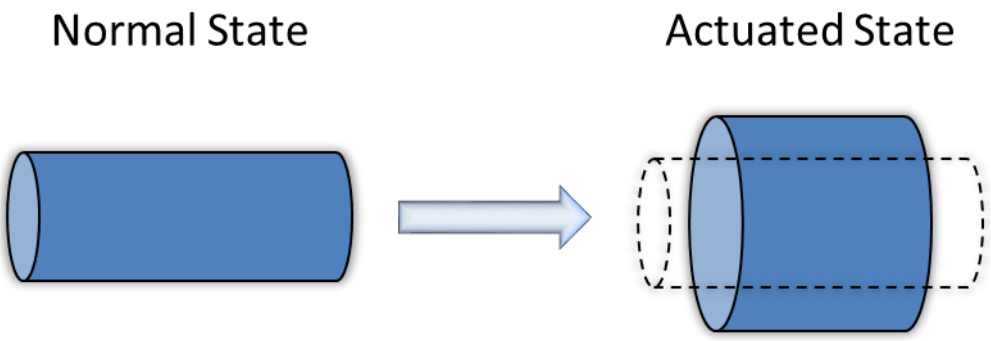

Figure 3.2 – Illustration of actuation principal of artificial muscle.

The first design, proposed by Bryant et al., employs a series of hydraulically or pneumatically pressurized cylindrical tubes.[128] Increasing pressure in the tubes causes them to

expand radially, and subsequently contract in length. The second design, proposed by Lima et al., uses carbon nanotube yarn.[129] The voids in the carbon nanotubes are filled with paraffin wax. Through either chemical, electrical (Joule heating), or photonic means, the wax is melted. The wax expands in liquid form creating pressure inside the carbon nanotubes. This pressurization creates the same effect of radial expansion and subsequent lengthwise contraction.

The advantage of using artificial muscle is that a more realistic motion is produced and designs may appear more human-like in appearance. The downside is that it is very difficult to achieve fine motor control of an exoskeleton with these methods. With the hydraulic/pneumatic artificial muscle, there are nonlinear hysteresis behaviors of the muscle trajectory depending on whether it is expanding or contracting, making control difficult, even if fine adjustments in cylinder pressure can be made. The carbon nanotube yarn is also difficult to control, in that the paraffin wax either melts, or it doesn't; meaning that there is either full actuation or no actuation. For these reasons, exoskeletons employing artificial muscles for actuation are nearly absent from the literature.

3.2.2.4 Active Exoskeletons

While the active exoskeleton was first reduced to practice by GE's Hardiman,[130] the current state-of-the-art in active exoskeletons is in the demonstration phase, with many players competing for the prize of implementation in a military capacity. The most high performance model of active exoskeleton belongs to Raytheon in the form of their XOS 2.[131] This exosuit is a quasi-anthropomorphic design allowing the wearer to carry 200 pounds of weight with relative ease, due to a 17:1 actual weight to perceived weight ratio capability. This total-body exoskeleton, while impressive, is currently tethered, meaning it can only perform great feats within cords-length of a power source. A similar suit is currently being used by Daewoo Shipbuilding and Marine Engineering, for workers to carry heavy ships parts, which used to require cranes or lifts to move.[132] Another quasi-anthropomorphic design, CADEN, was produced in the form of an upper-body powered exoskeleton.[133] While these designs are great advancements, the necessity of a tethered power source limits their use to specialized circumstances.

A total-body but untethered and anthropomorphic exosuit was produced in the Hybrid Assistive Limb (HAL).[134] Currently HAL 5 is the least intrusive and most visually appealing active exosuit. Molded plastic housings hide all actuator components. While not as outright

powerful as XOS 2, HAL 5 has a better power to weight ratio, and is much more practical since it is battery powered, with the battery lasting approximately 2.5 hours.

While industry is leading the way in terms of active powered exoskeletons, work in academia has been done by University of California Berkley, with their Berkeley Lower Extremity Exoskeleton (BLEEX).[135-138] This lower-body anthropomorphic design is also untethered and battery powered. BLEEX was meant primarily for carrying loads mounted on a back frame, supported by the legs of the exoskeleton. In this way, large loads can be carried by the suit wearer while the upper-body is kept free to perform dexterous tasks. While BLEEX does not stand out in any areas compared to the other referenced designs, the open distribution of knowledge regarding the studies on this exoskeleton were of great influence and aid to the design and fabrication of all following active exoskeleton generations.

3.2.2.5 Quasi-passive Exoskeletons

As the name suggests, quasi-passive exoskeletons bridge the gap between power augmenting active exoskeletons and efficiency increasing passive exoskeletons. All quasi-passive design still employ forced actuation of some kind with either the goal to augment power in certain motions to increase load carrying capability, or to assist the wearer's gait motion. The quasi-passive architecture is of best use in the lower-body, where most of the work is done, and the positive-negative work cycle of the lower limbs may be manipulated to aid the wearer. This type of exoskeleton can be divided into two main categories, load carrying and assistive gait. With load carrying augmentation left mostly to active designs the majority of quasi-passive designs seek to assist the wearer's gait motion. Assistance can either refer to using this technology to aid or restore lost mobility in a rehabilitative aspect, or to reduce the energy expenditure (metabolic rate) of the wearer during gait. Therefore, assistive gait is considered both to be used for rehabilitation and reduction of energy expenditure in walking and running.

The category of quasi-passive exoskeletons for load carrying augmentation is by far dominated by the work of the University of California Berkley.[139, 140] This anthropomorphic design uses hydraulic pistons on each leg to support the motion of the extension of the leg, allowing additional loads to be carried. The design is battery powered and lightweight. The conclusion of their work on a lower body exoskeleton resulted in the licensing of their technology to Lockheed Martin, producing the Human Universal Load Carrier (HULC).[141] In previous generations, the

HULC was also known as ExoHiker and ExoClimber. Of any exosuit discussed in this review, the HULC is the most suited and most ready for deployment to the military and public at this moment.

The same technology which went into the HULC has also been repurposed by a spin-off company from UC Berkley called Ekso Bionics. They use the Ekso (formerly known as eLegs) lower-body exoskeleton to help paraplegic patents regain strength and circulation in their legs and eventually develop feeling again.[142] The Ekso legs work by performing a preprogrammed stepping motion when the wearer either presses a button on the crutches (completely paralyzed) or attempts to initiate a step themselves (partially paralyzed).

Another quasi-passive exosuit meant for rehabilitation was investigated by Carnegie Mellon University where they actually used artificial muscles (pneumatic type) in an attempt to mimic the muscles of the lower leg.[143] Since the goal of the work was aimed toward rehabilitation, the lack of fine control of the exoskeleton was acceptable. The place where quasi-passive exoskeletons are advantageous is in reducing the energy expenditure of gait. Here, positive work is offloaded from the muscles of the leg to the actuators of the device, thus reducing the energy (of the wearer) necessary to perform gait.

Walking is distinctly different from running in that during a walking gait there are periods where both feet are on the ground at the same time. The quasi-passive assistance of walking is an area of research dominated by Harvard University. They first attempted to create an exosuit with an array of biologically mimicking pneumatic artificial muscles placed throughout the lower-body.[144] It was thought that the compliance of the pneumatic artificial muscles (PAMs) would not impede user motion. However, due to a sub-optimized design, the PAMs actually caused metabolic rate to increase when walking and wearing this exosuit.

In a more developed work, the same researchers use a Bowden cable (routed from the heel, around the leg, to the lower back in a biomimetic way) attached to an electric motor mounted at the lower back to assist in pulling the leg up when walking.[145-147] This so-called ‘soft exosuit’ used an ergonomic bracing structure to guide the Bowden cable around the leg where its tension would work in harmony with the muscles. From this work, it was proven that up to a 6.4% decrease in metabolic rate could be observed by wearing this soft exosuit.

In contrast to walking, the defining characteristic of running is that at some point in the gait cycle both feet are off the ground. This means that the muscles are pushing much harder than the body weight, essentially causing a jump from stride to stride. The length of the stride and

ensuing running speed is governed by how much force can be placed onto the ground. Supplying additional forces to enhance running was first shown by Applied Motion's Spring Walker Body Amplifier.[148] This device enabled even average people to run at 20 mph. In another work by MIT and Harvard, a knee brace with linear actuator was developed aimed at reducing the effort required by the quadriceps during running, thus reducing metabolic costs while running.[149]

3.2.2.6 Passive Exoskeletons

Since they do not contain actuators, passive exoskeletons cannot augment the performance of the body, nor insert energy into the gait cycle. Thus, passive exoskeletons can only store and reallocate energy at various phases of the gait motion. The most common approach is to attempt to collect energy during the negative work phase of gait. The collection of this energy, rather than muscles being to do negative work, reduces metabolic costs and fatigue. The stored energy from negative work can then be given back to the body during the positive work (push off) phase of gait to further reduce metabolic costs, or converted into electricity in an energy harvesting application to reduce metabolic costs by eliminating the weight of spare batteries no longer needed to be carried (ex. soldier on long patrol mission).

The energy saving mechanisms of gait are varied, complicated, and often coupled.[150] The key strategy is to avoid the muscles doing negative power functions and minimize the magnitude of the positive power required to perform the same motion.

The efficiency of motion in regards to rehabilitation can be increased with assistive passive exoskeletons. The Wilmington Robotic Exoskeleton (WREX) is a simple passive upper-body exoskeleton meant to assist in the performance of simple tasks, like eating, for patients who've experienced degradation of motor control due to stroke, spinal cord injury, and cerebral palsy.[151] The WREX exoskeleton provides a path for the arm to travel to make positioning of food to eat easier, as the wearer only needs to provide a forcing input, since the control and directing of that input is taken over by the exoskeleton. In this way, some level of independence is gained and self-confidence built in these patents, who were primarily children.

The reduction in total metabolic work performed by the muscles, both positive and negative, translates to a reduction in fatigue of the wearer. Extensive investigations have been conducted on this reduction when walking, however, a concept has been proposed that could also reduce fatigue when the wearer is stationary. The user does not have to be moving for a passive

exoskeleton to provide fatigue reduction. The Swiss company Noonee has developed the Chairless Chair, a passive lower-body exoskeleton that does not inhibit the straightening of the leg, such as when walking, but when the user squats, the exoskeleton reaches user prepositioned stops transferring a significant portion of the user's weight to the exoskeleton.[152] Creating a spontaneous chair, the Noonee device enables the wearer to sit in a near standing position, or preferred working position, so that they only need balance, rather than support their body weight in an awkward position. This advantage is claimed to reduce fatigue and increase productivity.

In walking, first method of passive fatigue reduction is the gravity balance method. This method seeks to balance the forces on the joints, caused by the moment induced on them by the body's center of mass, with a system of springs. Agrawal et al. showed that a 25% reduction in the electromyography (EMG) signal of the leg muscles could be seen via this technique.[153] It is interesting in this study that at some points the device requires more torque than without the device.

The use of exotendons to provide parallel pathways for work to be done alongside the muscle has been proposed, modeled,[154] and preliminarily implemented.[155] The theory of energy savings and metabolic rate reduction were there, however, no appreciable effect on metabolic rate was observed.

Finally, a study by Carnegie Mellon University proved that with their passive exoskeleton, an average of 7.2% decrease in metabolic rate was observed when tuning the stiffness of the device's spring just right.[156] This was a major discovery in the field. The reductions in metabolic rate were better than even those of powered devices. This device uses a mechanism similar to that of a seatbelt tensioner in a car. When foot strikes the ground, the ratchet locks and as the ankle rotates forward, the spring is tensioned. When push off is occurring, that stored energy in the spring is given back to the calf muscles. When in swing phase, the ratchet is open and the device does not interfere with motion.

3.2.3 Energy Harvesters

It is also proposed that rather than storing energy collected during negative work phase in the form of potential energy in a spring, it could be converted to electricity and stored in a battery. This energy would not available then to give back to the body during positive work, but the theory is that if the user could reduce the number of batteries they need to carry, that weight would make up for not giving the energy toward positive work, in terms of metabolic cost savings.

While many ideas for harvesting energy from people have been made, mostly revolving around the forces associated with heel-strike, and are thus not exoskeletons, there are a few examples of energy harvesting exoskeletons. The University of Michigan created a knee brace energy harvester, which only harvested energy during negative gait, and disconnected the generator during swing phase.[157] However, even though the generator is not electrically connected during swing phase, it is still spun by knee movements, robbing knee positive work. Therefore, a net benefit for wearing the device is not so easily seen. Though, this work has inspired a spin-off company called Bionic-Power to attempt to sell this idea, particularly to the military.

The company SpringActive in Arizona has produced an energy harvesting boot exoskeleton they call SPaRK (Soldier Power Regeneration Kit).[158] It is claimed that SPaRK boot can produce 3-6 W of power. These power claims were somewhat corroborated by researchers at U.S. Military Academy, West Point, who found that the SPaRK produced 2.5-3.5 W when walking at 3 mph.[159] Though, this came at the cost of increased metabolic rate. They also found marginal changes in kinematics.[160]

3.3 Selection of Energy Harvesting Strategy: Joint Rotation

It is because of the strong tie between us and our devices, that it is attractive to research ways of powering our mobile devices with our mobility itself. After all, if we are stationary, it is usually in a place where mains power is available for charging. It is only when we are on-the-go that charge depletion becomes a concern. Next, the various strategies of harvesting energy from human locomotion are examined. These techniques are represented in Figure 3.3, and consist of heel-strike, joint rotation, and center of mass motion.

Figure 3.3 – Three forms of mechanical energy harvesting from human gait. (Left) Heel strike, (Center) Joint rotation, (Right) Motion of center of mass.

Regardless of the method, when harvesting energy from human motion, the effect of the harvester on the person must be of primary consideration. This is as much a physiological as a psychological concern. A device can easily be made to produce tens of Watts of power from human movement, as the human body is capable of producing such a level of power to perform tasks. However, this would constitute a deliberately powered device (ex. peddle powered or hand crank generators). Thus, if an energy harvester is increasing the metabolic rate of the wearer, it means that it is trying to harvest positive work in the gait cycle. This is an inefficient means of producing power, and it would be better to use a deliberately powered device to produce the desired electric energy. This is why the key engineering concern is devising a mechanism whereby energy is only extracted during negative work phases of gait.

3.3.1 Heel Strike

During heel strike, a large ground reaction force is produced; approximately twice the body weight. However, while the force is large, the subsequent displacement associated with this event is quite small, meaning there is little work done during the heel strike. Though, this work is all negative work done during the double support phase of gait, and can be indiscreetly harvested. Additionally, the heel strike is only a brief moment in the total gait cycle, meaning that the average power from the heel strike is low. Power output can be increased through the use of mechanisms to effectively increase the displacement associated with the heel strike.[161-163] This practice, however, can compromise the stability of the walking motion, requiring the muscles to do additional work in stabilizing the body.

3.3.2 Joint Rotation

Joint rotation strategies seek to use the torque about a given joint to turn a generator. These torques are quite large, as they are directly responsible for the locomotion, and undergo a modest angular deflection, meaning that there is a substantial amount of work done by the joints. Coupled with the fact that each lower limb joints are active for at least half the gait cycle, the average power output can be tens of watts. However, since the work done at the joints is responsible for movement, there is both positive and negative work done. Harvesting energy from the positive work phases would make it more difficult to move and cause an increase in metabolic rate of the individual.[157] Conversely, harvesting energy during the negative work phases would relieve burden from the body, reducing metabolic rate while producing electricity, though this has yet to be demonstrated. Thus, only select portions of the work done by the joints during the gait cycle should be harvested. Still several watts of electrical power output can be obtained from this technique.

3.3.3 Center of Mass Motion

Energy can also be harvested due to the fluctuation in potential energy of the body's center of mass as it rises and lowers, thanks to the inverted pendulum motion of gait. Potential energy itself cannot be harvested. Therefore, for this type of device relative motion between the person's center of gravity and an oscillating suspended backpack load yields the necessary kinetic energy for power harvesting. Since the load in backpacks can be large, especially in the case of soldiers, the work done is significant despite the fact that the center of mass of the body only moves a few centimeters, giving good potential to harvest energy. Furthermore, by suspending the backpack load on springs, a vibration absorber can be created, whereby the dynamic loading of the backpack can be mitigated, as shown in Figure 3.4 when the curves fall below 10^0 around a normalized frequency of unity. However, vibrations can only be truly diminished when there is no damping in the system. Attempting to harvest energy from this system directly would induce damping, and as the green and blue lines in Figure 3.4 show. While the force necessary to carry the backpack is lessened, it is not diminished.

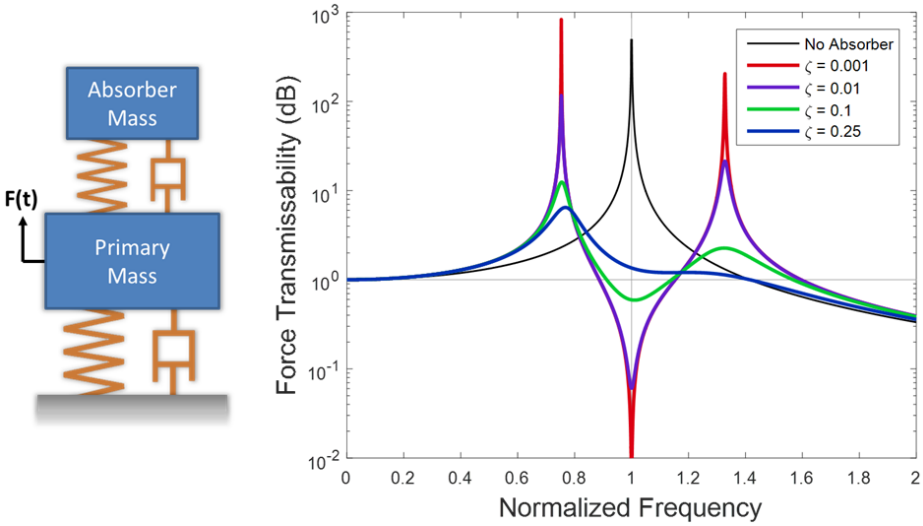

Figure 3.4 – (Right) Theoretical force transmissibility of the tuned mass damper system (left). Here the primary mass represents the person with the spring and damper being the legs and the absorber mass being the loaded backpack, the spring and damper being the backpack suspension.

It is in the issue of damping in a tuned mass damper system that explains the results of Rome et al. They were able to show a 6.2% reduction in metabolic rate when walking with a backpack vibration absorber with only springs (bungee cord) [164], but when harvesting several watts of electrical energy from a very similar system, an increase in metabolic rate was observed [165], meaning that the presence of the harvester made it more difficult to move.

3.4 Selection of Energy Harvester Location: Boots

Unlike harvesting energy from the environment (e.g. solar, wind), where the goal is to harvest as much of the incident energy as possible, whatever energy is harvested in this case comes from the human body and must naturally be produced by the body itself. It is thus paramount to design the functioning of the harvester such that it aids the functions of the body. It has been shown that passive mechanical devices can reduce metabolic rate during walking by performing some the negative work during the gait cycle, taking that load off the muscles of the lower leg [156]. Converting this work into electricity, such that fewer spare batteries need be carried on missions would reduce pack weight for soldiers, which is also shown to reduce metabolic rate [166].

Reducing metabolic rate mean the soldier is using less energy to move, reducing fatigue and probability of injury.

With these considerations in mind, it is apparent that the location of the energy harvester on the body will play the largest role in its function and perception by the wearer. As the upper body of the soldier is frequently occupied with other equipment, and the lower body outputs much more power than the upper body, the legs are examined for the placement of the harvester. The functions of the three major joints of the leg in the ankle, knee and hip are given in [126, 157, 167] in terms of angle of rotation, angular velocity, torque and power at each respective joint.

From examination of the literature, it is apparent that the largest torque and instantaneous power values are produced by the ankle. This is unsurprising as the ankle is the joint furthest away from the center of mass. What this means is that by placing an energy harvester at this location, the perceived effect of the device on the wearer is smaller than at the other joints. A representation of the gait cycle and power output of the ankle is given in Figure 3.5 below. Here it is shown that the power output is nearly zero when the foot is off the ground, as the power required to rotate the foot itself is many times smaller than what is necessary to stabilize and propel the body. Like any cyclic motion, the power goes through positive and negative phases. Though, since the positive work is much larger than the negative work/power, the gait motion can efficiently propel a person forward. There is also the intriguing opportunity here to aid the walking motion, if the incorporated energy harvesting device could harvest energy only from the negative work phase of the gait cycle.

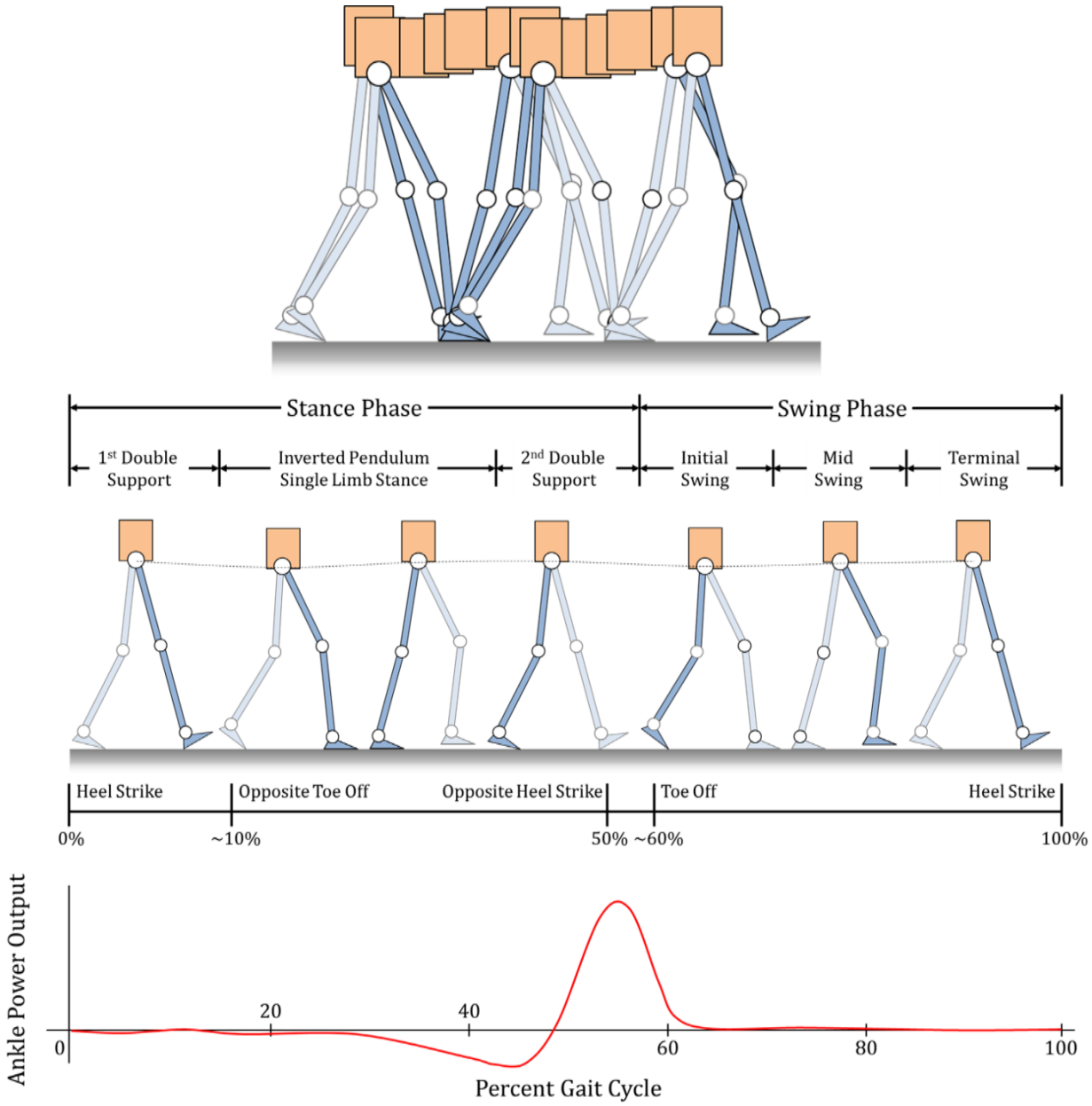

Figure 3.5 – Gait characteristics of Ankle, Knee and Hip. Negative work in the gait cycle is highlighted in a red box on the right graph.

Apart from the engineering advantages of harvesting energy from the ankle, a harvester fully integrated into a boot has additional intangible benefits. Boots are most nearly always worn by soldiers, whether in action or not. It is thus, natural for the soldier to wear boots, and it takes no abnormal effort on their part to DON the device, unlike, for example, strapping on a knee or hip brace. The extensive amount of time the device is worn also translates to greater energy

production across an expanded time frame compared to other energy harvesting devices, which would only be worn when on mission. The psychological normalcy of a boot would aid in its acceptance, as nothing is perceived as being different, unlike a knee or hip brace, which would appear abnormal.

With this impetus, the device which will be designed is named HERMES, standing for Harvesting Energy to Reduce Mass Encumbering Soldiers. Hermes was the Greek messenger god who, thanks to winged sandals, was able to move around swiftly. It is the goal of this work that solders will be able to move for efficiently thanks to the footwear developed in this chapter.

The energy harvesting device will be fully integrated into the boot, so that it maintains a normal appearance and function. This is a principal design consideration. If the energy harvesting devices developed causes the boot vary in appearance, feel, sound, etc. it will not be readily accepted by solders. After all, a wearable energy harvester which is not being worn is producing exactly zero power.

Therefore, to maintain as normal as possible appearance, the harvester mechanism itself will be housed in a cavity in the midsole of the boot. The housing will be made durable such that it can withstand forces exerted on it comparable to if the device were not present. Torque is transmitted to the device by a bracing structure, depicted in Figure 3.6, which runs between the inner and outer layers of the boot upper, so that it will be neither visible nor uncomfortable to the wearer. Electrical output from the boot will be transported via wire channeled through the pant to a central battery on the soldier's waist or flak vest. The connection of the wire in the pant to the boot will be made by a magnetic or some other form of quick connection, so that the joining can be made effortlessly.

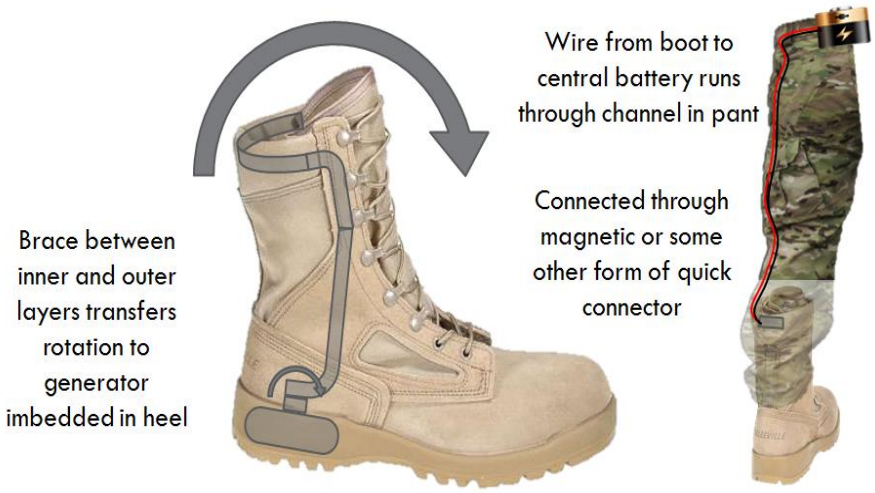

Figure 3.6 - Energy harvesting system layout.

3.5 Selection of Boot and Size

In order to have an accurate understanding of the space available for an energy harvesting device, the volume within a soldier's boot must first be quantified. To quantify available space, a space must first be chosen. It was decided to incorporate the device into an existing combat boot both to maintain a normal appearance, and to give a quality of construction from the point of view of the boot wearer, which could not be replicated without special machinery like that in a footwear company's factory. The boot chosen in which to unite the energy harvester mechanism is the Belleville 390 hot weather combat boot. This boot was chosen after consulting with a US army veteran, and a member of the Corps of Cadets at Virginia Tech, on what brand and model of boot is popular in the armed forces. Therefore, utilizing this boot platform will result in an energy harvesting boot that will appear familiar to those in the service and will be more readily accepted. The hot weather version of the Belleville 390 boot was chosen for its relevance to the current area of operations of the US Military. What's more, this boot model has a larger midsole than most boots, giving the most space for the energy harvesting mechanism to be placed.

Naturally, there is no one set of dimensions for a boot. The dimensions of the boot vary with its size. As a starting point a size 8 boot was chosen based on the thought process that:

- The mean foot size of an enlisted man is around 10.5 inches, corresponding to a 9 ½ shoe size. [168]

- A device designed for a smaller shoe size will fit into a larger shoe size
- 91% of enlisted men wear a size 8 shoe or larger. [168]
- A size 8 shoe will give adequate space restrictions for a preliminary device, and if need be, could be made smaller to fit reduced sized boots in the future.

3.6 Biomechanics Analysis

The rotational degree change of the ankle is of paramount importance to the harvester design, as it greatly influences the way in which the harvesting mechanism must be designed. Therefore, the motion capture tests were conducted to examine the joint rotation relationships of the lower limb joints, while wearing the chosen combat boots. In this section results are presented for a male subject (age: 25 year, height: 5’10”, weight: 150lbs) wearing a size 8 Belleville 390 hot weather combat boot, both wearing a 35 pound backpack and not wearing a pack.

Seven markers were tracked with a Vicon motion tracking system. As shown in Figure 3.7, markers were placed on the boot at the toe, metatarsal joint, heel, ankle joint, and the top of the boot leg, and on the subject’s knee and hip joints. The subject walked down a runway, stepping on a force plate while the points were being tracked. The addition of the force plate to the runway facilitated a reference point for aligning different trials for averaging, as well as, shedding insight onto the transition of forces across the foot from heel-strike to toe-off. A screen shot of the plotted test data across time is show in Figure 3.7.

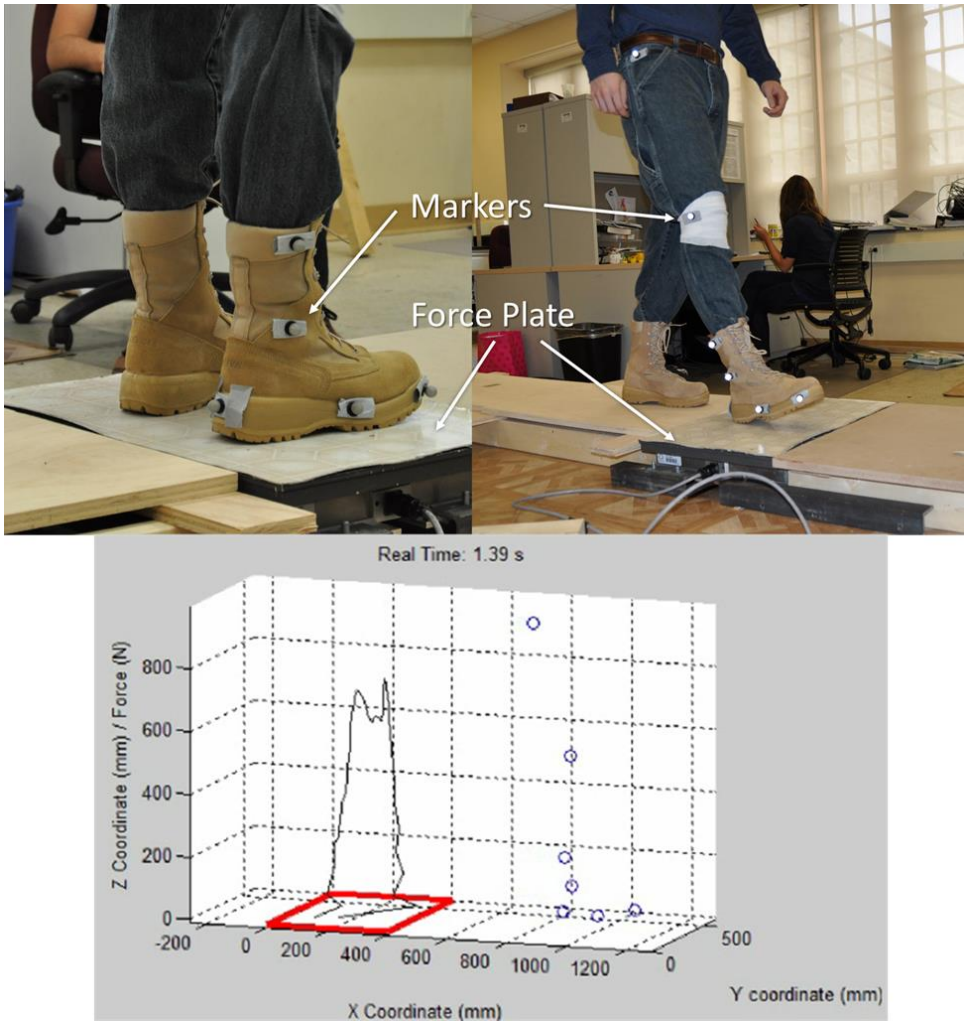

Figure 3.7 – (Top Left) Close up of boot markers and force plate. (Top Right) Picture of trial in progress, whereby subject would walk down a runway, stepping on a force plate. (Bottom) Rendering of experimental data, where the red lines highlight the force plate, the black line represents force magnitude in the Z direction, and the blue dots show the tracked location of the markers in space.

As the angles of the joints are of interest, it must now be found the relationship between the vectors made by the line segments adjoining specific marker points. This was done by examining the ratio of the slopes of adjacent line segments, as shown in Figure 3.8. To simplify the analysis, the subject walked in the direction aligning with the motion capture cameras x-axis, allowing for the y-component of the marker data to remain nominally constant and a two-dimensional angular analysis to be considered. Figure 3.8 also shows plots of the X and Z-coordinates of each marker over time.

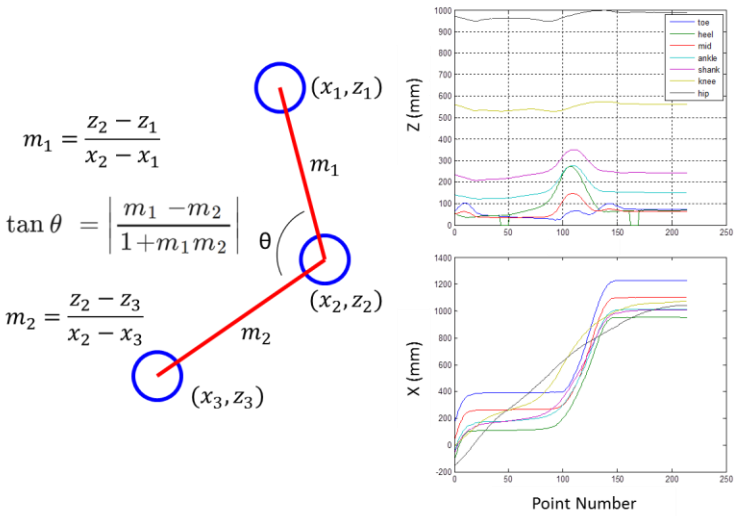

Figure 3.8 – Illustration of (Left) how joint angles were calculated using various motion captured points. (Right) Sample of typical X, and Z axis data points (note Z axis is perpendicular to the floor, with subject walking in X direction).

In this analysis, the normal vector to the line segment created between certain points was used, where the normal vector to a line with slope m is $-1/m$. This was used for defining the ankle angle, where zero degrees is defined as when the shank is perpendicular to the foot, and for the hip, where zero degrees is defined as when the thigh is perpendicular the ground. The results for angular rotation are presented in Figure 3.9 for the toe, ankle, knee and hip joints. These joint angles over the gait cycle match well when compared with another such study from literature for walking in shoes.[169] Here, the cycle starts at heel contact where the heel of the measured foot first touches the ground. Toe-off is the last instance in time when the foot is in contact with the ground. In this study, the start of the gait cycle is defined as heel-strike since time is referenced to the force plate reading, whereas the literature study references the toe-off.

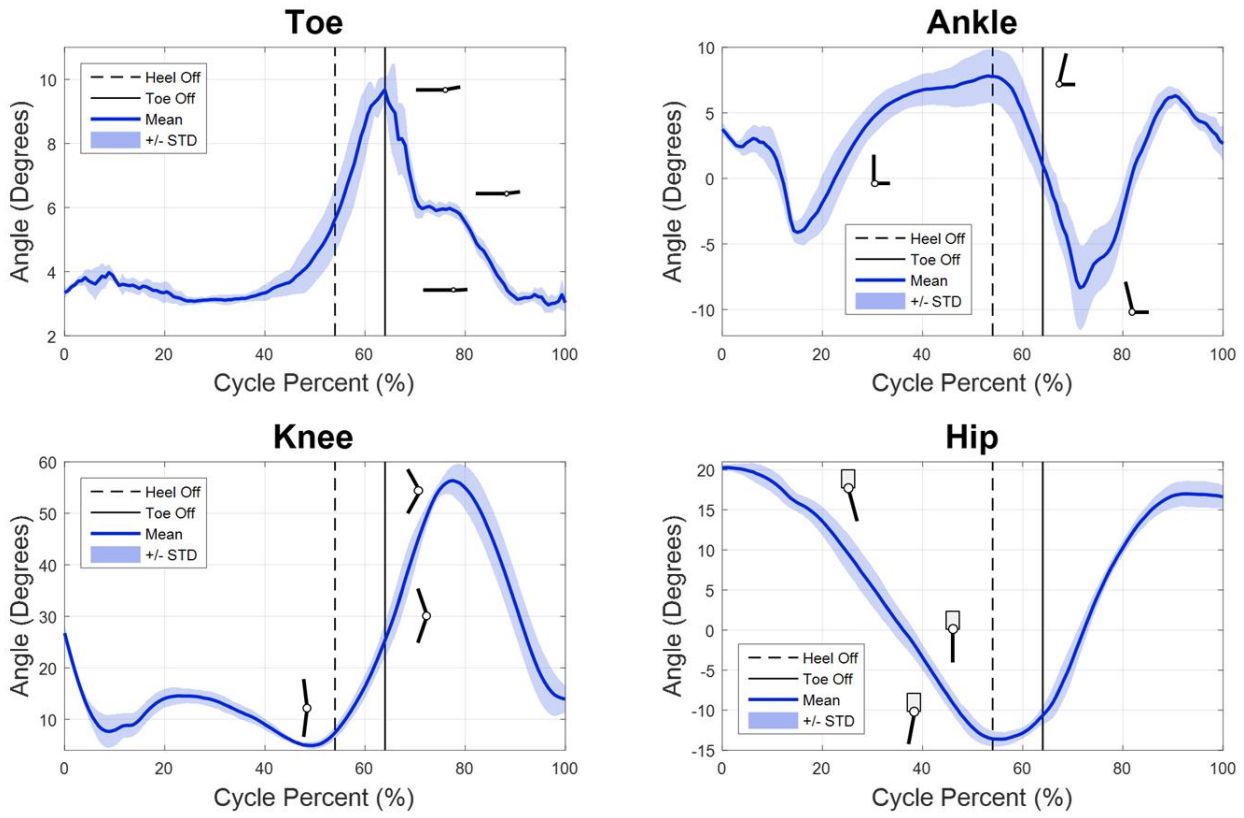

Figure 3.9 – Joint angle data derived from motion capture trials. Solid lines are average and shaded areas are ± one standard deviation computed over five trials.

Figure 3.9, reveals that wearing boots has very little effect on the motion of the hip and knee joints, however, the ankle is affected, although only when the foot is in the air, when compared to walking in normal shoes.[169] The ankle angle does not go as negative in angle as when wearing boots as when wearing shoes. A negative ankle angle corresponds to the foot being obtuse to the shank. What this means is that when loaded (i.e. foot on ground supporting weight) wearing the boot does not interfere with range of motion, however, when unloaded (i.e. foot in air swinging forward) does limit the maximum of the ankle joint. However, this has no impact on the harvester's function, as the energy harvester will be disengaged during this phase of the gait cycle.

The study was repeated for the same subject and setup, but with the subject donning a 35 pound backpack. The results for this study are shown in Figure 3.10 along with the no backpack case for comparison. Unfortunately, for this test the backpack obscured the hip marker, giving an inconsistent reading. Thus, only the ankle angle is calculated for the backpack case, which is the most important in any case.

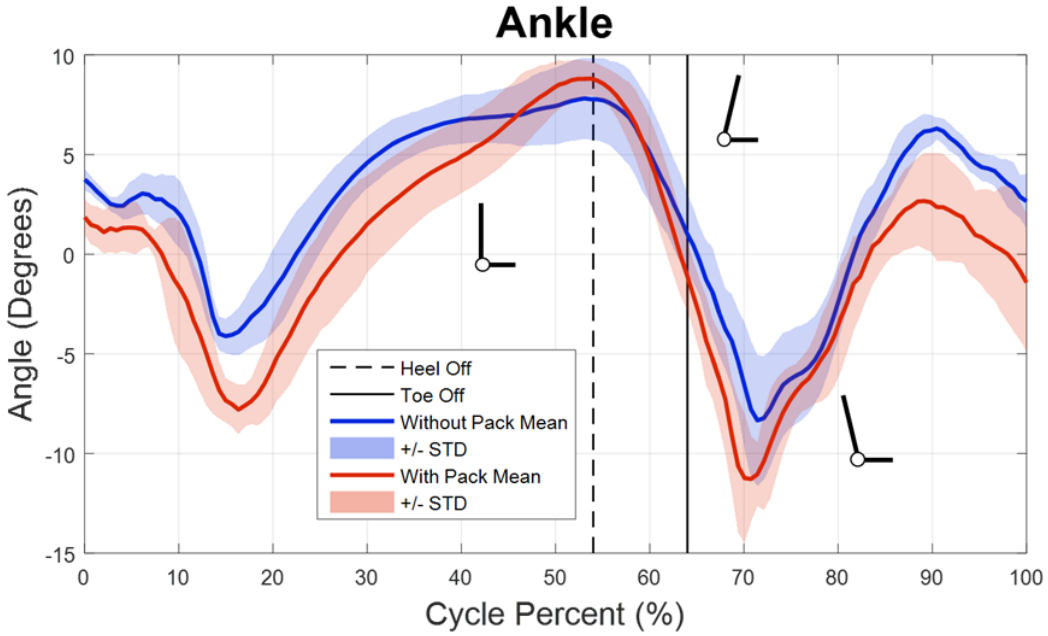

Figure 3.10 – Comparison of walking at preferred (normal) walking speed (Blue) with and (Red) without a 35 pound military backpack.

From Figure 3.10, it is observed that magnitude of ankle rotation is increased. This is due to the joints compensating for the increased load. The ankle must extend beyond its normal limits to address the added inertial load of the backpack. This means that the potential for harvesting energy is increased with increasing pack load.

Thus far, the ankle angle has been calculated using the segments between the heel-metatarsal and ankle-knee. However, to confirm that the leg does not move within the boot, which would result in wasted motion, the ankle angle was also calculated between the heel-metatarsal and ankle-boot top. Figure 3.11 shows the results of this comparison for both no backpack and 35 pound backpack cases. In both cases, the curves have nearly identical shapes. This corresponds to the boot-leg and leg move together. Since it is planned to run the brace structure torque input from the harvester up to the top of the boot leg, it is verified that all ankle rotation will be transferred to the boot leg and subsequently into the energy harvester device. The off-set of the two curves results from the improper placement of the boot top marker, which was placed slightly behind the tibia and thus computed a retarded angle. If the marker were placed in the correct location, then the two curves would lay nearly perfectly on top of one another.

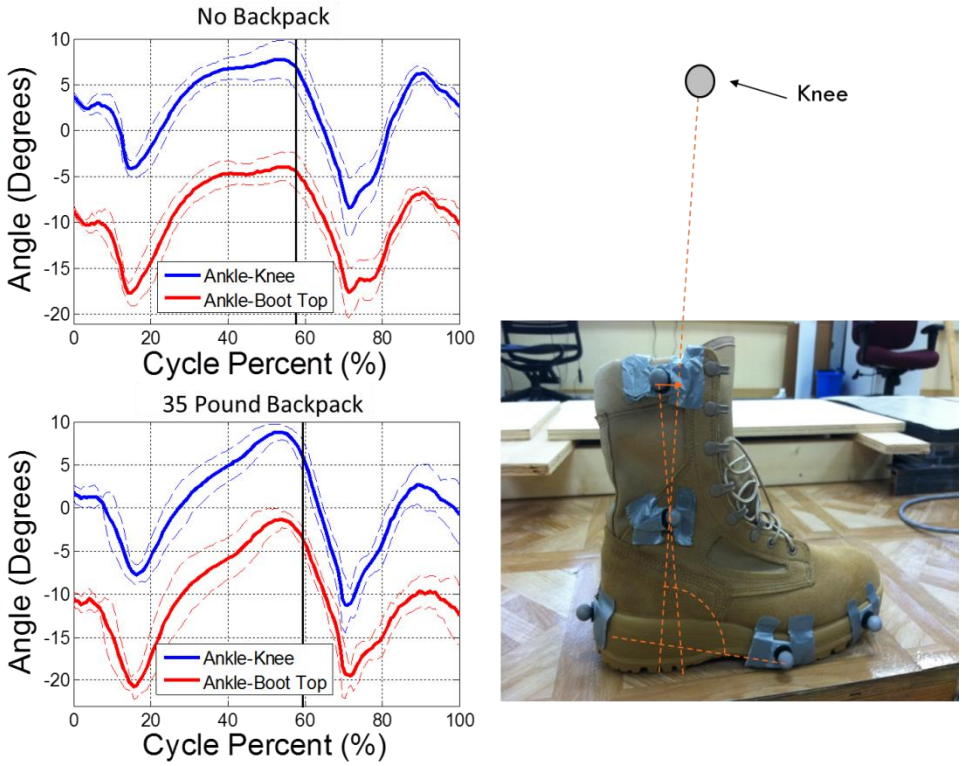

Figure 3.11 – (Left) Comparison of two methods for calculating ankle joint angle, with (Right) physical representation. Note lines are offset in angle due to misplacement of the marker at the top of the boot, but have nearly identical shape, indicating boot follow leg motion well (i.e. leg does not slide within boot).

Also of interest is the distribution of force between the heel and forefoot over the gait cycle. This distribution is of interest because the force on the heel section of the boot will be used to control part of the functioning of the energy harvesting mechanism, which is explained in later sections, such that the mechanism will act differently when the foot is on the ground (stance phase) compared to in the air (swing phase). Knowing the force distribution will also help validate the assumption that removal of material in the heel of the sole of the boot affects cushioning, when these tests are repeated with the energy harvesting mechanism installed.

It was difficult to estimate the force distribution, shown in Figure 3.12 below, due to the limitations of the measurement equipment used. The motion tracking points only give the position of the foot, while the force plate give only the magnitude and location of the center of pressure on the plate. Thus, the black (Total) line in Figure 3.12 is what was actually measured, while the blue

(Heel) and red (Toe or forefoot) lines were estimated. The estimation was made by first looking at the motion tracking markers to see when the forces should begin and end (i.e. no force attributed to the forefoot before the forefoot marker is actually on the ground). The total force is then divided between the two sections based upon the location of the center of pressure on the plate. This is a very rough estimate, and one will notice that the distribution of forces is questionable, as the Heel force in particular does not match the timing found in Figure 3.9.

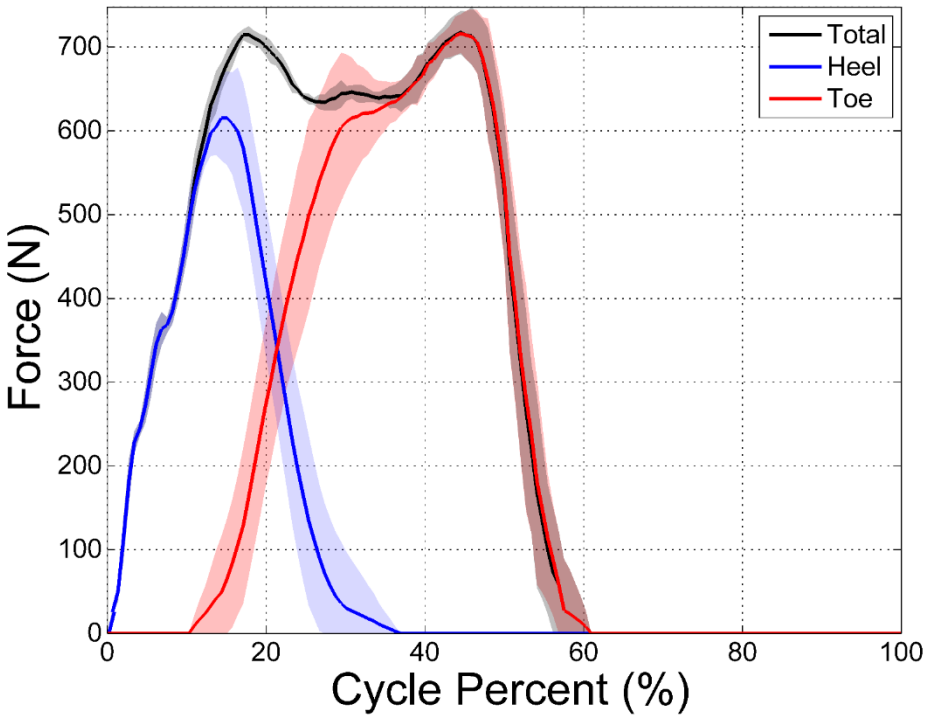

Figure 3.12 – Estimated for distribution between Heel and forefoot (Toe) during a typical gait cycle for the subject considered in this section. Shaded regions are ±1 standard deviation over five trials.

These biomechanics experiments are were a good starting point, and provided the basis by which the device was designed. However, since the study was done on a single subject, they should not be taken as a definitive representation for what a typical soldier's gait pattern will look like. For this reason, a proper gait study was conducted on 12 active duty military subjects wearing boots both walking and running, both with and without a 35 pound military rucksack. Since this new study involved individuals not directly involved with the study, this study received approval from the Institutional Review Board of Virginia Tech (IRB 15-080).

The premise of this study was the same as the previous one, with some upgrades. Compared to the previous study:

- 12 participants are used rather than 1
- Participants are active duty military accustomed to wearing combat boots
- 8 Vicon motion capture camera are used rather than 6
- 2 force plates are used rather than 1
- 8 marker points are tracked rather than 6 (and placed in more optimal locations)
- Jogging with and without backpack are also considered
- Pedar pressure sensing insoles are used in boot
- A longer platform is used to ensure participant reach steady-state speed before reaching the force plate(s)

As mentioned, the new study featured walking and jogging both with and without a 35 pound rucksack. This is a factorial experimental design with two factor (with pack, without pack) and two levels (walk, jog). There are therefore four treatment combinations. The treatments combinations were randomized, such that they could be administered in such a way that would not induce experimental bias. As an example, if every subject began by doing the two levels of pack trials, it may alter their gait when they do the without pack trails where they weigh less. The treatments were randomized such that each treatment occurred in each spot in the experimental order three times, since there are 12 participants in this study. The only alteration to the random order is that it was prescribed to the two treatments where the subject wore the backpack occurred in succession, so that the pack would not have to be don twice, out of convince. The experimental treatment order is given in Table 3.1 below.

The participants themselves were active duty military coming from the US Army, Air Force, Marines, and Virginia Tech Corps of Cadets. The subjects were 10 male and 2 female, with a mean weight of 184 pounds (max: 220 lbs, min: 160 lbs, STD 16.5 lbs). This weight is as tested, which all measurement equipment for the Pedar system worn. To accommodate the range of individuals, Belleville 390 boots were prepared in US sizes 8, 9, 10, 11, and 12, with the motion capture markers. These markers were pinned into the sole of the boot for a secure and rigid connection. Subjects were allowed to pick their boot size based on their comfort level. Pedar insole sizes were chosen based on the boot size, which were either sizes W, X, or Y.

Table 3.1 – Experimental treatment order for new gait study. Trial HT # is the participant's number.

Trial	Order			
HT 1	Walk Normal	Jog Normal	Walk Pack	Jog Pack
HT 2	Jog Normal	Walk Normal	Jog Pack	Walk Pack
HT 3	Jog Normal	Walk Normal	Walk Pack	Jog Pack
HT 4	Jog Normal	Walk Normal	Jog Pack	Walk Pack
HT 5	Jog Pack	Jog Normal	Walk Normal	Walk Pack
HT 6	Walk Normal	Walk Pack	Jog Pack	Jog Normal
HT 7	Jog Pack	Walk Pack	Jog Normal	Walk Normal
HT 8	Walk Normal	Jog Pack	Walk Pack	Jog Normal
HT 9	Jog Pack	Walk Pack	Jog Normal	Walk Normal
HT 10	Walk Pack	Jog Pack	Walk Normal	Jog Normal
HT 11	Walk Pack	Jog Normal	Walk Normal	Jog Pack
HT 12	Walk Pack	Jog Pack	Jog Normal	Walk Normal

The experimental setup is shown in Figure 3.13 below. The experimental area is shown in parts (a-c). Parts (a) and (b) show opposite views of the long platform with an arrow showing the direction of travel of the subject. Forces plates 1 and 2 are labeled in the correct orientation relative to the motion cameras picture in part (c). The equipment worn by the study participants is shown in parts (d) and (e). The Pedar insoles, shown in (f) are placed on top of the boot insole and measure the pressure underneath the foot. The signal from the insoles are transmitted wirelessly from the transmitter worn on the belt. Part (g) shows the placement of motion capture markers on the boot, while the other two markers, worn on the knee and hip joints, can be seen in (d) and (e). The backpack (rucksack) visible in (d) and (e) was worn for half of the test, and half the tests without the pack. Each experimental treatment was performed and recorded ten redundant times, such that a meaning full average and standard deviation could be performed.

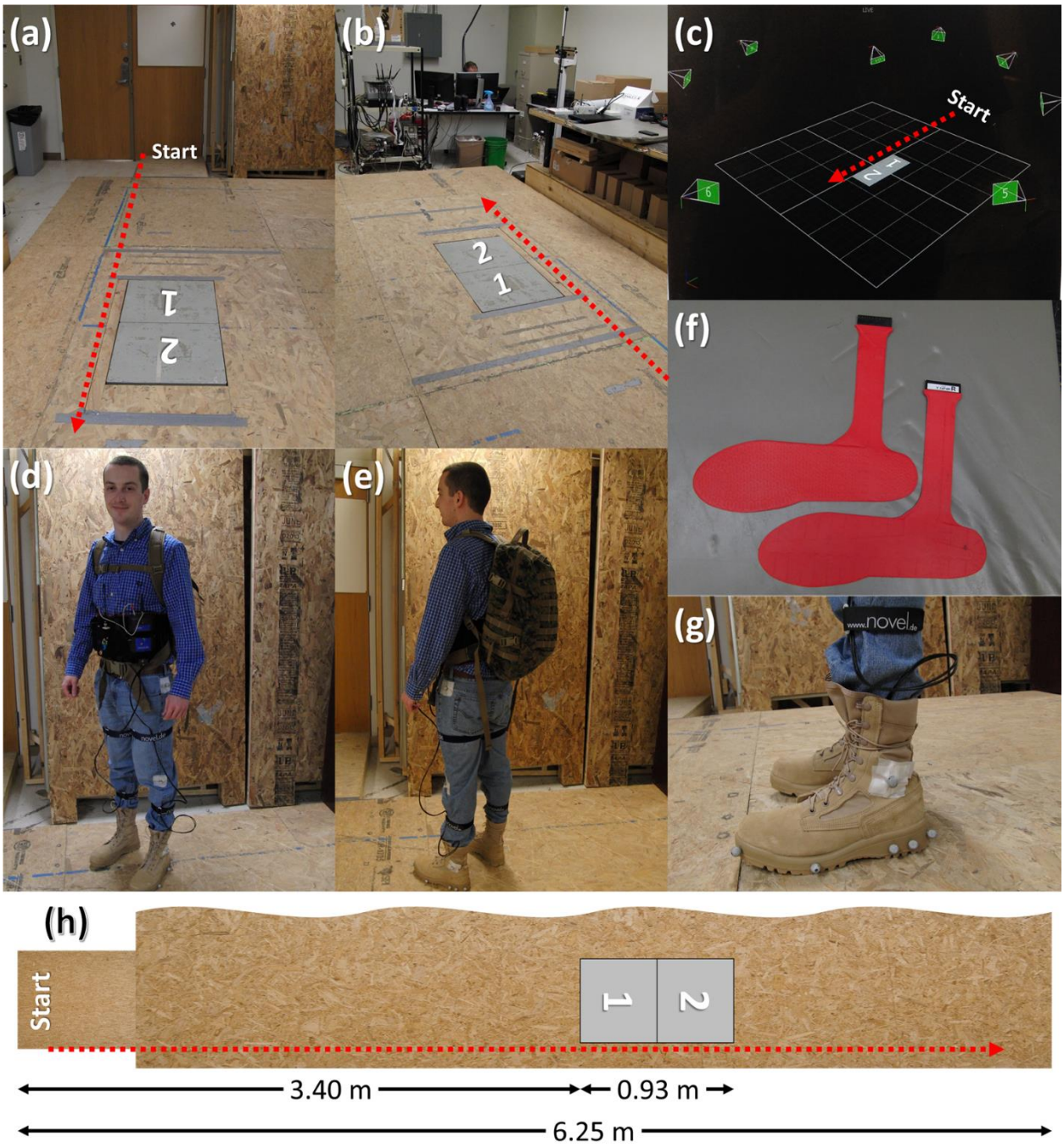

Figure 3.13 – (a) and (b) picture the platform and the two force plates (1 and 2) as well as the start position and direction of motion. (c) Illustrates motion capture camera positions and relative position of measurement coordinate system. (d) and (e). (f) Shows an example pair of Pedar pressure sensing insoles which lay directly on the boot insole. (g) Close up of marker placement on the boot. (h) Dimensioned illustration of testing platform.

Due to the large volume of data generated during this study, a complete data analysis is still ongoing. What will be gained from the completed data analysis is an updated versions of Figure 3.9, Figure 3.10, and Figure 3.12, along with a pressure map of the heel strike, averaged across all participants for each of the treatment conditions.

A sample pressure map is given in Figure 3.14 below. The figure shows the pressure on the heel of one study participant at an instance in time after heel strike.

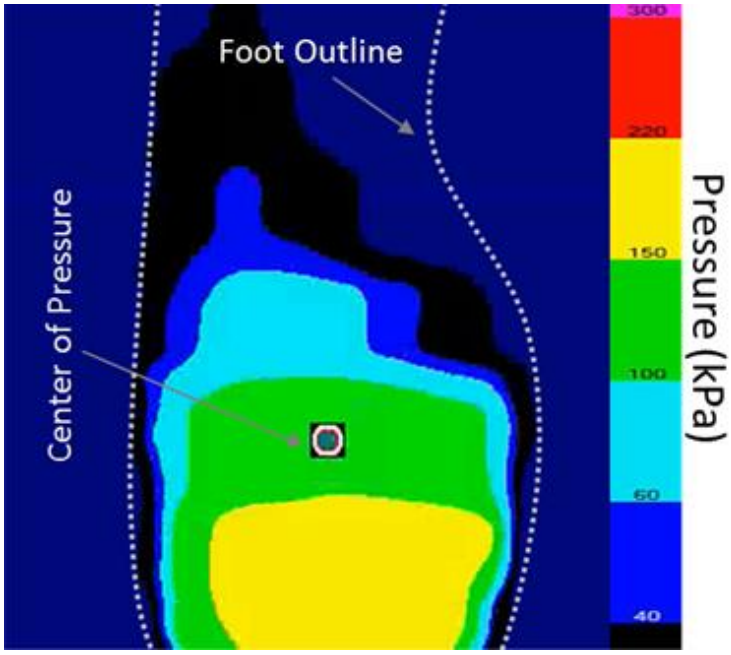

Figure 3.14 – Sample pressure map given by Pedar pressure sensing insoles for the left foot one study participant, the moment after heel strike.

3.7 Mechanism Description

The workings of the boot energy harvester are broken into four functions, as represented in Figure 3.15. Torque is inputted to mechanism via the bracing structure in the boot leg. This is a high-torque low-displacement motion, so it is converted to a lower torque but higher velocity motion using the torque conversion and mechanical energy storage sections. The ankle moves only about 10°-20° of rotation during the negative work part of the gait cycle, so this rotation angle is amplified using a gear train, which winds a power spring. The wound spring then rapidly unwinds,

turning the generator at high rpm, producing large power output, which is then processed in the circuitry and stored in the battery.

Due to the presence if the intermittent storage of mechanical energy in the power spring, the gait motion is never damped. That is to say that if the generator were connected directly to the torque conversion sections, the ankle would experience rotational velocity proportional damping, which would inhibit the walking motion. Though, since the torque conversion section connects to the power spring mechanical energy storage sections, motion is not damped, as there is essentially no energy penalty for winding the spring faster versus slower. Also, due to the non-linear torque profile of the power spring, the winding should feel normal to the walking motion.

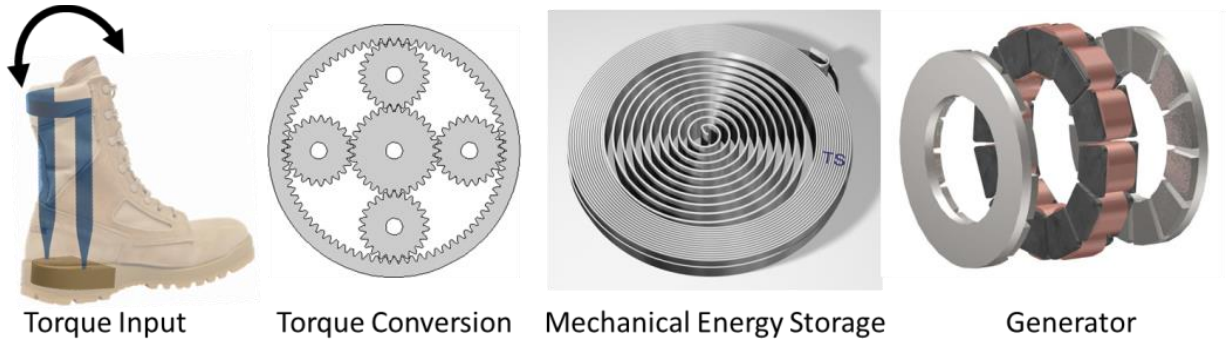

Figure 3.15 – Representation of energy flow through the five sections of the harvester design.

The design of each section will be explained individually in the subsequent sections. While it was decided to explain each phase of the design individually for the sake of keeping a clear focus and common theme of concentration in each section, the design of each phase of the mechanism inherently affects the other phases. Thus, changes in the design of one phase would have a cascading effect through the rest of the mechanism, necessitating the alteration of connection points, size of individual components, location of components and devices phases, etc.

Changes in each section were made iteratively with each new generation of the mechanism design, but also between mechanism generations as new discoveries were made. It is also for this reason that the individual phases of the design are explained individually, but will sometimes be placed in the context of the mechanism generation strategy that was being pursued at that time.

3.7.1 Device Housing and Design Strategy

The key design constraint with this device is the overall size it is allowed to occupy. It would be much simpler to allow the device to protrude from the sides of the boot or expand the midsole area to give more room, however, this would give a modified appearance to the boot, which is unacceptable. Therefore, since it is the goal that all components be embedded within the sole of the boot, an accurate understanding of the form of the boot must be obtained in order to know the solution space a given design is allowed to take up. This solution space is the device housing, which will replace material of the midsole removed to make room for the energy harvesting device mechanism.

To gain understand of the space available for the device and examine possible integration methods, the chosen boot was first dissected. The boot cross-section depicted in Figure 3.16 was prepared by taking a Belleville 390 hot weather combat boot (Size 8) and first removing the upper fabric portion. The remaining lower leather portion, insole (black), midsole (area between red and blue lines) and tread layers were bisected along the length of the boot. Measurements of the thickness of the midsole were then taken, as the proposed energy harvesting mechanism will have to fit within this thickness.

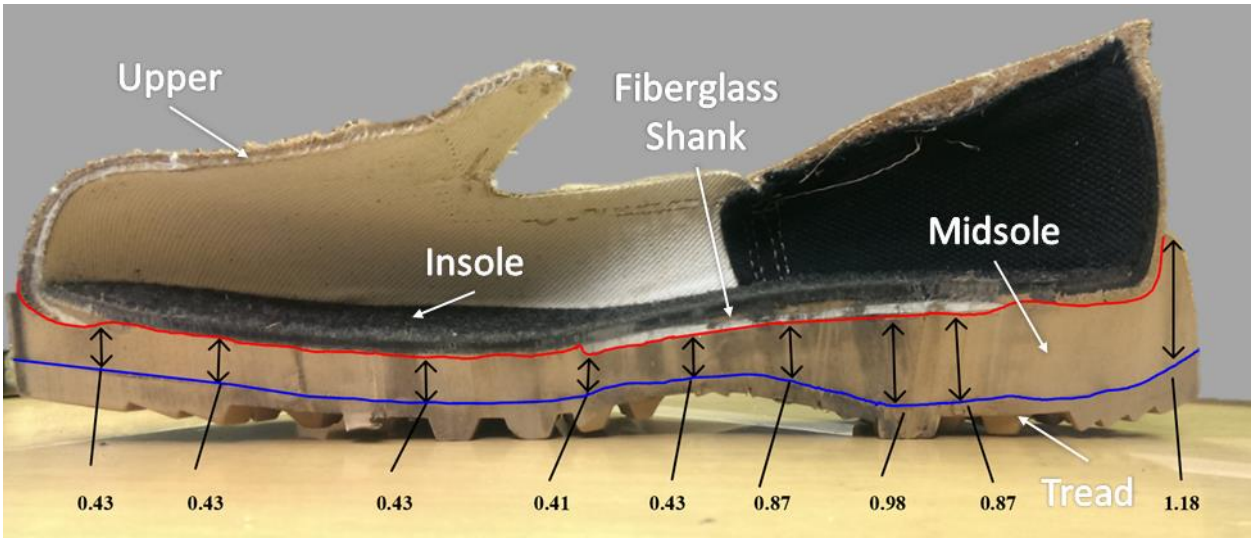

Figure 3.16 - Cross-section of Belleville 390 hot weather combat boot with upper fabric portion removed leaving leather upper, insole, midsole, and tread layers. Midsole thicknesses are labeled in inches. Note the white section visible between the insole and midsole is a fiberglass shank, which prevents the middle of the boot from bending, to mimic the flexibility of the foot.

The dimensions gained from the boot dissection were used to create a CAD model of the boot midsole was generated and is shown in Figure 3.17. Once the boot was quantified, components could then begin to be selected which would fit in the defined space.

Figure 3.17 - CAD rendering of midsole of Belleville 390 hot weather combat boot.

With the goal of having the entire energy harvesting devices embedded within the boot midsole, the mechanism housing could begin to take shape. From Figure 3.16, it is evident that the forefoot section of the boot is much thinner than the heel section. Moreover, the forefoot section is thin so that it can bend to following the rotation of the foot/toes about the metatarsophalangeal joints. Insertion of an energy harvester mechanism at this location would not be favorable, as the mechanism would either have to be compliant or else compromise the flexibility of the boot. Neither option would yield a worthwhile design. Therefore, it was chosen to keep the device only in the heel section of the boot, where more space is available and it is meant to be rigid. Indeed rigidity in the heel of the boot is the purpose of the fiberglass shank, seen in Figure 3.16. The shank is stiff, causing bending to occur in the forefoot while the heel section does not bend, since there are no joints in the heel of the foot which permit appreciable amounts of rotation.

It was reasoned that the device housing could take up the whole of the heel section space without significantly altering the feel of the boot, since the heel section is made not to bend and the device housing will certainly be rigid to protect the various rotating components inside. Though, while the heel section is made not to bend, it is made thicker to absorb the shock of the heel strike. Removal of the urethane midsole material and substitution of the device housing is considered to reduce some of this shock absorption. The saving grace, however, is that the boot's

insole will remained unmodified. The insole does most of the work in shock absorption, and even performs well in footwear with limited midsole cushioning, like military boots.[170] This is specifically applicable to the HEREMS boot where most of the midsole will be removed, and there is even less midsole cushion than normal.

As mentioned before, since the key design constraint is the volume of the device, the overall design strategy is governed by the design of the device housing. Therefore, in this section the device housing will be given along with some of the overall design strategies, the individual phases of which will be described in their own sections. Information is presented this way to yield a big picture of the design process and evolution of the design.

To start, a simple device housing was imagined. The housing consisted of the extrusion of the mating of a rectangle with a semi-circle. This shape, shown in Figure 3.18, gave clear and easy to work with geometric boundaries, unlike the complex three-dimensional shape of the boot sole itself.

Figure 3.18 – Housing Generation 1: (Left) Cross-section of Belleville 390 hot weather combat boot with overlay of cross-section of device housing size and locations, (Right) picture of 3D printed housing prototype with overlaid dimensions.

Even from this first stage, it was the goal of the design to maximize the size of the induction generator. There are many things one can tweak in the design of induction generators to achieve the desired performance. However, to increase power generation there is little substitute for having as large a generator as possible. Therefore, it was the original design intent to maximize the generator size and fit all other components around it. It was quickly realized though, that the sizes of the other components, especially the angle amplification section, could not be of secondary consideration. Consequently all sections were considered in parallel, as to their size and connection, with impetus, rather than prescription, on maximizing generator size.

Since there is much more room in the device housing's width and length (~70×70 mm) compared to the depth (~25 mm), it was decided to the generator should lay flat in the housing with the rotation axis perpendicular to the ground. In this way the diameter of the generator could be as great as possible. Conversion of the rotation axis from parallel to the ground at the torque input from the ankle, to perpendicular to the ground at the power spring and generator would be made from a bevel gear, or an axis change round belt pulley. A rough rendering of this initial design is shown below in Figure 3.19.

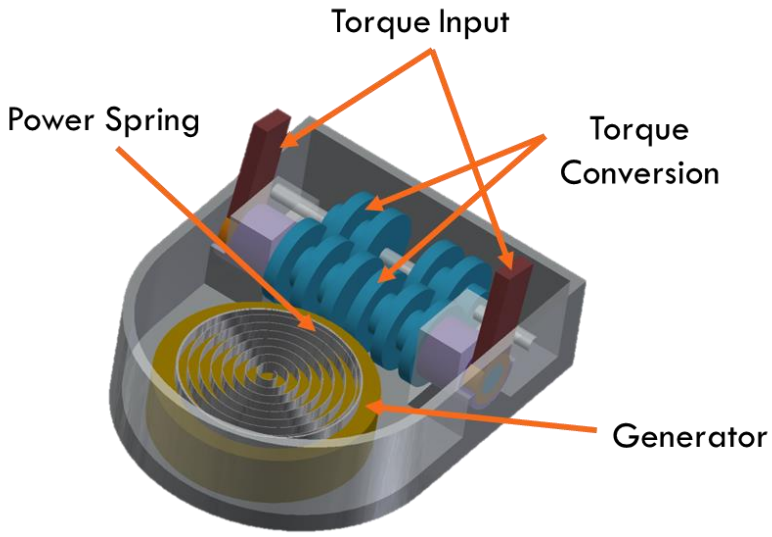

Figure 3.19 – First mechanism design layout.

From the rendering above, one will see that the generator is occupying the circular heel section, where it is of greatest space efficiency. The generator was mocked-up, such that is was as big as possible while allowing room for the torque conversion (angle amplification) section, which takes the form of compound gears here.

From this initial rendering, it was decided that the orientation of the generator would be best if it were parallel with the input axis. This decision was made after the consideration of failure modes of the device. If excessive force were applied to the boot heel, such as jumping from a large height or kicking in a door, and the device housing were to fail, there would be the chance of impaling the foot if the generator shaft (hardened steel) were mounted perpendicular to it. Consequently, for safety reasons, it was decided that all shafts, and subsequently rotation axis, should lie parallel to the ground. In this way, if failure of the device housing did occur the foot would only contacted only rounded urethane (3D printed) parts, reducing the change of serious injury.

By making the generator and power spring sections mounted horizontally, the optimal location was no longer in the rounded heel section, but along the front of the housing, as shown in Figure 3.20. With the generator and spring in the front, and torque input location at the same place, the secondary axis from angle amplification was shifted to the back of the housing.

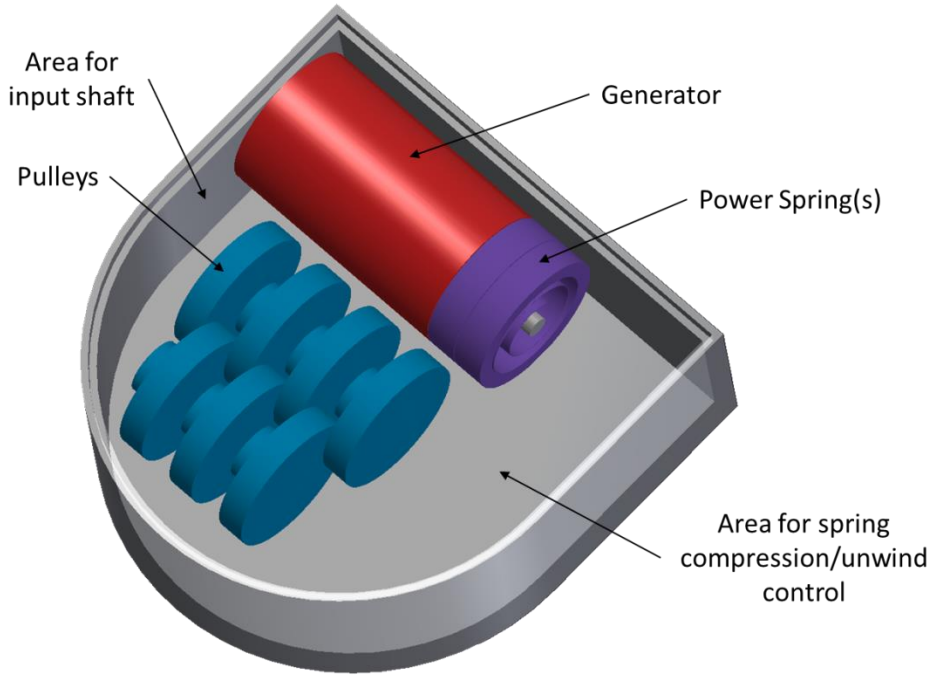

Figure 3.20 – Second design layout with horizontally mounted generator.

At this time, it was also decided to use some form of pulleys rather than gearing to reduce noise. Indeed, if one of primary goals of the device was to maintain a normal appearance, it would not be rational to allow the familiar high pitched whine associated with highly geared mechanisms

(e.g. robotics, transmissions, etc.). It was decided at this time to not use ratcheting mechanism as well, because of their noise.

In the way of pulleys, there are naturally two components; the pulley itself, and the belt. They pulley is defined by the belt which is used. There are four main types of pulley belts; flat, round, Vee, and timing, illustrated in Figure 3.21. The flat, round, and Vee types of belt rely on friction to transfer torque, which the timing belt has teeth, similar to a gear, which aid in transferring greater torques.

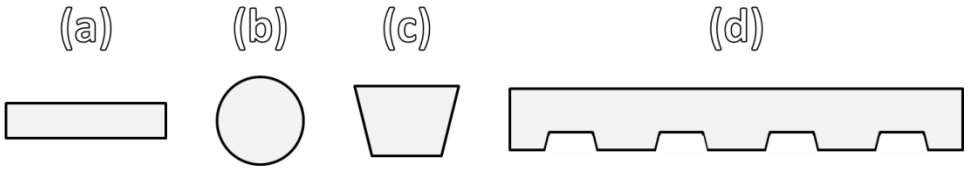

Figure 3.21 – Pulley belt types with (a) Flat, (b) Round, (c) Vee, (d) Timing. (a-c) are cross-sectional views, while (d) is a lengthwise view.

Initially it was desired to use the round belt pulley, since it has the unique ability of allowing rotational axis changes, due to the fact that the belt is the same in all directions, whereas, a flat, Vee, or timing belt would have to twist to change rotational axis awkwardly. While it was decided early on to keep all rotation axis parallel, the round belt continued to be of interest for use in a crossed belt design, capable of transferring more torque, which is discussed later. The other belt considered is the timing belt, since it can intrinsically transfer for torque. The two resulting concept designs, using timing and round belts, are rendered in Figure 3.22. Both these designs share the same layout as in Figure 3.20, but with increased detail of the pulleys.

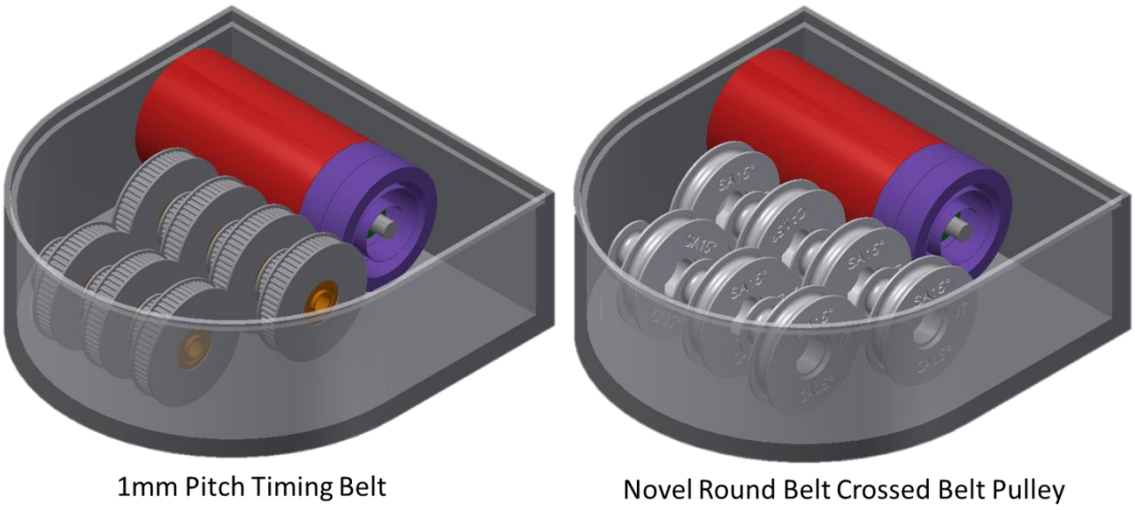

Figure 3.22 – Concept rendering energy harvester mechanism, utilizing timing belts (left) and novel round belt crossed belt pulley (right).

With to-scale prototypes showing that the round belt pulleys could not transfer sufficient torque, despite a novel design increasing torque transfer, timing belts were proceeded forward with as the means of torque to angular velocity conversion. Though it was desired to use a power spring to decouple the ankle from the generator, since at the time no method of controlling the winding-unwinding of the power spring had been developed, a prototype with a directly driven generator was designed. The rendering and assembly of the directly driven prototype is shown in Figure 3.23.

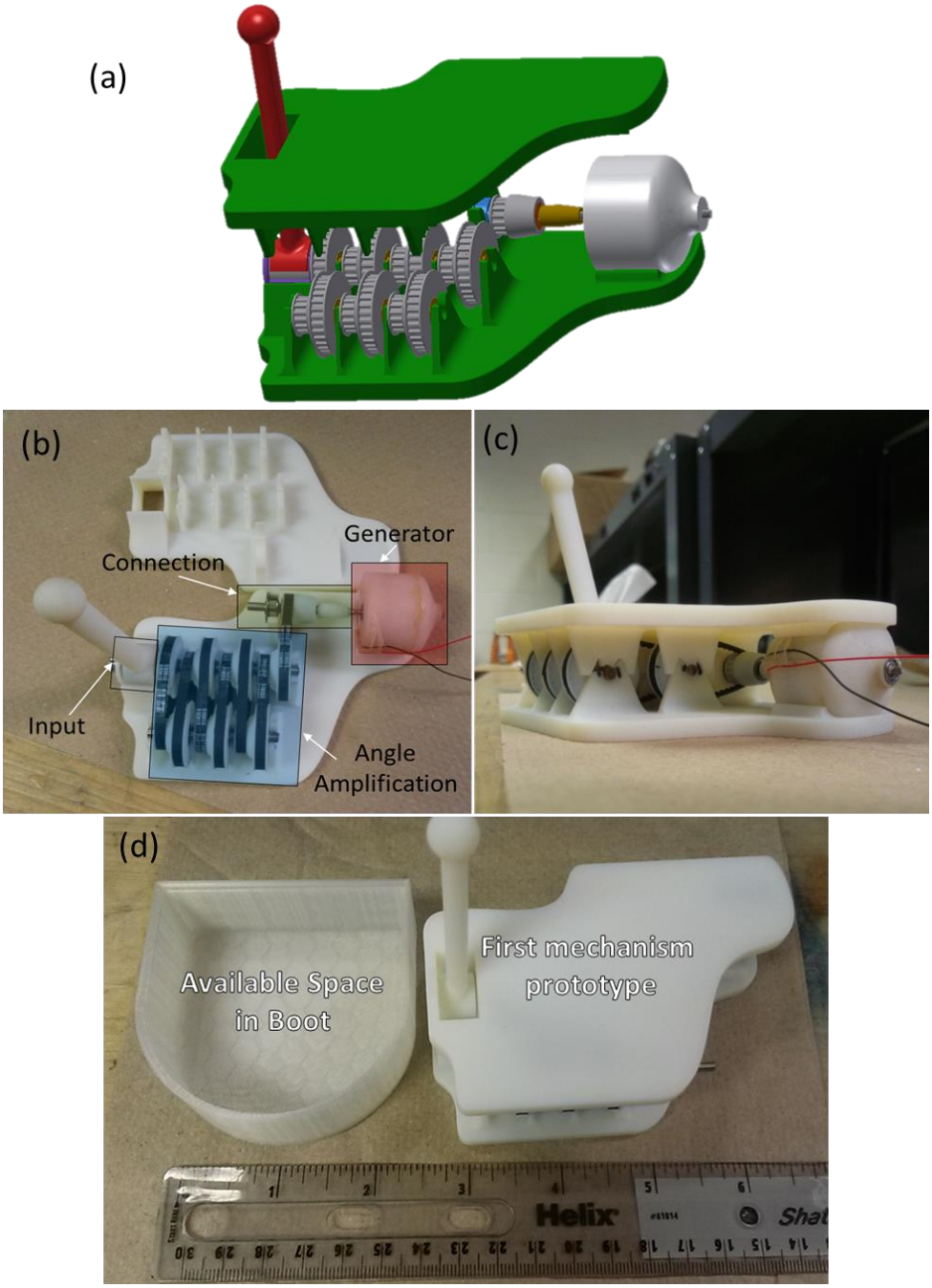

Figure 3.23 – (a) CAD rendering of directly driven prototype with different colors illustrating the different parts (timing belts not shown), (b) assembled prototype with top case removed and key areas labeled, (c) fully assembled prototype, (d) comparison of this prototype to available space in the boot.

As can be seen from part (d) of Figure 3.23, the design is not one which could actually fit in the available space in the boot. This is because of the generator used in this design, which is a generator made for a small wind turbine. It is thus slightly too large for the boot, so it had to be connected away from the input sections, rather than flipped back toward it, such that it would fit in the available space. Commercially made generators are not readily available to fit the size requirements specific to the boot. In future designs it was considered to the generator would be manufactured by hand.

All of the compound timing belt pulleys are of a 1:2 ratio, with 3mm wide GT2 2mm pitch timing belts. The mechanism functioned well when the angle amplification section was not connected to the generator. The angle amplification section carries a 64 times amplification. There is then an additional 1:2 ratio to the connection section and then the generator, making a total of 1:128 ratio. Even with the smooth rotation of the timing belt pulleys, there is still enough torque on the first timing belt to cause it to slip with the addition of the generator counter torque. This result was taken as a fine example of the downfalls of using a high gear ratio and a directly driven design.

To transition into a design making use of a power spring to decouple the torque input from the generator, a method of controlling the power spring winding had to be developed. By way of a first step, a layout allowing for spring winding control was realized. Such a layout is given in Figure 3.24 below as compared to the directly driven design. Since the winding of the power spring should occur when the ankle angle is becoming smaller (i.e. when negative work is being done), it was proposed to use the angle of the ankle as a means of control, using a cam-based mechanism. This mechanism was planned to use a drum brake, which would be pressed against the arbor (inner) shaft of the power spring at suitable ankle angles. As a result, while the outer housing of the power spring was being rotated by the torque input, the arbor would be held, allowing the spring to wind and store energy. When the ankle angle increased again the drum brake would pull away from the arbor, allowing it to unwind and turn the generator rapidly.

After much design work, the rendering in Figure 3.25 below was established, which follows the proposed layout of component sections in the right of Figure 3.24. The power spring is applied to this design, along with winding control. Additionally in this design, the device housing has been molded around the parts rather than having supports rise from a flat plate. This adds much more structural rigidity.

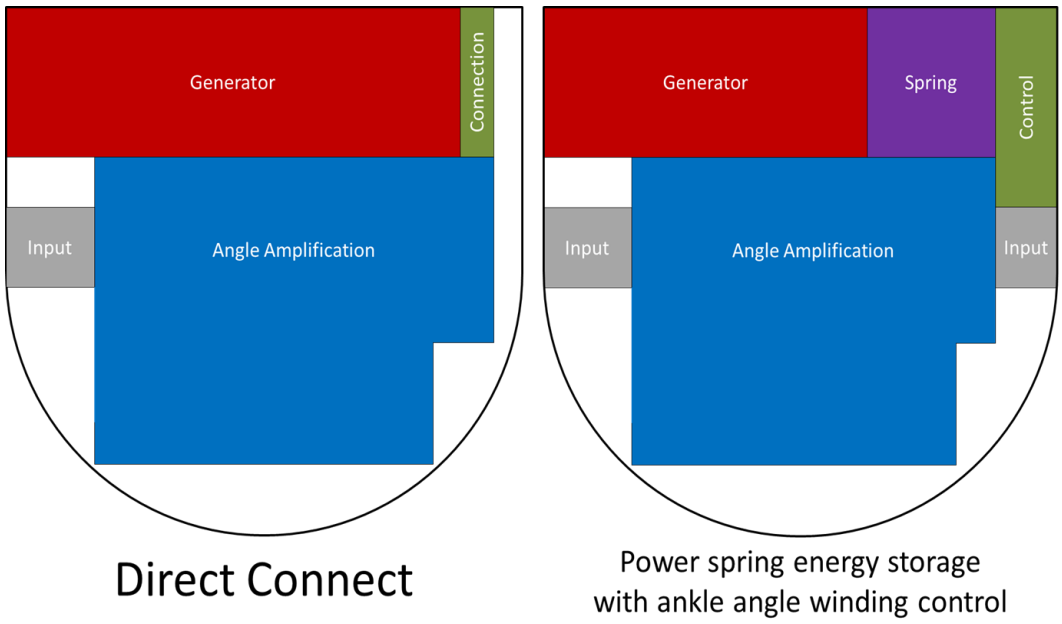

Figure 3.24 – Schematic layout of (Left) direct connect design and (Right) power spring winding control design.

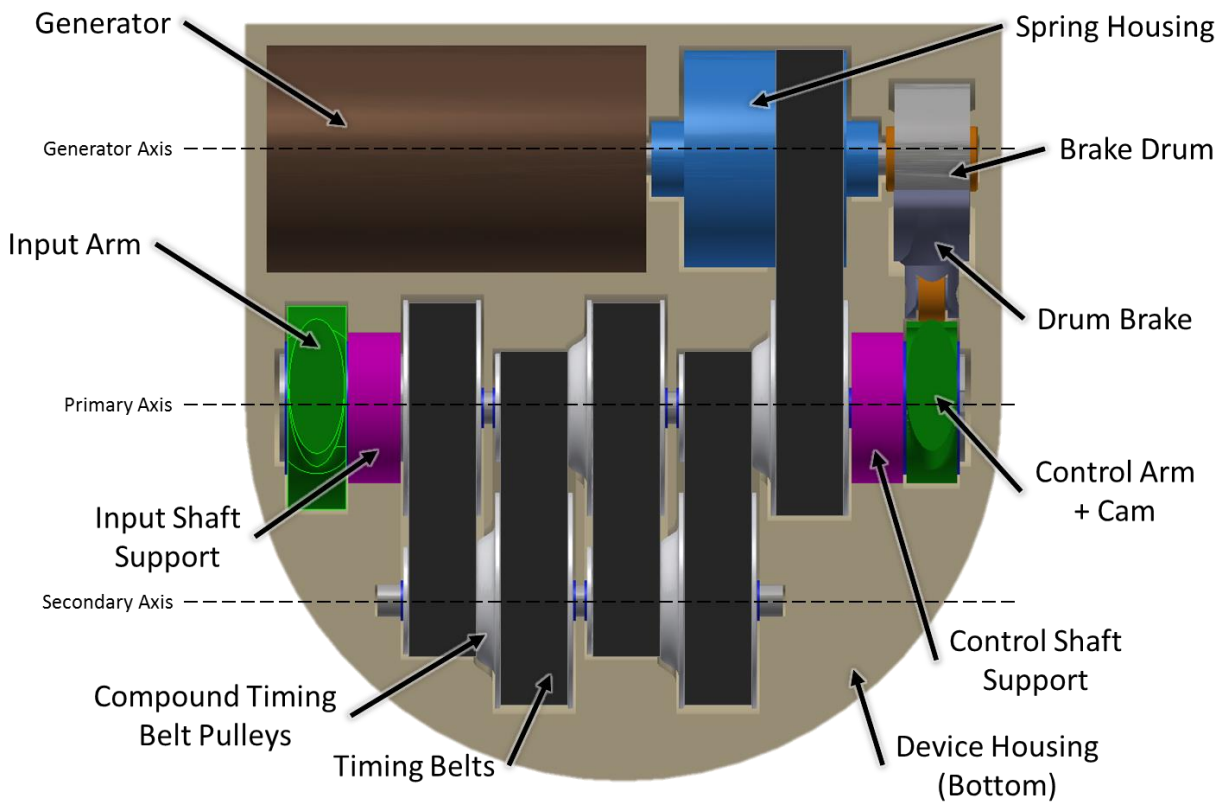

Figure 3.25 – Second mechanism design layout.

The device in Figure 3.25 receives a torque input from the Input Arm, which will run all the way up the leg of the boot and follows the motion of the tibia. The Control Arm is then connected to the Input Arm in the leg of the boot and the two rotate together. The input arm connects to the Primary Axis through a one-way clutch bearing, so that torque is only transmitted during the negative work part of the gait cycle. Therefore, the first pulley on the Primary Axis only spins when the clutch bearing is engaged. Rotational motion is amplified through cascaded stages of compound pulleys and spins the Spring Housing. At this time, the Drum Brake (actuated by the Cam on the Control Arm) prevents the arbor (inner shaft) of the power spring from rotating, allowing the spring to wind. When the Drum Brake is later released, the arbor of the power spring unwinds into the generator, producing power.

From the previous design, the manner in which Input Arm and Shaft are mounted has been updated to be more stable, the timing belts have been increased in width (from 3mm to 6mm) to allow more torque to be transmitted, and the control mechanism has been added. A consequence of increasing the width of the timing belt is that fewer compound pulleys could fit into the available area. Therefore, the current design produces a 1:16 ratio.

An isolated view and illustration of functionality of the spring winding control is shown in Figure 3.26. This section is necessary because in order to store energy in a power spring (wind it), either the inner or outer end of the spring must be held stationary while the other end is rotated. If neither end is fixed, and one end is rotated, the other end would simply rotate as well and not energy would be stored. It is sought to intermittently store energy during the step for two reasons. Firstly, by decoupling the ankle torque input from the generator, motion is not damped, and the person will only feel the fairly constant force of spring against their motion. This force is the same regardless of how fast the ankle angle changes (i.e. walking to running), whereas if connected directly to the generator, damping force would increase with speed, meaning there would be more resistance when running, which is not desired. Secondly, by storing energy in the power spring and releasing it rapidly, the generator will be spun more quickly and achieve a higher rotational speed than would be possible with direct coupling. Since the electrical output of the generator is most strongly dependent on rotational speed, this method of intermittent energy storage and release in the spring is thought to produce more power.

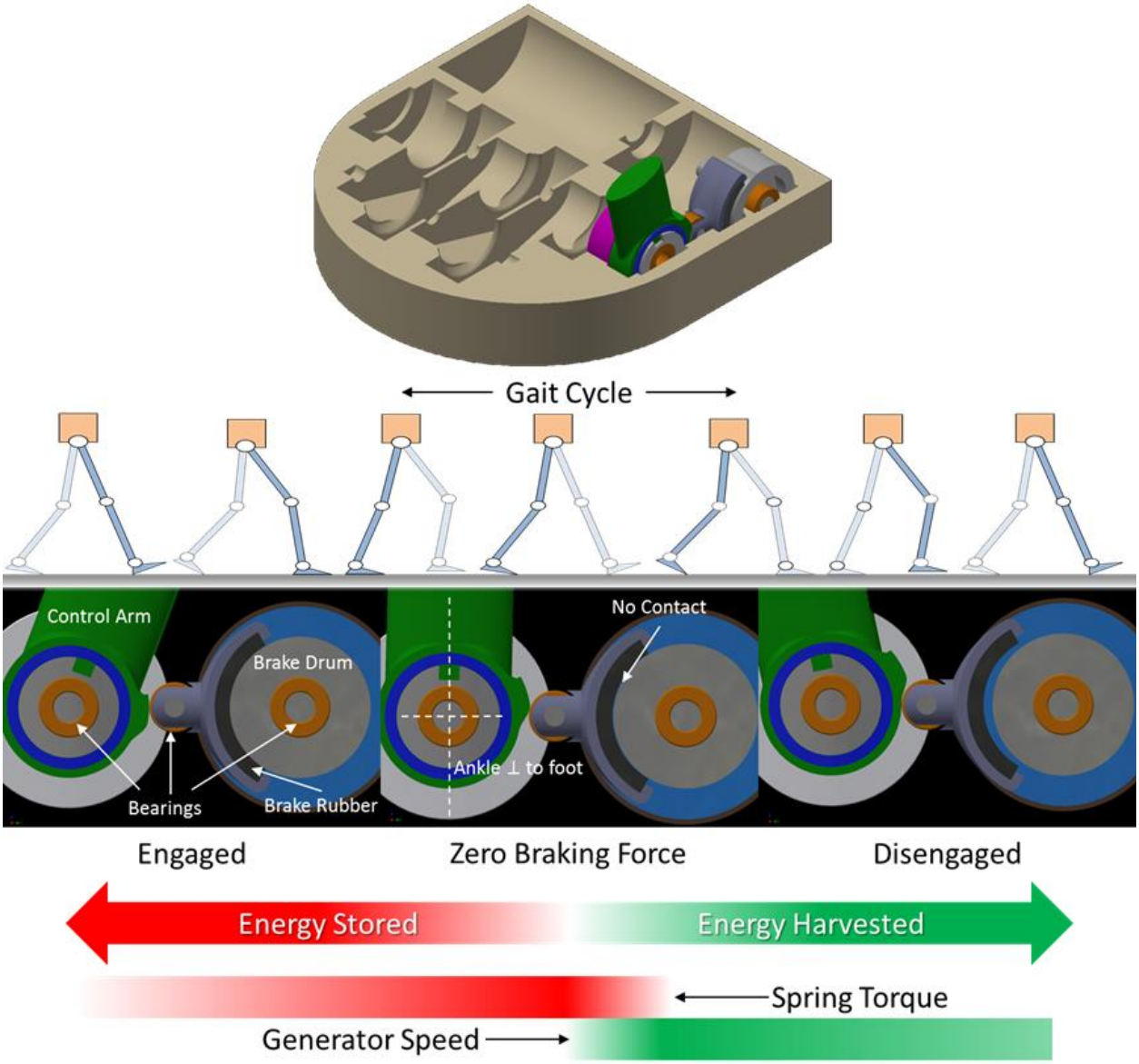

Figure 3.26 – Pictorial explanation of actuation of drum brake power spring winding control.

From the above figure, once can see that the control arm has a cam protrusion which contacts a ball bearing roller on the drum brake. As the ankle rotates and the cam goes from the lower to the raised profile, the ball bearing diminishes friction as the brake is pressed against the drum. Here it is shown that when the ankle reaches the position where it is perpendicular to the foot, or zero angle as it is defined, that this is the point of the brake contacting the drum. This timing can be easily adjusted and would do better to have been designed such that contact begins at approximately -5°, from what was learned from the gait analysis in Figure 3.9.

Applying this spring winding control strategy to gait cycle, it is found that this is still not the control scheme which will be successful. The problem arises from the fact that there are two times in the gait cycle in which the ankle angle is decreasing, once when the foot is on the ground and when it is intended to harvest the negative work done, but also when the foot is in the air during swing phase. With the aforementioned design of the spring winding control, the harvesting mechanism would be erroneously engaged during the swing phase, as shown in Figure 3.27.

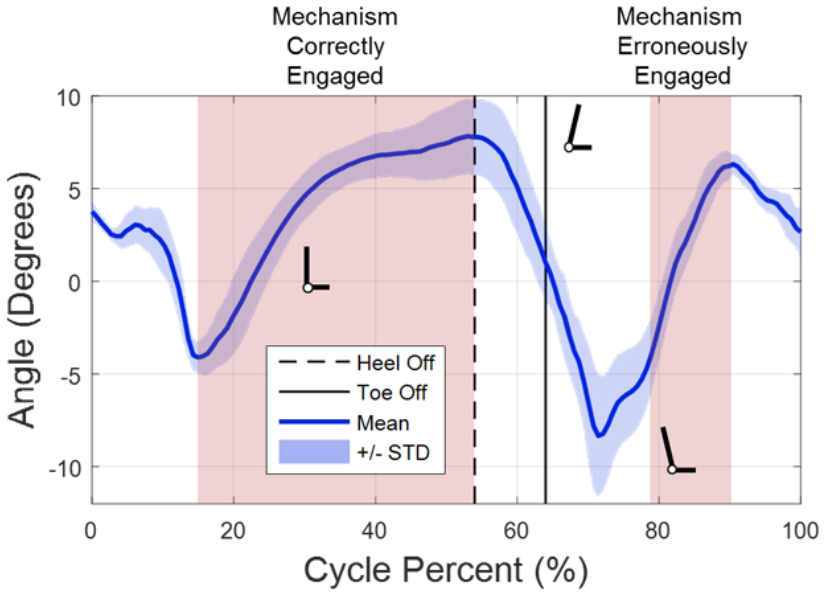

Figure 3.27 – Angular rotation of the ankle across the gait cycle with shaded regions for when the mechanism render in Figure 3.26 would be engaged.

There is only torque on the ankle when the foot is on the ground. This can be understood by considering that while on the ground, the ankle has a moment applied to it proportional to the subjects mass and distance from ankle to center of mass (approximately length of leg). There is naturally torque on the ankle when it is in the air (swing phase to next step), however it is only proportional to the mass of the foot, with moment arm approximately half the foot length. Therefore, the torque on the ankle in swing phase is negligible, as the mass and length of the foot are much smaller than the mass of the body and length of the leg.

As has been mentioned previously, a one-way clutch bearing is used on the torque input, so that energy would not be harvested on the "push-off" phase of gait, as positive work (i.e. propulsion) is done during this phase and harvesting energy would be parasitic to the walking

motion. Therefore, energy is only harvested when the ankle angle becomes smaller. The fact that the one-way clutch bearing would be engaged, and energy would attempt to be harvested, while the foot was in the air, see Figure 3.27, is undesirable. The device will be designed to receive high torque inputs. In the case where the foot it in the air, as discussed earlier, the natural torque the body expects is low, however, the device would demand high torque. This situation would most likely create an awkward feeling during the swing phase, which is undesirable. To correct this problem, the mechanism must somehow become disconnected while the foot is in the air.

Indeed, this problem of disconnecting the harvesting mechanism during the swing phase of gait is the key design problem not only facing this mechanism, but for all mechanisms attempting to harvest energy from gait. In their knee brace energy harvester, Donelan et al., use a potentiometer and computer control to disconnect their generator during the swing phase.[157] Despite this consideration, however, since their gear train still turns the generator, which is just in open-circuit during the swing phase, metabolic rate is still increased since additional energy is expended to overcome the inertia of the gear train and generator mass, when typically negligible energy is used by the body.

After much consideration, the strategy of using the body weight to control the engaging mechanism of the power spring was thought up. Since the device should only be active when the foot is on the ground, the body weight will be used to engage a coupling structure through a drum brake and spring. When body weight is relieved from this coupler, (i.e. foot is in the air) the torque input will be disconnected from the power spring drum brake. In this way, when the foot is in the air, the power spring will not store energy. However, there is still the problem that it will be turned by the timing belt pulley train. It is good that the spring won't store energy in the swing phase, which will reduce the torque place on the ankle by the device, which should be as close to zero as possible, but the mechanism would still suffer from the boot wearer having to turn the inertia of the gear train. It was reasoned that it was not enough to just prevent the power spring from winding during the swing phase, but the ankle angle amplification section must also somehow become disconnected from the torque input as well.

To accomplish this type of operation, it was clear that the pulley train would not suffice. Again after much consideration, a solution was theorized using a planetary gear setup. For a planetary gear setup, there are three types of gear (as illustrated in Figure 3.28a); ring gear (or annulus), planet gears, and sun gear. Depending on what type of gear ratio and rotation direction

is desired, one gear is held stationary, one set is driven, and one set is free to rotate. In the application of the boot it is proposed to alternate the configuration of the planetary gear set using the heel brake, which also controls the power spring winding-unwinding. As shown in Figure 3.28b, torque input for the planetary gear set will be the planet carrier, which will be turned from the ankle rotation. When the heel is on the ground, a drum brake will be depressed against the ring (annulus) gear, preventing it from rotating. In the example case, a 1:4 gear ratio is realized between the planet carrier and sun gear. The sun gear is then connected to the planet carrier of the next planetary gear set. For example, three gear sets could be used to produce a 1:64 (i.e. $4^3 = 64$) ratio for winding the power spring. To prevent torque on the ankle when the foot is in the air, the drum brake is released (via a small compression spring) as body weight is no longer on it. Therefore, there is now more resistance to rotation of the sun gear (as it is connected to the spring) than there is the ring gear. Thus the sun will be stationary and the ring gear will become the 'output'. In this state, only the ring of the first planet set will be spun at a 1:1.33 ratio. The torque necessary to spin this small plastic gear is negligible and will likely not be felt by the boot wearer. Thus ankle motion will feel very normal.

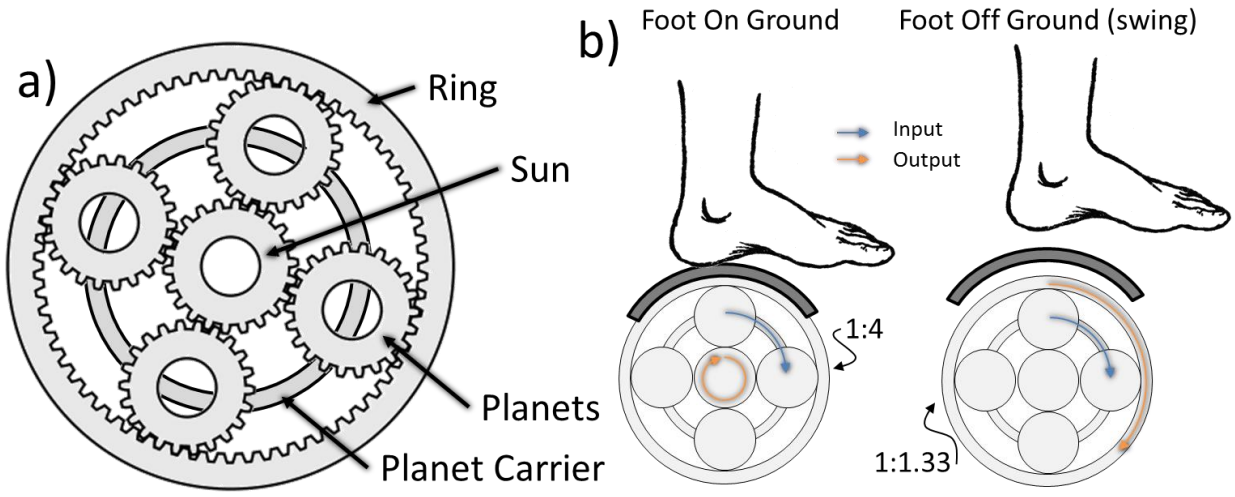

Figure 3.28 – a) Illustration and labeling of planetary gear train, b) example illustration (not to scale) of how planetary gear train will react with heel brake, allowing the mechanism to virtually disengage during swing phase.

To further illustrate this operating principal, and how it finally achieves the desired mechanism function such that energy is only harvested in the negative work phase of the stance phase of gait, Figure 3.29 was prepared. From the plot below, it is shown that the mechanism engages only when the clutch bearing and heel brake are both engaged. This is the case from approximately 15 to 55% of the gait cycle. This is exactly the performance which is desired.

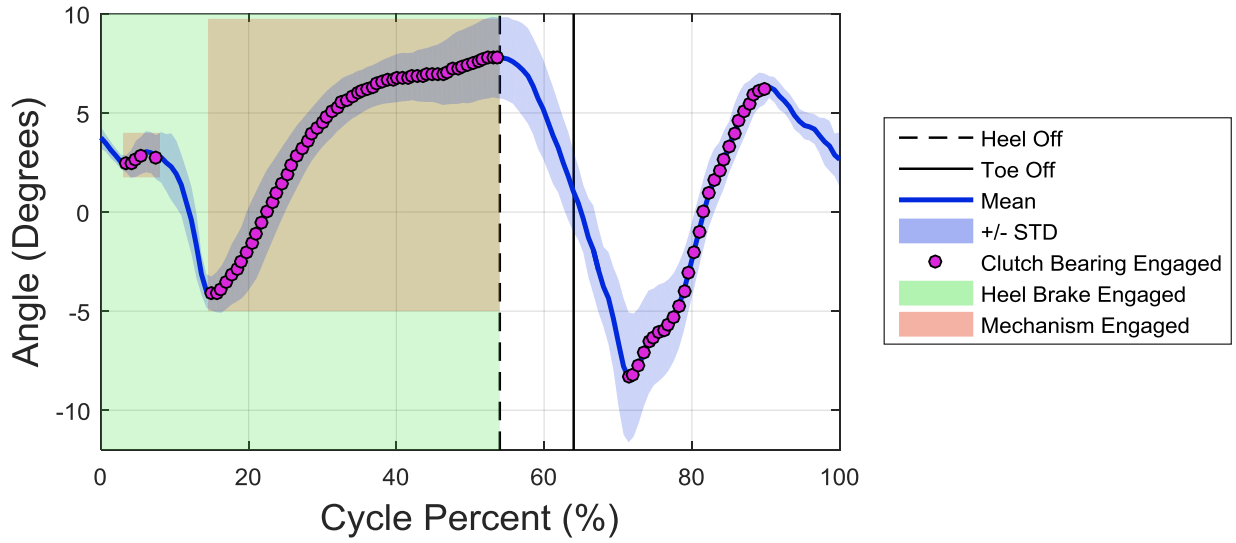

Figure 3.29 – Ankle angle rotation over one gait cycle (from Figure 3.9) with consideration of current mechanism design, highlighting when the clutch bearing would engaged, when the heel brake would be engaged, and subsequently when the mechanism as a whole would be engaged to harvest energy.

To accommodate the heel brake, the housing of the mechanism has to be changed. From Figure 3.18, one will notice that the fiberglass shank, insole, and some of the leather of the boot are between the foot and device housing. The presence of these elements of the boot would not allow force to be directly applied to a deformable part of the mechanism housing (i.e. a compression brake). To give room for, and allow the function of, addition components, the device housing was revised. The revision took place in two steps; the first was to widen the housing such that it replaced the whole boot heel section, and the second was to raise a section of the housing such that it would directly contact the insole below the heel foot. The widening of the housing was also done to allow for a new torque input strategy, discussed in that section.

With the goal of replacing the heel section with the device housing, it had to be given extra attention to exactly matching the shape of the boot, better than what was done in Figure 3.17. Therefore, it was employed a new method of producing a 3D model by stitching together many photos of an object from various angles, known a photogrammetry. To produce the photogram of the boot, 180 pictures of the boot from every angle were taken. Figure 3.30a) shows a sample picture of the setup. Here a PVC pipe of the diameter of a human calf was inserted into the boot to give the proper shape and elevate it away from other objects. Then using Autodesk Reality Capture (ReCap) services, a 3D representation of the environment captured was created. Then using Autodesk Memento software, superfluous objects were removed from the mesh, and the pipe digitally removed, leaving only the boot shown in Figure 3.30b). The program automatically overlays select textures from the pictures over the model, giving a realistic appearance. The mesh itself is shown in Figure 3.30c). Assigning a physical distance between two points on the mesh, the whole model is scaled to actual size. Unfortunately, due to the newness of this technique, the software are still in somewhat of a beta phase and the outputs of the model are only in formats conducive to 3D printing, while further 3D CAD modeling is needed to achieve a work volume for the heel shell where the harvester components will go.

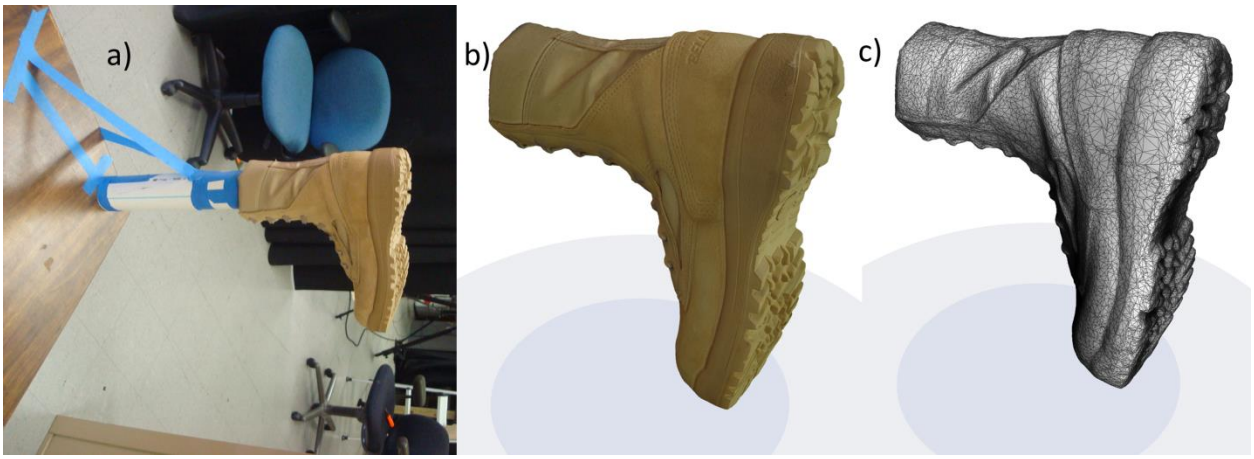

Figure 3.30 – Belleville 390 boot photogrammetry, a) photogrammetry setup b) processed model with photo overlay, c) mesh overlay.

Since the efforts in photogrammetry proved unfruitful, a model of the heel section of the Belleville 390 boot sole was created manually by taking measurements using a caliper at 5mm

increments along the boot. The measurement spacing is every 5mm in the y-direction, defined here as the axis along the length of the foot. As can be seen in Figure 3.31a), the measurement point marks appear unevenly spaced, as the boot curves in the defined x-direction along the width of the boot. The measurements are plotted in beige lines in Figure 3.31b) and c). Since the measurements were taking on a compliant boot sole, it was often difficult to get repeatable results, causing the plotted shape of the heel to be somewhat jagged, which it is not in reality. Therefore, an algorithm was written to smooth out these measurements using a moving average filter. The result of this smoothing is plotted in the black line of Figure 3.31b) and c), which much more accurately models the shape of the boot sole.

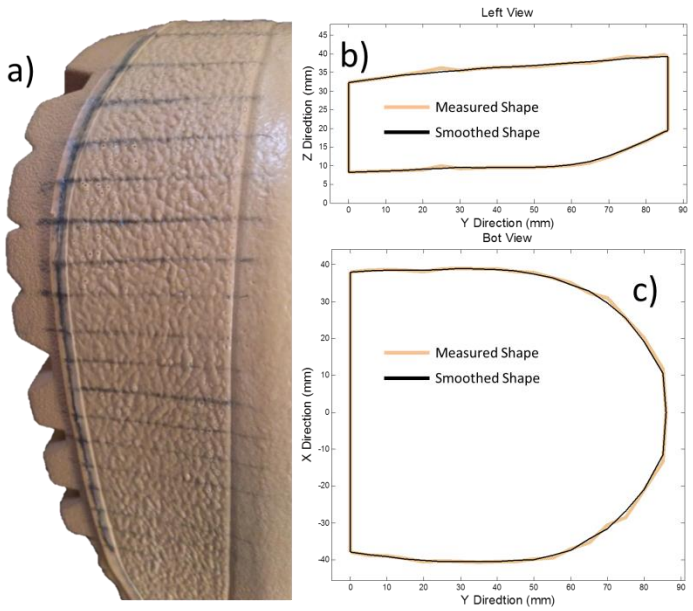

Figure 3.31 – a) Markings showing the 5mm spacing between caliper measurements of boot heel, b-c) smoothed shape of measured heel section in two planes.

The smoothed measurement values were then recreated in CAD and 3D printed. Naturally, as the new design takes the place of the entire heel sections, it is larger than previously, giving more room for energy harvester components. To validate the shape would fit the shape of the size 8 boot heel, the heel section of the boot was removed from the top of the tread to where the leather upper is embedded into the boot sole, as these were the locations measurements were taken. Figure

3.32 shows how the new designed heel shell, which fits well into the removed heel section, mimicking the preexisting shape of the boot.

Figure 3.32 – Housing Generation 2: (Left) Cross-section of Belleville 390 hot weather combat boot with overlay of cross-section of device housing size and locations, (Right) picture of 3D printed housing prototype with overlaid dimensions.

While the housing pictured above was a generation of a design, as mentioned before the housing needs to extend upwards such that it is directly below the insole and heel foot. To add this upward extension to the device housing, the foot bed of the insole was cut out, up to the point where the leather upper bonds to the midsole. Just like for the previous generation of the housing, measurements of width and depth were taking using a caliper and used to create a CAD model, which would then be 3D printed and test fit in the boot. The dimensions measured were draw in the CAD model and extruded into the existing shape. The resulting form of the housing is shown in Figure 3.33.

Figure 3.33 – Housing Generation 3: (Left) Cross-section of Belleville 390 hot weather combat boot with overlay of cross-section of device housing size and locations, (Right) picture of 3D printed housing prototype with overlaid dimensions.

The housing design shown in Figure 3.33 allows for the proposed spring winding control and torque to angle amplification strategies to be realized. With much of the focus in recent design changes given to the various other components, the generator was somewhat neglected. In housing generations mentioned thus far, the generation (a cylinder) was mated against the foremost wall of the housing. With generation 3, since the height of the housing was increased, a larger diameter generator could also be realized. A larger diameter generator, however, also pushes the rotation axis of the generator further toward to the heel of the housing, causing some interference with the placement of the other mechanism components.

The first three generations of mechanism housing all shared the common characteristic that the leading edge of the housing stopped at the place where the heel section begins to tapper into the thinner thickness of the mid and forefoot sections. The original thinking was that since the size of most of the mechanism components was governed by the depth of the housing that nothing of consequence could fit if the depth was narrowing or narrowed. Though, once focus was again placed on generator size optimization, the consideration that extending the device housing into the narrowing region of the midfoot would be useful. Since the generator itself narrows in depth moving away from the rotation axis, since it is a circle, a cylindrical bulge could be added to the

housing where the generator could be placed. In this way, the largest possible generator could be added in the most space efficient way, giving room for all other needed device components. The feature was added to the CAD model and 3D printed, and displayed in Figure 3.34.

Figure 3.34 – Housing Generation 4: (Left) Cross-section of Belleville 390 hot weather combat boot with overlay of cross-section of device housing size and locations, (Right) picture of 3D printed housing prototype with overlaid dimensions.

For all housing designs, a minimum wall thickness of two millimeters was prescribed, such that the final 3D printed build material (Stratasys VeroClear) would be sufficiently rigid and strong enough to support a person's weight. The housing for generation 4 yields the largest volume generator and most efficient use of space which has yet been theorized. A comparison of approximate generator volumes across the four generations of housing design are shown in Figure 3.35 below, with illustration of approximate generator size and location.

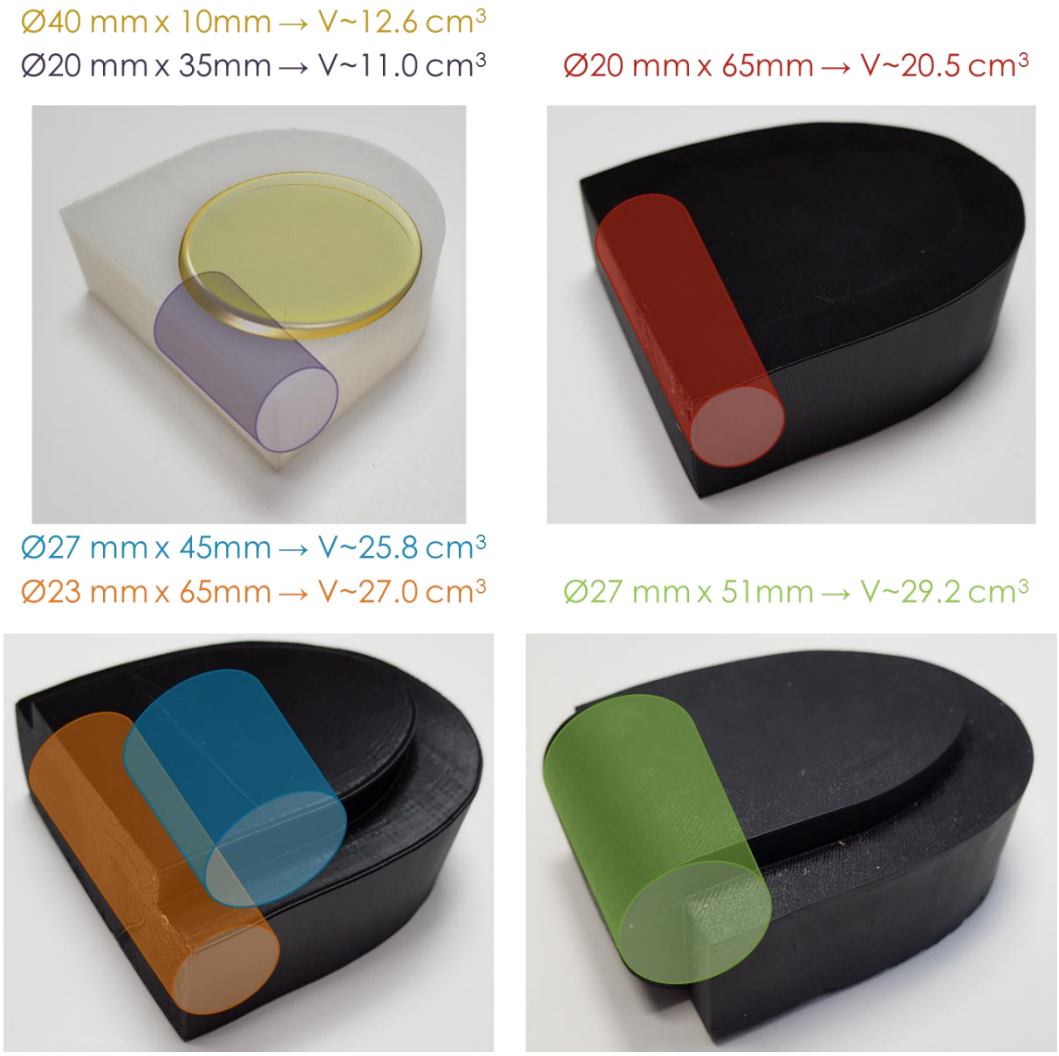

Figure 3.35 – Approximate generator volumes for the four generations of device housing. Housing generations go from; 1 top left, 2 top right, 3 bottom left, and 4 bottom right.

3.7.2 Torque Input

The functioning of the mechanism begins with torque being inputted to the primary axis. This torque comes from the talocrural joint (ankle joint) dorsiflexion during the gait cycle. This joint is an example of a hinge joint. To have an anthropomorphic design, it is therefore logical that the torque input of the mechanism also consist of a hinge joint, with pivot point and lever arm. Figure 3.36 shows the most basic realization of the hinge joint and mechanism housing. Here it is pictured a straight lever (a)), as well as a curved lever (b)) such that the lever may avoid rubbing against the tibia and fibula heads during rotation.

Figure 3.36 – Concept renderings of torque input, with a) simple straight lever, and b) more ergonomic curved lever to avoid tibia and fibula heads.

As discussed in the previous sections, torque will only be input to the mechanism during the dorsiflexion of the stance phase of gait. Therefore, some directionality must be associated with the torque input, to rectify motion. Motion rectification has been classical accomplished with a ratcheting mechanism, however, as discussed the noise from such a mechanism is not acceptable in this application. Thus, one of the key components of the design is the clutch bearing. The clutch bearing the compromise between a ratchet and a roller bearing. Though, because of its construction, motion rectification is permanent and cannot be "turned off" like disengaging the paw of a ratchet.

The clutch bearing operating principal is that it does not transfer toque in one direction (freewheel) while transferring torque (clutching) when rotated in the other direction, as seen in Figure 3.37. Moreover, the freewheel motion is what one would expect from, for example, a ball bearing, where minimal torque is transferred allowing maximal relative motion between inner and outer races. Here, the rollers are pushed up the ramp against the spring while maintaining contact with the shaft. Since the rotation pushes the rollers out of the way, they spin and slide against the shaft, allowing the shaft to spin. There is more friction associated with this motion than a ball bearing. In the clutching direction, the rollers are forced down the ramp via the rotation and spring force, pinching and locking the shaft and clutch bearing housing together, thus transferring torque.

This function is necessary for the mechanical rectification of the walking motion. Through the gait cycle, the ankle rotates back-and-forth and if the input shaft of the device where connected directly to the harvester, energy would be attempted to be collected during the positive work phase of gait, which is undesirable. This working is further illustrated in the context of the boot's torque input lever arm and primary axis shaft in Figure 3.38.

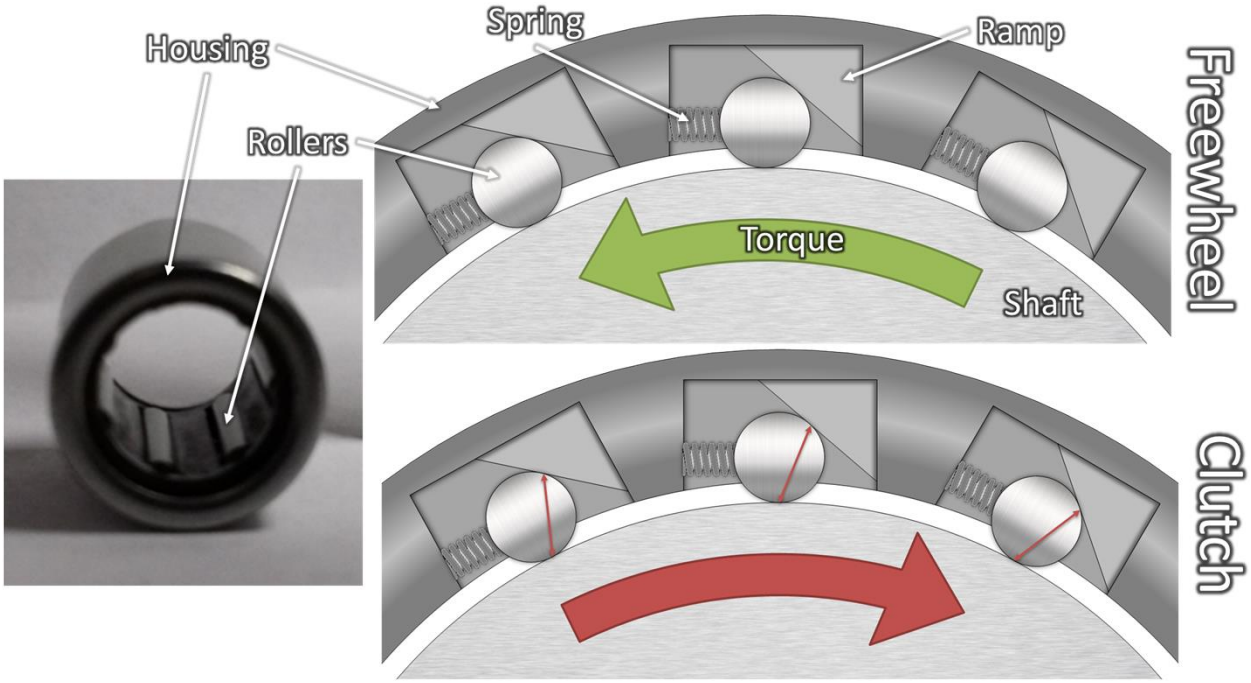

Figure 3.37 - Example of trapped roller clutch bearing with cut-away illustration of clutch bearing key parts showing how rollers are always held in contact with the shaft and housing via small springs. When rotating counter-clockwise the rollers freewheel similar to a ball bearing. When attempting to rotate clockwise, the rollers are wedged between the shaft and housing, preventing relative motion and transferring torque.

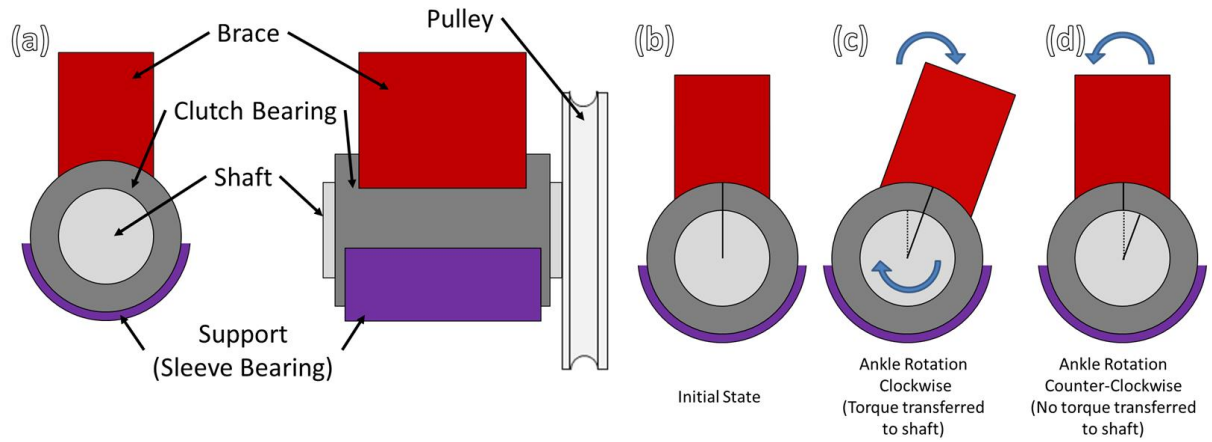

Figure 3.38 – Illustration of ankle rotation input device with (a) labeled sections in side and front views and (b-d) illustration of motion of device through one gait cycle (step).

In Figure 3.38(b), starting with the initial state where the leg is straight (i.e. perpendicular to the ground) and foot on the ground, as a step is begun in (c), the input brace is turned clockwise, engaging the clutch bearing and transferring torque, and subsequently rotation, to the shaft, upon which the first stage pulley is affixed. During this stage the step, the angle amplification section is in rotation as well and compressing the power spring, storing energy. During the propulsion portion of the step and as the foot lifts from the ground to swing forward, the ankle rotates (in this frame of reference) counter-clockwise. Now, the clutch bearing is disengaged in (d) and the input brace rotates back to its original position without transferring torque to or rotating the shaft. Therefore, the power spring is allowed to unwind into the generator, rather than be unwound by a reversal in the rotation direction of the pulley system, and placing unnatural and biomechanically unfavorable torque on the ankle.

The component structure in Figure 3.38(a) is the structure used in prototype pictured in Figure 3.23. This structure was modified for the design presented in Figure 3.25 to make it more robust. The principal change was fully encircling the clutch bearing with the input shaft for added strength, rather than having it bonded to a certain arc length. As shown in Figure 3.39, this change caused the support sleeve bearing to be moved beside the clutch bearing, rather than under it. The input shaft, which mainly supported by the sleeve bearing, it also kept collinear with the primary axis through the ball bearing connection.

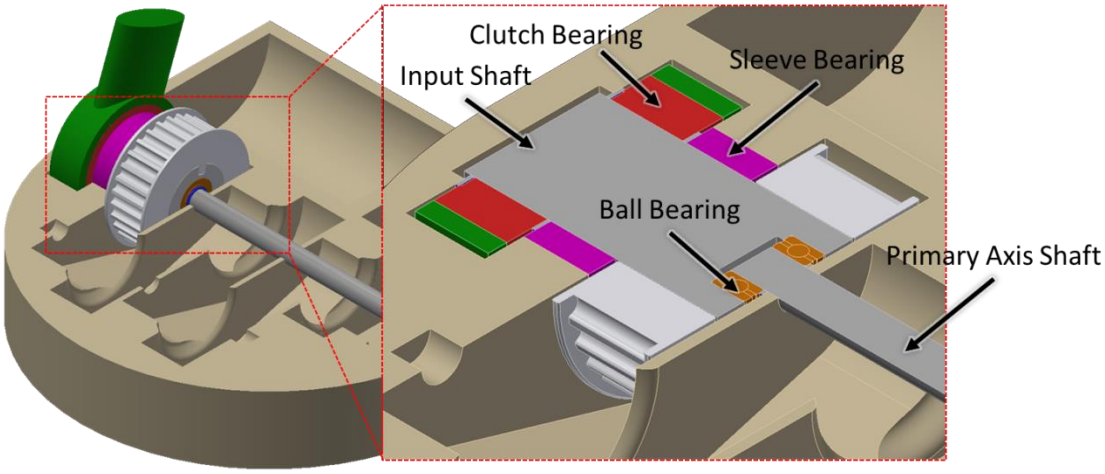

Figure 3.39 – Isolation of torque input structure from design given in Figure 3.25 with magnified half section view.

Upon additional consideration, it was found that a brace cannot simply be applied from the leg of the boot to the harvesting mechanism, because the ankle and brace would have different centers of rotation. This is to say that the brace lever and leg would follow different arc paths. Following different paths would mean the brace would move around in the boot, causing discomfort to the user, and wear to the boot. This concept is illustrated in Figure 3.40a), where the divergence of the red and blue arcs shows how the brace would have to move within the boot, which is not desirable for mechanism performance or comfort.

To address this design hurdle, concepts for the torque input to the harvesting mechanism in the sole of the boot were though up, and are shown in Figure 3.40b) and c). If the brace had a sliding joint, and was in line with the leg, then necessary change in length of the brace could be realized, as shown in Figure 3.40b). Although the centers of rotation are in line with the leg, they are in different locations. This results in the harvester input undergoing a smaller angle than the ankle actually rotates, with the disparity increasing as the ankle rotates further. As the range of motion the ankle undergoes during normal walking is already somewhat small, around 20 degrees, lessening this input rotation range is not desirable as it would need to be compensated for with higher gear ratios in the planetary gears, which is also not desirable.

Therefore, the design presented in Figure 3.40c) was thought up. This design mimics the type of design used in medical walking boots, whereby a brace segment is attached to the leg with

another segment attached to the boot sole, with a joint at the ankle. However, here add a timing belt is added from the ankle joint location which will transmit the full rotation into the input of the energy harvester in the boot sole. This design does however necessitate the use of components external to the existing boot outer layer as the timing belt will not fit within the boot upper and must therefore parallel it on the outside. A heel cup is also necessary to support the hinge joint, as shown. Here, the entire heel section will be replaced, rather than the harvester imbedded into a cavity in the sole. This is the best design from a functionality standpoint; however, the boot will no longer give a completely 'normal' appearance. The appearance will not be drastically changed, but alterations will be noticeable. However, the performance merits of using this design outweigh the slight aesthetic changes.

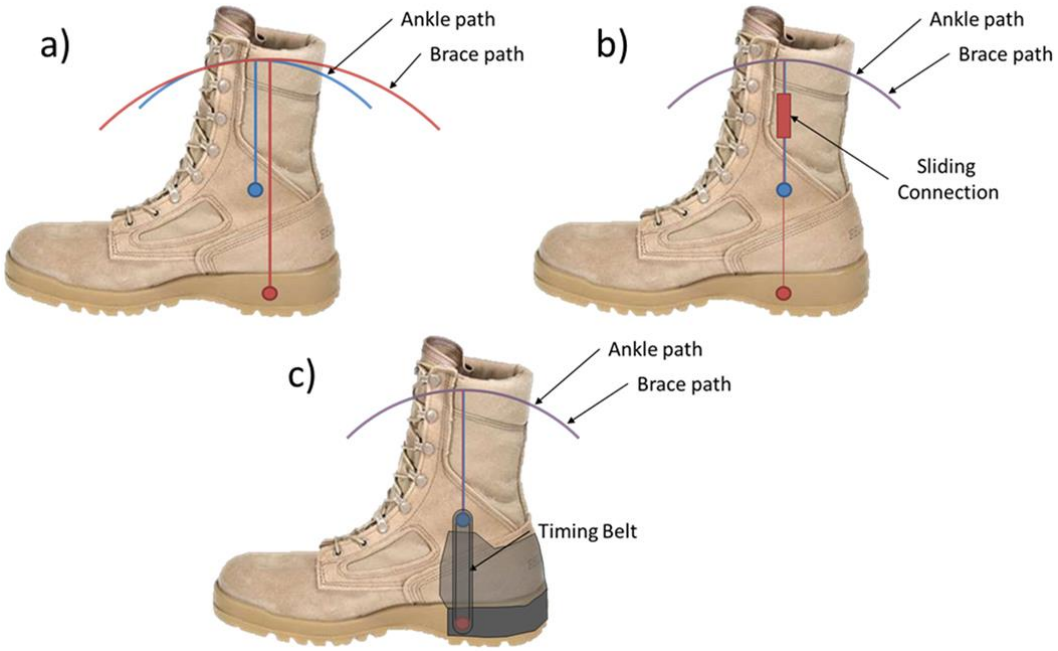

Figure 3.40 – a) Illustration of brace and ankle/leg motion path of current design, b) sliding brace and altered rotation point to bring motion paths together, c) use of timing belt and shorter brace to bring motion paths together.

3.7.3 Angle Amplification

The torque conversion sections controls the amplitude and winding timing of the power spring. As discussed in the previous section, a one-way clutch connects the torque input to the angle amplification section when ankle angle becomes smaller, as shown Figure 3.27.

The principal method for altering rotation speeds is gearing. After examining several gearing configurations, it was determined that achieving the initial desired ratio (1:36) would best be accomplished using a few smaller ratio compound gears stacked together rather than one large gear set, which would be impractical. A compound gear is a combination of a larger diameter gear and a smaller diameter gear in one. This decision was made largely in the interest of space, as a straight 1:36 gear would not be able to fit within the dimensions of a boot heel. Figure 3.41 below gives an example of such a gear train. The example shows how three compound gears can be arranged to make a larger gear ratio. Based on the size requirements for the thickness of the gears, between 3-5 gears can be stacked, like in the example, and fit within the boot sole of the first generation design shown in Figure 3.18. Since the desired gear ratio is 1:36, if three compound gears would be used, each gear would need an approximately 1:3.3 ratio, as in the test gear set produced and shown in Figure 3.41(a).

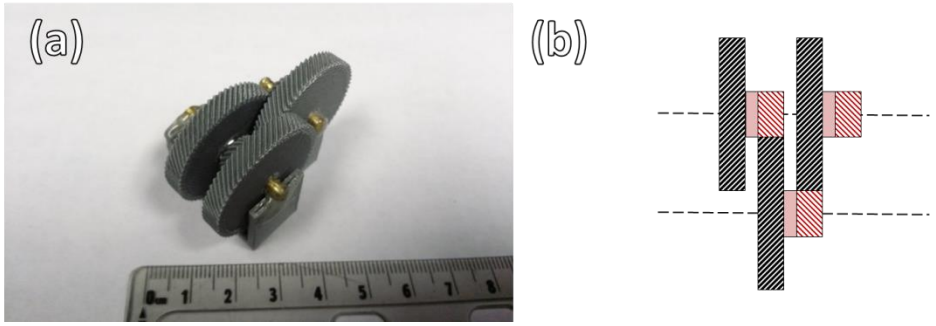

Figure 3.41 – (a) 3D printed example of compound helical gear train, shown schematically in (b).

In the interest minimizing the noise from the gears, an involute and helical profile of fine pitch was chosen for the gears so that they have the smoothest possible contact surface, thus reducing noise. Normally, such gear profiles are reserved for more demanding applications (e.g. automobile transmission) as they are difficult to produce. However, the gears in Figure 3.41(a) were 3D printed, so the gear profile was realized without outside tooling. As is illustrated in Figure 3.41(b), the gears alternate axes. In this way, the design becomes more compact. To incorporate this design it was only necessary to insure that the gears rotate freely about their fixed axis of rotation, allowing them all to spin at different rates.

It should also be noted that the test gear train was created at roughly double the scale of what will be used in the final prototype. At this stage, larger components are used so that they are

easily worked with. This scale of test stand was also chosen because all the parts used are also available or capable of being manufactured on the scale of the smaller final prototype. It is the intention to continue to produce the other stages of the design at this scale to illustrate and examine the functions of the concept design.

Despite using a favorable gear profile for noise reduction, it became evident after the gear stage prototype was built, that an undesirable amount of noise is produced from the gears, and there is no room in the final design (due to its compactness) for sound absorption material. It is forethought as discussed earlier that soldiers would not wear boots which emitted extraneous amounts of noise, as this would compromise their ability to move with stealth, or in general be annoying. It was then I sought an alternative to gearing.

This alternative comes in another form of torque transfer technique; the pulley. Pulleys are usually employed in cases where a complex set of rotations need occur or the rotation axes are comparatively far apart. Pulleys are, however, limited in the amount of torque they can transfer as they rely on friction and tension to transmit forces. As was discussed previously, there are several types of pulleys, illustrated in Figure 3.21. The round belt was also chosen initially for its unique ability to connect two perpendicular pulleys, as the pulley profile is the same in all directions. This characteristic is of importance because the rotation of the ankle will be in the vertical plane relative to the ground. To achieve the desired gear ratio, in the initial design of the mechanism, called for the pulleys to be horizontal in the boot sole. This layout is illustrated in Figure 3.42.

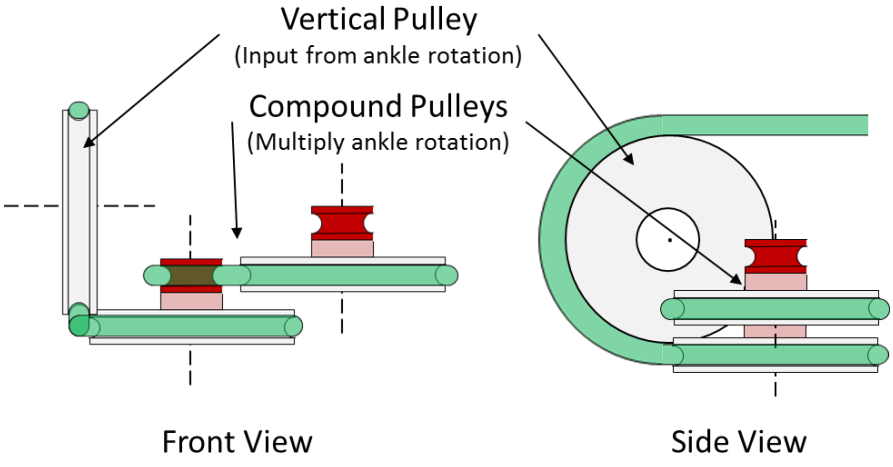

Figure 3.42 – Illustration of vertical to horizontal compound pulley connection.

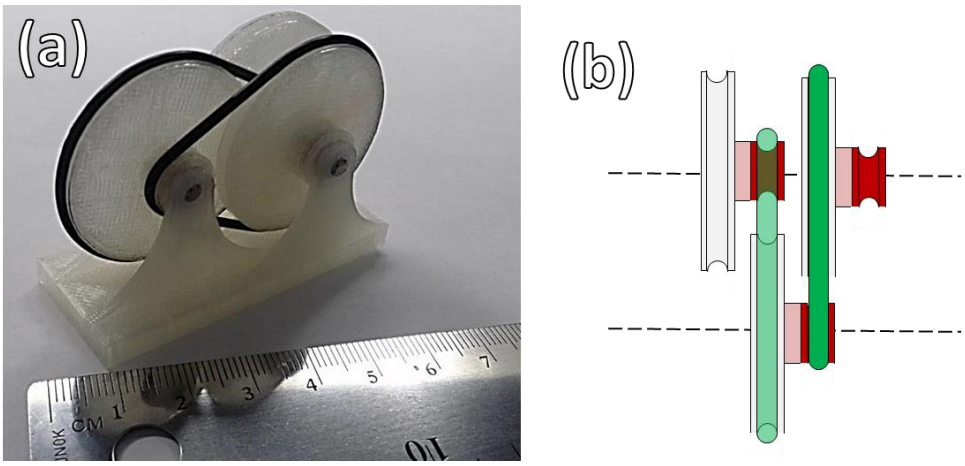

Figure 3.43 – Compound pulley test component with (a) constructed prototype and (b) illustration of pulley and round belt orientation.

Mimicking the alternating axis compound design used with the previous gear train (Figure 3.41), the pulley design implementation was constructed again using 3D printing, shown in Figure 3.43. Here, the pulleys are 35 mm in diameter, with the neoprene round belt being 1/16 inch in diameter. The compound pulley design has a ratio of 1:3.3 for each stage, totaling to 1:36 for the three stages.

Next, a CAD model was designed for this input section with the key criteria of it integrating into the existing pulley section test stand. The outer ankle pulley (outer vertical pulley in Figure 3.44), is connected to the shaft via epoxy bonding. The inner ankle pulley rotates freely about the shaft and is there solely to reroute the pulley belt from first stage of the angle amplification pulleys round the riser pulley and back to the outer ankle pulley. The riser section was necessary as the ankle pulleys were taken to be the same side as those in the amplification section. Thus, since it is mounted vertically, was taller than combination of the depth of three of the amplification pulleys. The riser is a design afterthought, essentially, and will be sought to be eliminated in the next iteration of this design.

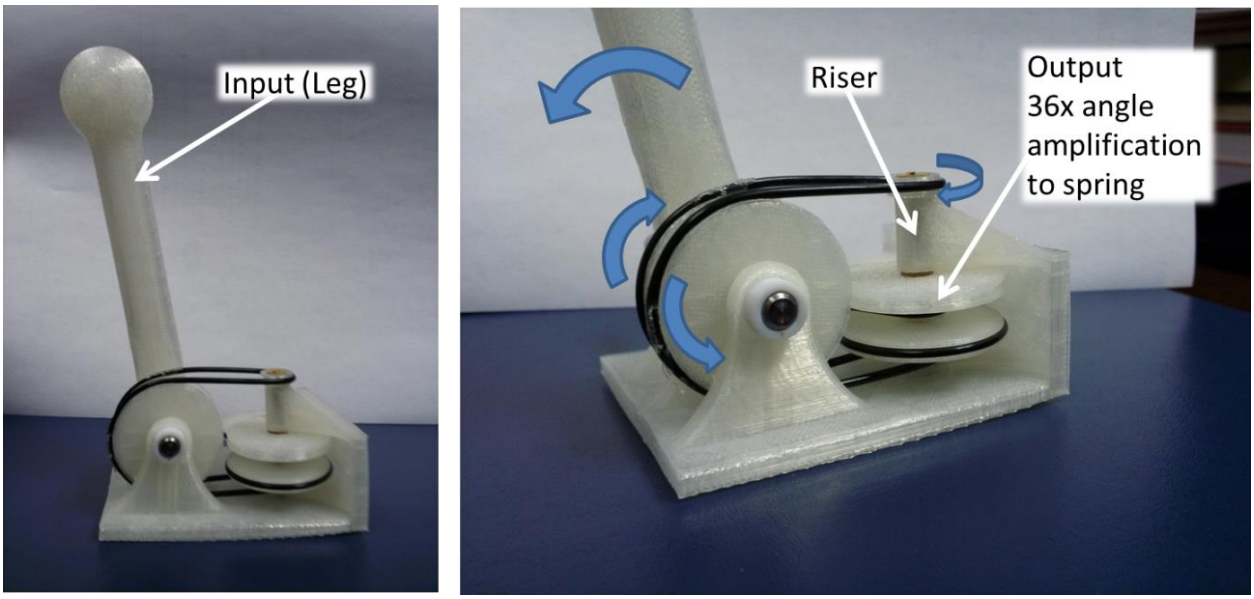

Figure 3.44 – Fabricated combination input and angle amplification test stand.

To better incorporate the input and amplification sections together, the individual gear ratios of the compound pulleys will be reduced. In this way, the ankle pulley will be made smaller in diameter (shorter) and will cause the number of pulleys in the amplification to increase to either four or five. The advantages of this will be twofold. First, by making the pulley ratios smaller, the pulley belt will be in contact with the smaller section of the compound pulley over a larger angle, increasing grip and reducing the likelihood of slipping. Secondly, making the overall footprint of the pulleys smaller lends itself to better fit into the final design embedded in the boot heel.

From examination of the current design, it appears that slipping of the pulley belt may be a larger issue than previously anticipated. In the next iteration it will be examined how to increase the grip of the pulley by either increasing the diameter of the pulley belt (currently 1/16 inch), choosing a different pulley/belt material (currently belt: neoprene, pulley: PLA) or adopting a crisscross belt pattern in the pulley. Rather than run the pulley belt from the top of one pulley to the top of the next pulley, the belt can be run from the top of one pulley to the bottom of the next. This strategy, **Figure 3.45**, makes it so that the belt is in contact with the pulleys over a larger angle, increasing grip.

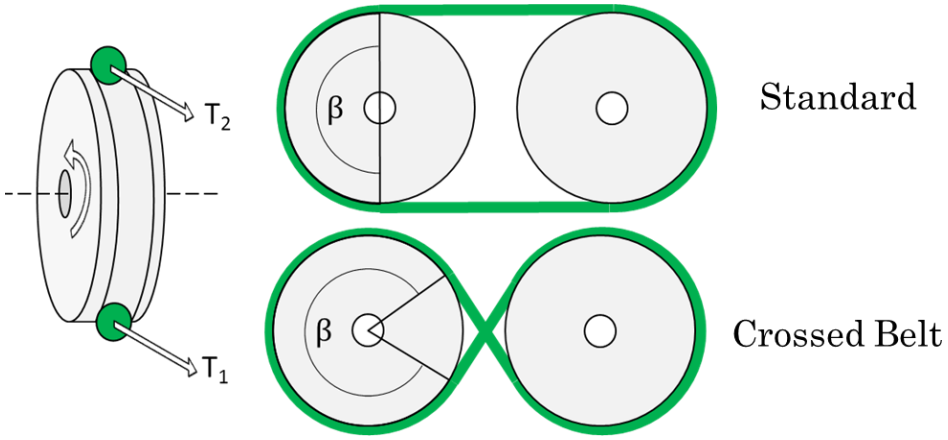

Figure 3.45 – Illustration of standard and crossed belt pulley configurations, and subsequent contact angle.

The "grip" of the pulley is realized in the torque transferred, or the difference in tension in the belt between the ingressing and egressing sides of the belt. Tension is higher in the ingressing side of the pulley and less in the egressing side, which is why it is sometimes called the "slack" side. If we call the T_2 the tension in the ingressing side of the pulley and T_1 the tension in the egressing side, then the ratio of these tensions, akin to the torque transferred, is,

$$\frac{T_2}{T_1} = e^{\mu\beta} \quad , \tag{3.1}$$

where μ is the coefficient of friction between the belt and pulley, and β is the contact angle or angle over which the belt is in contact with the pulley. The contact angle is determined by the design of the pulley. For example, Figure 3.45 shows that for two pulleys of equal diameter in a normal configuration has a contact angle of 180 degrees. For a particular separation distance of the pulleys, the contact angle is increased to 235 degrees in a crossed belt configuration. This 30% increase in contact angle would result in a 74% increase in possible torque transfer. It has therefore been a keen focus on getting the design of the pulleys just right, as large increases in performance can be realized.

If the pulleys are of a different size, however, the contact angle is less obvious. The contact angle for pulleys of different sizes is of concern to this application, as to achieve a gear ratio and subsequent rotation speed amplification, it is necessary that the pulleys be of different sizes. Of greatest concern is the contact angle of the smaller pulley. As shown in Figure 3.46, the contact

angle of the smaller pulley is less than 180 degrees. Thus, the smaller diameter pulley will be the weak link, and is where slippage would occur should too great a torque attempt to be transferred.

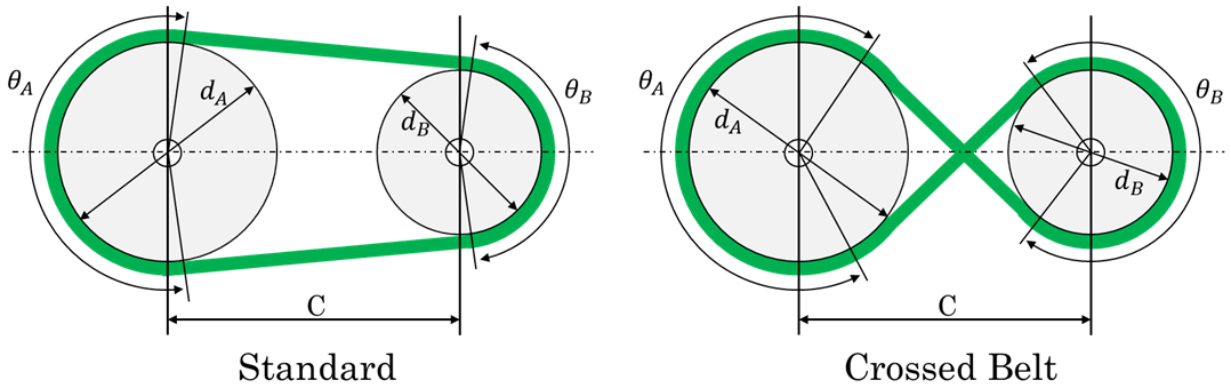

Figure 3.46 – Illustration of standard and crossed belt pulley configurations, with contact angles considering pulleys of different sizes.

For the standard configuration, the contact angle for the larger and smaller pulleys, θ_A and θ_B, respectively, as well as, the overall length of the belt, L, can be found as,

$$\theta_A = \pi + 2\sin^{-1}\left(\frac{d_A - d_B}{2C}\right) \quad , \quad \theta_B = \pi - 2\sin^{-1}\left(\frac{d_A - d_B}{2C}\right) \tag{3.2}$$

$$L_S = \sqrt{4C^2 - (d_A + d_B)^2} + \frac{1}{2}(d_A\theta_A + d_B\theta_B) \quad , \tag{3.3}$$

for a given center distance, C. By contrast, for the crossed belt design, the contact angle and length of belt for the crossed belt configures are found by,

$$\theta = \pi + 2\sin^{-1}\left(\frac{d_A + d_B}{2C}\right) \tag{3.4}$$

$$L_{CB} = \sqrt{4C^2 - (d_A + d_B)^2} + \frac{1}{2}(d_A + d_B)\theta \quad . \tag{3.5}$$

Regardless of the relative size of the two pulleys, the contact angle of either pulley is the same.[171]

It is obvious that using the crossed belt configuration yields a significant increase in available torque transfer, as the torque transfer is exponentially proportional to the contact angle. However, in the crossed belt configuration, the belt is in interference with itself and rubs together in the middle area between pulleys, drastically increasing friction in the system. The trouble with simply crossing the pulley belt is that in the middle of its path, the belt overlaps and is traveling in

opposite directions, as shown in Figure 3.47, creating performance dimensioning friction. This effect can be minimized by using a "slippery" belt (such as nylon), however, this then reduces the torque which can be transferred, by affecting the coefficient of friction, μ. It was then considered a more behooved endeavor to find a way to separate the pulley belt as it crosses.

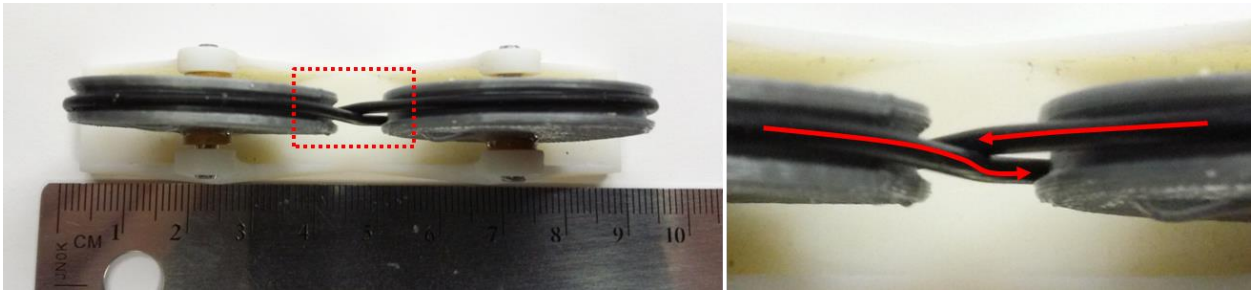

Figure 3.47 – Crossed belt pulley with highlighted center belt interference.

To counteract the rubbing interference of the crossed belt configuration, a novel pulley design aimed at allowing then crisscross pattern but evading the interference is explored. It was proposed that spiraling the belt profile around a thicker pulley with a pitch of one belt diameter per revolution, that it would be possible for the crossed belt to be separated. This concept pulley is shown in Figure 3.48a). After evaluation of this concept pulley (3D printed pulley shown in Figure 3.48d) in the test stand in Figure 3.49a), it was found that for the position in which it was drawn, the belt is separated, however during the phase of rotation where the pulley is rotated 180 degrees from its initial position, the belt again interferes with itself. It was next examined if having a reverted spiral (i.e. a spiral which reverses pitch direction at the end of a pitch length) that the belt could be guided past itself. This concept is rendered in Figure 3.48b) and 3D printed prototype shown in Figure 3.48d). Evaluating this concept in the test stand (Figure 3.49b)) showed that the pulley belt would not interfere for one revolution, but after which would not follow the guides back to its original state. Also, the designs still caused some interference when rotating, during parts of the cycle. A third attempt, rendered in Figure 3.48c, will seek to wrap the belt around a pulley channel two belt diameters wide, which a contact angle of greater than one and a half revolutions.

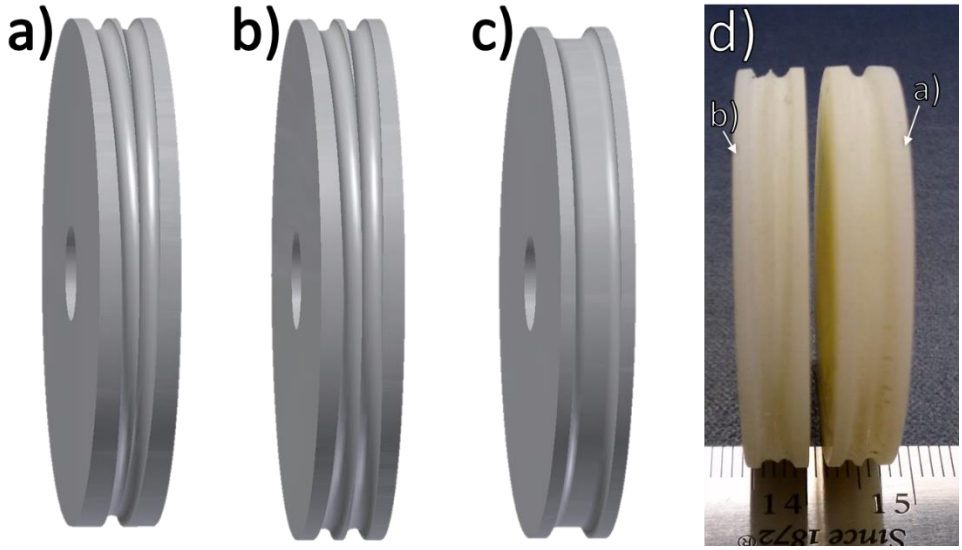

Figure 3.48 – First crossed belt interference elimination pulley concepts.

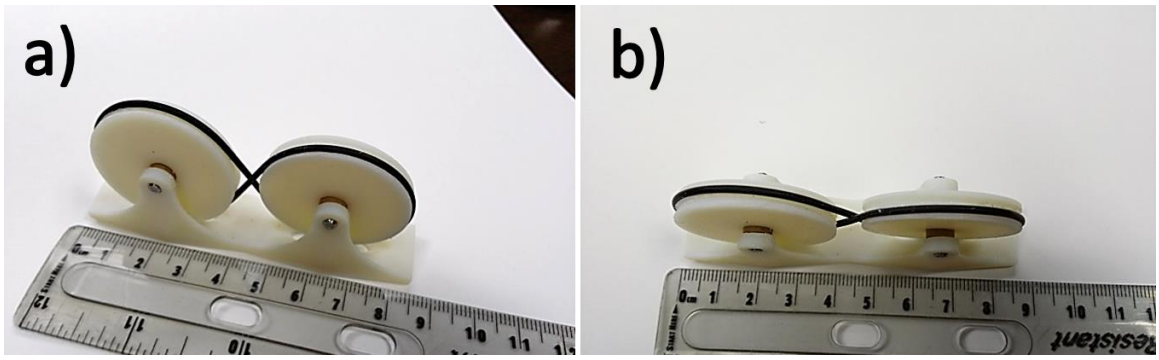

Figure 3.49 – Concept pulleys in test stand: a) corresponds to the concept pulley in the rendering of Figure 3.48a) and b) corresponds to Figure 3.48b).

The design of Figure 3.49c), given in more detail in Figure 3.50, keeps the belt from rubbing during the entire cycle, unlike the first two prototypes. Although, it is now the problem that the belt essentially pushes itself off of the pulley. This stems from the wrapping of the belt around the pulley producing a screw-like action, sliding the belt across the pulley. In this way, the belt either ends up falling off of the pulley, or stacking on top of itself. When the belt stacks on top of itself, energy is stored in stretching the belt, which is not desirable as when energy is being stored in the belt it is not going toward turning the pulley train, and ultimately not turning the power spring. In any event, the pulley can now transfer much more torque, as the belt has a large angle of contact. What's more, this contact angle is the one given in Equation (3.4) plus 360

degrees, as the belt wraps around pulley an extra time, giving a theoretical extra nearly order of magnitude more possible torque transfer.

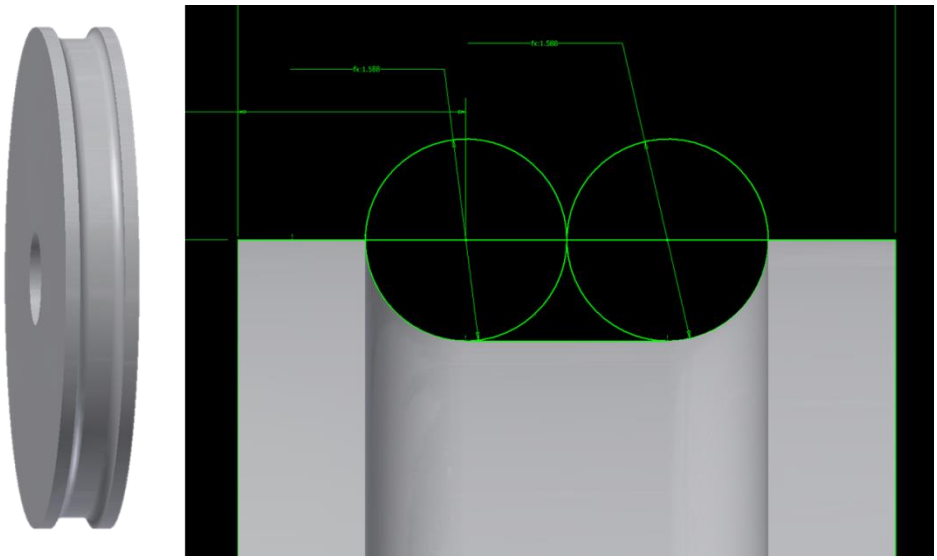

Figure 3.50 – Version 3 of crossed-belt pulley design (Flat).

To address the undesired migration of the pulley belt in Version 3 of the design, a pulley wheel profile was made that separated the belts slightly and added in a linear slant, such that the belt section of the lower pass of the belt was one belt radius below the upper pass of the belt. Because of this orientation, the upper pass of the belt will push the lower pass in opposition of the direction the belt would naturally migrate during rotation. Therefore, the belt will stay in place within the walls of the pulley wheel. This design functions nicely, and is shown in Figure 3.51.

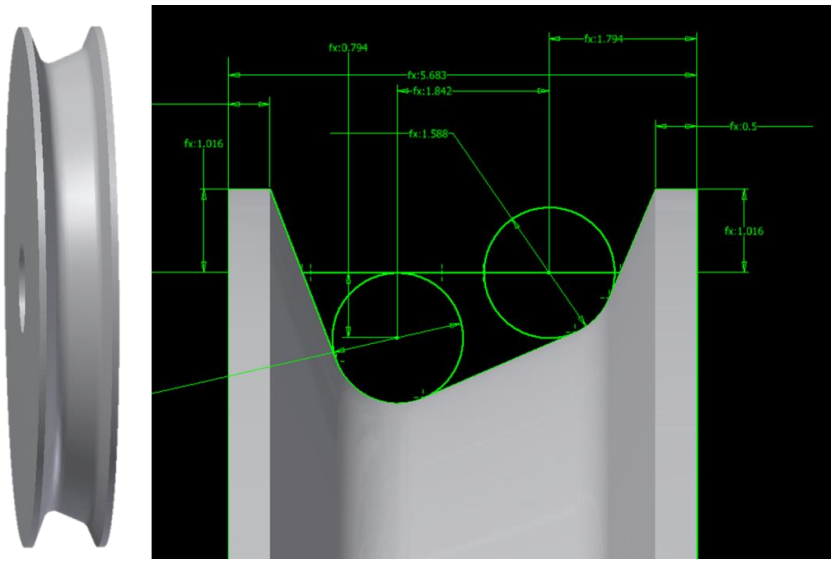

Figure 3.51 – Version 4 of crossed-belt pulley design (Linear Slant).

It was next examined the effect of the slant angle on the ability to keep the belt in position. In Version 4, the belts had an overlap of half the belt diameter, meaning that the slant angle in that case was 30 degrees. Several more pulleys of a similar art were 3D printed as is shown in Figure 3.52. The slant angles chosen ranged from 5 to 30 degrees. The pulleys were then mounted in the crossed belt configuration on the test stand and qualitatively examined for rotation performance. Here it is found that a slant angle of 15-20 degrees is optimum.

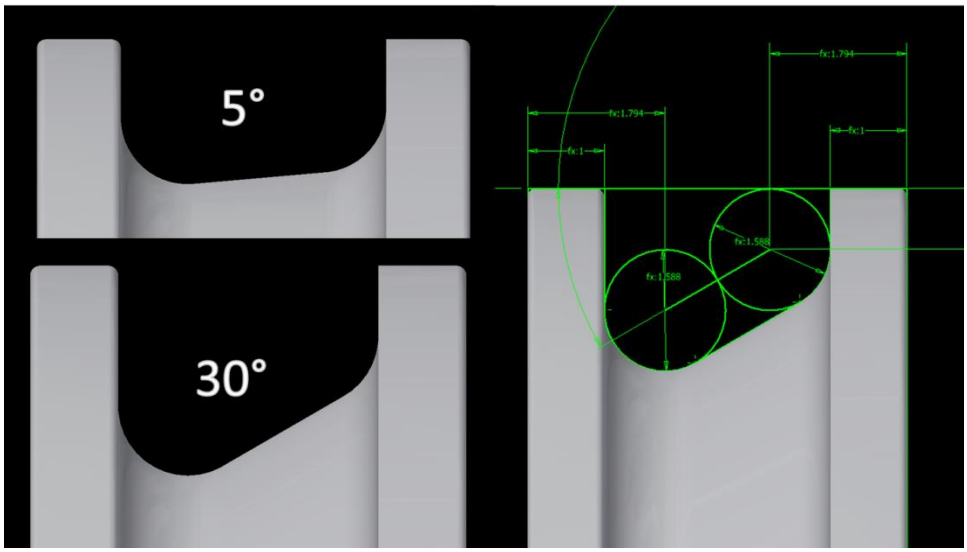

Figure 3.52 – Parametric analysis of crossed-belt pulley design (Version 5).

While version 5 solves the problem of the previous versions, a new one arises. When the pulley crosses from one side of the wheel to the other it pinches the egressing belt section. While this interference is less severe than that of the simple crossed belt, given in Figure 3.51, it should still be eliminated to have the best possible performance. The egress interference is shown in **Figure 3.53**. The belt enters onto the pulley at point 1 and wraps around to the back of the pulley at point 2. It reemerges at point 3 and crosses over to point 4 where it again goes to the back side. Then, at point 5, egress occurs. It is as the belt goes from point 3 to point 4 that it pinches the egressing belt section at point 5.

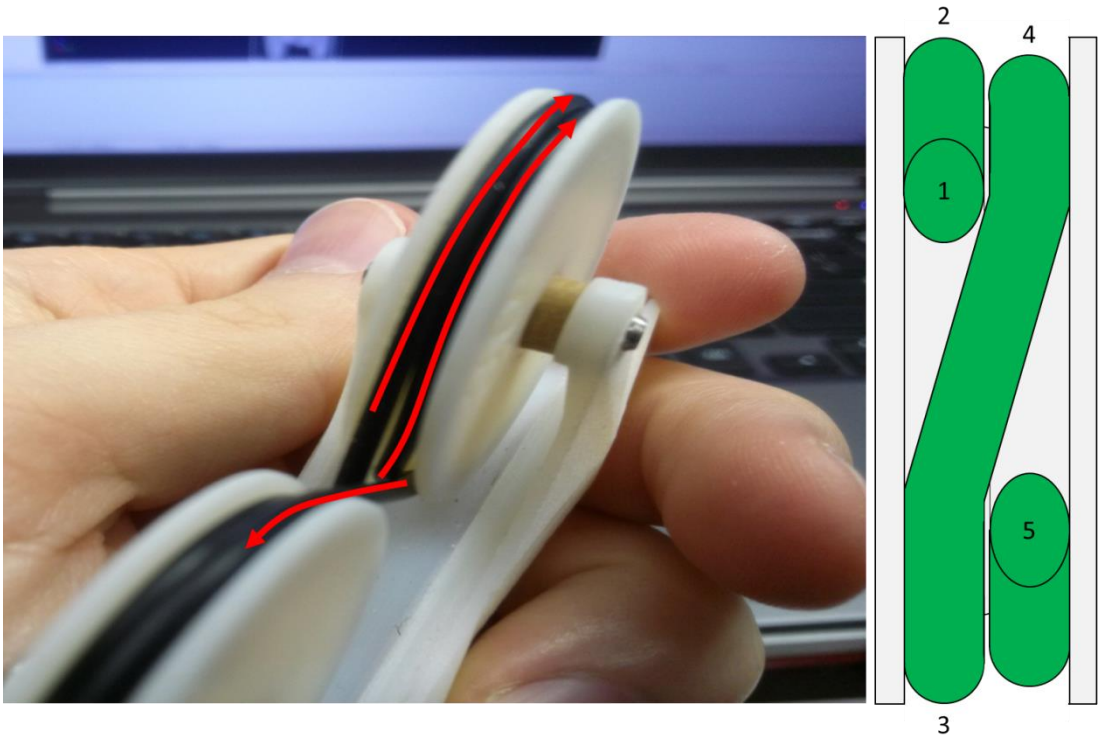

Figure 3.53 – Illustration of pulley belt egress interference in Version 5.

To address this pinching effect, versions 6 and 7 were created with varying types of spline functions, defined by different belt location parameters. This was done in an attempt to delay when the belt crosses from the high side to the low side, thus avoiding the severity of the pinching effect. The designs had varying degrees of success, with some even preventing the cross over from high to low, which is undesirable. Some of these designs are shown in Figure 3.54. What was leaned from these versions was that the belt cross over was not sensitive to the spline shape, but more

influenced by the subsequent addition of belt cross-section contact angle with the upper belt section. This addition of contact surface, compared to the linear slant is very favorable. While the equation for torque transfer of pulleys, Equation (3.1), is not explicitly related to contact surface area (there is no term for such a parameter in the equation), the contact surface area does influence the coefficient of friction and the torque transfer is exponentially related to the coefficient of friction. It was thus sought to maximize this holding angle, as it was named, but not to the point where the belt no longer naturally crosses over from high to low sides of the pulley. In addition, since the cross over is delayed, it should thus happen faster, meaning a sharp slant should occur, to encourage rapid cross over. With these in mind, version 8 was designed and is rendered in Figure 3.55.

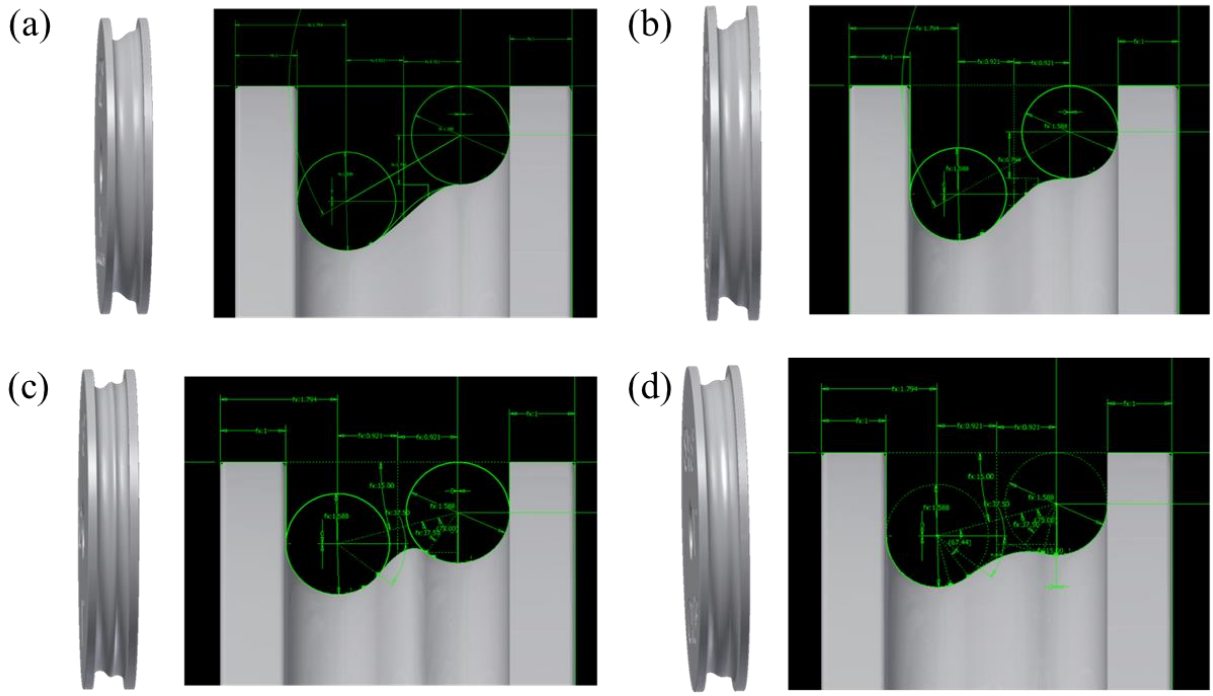

Figure 3.54 – Version 6 (a)-(b) & 7 (c)-(d) of crossed-belt pulley design utilizing various spline definitions, based on belt position parameters

Version 8 features a defined holding angle and short spline which mates tangent to the slant angle at the center point between the belts. In this way an optimum holding angle can be realized and the abruptness of the spline encourages rapid cross over after the delay. Holding angle was varied across several values, where it was found a holding angle of 10 degrees worked quite well.

Of note is that some degree of pinching still occurs, as it is inherent to the design. However the great increase in available torque transfer and subsequent eliminate of slippage makes this minor increase in friction acceptable. For the version 8 pulley, it was found that a slant angle of 20 degree and holding angle of 10 degree was the best design.

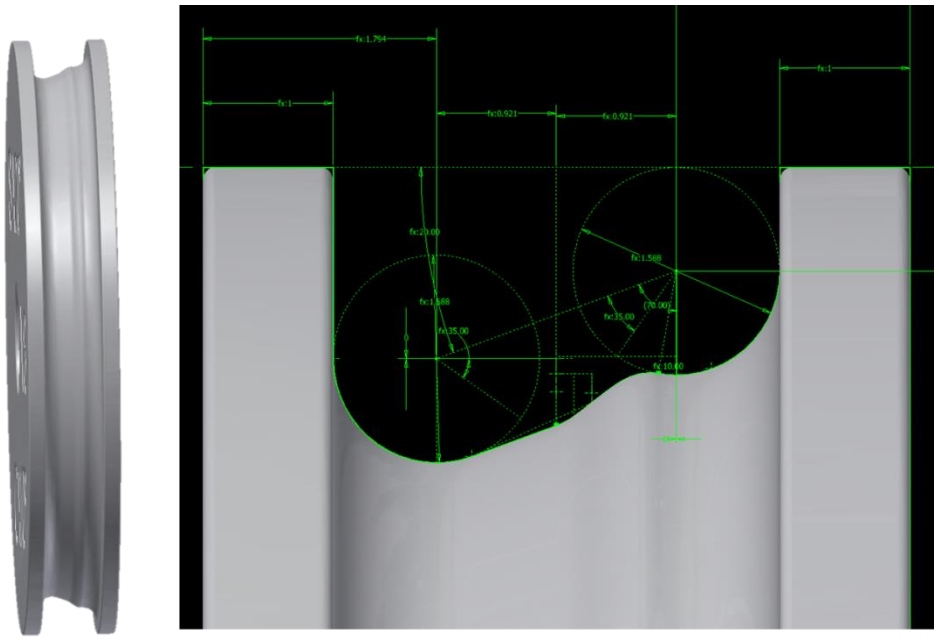

Figure 3.55 – Version 8 of crossed-belt pulley design (Holding Angle).

Though the design study of the pulley yielded a fantastic improvement in round belt pulley design, capable of transferring an order of magnitude more torque, with the decision to keep all rotation axis parallel, going from the design philosophies of Figure 3.19 to that of Figure 3.20, the need for a round belt pulley became less pertinent, due to removal of the need for a pulley which could easily change rotation axis. With the pulleys now being mounted in such a way that their diameter would be constrained by the depth of the device housing, they are considerably smaller in diameter than if they were mounted with their rotation axis perpendicular to the ground. As mentioned before, while the absolute area of contact between the pulley and belt is not captured in the simplified model of pulley torque transfer in Equation (3.1), it does affect the coefficient of friction. When making the pulleys smaller, the coefficient of friction dropped to the point where they were not longer effective.

At that time, the timing belt pulley was evaluated. Since the timing belt has teeth, it does not rely solely on friction to transfer torque, but also the grip of the teeth, and can thus transfer much more toque inherently. Since several teeth are engaged in pulley as the timing belt wraps around it, illustrated in Figure 3.56(a), there is less noise generated than that of a traditional gear, where only one tooth is engaged at a time. The timing belt is constructed from neoprene or similar material with embedded fiberglass strands in the base, shown in Figure 3.56(b). The fiberglass strands ensure the rigidity of the belt in tension along the strand direction, while retaining flexibility. The most common timing belt tooth profiles mimic traditional gear teeth, however, there are newer design using rounded tooth profiles, such as the GT2 profile manufactured by Gates (shown in Figure 3.56(c)), which is shown to run quieter than a traditional design, like the MXL.[172] Thus the GT2 type timing best was used in most of the timing belt pulley applications, like that discussed in Figure 3.25.

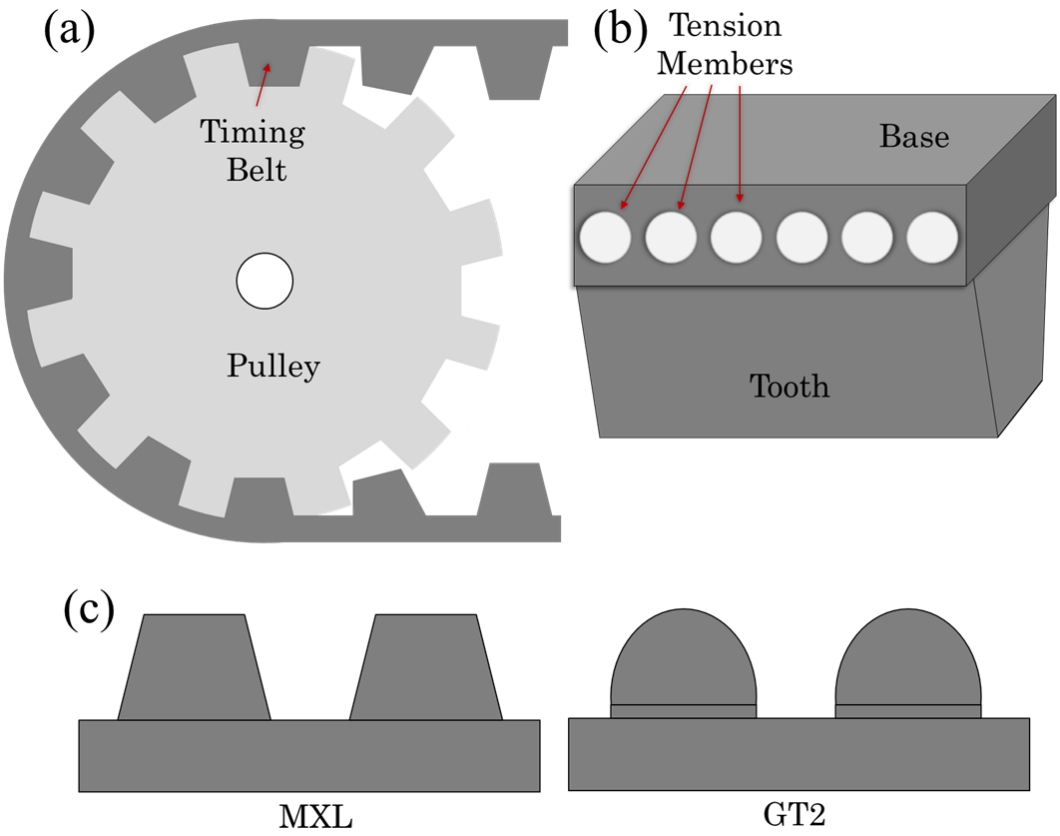

Figure 3.56 – Illustrations of (a) timing belt and pulley, (b) cross-sectional view of timing belts showing tension member cords, and (c) two common types of tooth profile.

Though, as was mentioned when discussing Figure 3.23, there is a limit to the torque which can be transferred with a timing belt, which is a function of the number of teeth engaged in with the pulley and the tensions of the belt. Then, as illustrated in Figure 3.27, using the timing belt, or pulleys or gears for that matter, would not produce the desired behavior and means of disconnecting the angular amplification section from the ankle torque is needed. Additionally, as discussed previously, as in Figure 3.29, planetary gears can yield the desired performance.

Epicyclic gear trains (planetary gears) have a set of criteria for meshing or when all the gears will work together.[173] The principal criteria is that all gears have the same module, or number of teeth per unit length. This is the only mesh criteria for regular spur gears, however, since there are more than two gears to a planetary gear setup, more conditions must be met. The different parts of the planetary gear configuration are labeled in Figure 3.28, but are given in Figure 3.57 below with several labeled parameters used to calculate the meshing criteria.

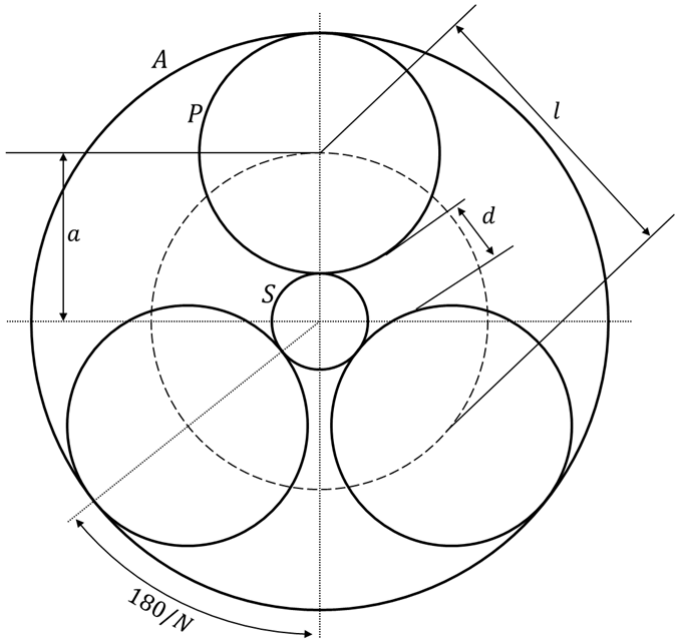

Figure 3.57 – Illustration of epicyclic gearing with several labeled parameters. A is the diameter of the annulus (or ring) gear, P is the diameter of the planet gears, S is the diameter of the sun gear, with $z_{A,P,S}$ being the number of teeth of the annulus, planets, or sun.

For the second criteria, the sum of the number of teeth in the ring gear and the sun gear when divided by the number of planet gears, N, must result in a whole number, K.

$$\frac{z_A + z_S}{N} = K \tag{3.6}$$

The number of teeth in the planet gears is then fixed as,

$$z_P = \frac{z_A - z_S}{2} \tag{3.7}$$

Of tertiary criteria is the maximum number of planet gears. In general, more planet gears give smoother performance. Though it is more efficient to keep the sun and planet gears close to the same size. The maximum number of planets is governed by the condition that the planets not interfere with each other, plus some spacing, or,

$$l = P + d \tag{3.8}$$

where,

$$l = 2a \sin\left(\frac{\pi}{N}\right) \tag{3.9}$$

resulting in,

$$N = floor\left(\frac{\pi}{\sin^{-1}\left(\frac{P+d}{2a}\right)}\right) \tag{3.10}$$

Three planet gears are standard for stability, but more may be used if space allows, according to Equation (3.10), though a minimum of one planet is all that is necessary. A calculation table was developed to find possible configurations and is displayed in Figure 3.58, which takes into account the criteria given above. Here, the module of the gears is 0.5, which is somewhat of a small tooth size, but allows for a fine pitch such that there is little play and thus less wasted motion in the gear train. A finer pitch is also good for lessening noise generation. The table was generated by first defining the number of teeth in the ring gear. This defines the overall size of the planetary gear set as limited by the depth of the boot housing. Note, the diameter, A, is the pitch circle diameter, though the extra thickness to complete the gear profile and extra thickness to add rigidity to the ring gear means that effective diameter of the planetary gear set greater than A, which was set to the maximum possible size to fit in the boot housing. Then, the number of teeth in the sun gear are iterated as shown, which then sets the number of teeth in the planet gear(s). Since the gear module is 0.5, only every other addition of teeth to the sun gear yields a whole number of teeth in the planet gear(s). The minimum planet spacing, d, was set to 1 mm.

With the geometry of the planetary gears known for each configuration, the performance of the gear train can be calculated. Figure 3.58 considers the case where the ring gear is held

stationary (the case when the harvester is engaged) and thus the velocity of the ring gear (annulus), Va, is set to zero. The planet carrier is then chosen as the input member and thus has velocity, Vc, of unity. Of principal consideration is the velocity ratio of the sun gear, which will be output. The velocity ratio of the sun gear is found by,

$$V_s = \frac{A+S}{S} \quad . \tag{3.11}$$

Of lesser consequence is the velocity ratio of the individual planets, but is found by,

$$V_p = \frac{A}{P} \quad . \tag{3.12}$$

	mod	0.5										N		
A	zA	P	zP	S	zS		Vs	Vc	Vp	Va	R	3	4	5
17	34	7	14	3	6		6.67	1	2.43	0	0.43			
17	34	6.75		3.5	7		5.86	1	2.52	0	0.52			
17	34	6.5	13	4	8		5.25	1	2.62	0	0.62	OK		
17	34	6.25		4.5	9		4.78	1	2.72	0	0.72			
17	34	6	12	5	10		4.40	1	2.83	0	0.83			
17	34	5.75		5.5	11		4.09	1	2.96	0	0.96			
17	34	5.5	11	6	12		3.83	1	3.09	0	0.92			
17	34	5.25		6.5	13		3.62	1	3.24	0	0.81			
17	34	5	10	7	14		3.43	1	3.40	0	0.71	OK		
17	34	4.75		7.5	15		3.27	1	3.58	0	0.63			
17	34	4.5	9	8	16		3.13	1	3.78	0	0.56			
17	34	4.25		8.5	17		3.00	1	4.00	0	0.50			
17	34	4	8	9	18		2.89	1	4.25	0	0.44		OK	
17	34	3.75		9.5	19		2.79	1	4.53	0	0.39			
17	34	3.5	7	10	20		2.70	1	4.86	0	0.35	OK		
17	34	3.25		10.5	21		2.62	1	5.23	0	0.31			
17	34	3	6	11	22		2.55	1	5.67	0	0.27		OK	
17	34	2.75		11.5	23		2.48	1	6.18	0	0.24			
17	34	2.5	5	12	24		2.42	1	6.80	0	0.21			

Figure 3.58 – Table used to determine possible planetary gear arrangements, with green highlighted row for the gear type fabricated.

For the case where the annulus is free to rotate (foot of the ground) the planet carrier is still the input, so Vp is remains one, though now, by virtue of the friction in the rest of mechanism and torque of the attached power spring, the sun gear is the de facto station member, so Vs becomes zero. Subsequently the ring gear is the "output" gear, though nothing it attached to it. The velocity ratio of the ring gear becomes,

$$V_A = \frac{A+S}{A} \quad . \tag{3.13}$$

Since the annulus inherently larger than the sun gear, the ratio in this configuration is small, slightly above unity. It this way, only negligible torque is necessary from the ankle to turn the first stage

of planetary gears in this configuration, and the rest of the mechanism is effectively decoupled from the ankle.

Additionally, the ratio of the sizes of the sun and planet gears is also important. If the velocities are significantly different from one another, then this negatively affects the efficiency of the overall gear train. It is better for the size ratio, R, to approach unity. At the same time of all other criteria is the consideration of other assembly necessities, such as bearing size and placement. For the reasons of large gear ratio (1:5.25), location and size of bearing, and meshing criteria, the configuration highlighted in greed in Figure 3.58 was chosen to make an evaluation prototype. A prototype was sought to be made to assess the operation of the alternating stationary vs free ring gear. The design of the evaluation prototype is rendered and assembled after 3D printing is given in Figure 3.59 below.

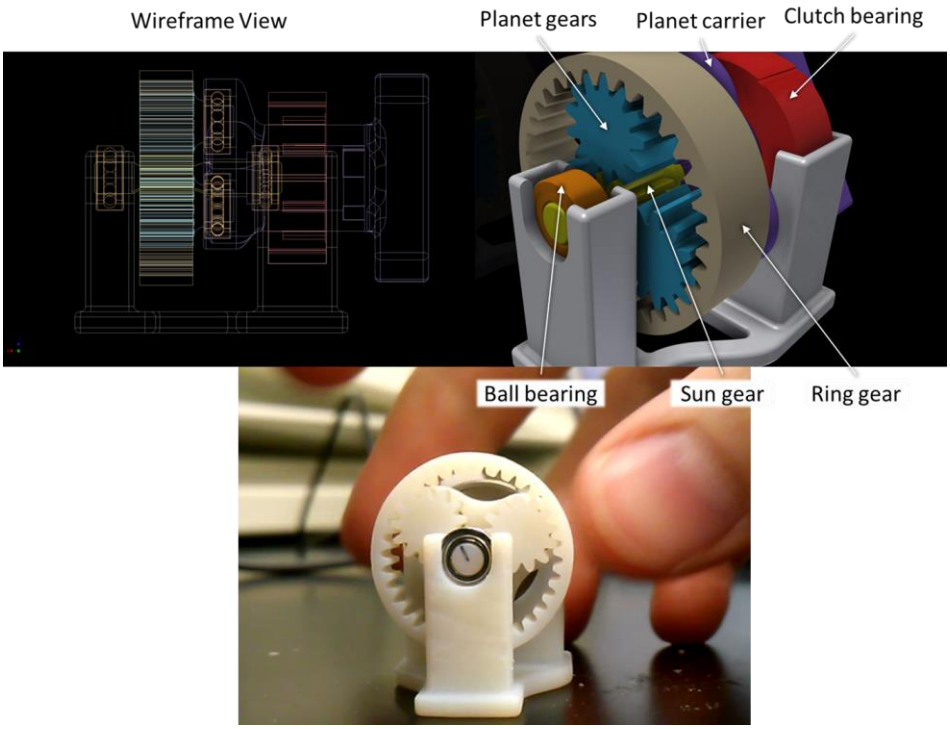

Figure 3.59 – Wireframe view of planetary gear test stand and labeled rendering of test stand, along with fabricated planetary gear verification setup.

The fabricated prototype was found to function as intended, with all rear ratios verified as properly calculated. When the ring gear is held stationary, by pinching with the fingers, the

inputted rotation (via the fingers of the opposite hand) was amplified by a factor of 5.25. When the ring gear was let go, it was observed to rotate slightly more than planet carrier (~1.24x) and the gear train was felt easier to turn, as was intended.

As was noted, the size ratio of the planet and sun gears was far from unity (0.62), which would yield a poor efficiency. With the fourth generation of mechanism housing, there was some space to make the ring gear slightly larger. With the extra space, several more configurations presented themselves. The new calculation table and chosen gear train rendering are given in Figure 3.60. As shown in the figure, a design with the planets and sun gears being the same size is possible. In addition, four planets can be used instead of three. Using more planets would be more torque could be transferred and smoother performance realized. What's more, by having larger than previous planet gears bushings may be placed inside the planets rather than beside them, making for a more compact design.

	mod	0.5									# P		
A	#A	P	#P	S	#S	Vs	Vc	Vp	Va	R	3	4	5
18	36	7.5	15	3	6	7.00	1	2.40	0	0.40	OK		
18	36	7.25		3.5	7	6.14	1	2.48	0	0.48			
18	36	7	14	4	8	5.50	1	2.57	0	0.57			
18	36	6.75		4.5	9	5.00	1	2.67	0	0.67			
18	36	6.5	13	5	10	4.60	1	2.77	0	0.77			
18	36	6.25		5.5	11	4.27	1	2.88	0	0.88			
18	36	6	12	6	12	4.00	1	3.00	0	1.00	OK	OK	
18	36	5.75		6.5	13	3.77	1	3.13	0	0.88			
18	36	5.5	11	7	14	3.57	1	3.27	0	0.79			OK
18	36	5.25		7.5	15	3.40	1	3.43	0	0.70			
18	36	5	10	8	16	3.25	1	3.60	0	0.63		OK	
18	36	4.75		8.5	17	3.12	1	3.79	0	0.56			
18	36	4.5	9	9	18	3.00	1	4.00	0	0.50	OK		
18	36	4.25		9.5	19	2.89	1	4.24	0	0.45			
18	36	4	8	10	20	2.80	1	4.50	0	0.40		OK	
18	36	3.75		10.5	21	2.71	1	4.80	0	0.36			
18	36	3.5	7	11	22	2.64	1	5.14	0	0.32			
18	36	3.25		11.5	23	2.57	1	5.54	0	0.28			
18	36	3	6	12	24	2.50	1	6.00	0	0.25	OK	OK	OK

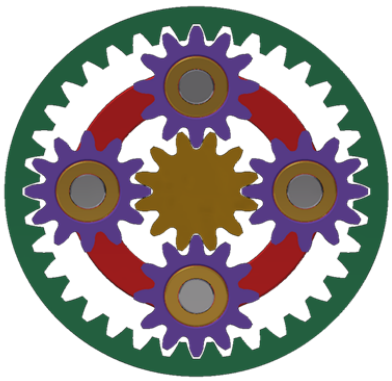

Figure 3.60 – Table used to determine next generation of planetary gear arrangements, with green highlighted row for the gear type chosen, and rendering of gear train.

With this new configuration, the amplification ratio for each stage would be 1:4, with the decoupled ratio being 1:1.33.

3.7.4 Energy Storage

Another key component of the design is the non-linear "Power" spring. The power spring is what decouples the input motion from the ankle from the energy conversion damping effects of the generator. This spiraling type spring can take different forms and is also commonly referred to

as a constant force spring or a hair spring. Each has subtle differences and applications, but are the same in they are used to exploit their non-linearity in spring force as a function of rotation angle relationship. An illustration of the power spring and its parts is given in Figure 3.61 below. In the typical application, the arbor is turned, winding the spring, and then the stored energy returns or retracts whatever initially wound the spring to its initial position. However, in the boot mechanism, the housing will be turned while the arbor is held stationary, winding the spring. Then the housing is held stationary and the arbor allowed to unwind the spring and turn the generator. This functioning decouples the boot wearer from the generator, eliminating any significant damping of the ankle joint.

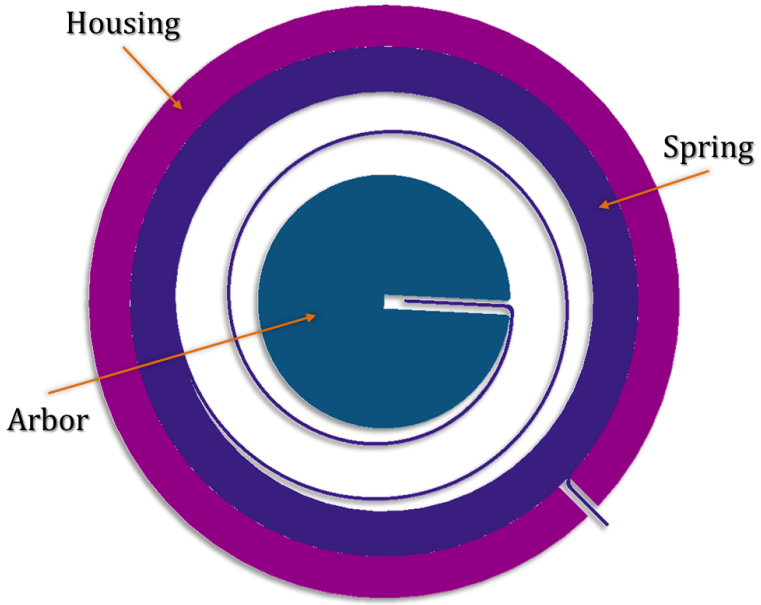

Figure 3.61 – Illustration power spring and labeling of key parts.

Two different sized commercial power springs, used in retractor applications, are shown in their holders in Figure 3.62(a) and in their unstressed state in Figure 3.62(b).

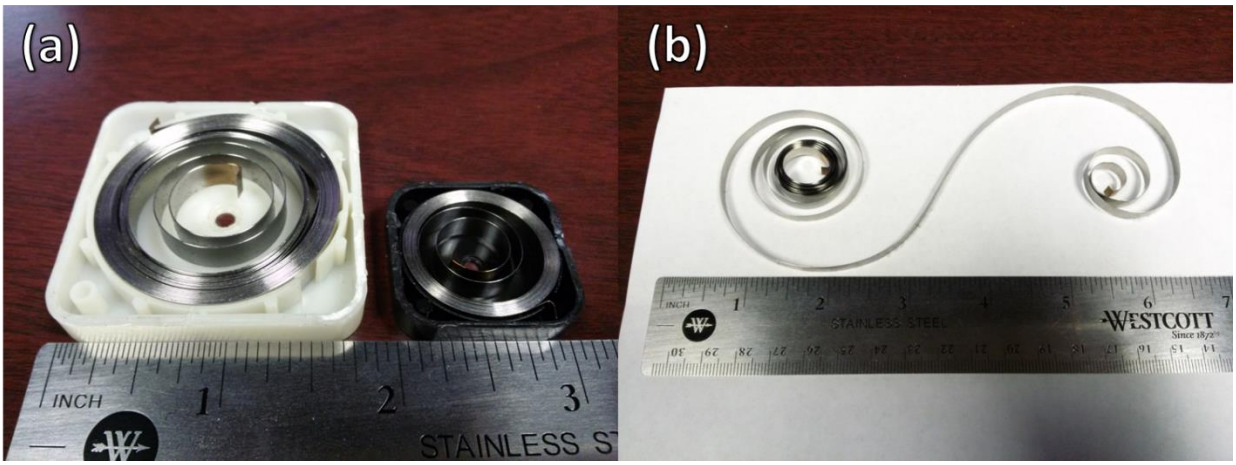

Figure 3.62 – (a) Two sizes of power springs in their holders. (b) Power spring in unstressed state. Outer spring windings are wrapped the in the direction opposite to their natural curvature.

The spring in the white holder in Figure 3.62(a) is approximately 1.5 inches in diameter when wound in the holder, approximately 0.125 inches wide, and is rated to one pound. As is evident from Figure 3.63, a one pound rated spring produces one pound of force when fully rotated. However in the range of 90 to 1260 degrees rotation, the profile is largely flat. This is the intended region of operation, highlighted in green.

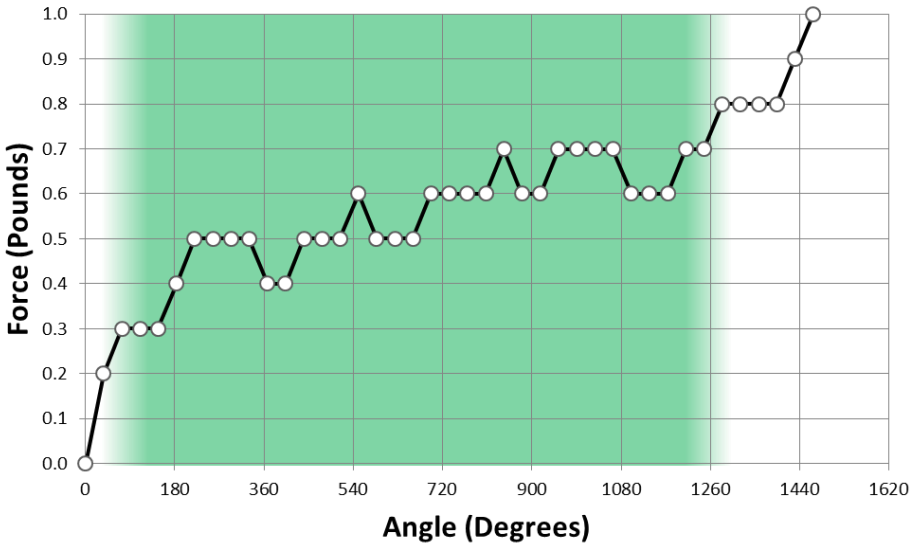

Figure 3.63 – Spring force as a function of angle of rotation for the spring shown in Figure 3.62(a). Green area highlights intended region of operation, where spring force is approximately constant.

While the mean force in the region of operation is around only 0.6 pounds, bear in mind that the force in the spring will be applied back to the ankle through a gear ratio to amplify the ankle's rotation. For example, if the ankle rotates 20 degrees in order to put 720 degrees of rotation into the spring, a gear ratio of 1:36 to 1:72 would be necessary to use. The resulting force from the spring multiplied through the gear ratio will be tuned such that it matches the torque during the negative work phase of gait.

The spring holder and winding mechanism itself is conceptualized in Figure 3.64. The device in Figure 3.64 fits into the purple area marked "Spring" in the picture on the right in Figure 3.24, as shown in Figure 3.25. The housing section will be turned by a timing belt pulley either attached to it or perhaps incorporated into the housing itself during the negative work part of the gait cycle. While the housing is turned the motion control shaft will be held stationary by some method of braking, as mentioned before. Therefore, the power spring will wind and store energy. During the positive work of the gait cycle the motion control shaft will be allowed to rotate, unwinding the inside of the power spring. Consequently, the generator shaft will also be rotated, producing electrical power in the generator to be harvested. The spring unwinds quickly, spinning the generator quickly. To allow the generator to continue spinning after the spring is unwound, a clutch bearing is used on the generator shaft allowing for overrunning of the generator after the spring is fully unwound.

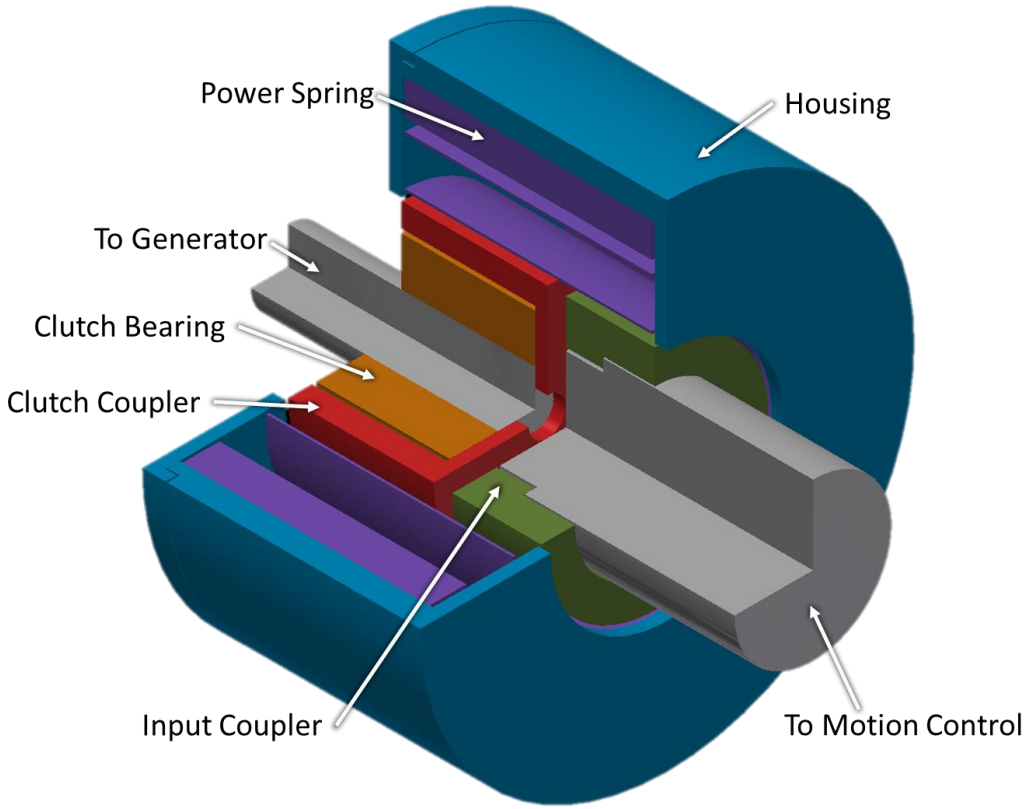

Figure 3.64 – Concept spring housing and torque transfer mechanism.

The commercially available springs are too large to be used in the boot. The design of Figure 3.64 calls for a wide and small diameter spring, while most commercially available examples are the opposite, being thin width and relatively large diameter. In order to examine what geometry of spring should be used, an experiment of varying parameters, namely spring thickness, was conducted. In order to examine multiple spring types, the test stand design was designed so that a consistent setup could be used for all spring measurements. This involved incorporation of alignment bearings into the spring housing. In addition, slots by which the spring attached to the housing and arbor were made to closely match what would be used in the actual boot mechanism. This design is reflected in Figure 3.65, along with the manufacturing process for the three spring thicknesses considered (.005”, .006”, and .008”).

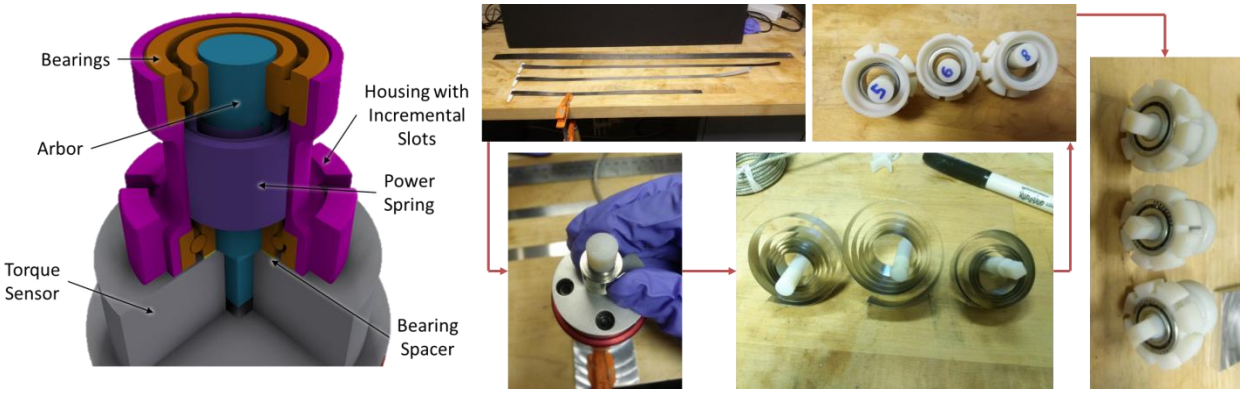

Figure 3.65 – Rendering of power spring testing setup for variation of spring thickness measurements. Strips of spring material are bonded to the arbor and wound tight. They are then unwound, then wound again and fitted into its housing. Bearing are added to either end to ensure housing and arbor remain concentric.

For the spring material, 301 stainless steel was chosen for its high strength, yet ductile, and corrosion resistance, which will be needed for the final product. Figure 3.65 shows strips of 301 stainless steel of half inch width cut to a length allowing for several turns to be placed in the housing. The ends of the spring material are bent to a 90° bend and bonded into a slot in the arbor, with Loctite 120HP epoxy. The spring is then wound tight (wound to solid) to the arbor, where it is plastically deformed into its new shape. The spring is then allowed to return to an unstressed state, before it is again wound and placed into its housing, and bonded in place, along with the alignment bearings.

The lengths of the springs were chosen such that when wound, half of the area inside the spring housing would be filled with the spring. This is the optimum configuration, as any more turns would inhibit the spring from winding fully, and any less turn would not take full advantage of space. Additionally, the power springs manufactured were of the conventionally wound, rather than the prestressed winding shown in the commercial spring of Figure 3.62. There are some advantages in terms of higher torque for a thinner material for a prestressed design, however, it is difficult to manufacturer, particularly by hand. Since the springs were manufactured by hand, the conventional winding was chosen. What's more, the power spring stores energy in the bending of the spring material. This means that the torque produced is geometrically proportional the cube of the thickness, and linearly with the width of the spring.[174-177] This is why three springs of varying thicknesses were initially made.

The three spring test specimens were measured for torque as a function of rotation angle. This was done by rotating the spring housing in 45° increments, while the arbor was fixed inside the torque sensor. At each incremental rotation, the torque reading was average over a period of several seconds. The torque sensor was clamped to the table through a custom machined holder. The incrementing tower fit around the torque sensor and fit again the lower portion of the machined torque sensor holder. In this way, the spring could be rotated to the next 45° increment and held with the stopper, while not compromising the ability to isolate the torque measurement to the spring only. The results of this experiment are summarized in Figure 3.66.

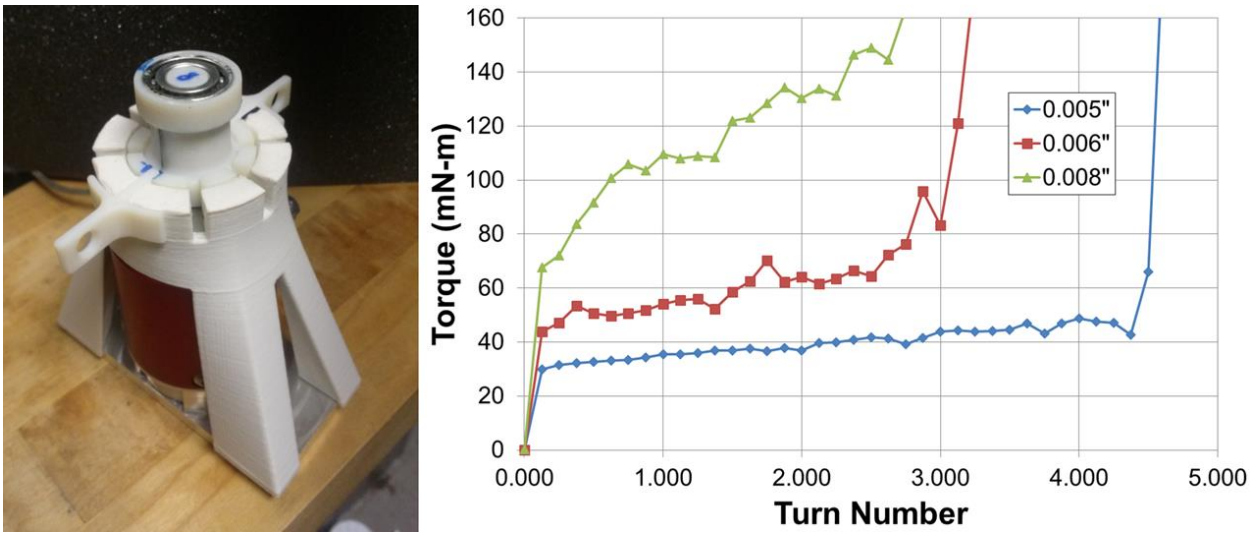

Figure 3.66 – (Left) Picture of test setup. (Right) Torque as a function of Turn Number (where 1 turn = 360° rotation) for three considered spring thicknesses.

From Figure 3.66 it can be seen that the thinner the spring material, the flatter the torque curve. This is desirable as the torque load to the boot wearer will feel more uniform and less noticeable. However, the thicker the spring material, the larger the magnitude of torque produced. The larger the torque produced, the faster the generator will be able to be spun, creating a higher power peak, and the less ankle angle amplification is necessary. It is preferable to keep the initial gear ratio lower such that friction and other losses are less multiplied on the boot wearer. The part of the graph where torque suddenly rises is where the spring is fully round and begins to act as a solid, indicated by a dramatic rise in stiffness.

It should be noticed that all springs had a different maximum turn number. As mentioned, all three springs were made with lengths such that half the volume of the inside of the spring

housing was filled with the spring. Having less area filled reduces the maximum turn number, as there is less spring. Having more area filled also reduces the maximum turn number as the spring cannot become fully wound, as there is not enough space. Thus, since all springs occupy the same area within the housing, the thicker springs cannot be as long, as each turn takes up more space inside the housing. This is why the thicker the spring, the less the maximum turn number.

The design of Figure 3.64 functioned as intended, which is discussed in the next section (Figure 3.70). The geometry of the design calls for an inner housing diameter of 18 mm and an arbor diameter of 9 mm. The reason for the sharp rise in the torque curves of Figure 3.66, followed by the flatter section, is due to the relatively large arbor diameter. As can be seen in Figure 3.65 in the picture after the spring is placed in the housing and before the alignment bearings are installed, one can see that spring goes directly from the outer loop to the arbor, with no spiraling. This means that spring material is transferred directly from the outer winding to the inner winding. Having an area of spiraling, or a gradual transition from outer to inner winding circles, like the illustration of Figure 3.61, would give a more gradual transition.

The arbor diameter was selected to be 9 mm due to the incorporation of the clutch bearing, which has a 7.2 mm diameter. Thus, there was little radial dimension for the spring-arbor connection trench. It was undesirable to increase the arbor diameter further, as it would really begin to negatively affect the maximum turn number. Though, since there was little surface area in the spring-arbor connection trench to bond the two together, deboning and subsequent disconnection between the spring and arbor became a problem when winding. To address this problem, the power spring section layout concept of Figure 3.67 was designed. With this design, the clutch bearing was moved to inside the arbor brake and outside the power spring housing.

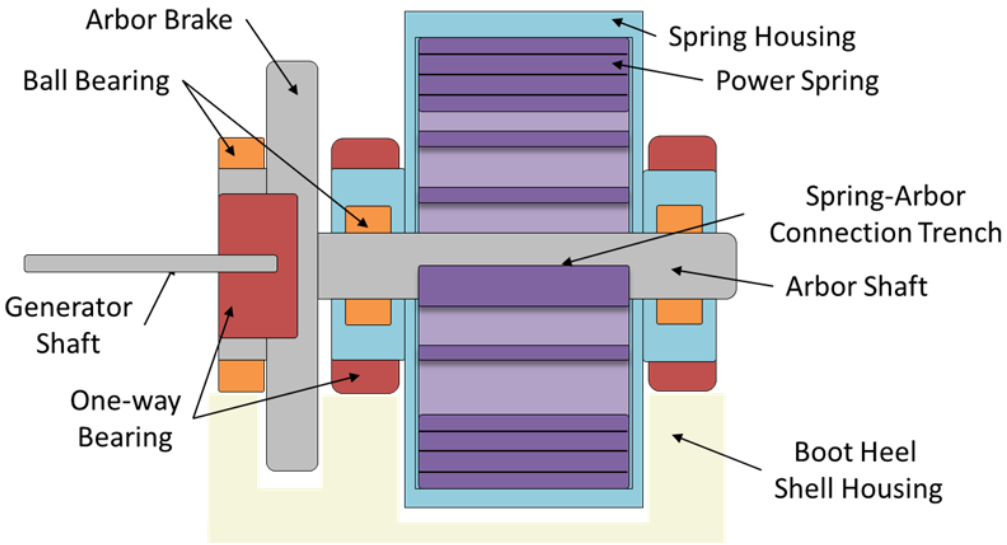

Figure 3.67 – Concept of version two of generator to power spring and brake connection scheme.

The new spring layout design resulted in the arbor diameter being able to reduce to 5 mm. Also at this time, generation 4 of the device housing was realized, which gave more space to place the power spring. Subsequently, the diameter of spring housing increased slightly to 18.5 mm, but the width of the spring was now able to be further adjusted. Previously, a half inch spring width was all that there was room for. Though now with the generator being moved to its own place in the front of the housing (see Figure 3.35), rather than on the same axis as the spring, the spring could be made wider. As mention previously according to theory, and verified in measurement, the spring has a cubic torque relationship with the spring material thickness, though is linear with width. So increasing the spring width has less effect on the torque levels, but helps since the spring material cannot be continued to increase in thickness, as it becomes less bendable.

Taking the 0.008 inch spring material, and making springs (with the new housing dimensions) of 0.5, 0.75, and 1.0 inch widths, the torque curves of Figure 3.68 were generated using the same manufacturing and test procedures chronicled in Figure 3.65 and Figure 3.66. Here the linear relationship of torque to spring width is evident, as the curve for the 1.0 inch wide spring is approximately twice that of the 0.5 in wide spring. It is also noted that the torque curves are more gradually flattening than previously. As can be seen in the assembly picture in Figure 3.68 of a spring in the housing before the alignment bearings were installed, there are a few spiraled turns of the spring, creating the smoother transition that was mentioned before. This effect comes about due to the arbor being smaller and spring being more plastically deformed when wound

about it. Though, this effect is not truly desired. It may feel better for the boot wearer to have this gradual torque profile, which remains to be seen, but it would be better for the device performance is the torque curved stayed higher at lower turn number. The torque curve could be altered by using more advanced techniques, such as winding the spring about a larger arbor and then affixing it to a smaller diameter one, which will be explored in the future.

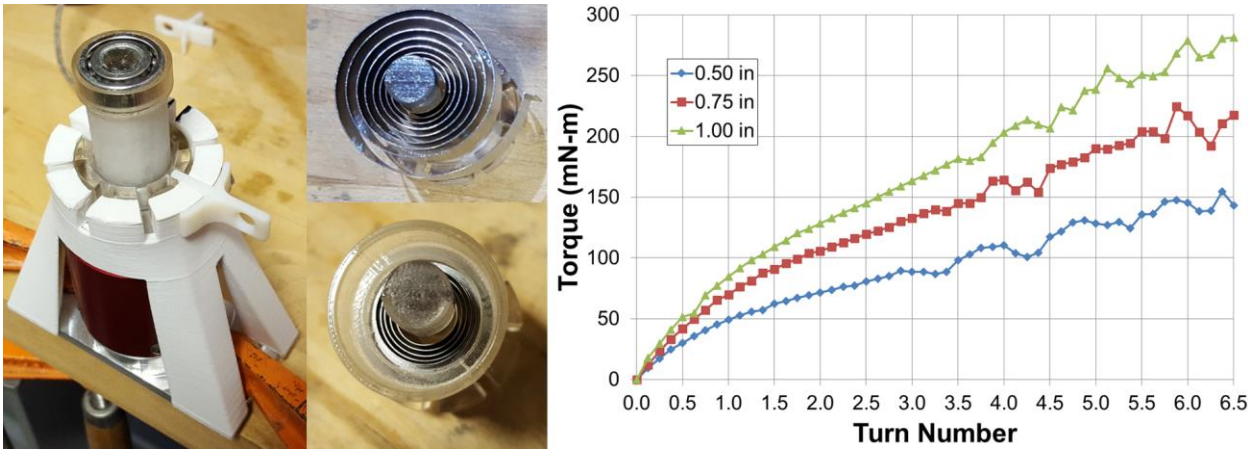

Figure 3.68 – (Left) Picture of test setup. (Right) Torque as a function of Turn Number (where 1 turn = 360° rotation) for three considered spring widths.

3.7.5 Mechanical to Electrical Conversion

The generator design is a compact, multistage, permanent magnet axial flux alternator design, illustrated in the 'New Design' of Figure 3.69. This type of generator is good for this application as it has negligible cogging torque, which results from a generator having a rotating and stationary magnetic component, resulting in potential wells, which make radial flux generators difficult to spin. Since the axial flux design spins smoothly, since magnet pairs spin together, vibrations are negligible and the generator will continue to spin for a small amount of additional time after the power spring is unwound, giving a bump to efficiency by eliminating the cogging losses. Furthermore, the axial flux design is the most efficient use of space, creating the highest energy density generator.[178]

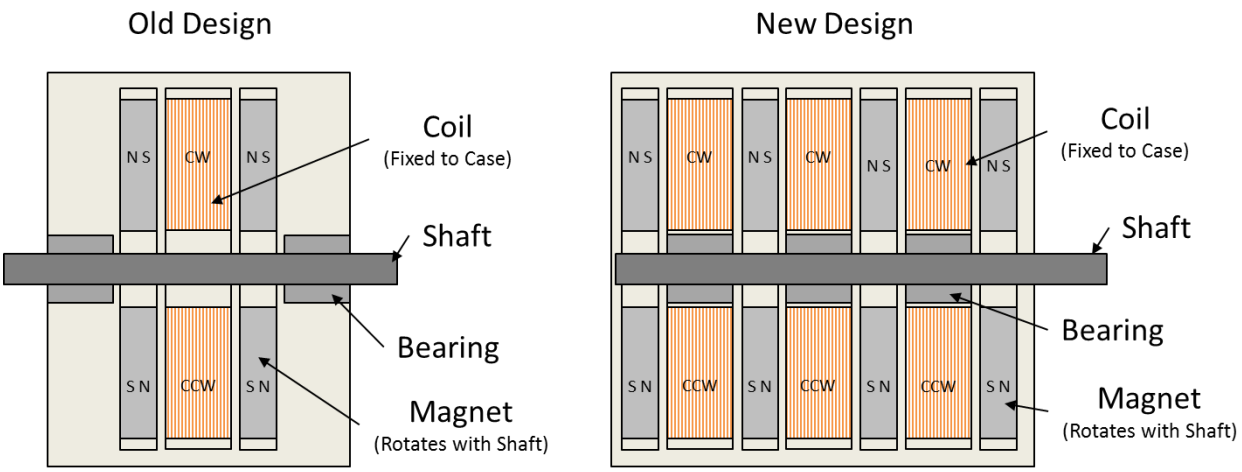

Figure 3.69 – Comparison of old (left) and new (right) generator designs. Magnets are designated with "N" and "S" for north and south poles, while coils are labeled with "CW" and "CCW" for clockwise and counter-clockwise direction of wrapping.

The design of the generator improves on the design of Kishore et al. [179](which was for a micro wind turbine), and Figure 3.70 shows the fabrication steps taken to fabricate this part along with connection to the power spring. The magnet holder rotor, coil holder, and coil holder holder stator are 3D printed. Coils are wound around the coil holder and marked in blue where clockwise winding and left white where counter-clockwise winding. Coils are then placed into the holder, along with a bearing for the generator shaft to be supported by. Windings are alternated in direction as the magnets in the rotor are placed with alternating North and South poles facing, so as to induce alternating current. However, since all coils are connected in series, they must alternate winding direction, so that current is always driven in the same direction as North and South poles alternatively rotate by. This results in a single phase generator. The magnet holder has a keyway which attaches to a keyway cut into the generator shaft, allowing them to spin as one. The power spring is placed in its housing, as discussed in the previous section, along with the arbor brake.

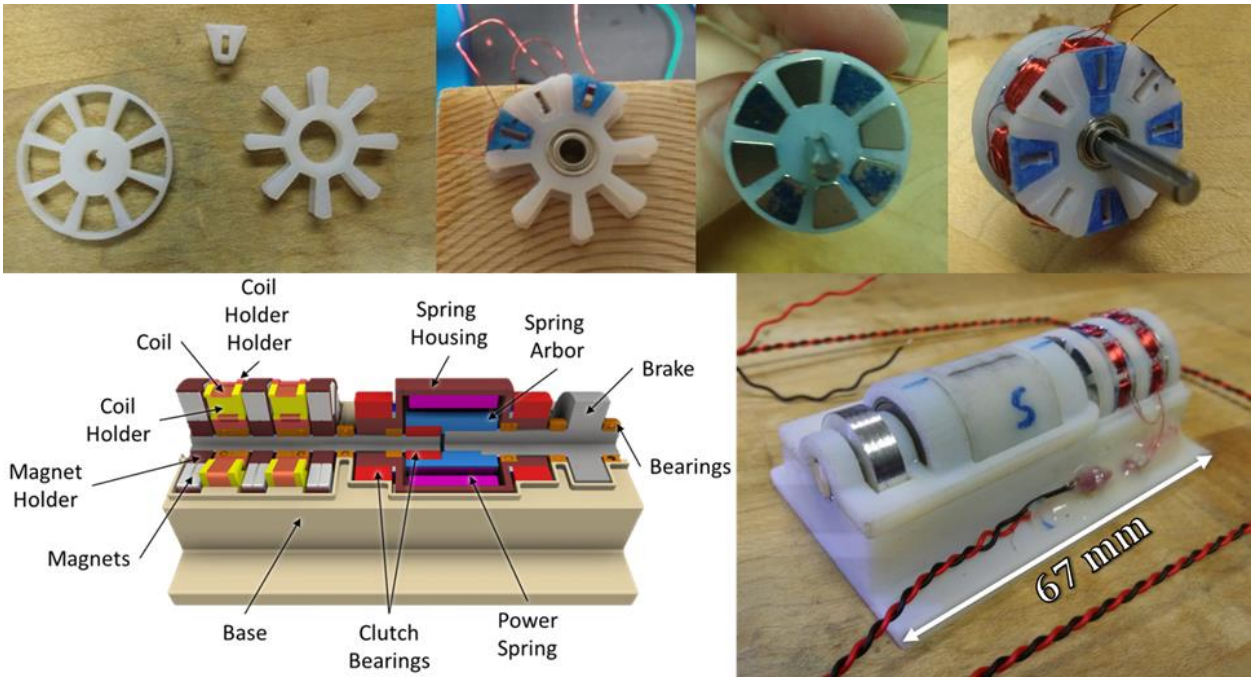

Figure 3.70 – Fabrication steps to complete the spring-generator test stand.

This design was made with respect to the housing constraints of Generation 1 of the boot mechanism housing. The stand was preliminarily tested, where it was observed to make approximately 100mW of power on average, when the power spring was wound (by hand) to a winding like would be experienced in the boot. Hand winding was accomplished by using the index finger of the right hand to hold the arbor brake, while using the index finger of the left hand to turn the spring housing. The spring housing can only rotate in the winding direction thanks to the larger clutch bearings holding the housing. Thus, the spring cannot unwind and turn the generator until the brake is released.

This power was measured after the signal was rectified (full-bridge diode rectifier) and stored in a capacitor. The energy in the capacitor was divided by the time period of one step (~1.3 seconds). Note that the spring unwinds and the generator finishes spinning before the step period is completed. Therefore, during some parts of the average power include this period of zero power production. This is a better estimate of the energy which could be delivered to a battery or load, than simply reporting the power directly from the generator. Unfortunately, the connection between the power spring and arbor connection broke before formal parametric testing was conducted. Therefore, no plots of power output are available as no data was saved, though a plot

of the open circuit voltage output of the generator from one preliminary test is given in Figure 3.71.

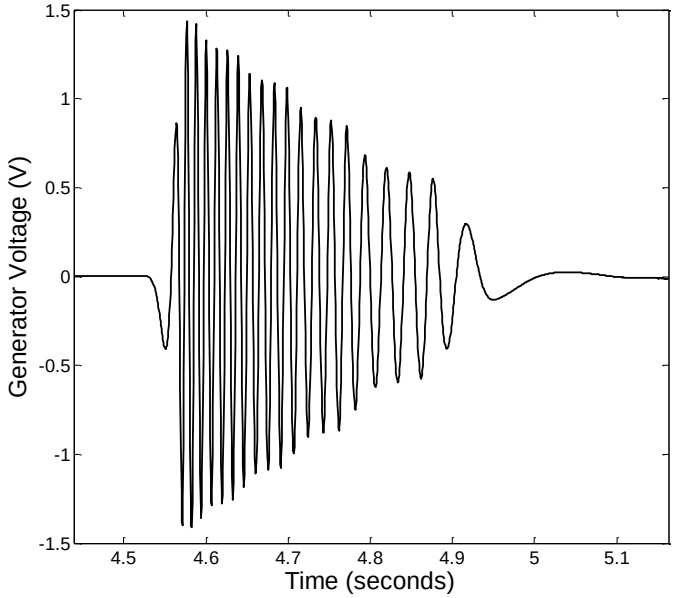

Figure 3.71 – Open circuit voltage output form preliminary test of the mechanism test stand show in Figure 3.70.

The connection between the spring and arbor was designed too weak for the force spike produced when the spring is fully unwound and abruptly stops at the end of its windings. Essentially the trench the spring was epoxied into was too shallow and the 3D printed material too weak to withstand the stress. The shallowness of the connection trench was due to the presence of the clutch bearing inside the spring winding taking up a lot of radial space, necessitating a thin connection or else a reduction spring space. A new connection scheme is sketched in Figure 3.72. The main change in this design over the previous one is flipping the arbor brake from the outside of the boot to the generator side. This change allows the one-way clutch bearing connecting the generator to the spring to be placed inside the arbor brake. This eliminates the need for a split shaft design and allows for a solid arbor. With a solid arbor, the trench holding which the end of the power spring slots into can be made much deeper (as it was for the power spring test stand arbors). This solves the strength issue faced before and should make for a privately fixed spring-arbor.

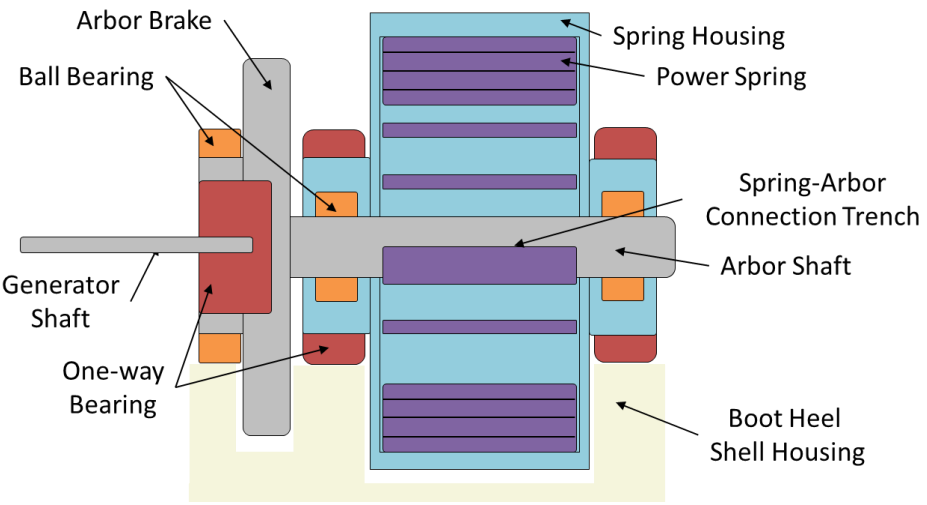

Figure 3.72 – Concept of new generator to power spring and brake connection scheme.

While the spring connection and component layout was being updated, the design of the generator was also updated. It was clear that from the power output of the previous test stand, which was mostly made to verify mechanism function and component interactions, that the generator would have to produce more power if the device would be useful. Part of generating more power was using a larger generator, as has been discussed, but an accompanying change was switching from a single phase to a three phase generator design. With the significant increase in number of coils compared to the previous test stand, if a single phase where used the voltage produce would quickly become too large. This is more of a problem from a circuitry standpoint. Since the goal is ultimately battery charging, a DC-DC converter will have to arbitrate between the voltage produced by the generator and the current battery voltage. If the converter has to convert a much larger voltage into a much lower voltage, efficiency could suffer. Additionally, the consistency of the power delivery to the battery is important for battery health.

From the plots and circuit diagrams shown in Figure 3.73, it can be seen how, once rectified, a three phase generator produce a much smoother output voltage waveform. Here, the voltage waveforms produced by each coil phase in a) are rectified by the circuit in b) resulting in the black line of c). Only the phase currently producing the highest voltage is output, as the other two are blocked. As a result, for a three phase generator, the RMS output is around 95% of the peak voltage amplitude, compared to about 71% for a single phase generator. Additionally, the smoothness of the waveform yields higher mechanical efficiently as less vibrations are induced by

the fluctuating counter torque on the generator shaft as a result of the energy conversion. The three phase generator will thus rotate more smoothly.

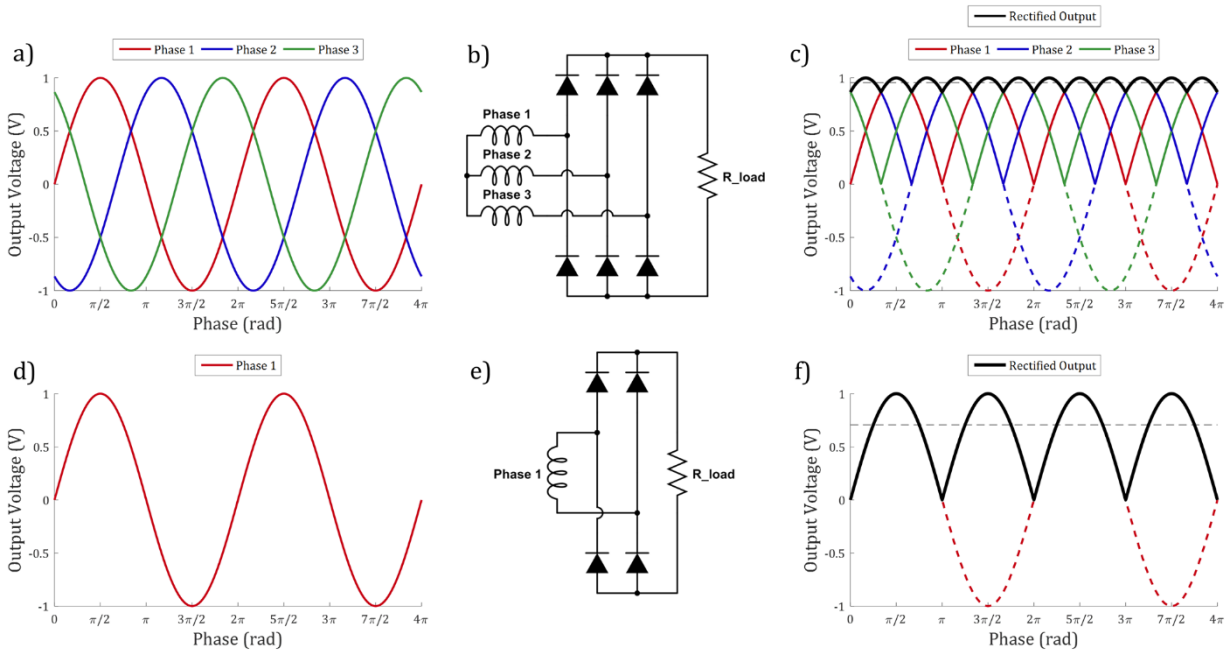

Figure 3.73 – Three phase (a, b, c) and single phase (d, e, f) representations of generator phase voltages (a, d), full bridge rectifier circuit diagrams (b, e), and resultant output voltages (c, f).

As Figure 3.69 shows, the design of the axial flux generator for the boot will have several stages of magnets and coils, since the volume for the generator, quantified in the 4th generation picture of Figure 3.35, allows for a longer length of generator. This then leads to several design questions. Namely, how many stages will be used, and what is the optimal size of magnets and coils to use? These are not trivial questions to answer. The ultimate goal is to maximize the power output of the generator, though as Figure 3.74 illustrates, most of the design parameters affecting generator power output are interrelated. With such a convoluted set of interactions, a true optimization is not readily achieved. Though, if one dissects these interactions it becomes evident that there are parameters that only affect the radial direction of the generator, such as magnet shape and coil area. These two parameters are simple enough to optimize.

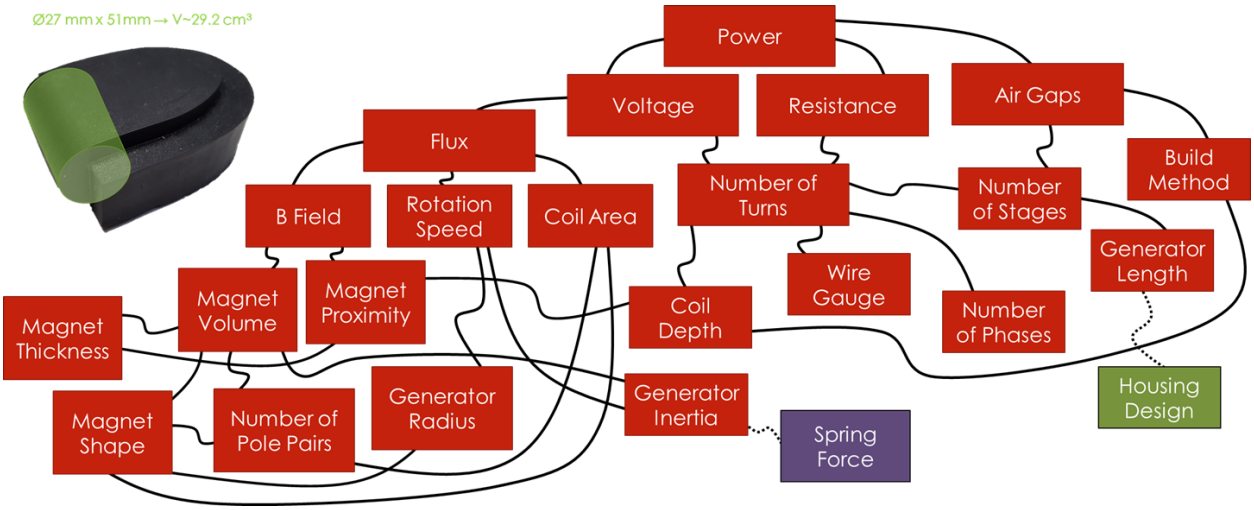

Figure 3.74 – Illustration of interdependence of several key generator design parameters which ultimately relate to the variable of interest, the power output.

For the circular cross-section of the generator volume, it is intuitive that for a discrete number of magnet pole pairs that the magnets should take the shape of arc segments to achieve the greatest volume. It is desired to have a magnet of greatest volume, since the magnets field strength is directly related to its volume through the residual flux density (a material property) and its shape. Knowing roughly the shape of the magnets (arc segments), the design question becomes how many pole pairs to utilize in the design. In a commercial generator design, the number of pole pairs are chosen such that at a desired operating rotational speed that a desired frequency of electrical output will be achieved. For the purposes of this design, a constant frequency cannot be realized since it will increase and decrease across the gait cycle as energy is alternatingly input from the power spring (increasing generator speed) and converted into electricity and lost to friction (decreasing generator speed). What's more, the frequency of electrical output does not need to be well controlled. Therefore, the choice of number of magnets is largely arbitrary.

Though the choice number of magnets may be with little bounds, there are some guidelines which aid the design. From Equation (1.17) it is known that voltage is only produced when there is a time rate of change in the magnetic flux. Therefore, the faster the flux can be made to change, there higher voltage will be produced. Though, at the same time, more poles means the magnets will be smaller, lowering the magnetic field strength. Also, in the magnet rotor, there will be some

radial thickness between magnets to hold them in place. The greater the number of magnets, the more of these separators will be necessary, and the more space is wasted. These are the trade-offs.

Another criteria is the number of magnets it would take, in combination with a certain number of coils, to create the desired number of phases in the output signal. The relationship is described as,

$$M = \frac{C(P+1)}{P} \quad . \tag{3.14}$$

Here, M is number of magnets, C the number of coils, and P is the number of phases. Of note is that Equation (3.14) gives the simplest solution. There are other solutions to the manget, coil, phase relationship, though all are more complex and Equation (3.14) is regarded as the optimal solution. Table 3.2 below shows all of the possible configurations for two to five phases and two to ten coils. Here, one can see that a rotor with 12 magnets could produce two, three, or five phase current with eight, nine or ten coils respectively. Though, as it has already been noted, three phase power is deemed the necessary increase in complexity for a given increase in performance.

Table 3.2 – Possible number of magnet and coil combinations necessary to create the desired number of phases in the output signal. Dashed cells "-" are those which no solution is possible.

P	2	3	4	5
C	M	M	M	M
2	3	-	-	-
3	-	4	-	-
4	6	-	5	-
5	-	-	-	6
6	9	8	-	-
7	-	-	-	-
8	12	-	10	-
9	-	12	-	-
10	15	-	-	12

To achieve three phase output, it is clear from Table 3.2 that either four, eight, or twelve magnets should be used in the rotor. For the chosen 3D printing manufacturing method, a 0.5 mm wall thickness of the magnet holder rotor was chosen. Each of the three magnet configurations were examined, where it was found that ~5%, ~9%, and 12.5% of the space is wasted with the

four, eight, and twelve magnet configurations respectively. As will be the theme for this generator design, the middle ground of eight magnets in the rotor was chosen as the best design. This configuration gives the necessary increase in complexity for performance while still keeping component sizes, both magnets and coils, large enough to be assembled by hand. The resulting magnet rotor configuration is illustrated in Figure 3.75, where the magnets are poled through their thickness and alternate which pole is facing out.

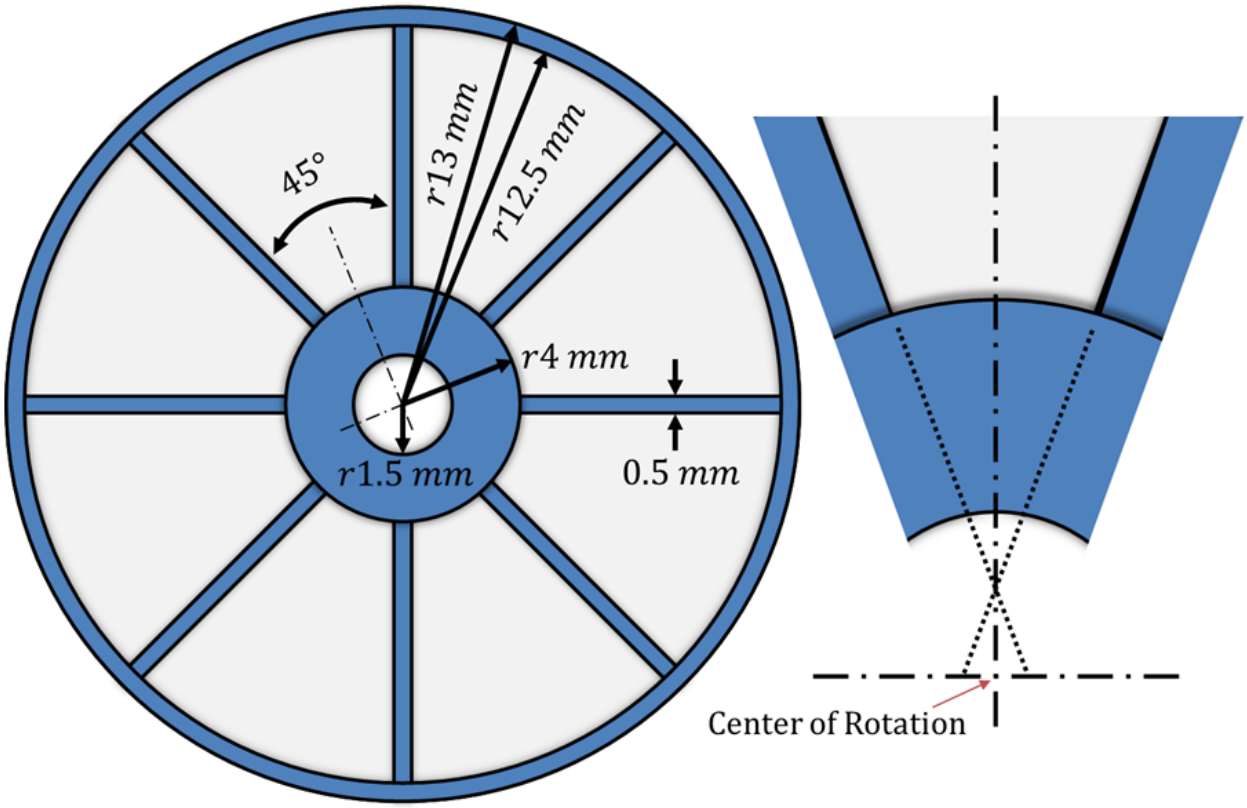

Figure 3.75 – Eight magnet rotor design with important dimensions and diagram of magnet shape necessary to achieve a constant wall thickness.

Here, to achieve a constant wall thickness of the 0.5 mm separation gap necessary for structural stability, the magnets are designed such that they still sweep a 360° / 8 magnets = 45° arc, though the slope of the sides is such that two adjacent magnet sides are parallel. This means that the lines made by the sides of the magnets to not intersect the center of rotation. These lines did intersect the center of rotation, then the wall dividers would be wedged shaped, rather than constant thickness, tending toward zero thickness as they approached the center, which is naturally

undesirable for mechanical strength. The inner radius of the magnets is made to be 4 mm. This decision was largely made with the coil shape in mind. Having a smaller inner radius would only add slightly more volume to the magnet, while making the inner turn on the coil holder sharper. Therefore, to maintain a minimum radius and not stress the coil wire by making it follow sharper turns, the 4 mm inner radius was chosen. The outer radius of 12.5 mm because with a 0.5 mm wall thickness on the periphery, there would still be a 0.5 mm air gap between the magnet rotor and the generator housing, which is 27 mm in inner diameter.

Following the radial shape of the magnets is the subsequent layout of the coils. The coils take a trapezoidal shape, as shown in Figure 3.76, such that the sides of the coil are parallel to the sides of a magnet when they are in phase. The sides are made parallel so that when the flux lines rotate with the rotation of the magnet rotor, they will cross through the coils orthogonally, resulting the greatest output. According to the criteria of three phase output, six coils are evenly spaced around the circle.

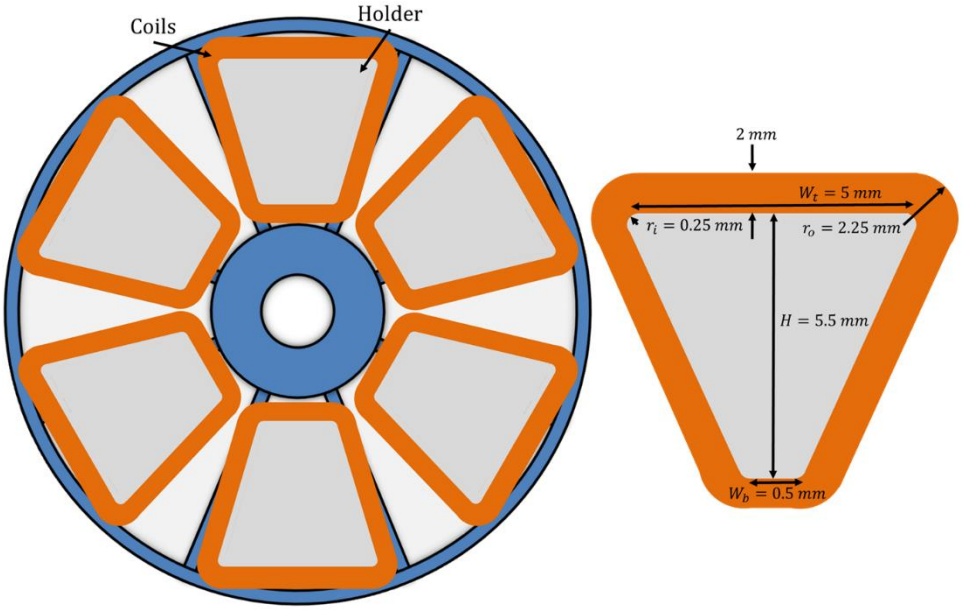

Figure 3.76 – Illustration of coil and holder shape with expanded and dimensioned coil, and arrangement with magnet rotor behind for reference.

The area enclosed by the coils (represented in orange in Figure 3.76) is the area used in Equation (1.19). Naturally, as the coil is wound it grows in thickness and the enclosed area

increases. Therefore, the area used in calculation is considered to be the mean area enclosed, which can be found using Equation (3.15), while the perimeter is found using

$$A = H\left(\frac{Wt + W_b}{2}\right) - (4 - \pi)\left(\frac{r_o + r_i}{2}\right)^2 \quad . \tag{3.15}$$

$$p = 2H + W_t + W_b - (8 - 2\pi)r \quad . \tag{3.16}$$

Building from Equation (1.17), which is the electromotive force produced from a time varying flux through a conductor area, Equation (3.17) below adds the term, N, which is the number of identical turns of the conductor, since multiple turns of wire will be used to increase voltage.

$$\mathcal{E} = -N\frac{d\Phi_B}{dt} \tag{3.17}$$

With the cross-sectional shape and radial dimensions of the generator know, attention is now given to perhaps the more involved design considerations in the longitudinal direction. The considerations are namely the thickness of the magnets, depth of the coils, and number of stages, where all three of the parameters desire to be maximized, again creating trade-offs. An example of the trade-off between magnetic field strength and number of turns is shown in Figure 3.77. Having a larger spacing between magnets gives more space for the coils to occupy, yielding a large number of turns. Though, since magnetic field decays with the square of distance between magnets, the magnetic field suffers with separation distance. This opposite of this is also shown in Figure 3.77, where nearer magnets create a stronger field at the cost of coil space and number of turns.

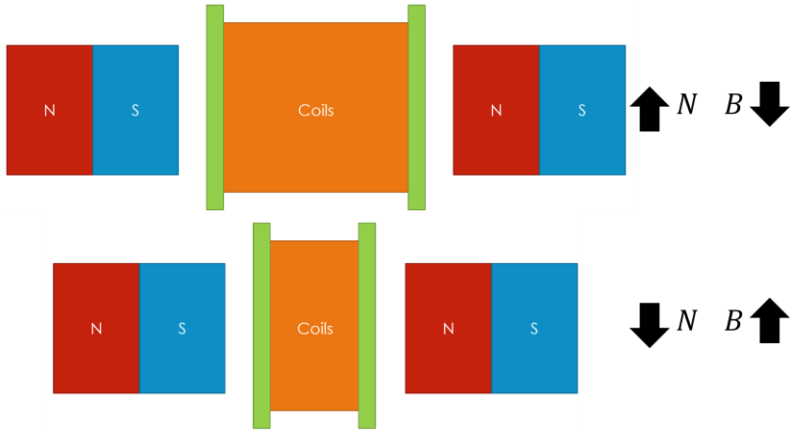

Figure 3.77 – (Top view) Illustration of tradeoff between magnet proximity and coil depth, and its relation to number of turns and magnetic field strength.

The trade-off of size of components vs number of stages is illustrated in Figure 3.78. Having multiple stages is mostly a means of increasing the number of turns. Since there are multiple number of stages, a large number of turns can be realized while keeping the magnets close together. Though, the thickness of the magnets must also vary with the other design considerations. Ultimately there is not absolute best answer to this configuration problem, rather it is constrained by the length of the generator. Perhaps there exists a configuration which performs very well within each stage, though it does not maximize the space. It would better use a slightly less optimal stage configuration to fit in an extra stage, yielding an overall increase in performance for the generator as a whole. Though again, having a large number of stages also necessitates the wasting of space in the forms of air gaps between the rotating magnets and stationary coil, as well as the thickness of the coil holders.

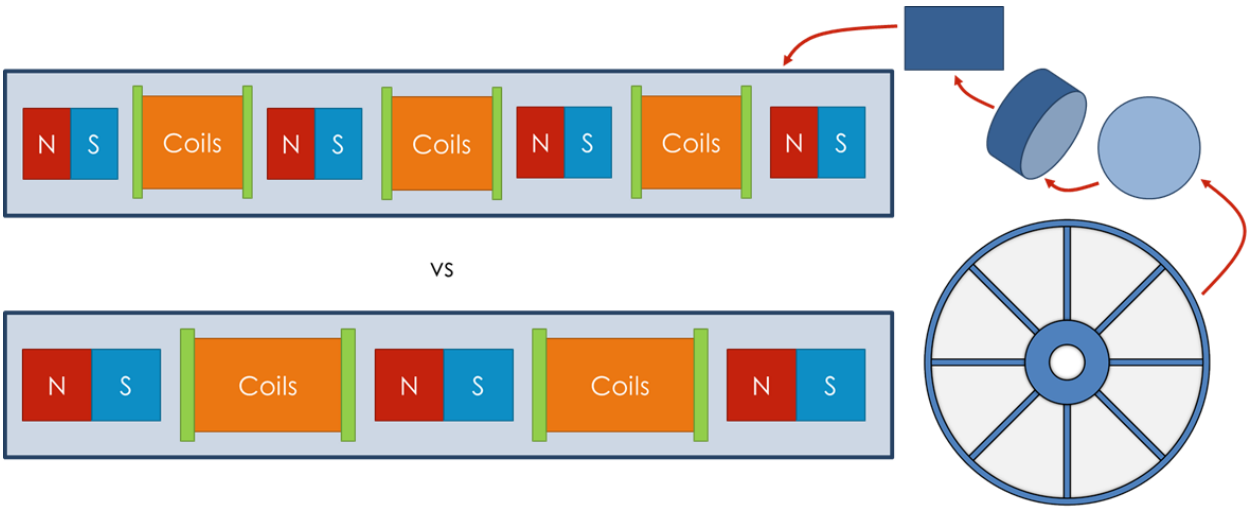

Figure 3.78 – Lengthwise illustration of component layout for varying number of stages.

To quantify the performance of a given configuration, it is first examined the magnetic field strength of the chosen magnet cross-section shape as a function of thickness. Magnet fields were simulated using the Magnet Calculator tool on the K&J Magnets, Inc. website (where the custom sized are magnets were purchased from, simulating N52 grade Neodymium magnets of the equivalent rectangular shape to the arc segments, as the Magnet Calculator only offers simulation

of several simple shapes. The simulations as a function of thickness are pictured in Figure 3.79 below.

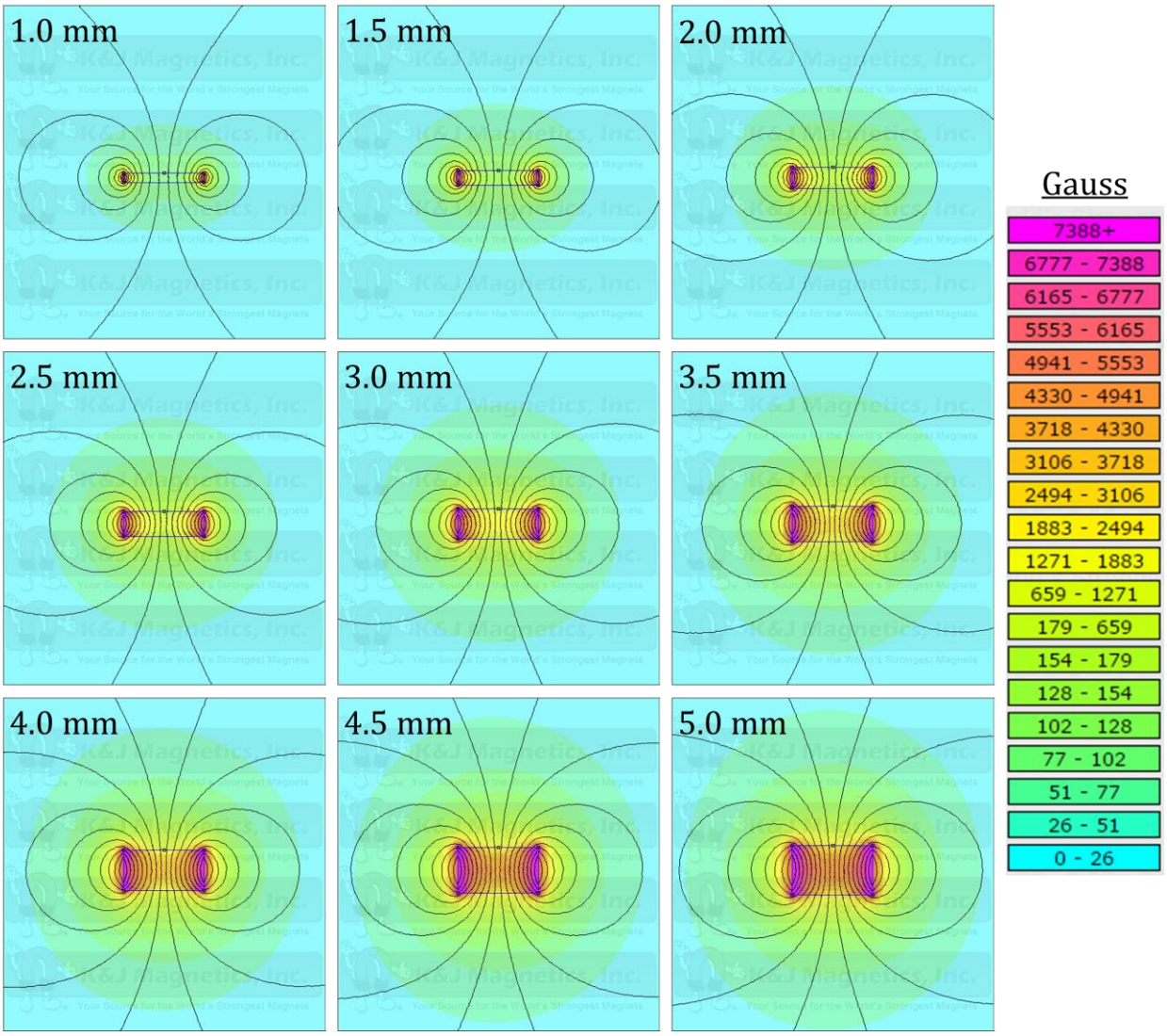

Figure 3.79 – Magnetic field simulation as a function of magnet thicknesses for magnet cross-section given in Figure 3.75.

It is clear from the simulations that magnetic field increases with thickness. From the simulations pictures it is however difficult to establish the trends which exist between field strength, thickness, and proximity to the magnet surface. Looking at the magnitude of the field vector directly above the center of the magnet, moving away from the surface in the vertical direction (shown as the red arrow on the inset of Figure 3.80), the surface plot of Figure 3.80

results. Here, the expected exponential decay in field strength as a function of distance away from the surface is observed, while the inverse relationship appears for magnet thickness, increasing with the root of thickness. This results from the fact that field strength is a volumetric function, and here only one aspect of the volume, the thickness, is varying.

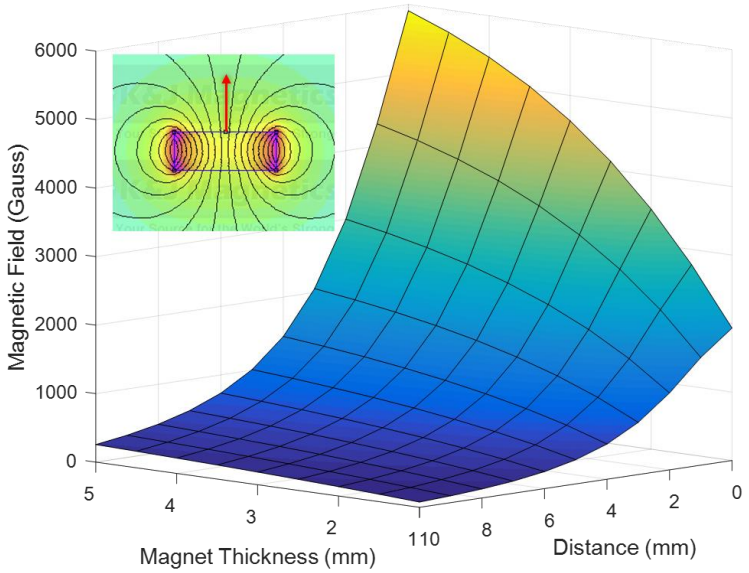

Figure 3.80 – Magnetic field strength as a function of magnet thickness and distance from the center of the top surface of the magnet, shown by the red arrow in the inset. Data taken from the simulation of Figure 3.79.

Knowing the field on a magnet by itself is a good starting point, but the beauty of the axial flux generator is that two oppositely poled magnets face each other across the coil face, concentrating the magnetic flux. Magnets far apart from one another do not appreciably interact with one another and their fields are as show in the simulations of Figure 3.79 and illustrated on the top picture of Figure 3.81. As the magnets are brought closer together the fields lines will tend terminate on the opposing pole of the nearing magnet, rather than arc in a larger loop back to its own opposite pole. For magnets with broad faces, like the ones used in this design, the fields becomes rather flat and concentrated between the two magnets, as shown in the bottom picture of Figure 3.81.

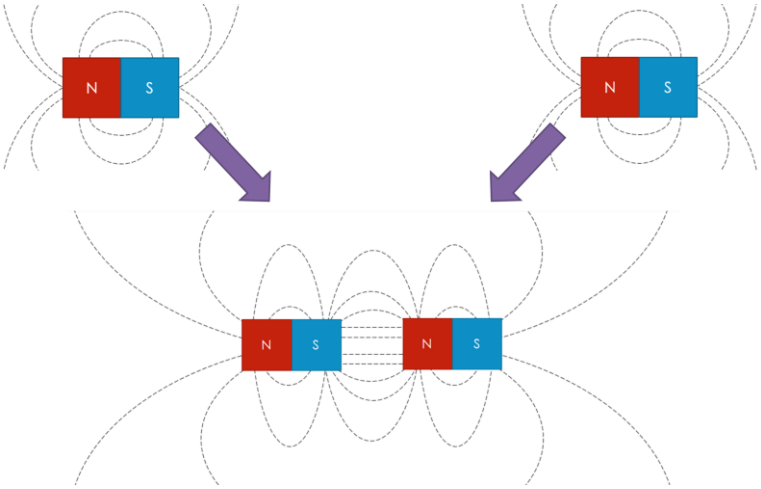

Figure 3.81 – Illustration of magnetic interaction of magnets far away and close together.

Since magnetic fields act as vectors, one would expect the fields of two magnets to add as vectors, and indeed they do. To simplify the interaction and get a sense of the mean magnetic field between two magnets, the data from Figure 3.80 is used to calculate the field strength at the center normal between two approaching magnets of varying thickness.

From the figure below it is observed that the magnetic fields are the same at either end of the curves, because this is where each face the opposing magnets would be. Between the magnets, the field distributes in a parabolic fashion. This is unsurprising since for a single magnet the field decays with the square of the distance away. As the magnets move further and further apart, the field between them drops significantly. Indeed, the simulation were continued for greater separation distances the field between the magnets could become negligible, however, this information is irrelevant in this study as it is the goal to maximize the field.

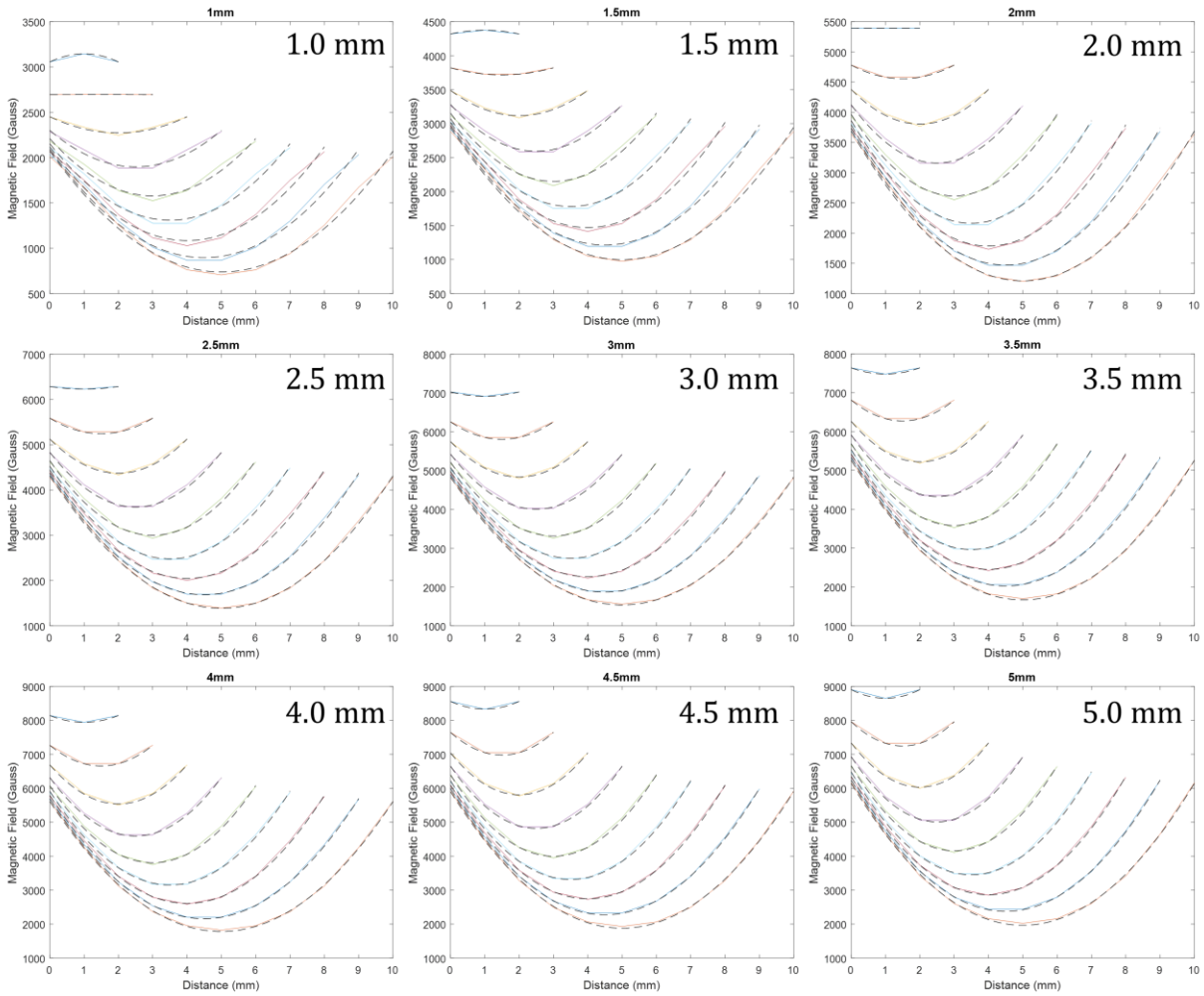

Figure 3.82 – Simulated magnetic field as a function of magnet thickness and separation distance, along the normal of the North face surface center line.

In the curves of Figure 3.82, there are colored solid line which represent the raw data, and the dashed black lines which represent a quadratic curve fit for each curve. The curve fit data was used to calculate the mean field strength for each curve. The resulting data is plotted on the surface plot below in Figure 3.83. Here the trends from Figure 3.80 remain largely intact, through the presence of another magnetic field akin to a simply supported beam, rather than a cantilever. As before, highest magnetic field results from the largest magnets being placed the closest distance together. Though, field strength does not drop off as quickly as before, at least in the sense of the mean field across the gap.

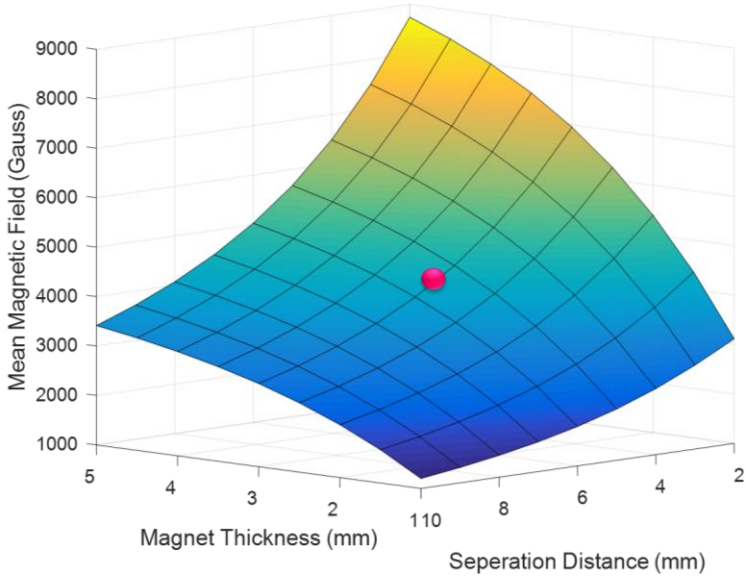

Figure 3.83 – Mean magnetic field between two attracting magnets of the cross-section shown in Figure 3.75 as a function of magnet thickness and separation distance between magnets. Magenta point represents chosen magnet thickness and separation distance to use in the design.

With all simulation of the magnets quantified, next the decision on final magnet thickness and separation distance can be made, concurrently with the consideration of coil depth, which determines the number of turns which can be made. First, the necessities of the manufacturing and assembly process are considered. The coil holder must have wall that extend up past the area form to contain the coils. Otherwise, the coils would slip off the side the form creating a mounded for, rather than the desired rectangular filling. These sides walls will have a 0.5mm thickness, as is considered the minimum wall thickness to create a sufficiently rigid wall bearing small loads, for the 3D printing process used to create this part. Next, a 0.75mm air gap between the coil stator and magnet rotor is chosen out of the manufacturing tolerances though to be achievable when assembling by hand with the various 3D printed parts, such to avoid any possible rubbing of the rotor against the stator which would naturally greatly hinder performance.

At this point, it can be ascertained that the separation distance between magnets must be,

$$Seperation\ Distance = 2 * air\ gap + 2 * wall\ thickness + coil\ depth\ \ , \qquad (3.18)$$

which, as defined by the manufacturing considerations, is a minimum of 2.5 mm (for zero coil depth). The coil depth then represents the key quantity in determining the magnet separation distance. As mentioned, the coil depth determines the number of turns which can be made via the

space available for packing the wire around the coil holder. Another key parameter comes into play here, which is the wire itself. So-called "magnet wire", used for making generators, is sold in AWG (American Wire Gauge) sizing, where the diameter of the single conductor wire in millimeters follows,

$$d_w = \quad 0.127 * 92^{\frac{36-AWG}{39}} + .0075\,, \tag{3.19}$$

where d_w is the wire diameter plus the insulator coating (~7.5 μm) and AWG is the wire gauge. Here it is noted that a smaller gauge wire is actually thicker than a larger gauge wire (e.g. 30 AWG wire is larger than 40 AWG wire). It is preferable to use smaller diameter wire as more turns can be had. The consideration then is the strength of the wire (will is break in the winding process?) and can it withstand the current which will be pushed through it (will it get too hot?), as smaller wires have more resistance and heat up at lower currents.

The number of turns which can fit into the coil holder cross-section can be approximated by comparing the coil holder's wire holding area, to the wire's cross-sectional area and a fill factor, f_f, determined by the arrangement of the wires. This fill factor is the comparison of the available space to the space occupied by the circular wires, and is illustrated in Figure 3.84 below.

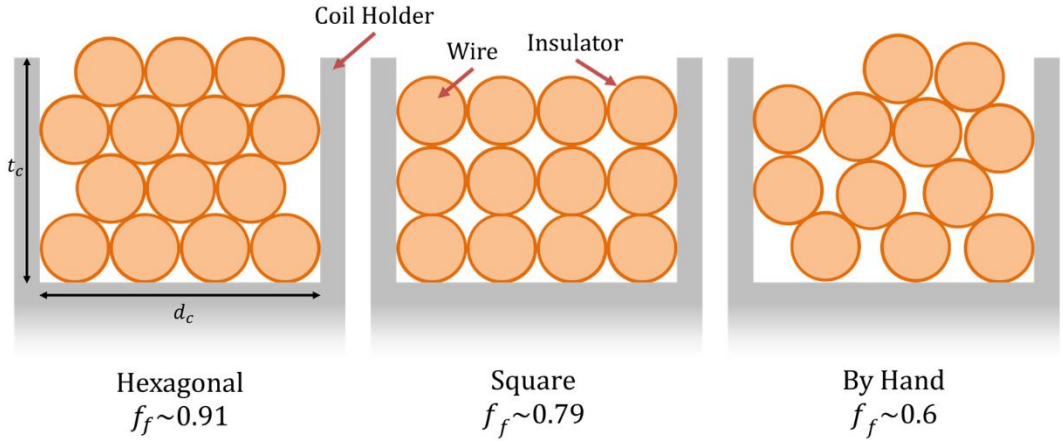

Figure 3.84 – Fill factors for the theoretical best packing scheme, Hexagonal, next best, Square, and illustration of type of packing achieved when done by hand.

The coil holder's wire holding area has a rectangular shape according to the thickness of the coil, t_c, which was previously defined in Figure 3.76 to be 2 mm, and the depth of the coil, d_c, which is to be determined. The theoretical best means to pack equal circles in a rectangle is the

hexagonal pack, yielding a fill factor of approximately 91%. Many other packings are possible, though in reality when manufacturing the coils by hand, a fill factor of approximately 60% has been observed, and will be used calculations. Thus, the number of turns which could be expected from a single coil is,

$$N_t = \frac{t_c d_c}{\frac{\pi}{4} {d_w}^2} f_f \, . \tag{3.20}$$

Then, the total number of turns used to calculate the voltage output of a single phase would be,

$$N = N_t N_{cpp} N_{cs} \, , \tag{3.21}$$

where N_{cpp} is the number of coils per phase, which equals two for the design given, and N_{cs} is the number of coil sections, which is yet to be determined.

After much consideration and examining many possible configurations, the layout illustrated in Figure 3.85 was decided upon. The five stages fit uniformly into the Generation 4 housing when a 3 mm magnet rotor with 5.5mm spacing. With all considered spacing and wall thicknesses, this leaves the coil depth to be 3 mm per stage. This operating point is shown with a magenta dot in Figure 3.83.

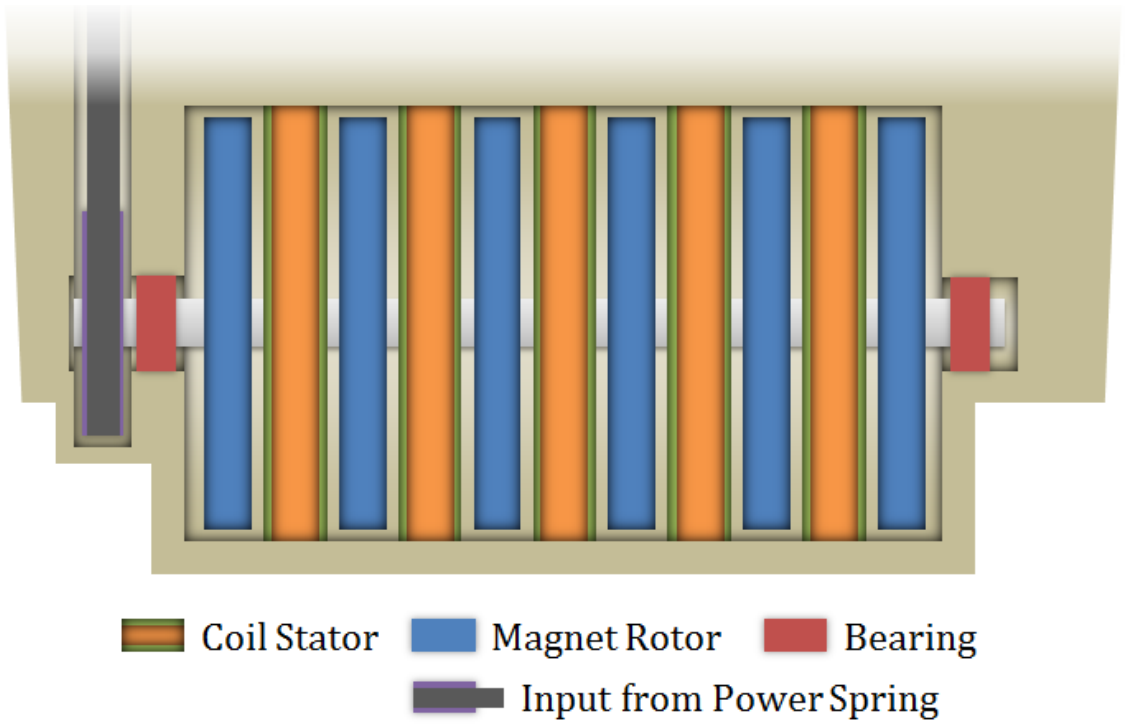

Figure 3.85 – Illustration of chosen generator layout within the Generation 4 mechanism housing.

Knowing the final layout, the mean magnetic field through the coils can be found. Figure 3.83 shows the mean field between magnets of a given spacing, through the coil does not fill this spacing, as there is the air gaps and coil holder wall thickness. The mean magnetic field through the coil is found in Figure 3.86 to be 3840 Gauss.

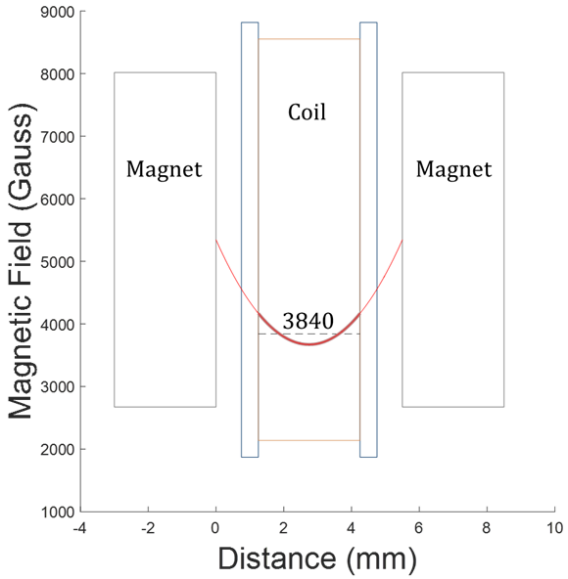

Figure 3.86 – Scale drawing (longitudinally) of magnets and coil spacing, with mean magnetic field in the coil noted.

Next, with all parameters of the generator now known, to establish the performance of the device some analytical modeling was performed. The interaction of the generator with the power spring input can be modeled as a second order differential equation of the form,

$$\begin{cases} J\ddot{\theta} + \dfrac{P}{\dot{\theta}} + (c_b) = K(\phi) & \phi > 0 \\ J\ddot{\theta} + \dfrac{P}{\dot{\theta}} + (c_b + c_{cb}) = 0 & \phi = 0 \end{cases}, \tag{3.22}$$

where the power spring winding angle, ϕ, is greater than zero, the generator receives torque, $K(\phi)$, from it according to the curves of Figure 3.66 and Figure 3.68. After the spring is unwound (i.e. $\phi = 0$), the spring is decoupled from the generator via the clutch bearing, which is why the forcing term goes to zero and the term for the clutch bearing free-wheel friction, c_{cb}, appears. The term,

c_b, is the frictional torque of the ball bearings supporting the generator. c_{cb} is taken be a 2 mNm [180], while c_b is assumed as 0.5 mNm. The mass moment of inertia of the generator, J, is

$$J = \frac{1}{2} m(r_o^2 - r_i^2) \tag{3.23}$$

where,

$$m = \pi(r_o^2 - r_i^2) t_m \rho_{neo} (N_{cs} + 1) \quad . \tag{3.24}$$

Here, t_m is the thickness of the magnets (3 mm) and ρ_{neo} is the density of neodymium magnets (7.5 g/cm^3)[181]. P is the instantons power produced by the generator and θ the angle of rotation of the generator. The generator power divided by the rotational speed, $\dot{\theta}$, yields the counter-torque of the generator, which is the resistance to motion caused by the energy conversion. This damping is a key reason why the generator needs to be decoupled from the human body motion. Power is calculated as,

$$P = \frac{V_o^2}{R_L} \ , \tag{3.25}$$

where V_o is the output voltage, or the greatest of the rectified three phases, across load resistance, R_L, as the simulation takes into account the three phase rectifier circuit given in Figure 3.73b). The instantons voltage of a phase of the generator is,

$$\mathrm{V_o} = \max\left(\begin{vmatrix} NAN_p \dot{\theta} B_m \sin(N_p \theta) - V_{diode} \\ NAN_p \dot{\theta} B_m \sin\left(N_p \theta - \frac{2\pi}{3}\right) - V_{diode} \\ NAN_p \dot{\theta} B_m \sin\left(N_p \theta - \frac{4\pi}{3}\right) - V_{diode} \end{vmatrix} \right) \frac{R_L}{R_L + R} \ , \tag{3.26}$$

where N_p is the number of poles of the generator (eight), B_m is the mean field strength (from Figure 3.86), and V_{diode} is the forward voltage drop across the rectifier diodes, which is taken to be 0.7 Volts for a standard silicon diode. Note Equation (3.26) is valid when the electromotive force is greater than V_{diode}, and otherwise $V_o = 0$. The resistance of the generator windings, R, is,

$$R = \frac{\rho_w L_w}{\frac{\pi}{4} {d_w}^2} \ , \tag{3.27}$$

where ρ_w is the resistivity of the wire (copper ~1.7×10^{-8} Ω-m) and L_w is the length of the wire through each phase, found by,

$$L_w = Np \ . \tag{3.28}$$

Finally, the output current is found by,

$$I_o = \frac{V_o}{R_L}. \tag{3.29}$$

With all parameters defined, the above equation were discretized and solved in MATLAB. The simulation takes into account the timing of the winding and release of the power spring in accordance with the gait data collected in Section 3.6. The simulation mimics a person walking at approximately 3 mph (1.3 s step period), with a temporal resolution of 1 ms. In the simulation, one chooses the power spring to use, and the winding angle per step, ϕ_0, along with the wire gauge to employ.

Being the only driving force in the system, the power spring governs the performance of the design. In this chapter, six different power springs are fabricated and measured. It was found that the largest power spring (1 inch width, 0.008 inch thickness) yielded the best performance. Using a realistic winding angle per step and wire gauge, the simulated results are shown in Figure 3.87 below.

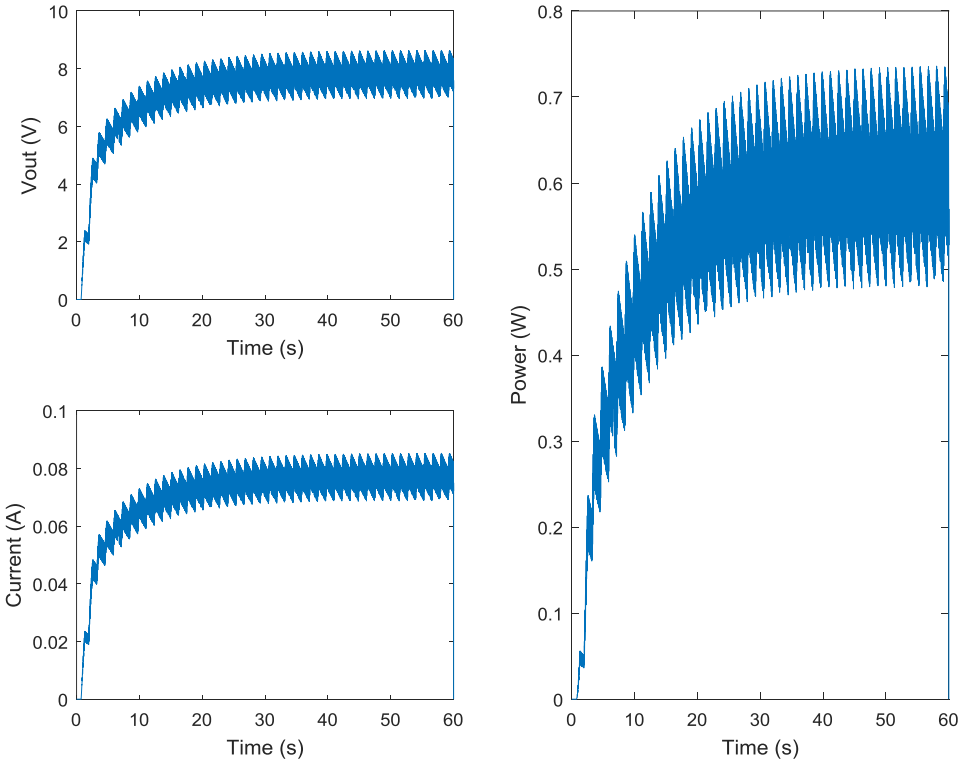

Figure 3.87 – Simulated voltage, current, and subsequent power output for continuous walking of one boot when $\phi_0 = 720°$, the 1 inch wide, 0.008 inch thick power spring from Figure 3.68 is used, and the wire is 38 AWG.

Since the generator is composed of several stages of magnet rotors, it does have quite a bit of inertia thanks to the density of the magnets and maximized generator diameter. For this reason, it takes several steps for the generator to reach steady-state speed and thus steady-state power output. In the case above it takes about 15 steps to reach the steady-state power output of around 600 mW. The power output then naturally fluctuates as each step the power spring speeds up the generator before it is unwound and the generator speed again decays through the counter-torque damping, and friction.

This type of action could be thought of like a basketball player spinning the basketball on the tip of their finger. Initially, the player springs the ball as hard as possible while tossing it onto their finger. Though, at that time the spin is still not fast enough. Therefore, the player slaps the tangential edge of the ball several times with the opposite hand, until the ball reaches a steady-state rotational speed.

4 POWERING PERIPHERAL WIRELESS DEVICES: OCCUPANCY SENSORS IN SMART BUILDINGS

4.1 Introduction

The increasing reliance of society on technological applications within the building environment has resulted in a necessity to find methodologies for reducing overall power consumption. In this decade, energy consumption in the United States has risen to more than 93 quadrillion Btu per year, with around 41% of this energy consumption coming from buildings in the residential and commercial sectors [182]. The concept of the smart building, or a building that is aware of its occupancy and power consumption, can help in reducing the overall power draw of buildings [183]. Specifically, significant improvements can be made in the highest power consuming building functions, such as HVAC and lighting, by controlling them in real-time based upon building occupancy information [184, 185]. However, the increased number of sensors necessary to realize the smart building concept can also lead to extra power draw and complexity in wiring. Therefore, a self-powered occupancy sensor (one not requiring grid or battery power) would be of great benefit and major step toward realizing the smart building concept. Such a device must then power itself by deriving the energy from its environment. To fill this need, a floor tile energy harvester is proposed for the purpose of creating a wireless and self-powered occupancy sensor. This "Smart Tile Energy Production Technology (STEP Tech)" developed in this dissertation could provide a versatile way to automate and control various functions in smart buildings, such as lighting and climate control, based upon the real-time building occupancy mapping. In realizing such a device, there are several challenges that need to be addressed: (i) selection of the electromechanical transducer, (ii) modeling and optimization of the electromechanical transducer, (iii) development of a packaging technique and construction of a durable floor tile enclosure that can not only protect the transducer but also the harvesting circuitry, and (iv) integration of the tile harvester with the wireless controls. In addition, there should be limited deflection of the tile to a level on the order of the deflection of shoe soles, so that the gait of the human occupants within the building is not disturbed as they walk over the tile.

In order to not disturb the motion of occupants in the building, the operation of a floor tile energy harvester should most closely mimic that of a normal floor surface in terms of appearance

and mechanical stiffness. For this reason, STEP Tech tiles are designed to be placed directly below the top floor surface (e.g. carpet, laminate, decorative tile, etc.), as is illustrated in Figure 4.1(a), so that the floor surface appears normal. STEP Tech is also designed to fit the dimensions of standard size decorative tiles (12in x 12in) and be as thin as possible, so that it can be easily retrofitted into existing tile or other flooring alternatives. Additionally, STEP Tech is meant to be placed at doorways or at boundaries between rooms and building sections, so that when stepped upon, a signal is wirelessly transmitted to the centrally located smart building receiver/controller, as depicted in Figure 4.1(b). In this manner, real-time occupancy of individual rooms within a building can be recorded and used, for example, to turn the lights on/off (Figure 4.1(a)).

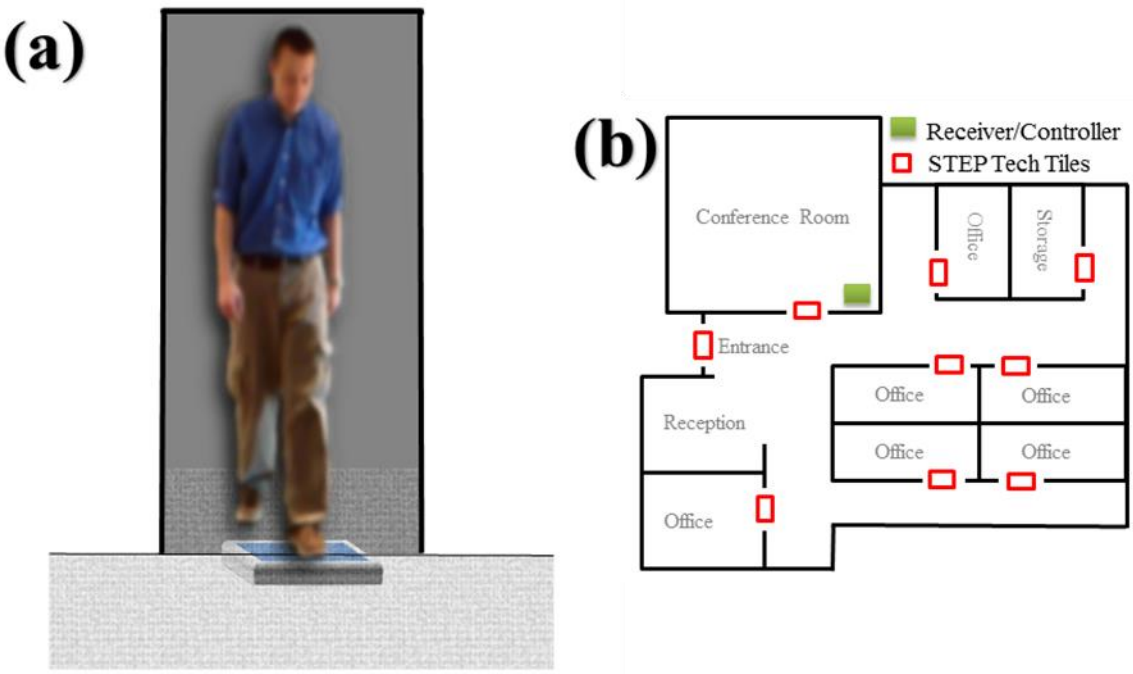

Figure 4.1 – Illustration of (a) intended placement of individual STEP Tech tiles under floor surface in doorways and (b) distribution of STEP Tech tiles in a sample floor plan.

Mechanical stiffness of walking surfaces plays a key role in controlling many aspects of the human gait cycle, as we are very perceptive to even small changes in stiffness (or cushioning) of walking surfaces [186]. Therefore, a floor tile energy harvester must feel (i.e. have similar stiffness and deflection) like a normal floor, if it is to avoid the perception of building occupants

and not alter their normal gait patterns (i.e. not affect their normal behavior). If an area of the floor is perceived as different, individuals will avoid (i.e. simply step over) those areas, and thus the data on room occupancy will have inherent inaccuracy. While terrestrial locomotion of humans is capable of many different adaptations [150], a sudden change in ground conditions (i.e. stepping on a "soft" tile) is not desirable. This consideration is a hindrance to the energy production of the tile, as available potential energy to be harvested is in direct proportion to the tile deflection. Though, when harvesting energy from humans, consideration of human behavior is of paramount importance.

4.2 Transducer Selection

Previous efforts on floor tile energy harvesters have been left largely to the commercial sector, and have relied on linear to rotation conversion mechanisms to change the vertical deflection of the tile surface into rotary motion for induction generators [187-190]. These studies have reported vertical deflections of around 10mm that is dependent on the applied force (i.e. body weight). These relatively large deflections have been generally accepted, as the novelty and "greenness" of this technology has, thus far, outweighed the encumbrance. Allowable floor deflections are not only left to subjective human perception, but also objectively defined by law [191]. Section 1604.3.1 of the Virginia Construction Code defines the maximum allowable deflection of floor members subject to live (i.e. human, animal) loads as $l/360$, where, l, is the length of the floor member. By this rule, both the Pavegen [187] (600mm in length dimension = 1.67mm allowable deflection), and Sustainable Dance Floor [188] (650mm in length dimension = 1.8mm allowable deflection) would not be allowed to be installed in buildings in the state of Virginia, as they exceed allowable deflections limits by several times.

Since electromagnetic transducers require unacceptably large tile deflections, a piezoelectric transducer is sought for this high-force, low-displacement application. Many shoe-mounted piezoelectrics from the literature rely on forced bending to stress the piezoelectric materials [163]. This approach is acceptable for shoes, which will last a couple of years, however, for a tile, which must last some tens of years, this technique will become less effective over time. Piezoelectrics may also be stacked in a column and compressed in the d_{33} direction [192]. It is preferable to use piezoelectrics in the d_{33} mode, as it is typically 2-3 times larger than the d_{31}

coefficient [193]. However, for d_{31} mode transducers, mechanical amplifiers can be used to manipulate the input forces, as exemplified in the cymbal transducer. Instead of using the cymbal shape to increase displacements as an actuator [194, 195], it can be used to increase the force on the piezoelectric materials as an energy harvester [196-198]. It has been shown that rather than using a circular cymbal, a rectangular cymbal could be used to take better advantage of the crystal orientation in the piezoelectric material [199].

4.3 Modeling

Prior studies on the cymbal transducer have mostly utilized finite element simulation and experimental methods [194-199] to predict the behavior of cymbal shape. However, a simplified analytical model is lacking that can be used on a regular basis for the design and performance optimization. With an analytical model, one can easily examine the performance of different geometries in order to identify the optimum for a given set of boundary conditions. After the optimum dimensions have been identified, finite element analysis can be conducted to verify the predictions of the analytical model. This dramatically reduces the quantity of experimentation required to achieve the desired results. In this study, this thought process is followed to arrive at the optimum STEP Tech tile.

4.3.1 Analytical

Analysis is begun by first defining the schematic representation of the cymbal transducer, shown in Figure 4.2(a). The vertices of the angle bends in the end caps are labeled A-F so as to identify the individual segments of the cymbal by the lines connecting the two points. Distributed load, P, is applied to section BC, and section EF is considered to be resting on a rigid surface.

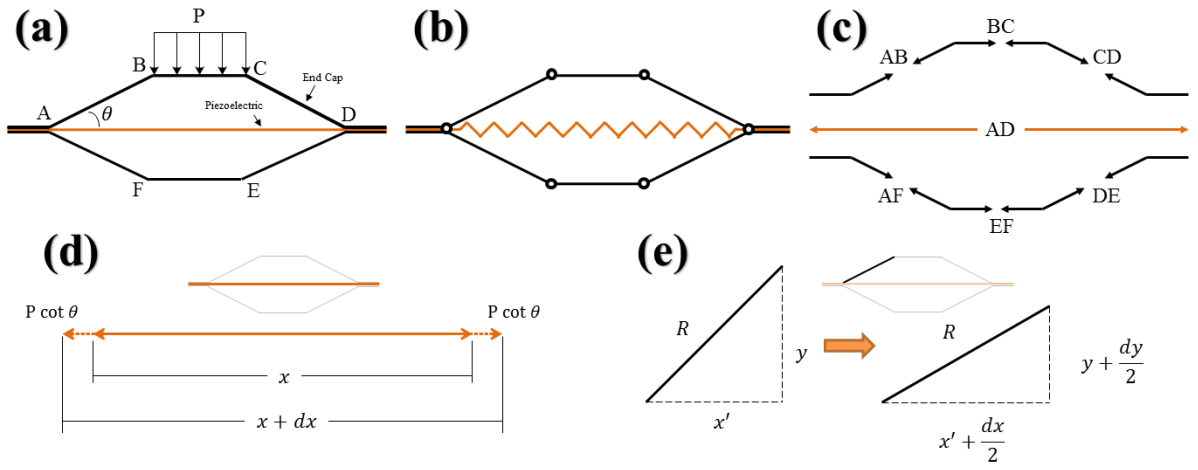

Figure 4.2 - Schematic representations of analytical model with cymbal end caps in black and piezoelectric material in orange, and (a) diagram of cymbal with labeled points and applied force, (b) diagram with ideal model assumptions, (c) illustration of force sign in the cymbal members, (d) member responsible for horizontal (x-axis) deflection and (e) member responsible for vertical (y-axis) deflection.

Following the assumptions of Fernandez et al. [194] that cymbal end cap bends behave as pin connected joints and the end cap members are rigid, such that there is no energy loss due to end cap bending, the conjecture is added that the bulk piezoceramic between the end caps behaves as a stiff spring. These assumptions are represented in Figure 4.2(b). Therefore, each cymbal section is considered to be a simple truss, and the force distribution in the structure is solved using the method of joints. Figure 4.2(c) shows the sign of the force in each section, with the cymbal end caps being in compression, and the piezoceramic layer being in tension. By the method of joints,

$$AB = CD = DE = AF = \frac{P}{2\sin\theta}\ , \tag{4.1}$$

and

$$BC = EF = \frac{P}{2}\cot\theta\ . \tag{4.2}$$

Therefore,

$$AD = P\cot\theta\ . \tag{4.3}$$

It is worth noting here that the cotangent of the angle θ essentially acts as an amplification factor to the applied force, P, as for any angle θ less than 45°, the $\cot\theta$ is greater than one.

With force exerted on the piezoelectric layer known, it can now be examined the resulting deflections of the cymbal in both the horizontal (x-axis) and vertical (y-axis) directions. The deflection in the horizontal direction is caused by the lengthening of the piezoelectric layer under tensile forces, and following the assumptions for a member with initial length, x, the deflection, dx, as shown in Figure 4.2(d), is equal to,

$$dx = \frac{(P \cot\theta)x}{E_p A}, \tag{4.4}$$

where, E_p, is the Young's modulus of the piezoelectric, and, A, is the cross-sectional area of the piezoelectric layer, which for a rectangular cymbal is the thickness of piezoelectric, t_p, multiplied by its depth, b. The elongation of the piezoelectric materials in the horizontal x-direction is accompanied by a subsequent compression of the end caps in the vertical y-direction. Examining one of the slanted segments of the cymbal end cap, such as segment AB, it has some initial length, R, and rectilinear components x' and y. From the assumption of rigid cymbal end cap members, as deflection occurs, the length of segment AB remains R, however, the rectilinear components are given the addition of $dx/2$ and $dy/2$ respectively, as is presented in Figure 4.2(e). The deflections are halved in this case since the cymbal structure is symmetric about the center planes of the horizontal and vertical axes, and the analysis is of a single end cap segment. Finally, with this information the deflection in the y-direction can be solved for, by applying the Pythagorean Theorem to the deflected segment in Figure 4.2(e), where it's found that,

$$dy = 2\left[\sqrt{R^2 - \left(x' + \frac{dx}{2}\right)^2} - y\right]. \tag{4.5}$$

Note that for this application, where the cymbal transducer is used as an energy harvester, the quantity, dy, will always be negative.

After establishing Equations (4.1)-(4.5), it becomes evident that the performance of the cymbal transducer is largely dependent on the angle, θ, which is governed by the cymbal height, h, and inner width, d_i, labeled in Figure 4.3(a). Using the analytical model presented thus far, the plots in Figure 4.3(c)-(h) are generated employing the values in Table 4.1, with Figure 4.3(b) offering a qualitative illustration of cymbal cap geometry over the parametric sweep of d_i and h. The applied load, P, for these simulations is 80 N, which is several times smaller than an average adult's weight, but was chosen because multiple cymbal transducers will be used inside the floor

tile, which will distribute the applied load. The determination of the number of cymbals is described in the later sections.

Table 4.1 – Model parameter values used for plots in Figure 4.3.

Parameter	Unit	Value	Description
P	N	80.0	Applied load
d_c	mm	50.0	Overall width of cymbal
d_o	mm	40.0	Width of outer cymbal bends
d_i	mm	1.0 - d_o/2	Inner width of cymbal
h	mm	1.0 - d_o/6	Height of cymbal cap
E_p	GPa	63.0	Young's Modulus of piezoelectric (PZT)
t_p	µm	508.0	Tickness of piezoelectric
b	mm	50.0	Overall length of cymbal
E_c	GPa	200.0	Young's Modulus of end caps (Steel)
ν_c	-	0.3	Poisson Ration of end cap (Steel)
t_c	mm	0.1 - 1.0	Thickness of end caps

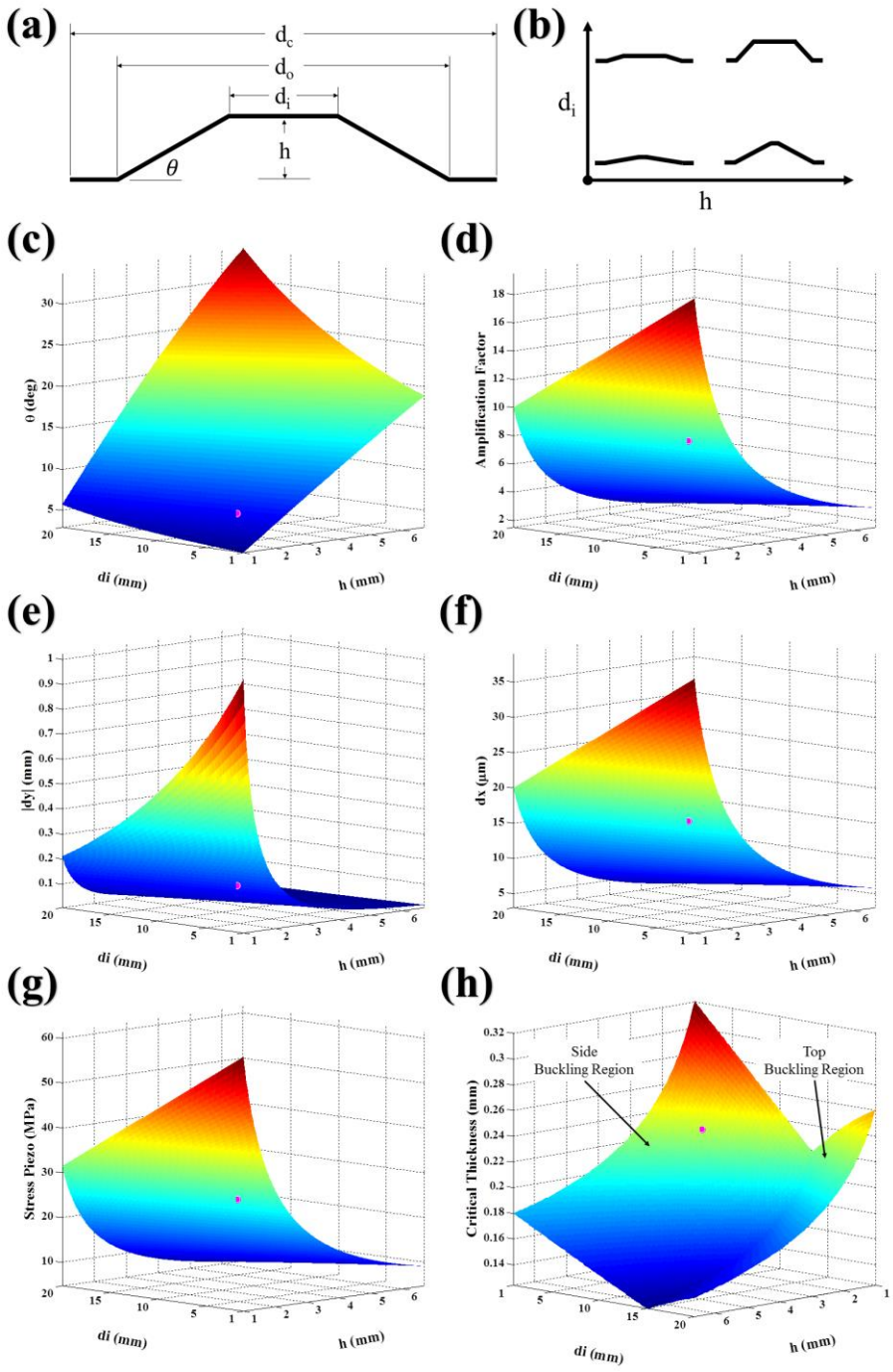

Figure 4.3 – Results of cymbal transducer analytical modeling with (a) notation of model parameters, (b) qualitative illustration of cymbal geometry as function of parameters d_i and h. Plots (c)-(h) reveal the dependency of angle θ, Amplification Factor, magnitude of dy, dx, Stress in the piezoelectric layer and Critical Thickness (to buckling) of cymbal end caps, respectively. All responses are to a static 80N load.

From Figure 4.3(d) it can be seen that the largest amplification factors (the cotangent of Figure 4.3(c)) are observed where d_i and h become small. Naturally, as amplification factor is increased, higher force is applied to the piezoelectric layer, subsequently increasing the magnitude of displacements in both x (Figure 4.3(f)) and y (Figure 4.3(e)) directions. However, the deflection in the y-direction, which is what would be felt by the person stepping on the tile, is still significantly small, thus meeting the tile design requirements. The stress in the piezoelectric layer, plotted in Figure 4.3(g), is a direct result of x-direction displacement and follows the same profile as Figure 4.3(f). Certainly, the higher the amplifications factor, the more energy can ultimately be harvested per footstep on the tile. However, the limiting factor is the stress in the piezoelectric layer, which for the chosen material (APC 850) has a yield strength of approximately 36 MPa [193].

In order to realize the assumption that a negligible amount of energy is lost to bending of the cymbal end caps, the end caps themselves must be as thin as possible, up to the point where they fail due to buckling, as they are under compression. The cymbal end cap members are treated as pinned-pinned plates under axial compression, as per the assumptions. The critical load for plate buckling is found using Euler's formula,

$$P_{cr} = \frac{\pi^2 EI}{L_e^2}, \tag{4.6}$$

where P_{cr} represents the minimum load which can be applied to a plate before causing buckling, E the Young's modulus of the material, I the moment of inertia and L_e the effective length (a multiple of the physical length, determined by the boundary conditions). For this case, a load is prescribed and it is then found the necessary geometry to support that load. Equation (4.6) is then re-written as,

$$P = \frac{\pi^2 E_c \left(\frac{1}{12} b t_{c_{min}}^3\right)}{(1-\nu_c^2)a^2}, \tag{4.7}$$

where the effective length is now $(1-\nu_c^2)a^2$, because pinned-pinned joints are assumed [200]. Here ν_c is the Poisson's ratio of the cymbal end cap, a is the physical length, b the width and $t_{c_{min}}$ is the minimum end cap material thickness necessary to prevent buckling due to prescribed applied load, P. Next, Equation (4.7) is solved for the minimum thickness,

$$t_{c_{min}} = \left(\frac{12P(1-\nu_c^2)a^2}{\pi^2 E_c b} \right)^{\frac{1}{3}}. \quad (4.8)$$

The cymbal structure can experience buckling either on the slanted side sections or along the top member, depending on the relative values of d_i and h. Therefore Equation (4.8) makes two distinct curves as a takes the value of d_i to examine buckling in the top section and takes the value of R to examine buckling in the slanted side section. These two curves are plotted in Figure 4.3(h), where the greater of the two solutions is displayed for the varying geometry.

With this analysis, cymbal dimensions were chosen such that the stress in the piezoelectric layer would be approximately 75% of the yield strength, giving a Factor of Safety of 1.33, while keeping y-axis deflection at a minimum. The Factor of Safety is kept low to maximize the performance, and because the tile will be protected from overloading, as is described in a later section. Other considerations were to keep the height of the transducer small, such that the overall height of the floor tile could remain slim, making it easier to install in a floor, and keeping the inner width of the cymbal (d_i) large enough, such that the top plate of the floor tile could have a good surface to rest upon. The chosen design point is highlighted on plots of Figure 4.3 with a magenta marker and corresponds to d_i = 5mm and h = 2mm. For this geometry, the cymbal end caps would need to be at least approximately 230μm thick. In keeping with the Factor of Safety of 1.33, the next closest available material thickness (material sold in standard thicknesses) was chosen to give t_c = 305μm.

4.3.2 Finite Element

To check the validity of the analytical model and assumptions prior to fabrication, a finite element analysis of a cymbal transducer of the dimensions chosen in the previous section was conducted. The dimensions are detailed in Figure 4.4(a), along with the mesh view overlaid on the cymbal transducer assembly. The material properties for the steel end caps and PZT piezoelectric layer were estimated using the available material information and were identical to that used in the analytical model, listed in Table 4.1. The interface of the cymbal end caps and piezoelectric layer was taken to be rigidly bonded. This analysis considers 32,115 tetrahedral elements with an equivalent 80N distributed load applied across the top surface of the transducer and was conducted using the Stress Analysis Environment of Autodesk Inventor Professional 2013.

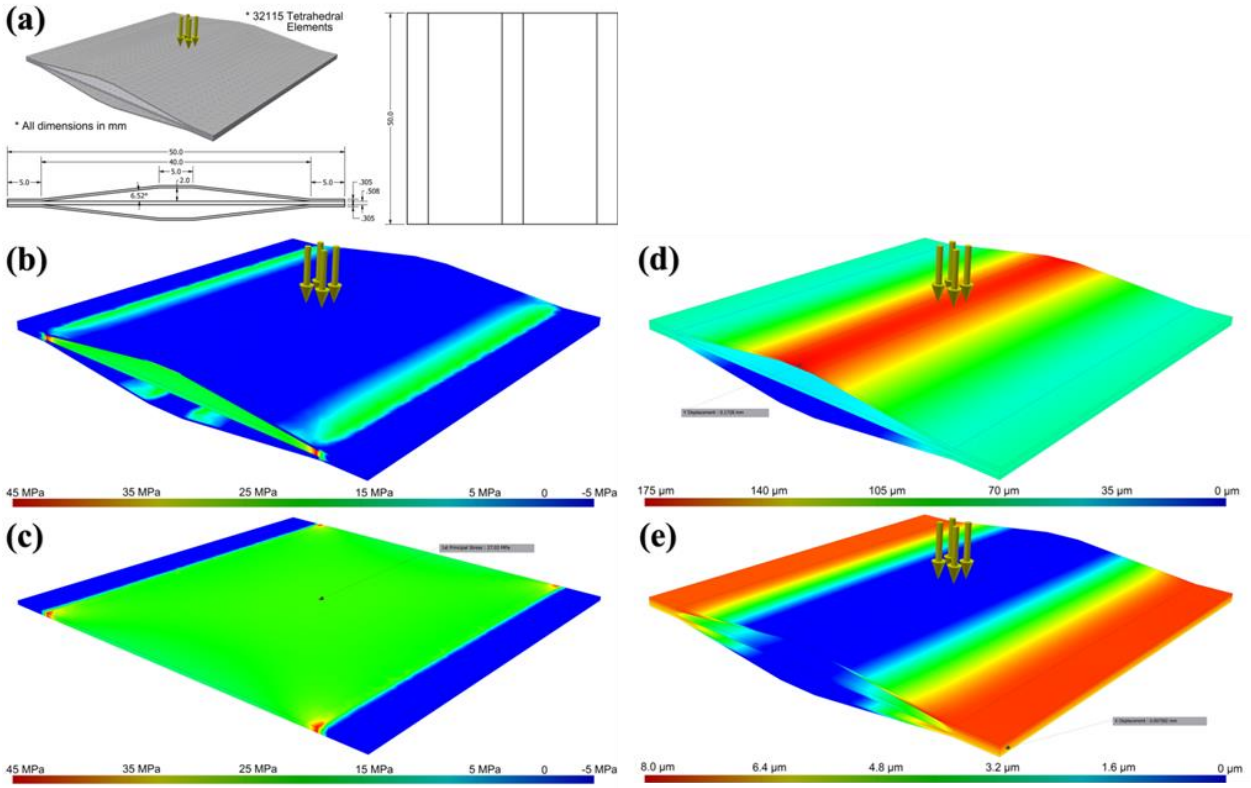

Figure 4.4 – Results of finite element analysis of cymbal structure subject to an equivalent 80N distributed static load across top surface using 32115 tetrahedral elements with (a) model dimension drawings and finite element mesh, (b) first principal stress of assembly, (c) first principal stress in piezoelectric layer, (d) vertical (y-axis) displacement and (e) horizontal (x-axis) displacement.

Table 4.2 – Comparison of Analytical Model and Finite Element Analysis of the cymbal assembly of the chosen dimensions. Analytical Model shows good agreement with FEA and discrepancies are due to the small amount of bending in the cymbal caps.

Parameter	Unit	Model	FEA
dy	µm	156.6	172.8
dx	µm	17.52	15.16
Piezo Stress	MPa	27.6	27.03

Examining Figure 4.4(b), where the coloring represents the First Principal Stress, it is shown that the cymbal end caps are largely in uniform compression within each segment, with only a slight amount of tensile stress on the surface by the obtuse angles due to the occurrence of some finite bending in that region. Looking at the First Principal Stress in just the piezoelectric layer, shown in Figure 4.4(c), it is found that this layer is in uniform tension, with the exception of stress concentrations in the corners caused by material necking as it meets the bonded boundary condition. The dark colored regions on either end of the piezoelectric layer are located where the end caps are bonded and are in slight compression to support the vertical component of the reaction load applied by the end caps. Vertical (y-axis) displacement of the cymbal transducer is shown in Figure 4.4(d) and horizontal (x-axis) displacement is shown in Figure 4.4(e). Note the displacement in the horizontal direction is axisymmetric and thus the displacement, dx (elongation of the piezoelectric layer), is taken to be twice the maximum value of the Figure 4.4(e).

A comparison of the results from the analytical and finite element models is shown in Table 4.2. Here, there is good agreement between the two models, with the slight differences being attributed to the bending of the cymbal end caps, which is neglected in the analytical model. The bending predicted by the FEA gives additional vertical displacement, dy, which subsequently takes away from horizontal displacement, dx. This energy loss is then reflected in the slightly reduced stress observed in the piezoelectric layer. The analytical model was subsequently concluded to be sufficiently accurate and a slightly conservative representation of the performance of the cymbal transducers in this specific application.

4.4 Fabrication

The cymbal transducers deflect only a small portion of their height (around 3%) when fully compressed. For this reason, it is necessary to develop a manufacturing technique such that the dimensions of each of several cymbal transducers in the floor tile are most nearly the same. Therefore, a press-brake manufacturing technique was adopted in order to produce a consistent cymbal end cap. The press, shown on the left, and the brake, shown on the right, in Figure 4.5(a), were machined in a Tormach PCNC 1100 mill in a slightly exaggerated profile to allow for spring-back in the steel end caps after pressing. Flat pieces of steel shim were inserted into the press brake and bent into the desired shape, as seen in Figure 4.5(b). The bending pressure was applied by a

hydraulic press, shown in Figure 4.5(c), operating at approximately 20kpsi. Piezoelectric elements were then packaged (discussed in a later section) as shown in Figure 4.5(d). The elements were arranged in five parallel 60mm by 10mm pieces rather than one 50mm by 50mm piece due to material availability. The assembly was then bonded together using Loctite 120HP epoxy, which was allowed to cure in a kiln at 65°C for no less than 12 hours. The completed assembly is shown in Figure 4.5(e).

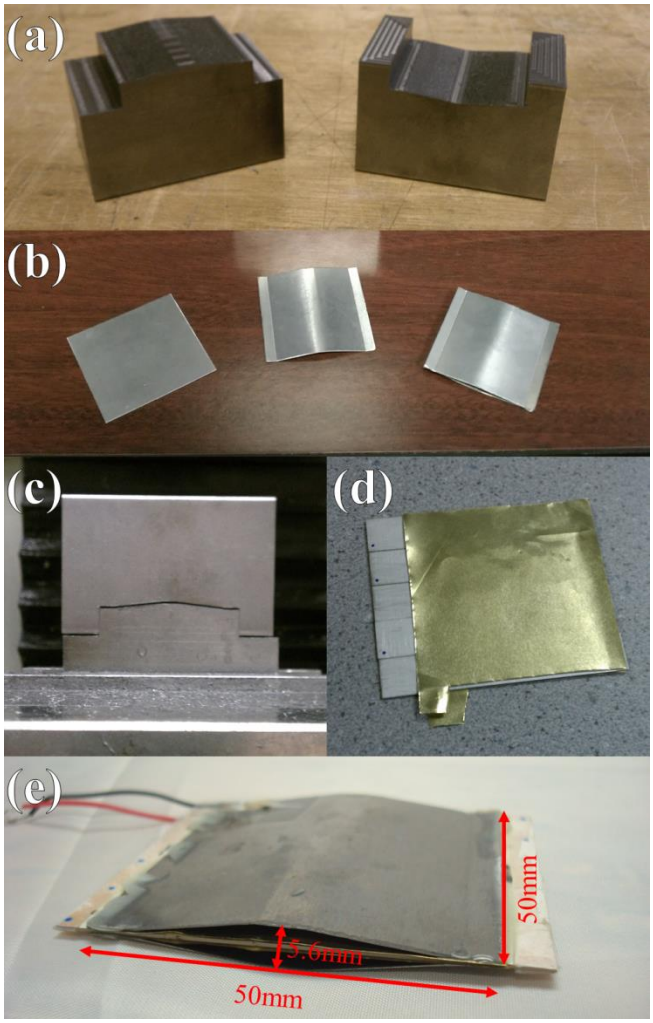

Figure 4.5 – Manufacturing process for production of cymbal transducers whereby (a) press (left) and brake (right) are machined and used to bend (b) flat pieces of steel into shape when under pressure from (c) a hydraulic press. (d) Piezoelectric elements are then packaged and (e) the assembly is bonded together using epoxy.

4.5 Testing Procedure

In order to verify the performance of the cymbal transducers in the target application, it is necessary to have the ability to impose a repeatable force input onto the system. The force applied to the ground during walking varies from person to person and even between steps made by the same person. Thus, I first seek to find a mechanical means of applying force onto the cymbals so that the same force profile may be applied across multiple tests. This will allow for comparative analysis across a range of cymbal variables. To establish the requirements of the mechanical test stand, I first institute the force profile that needs to be simulated. In prior work, Martin and Marsh [201] have provided the ground reaction force for persons walking at their preferred pace, from which the fourth-order polynomial curve fit in Figure 4.6(a) was derived. The curve was obtained under the assumption that the first peak (heel strike) occurs at 25% of the contact time, the trough (when both feet are on the ground) occurs at 50% of the contact time, and the second peak (toe-off) occurs at 75% of the contact time. The constraints were also set such that the first and second peaks were of the same approximate amplitude, which is true under steady-state walking, and the curve tends to zero at 0% and 100% contact time. With these constraints in place, the coefficients of the polynomial were solved as a function of T, the total contact time (i.e. period of the step), F_p, the peak force, and F_v the force in the valley of the curve as shown in Figure 4.6(a). The values of T, F_p, and F_v were chosen to be 0.63, 1.17, and 0.7, based on the findings of Martin and Marsh [201]. Note the ground reaction force (Vertical Force in Figure 4.6(a)) is given as a multiple of body weight (BW).

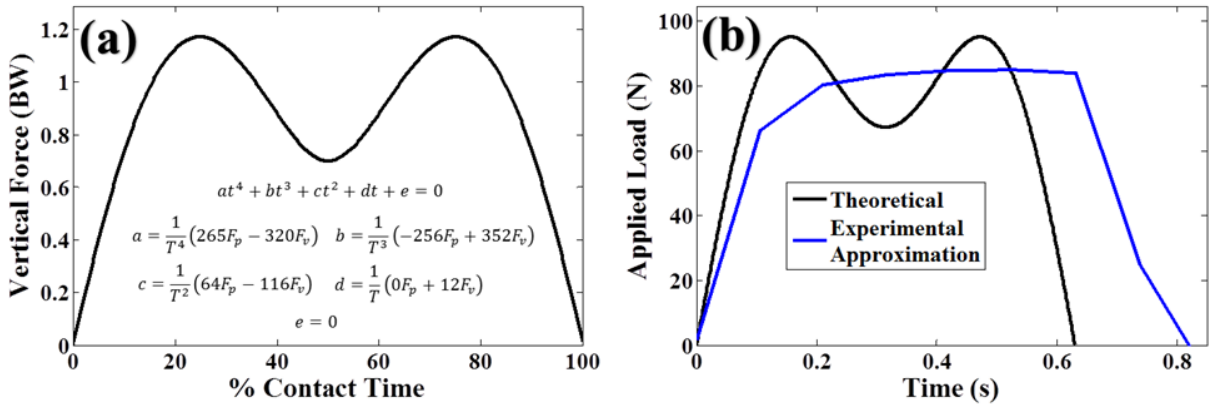

Figure 4.6 – (a) Fourth-order polynomial curve fit of vertical ground reaction force data from Martin and Marsh [201] and (b) typical experimental step force approximation compared to theoretical actual force profile (example for target 80N load).

To impose the desired force profile on the transducers, the test stand shown in Figure 4.7(a) was constructed. The stand consists of a rigid aluminum frame, pneumatic piston, control valves, and measurement sensors. High pressure air (~110 psi building supply) was fed into the system which was then regulated to the desired pressure by either an electronic or manual pressure regulator. A three-way solenoid valve (Parker 71315SN) then applies the supply pressure to the piston or exhausts the piston pressure to the open atmosphere. Pressure inside the piston was monitored using a Wika model A-10 pressure transducer. The force exerted on the cymbal transducer was then inferred from the piston pressure using the piston geometry. For this work, a Bimba double acting piston of 2in diameter was used.

In practice, the force profile of Figure 4.6(a) is difficult to be accurately recreated using the described test rig. The difficulty arises from the limitations of various commercially available electronic pressure regulators to regulate the pressure quickly enough or without unacceptable amount of overshoot. After several trials, the electronic pressure regulator was replaced with a manual regulator, which was set at a pressure that results in the desired force amplitude. The three-way solenoid valve then creates a pseudo-square-wave of force, which was taken to be an experimental approximation, and is shown in Figure 4.6(b). For this approximation, inlet and exhaust pneumatic piping size was chosen such that the rising and falling slopes of the approximated force profile most closely matches the theoretical gait force profile.

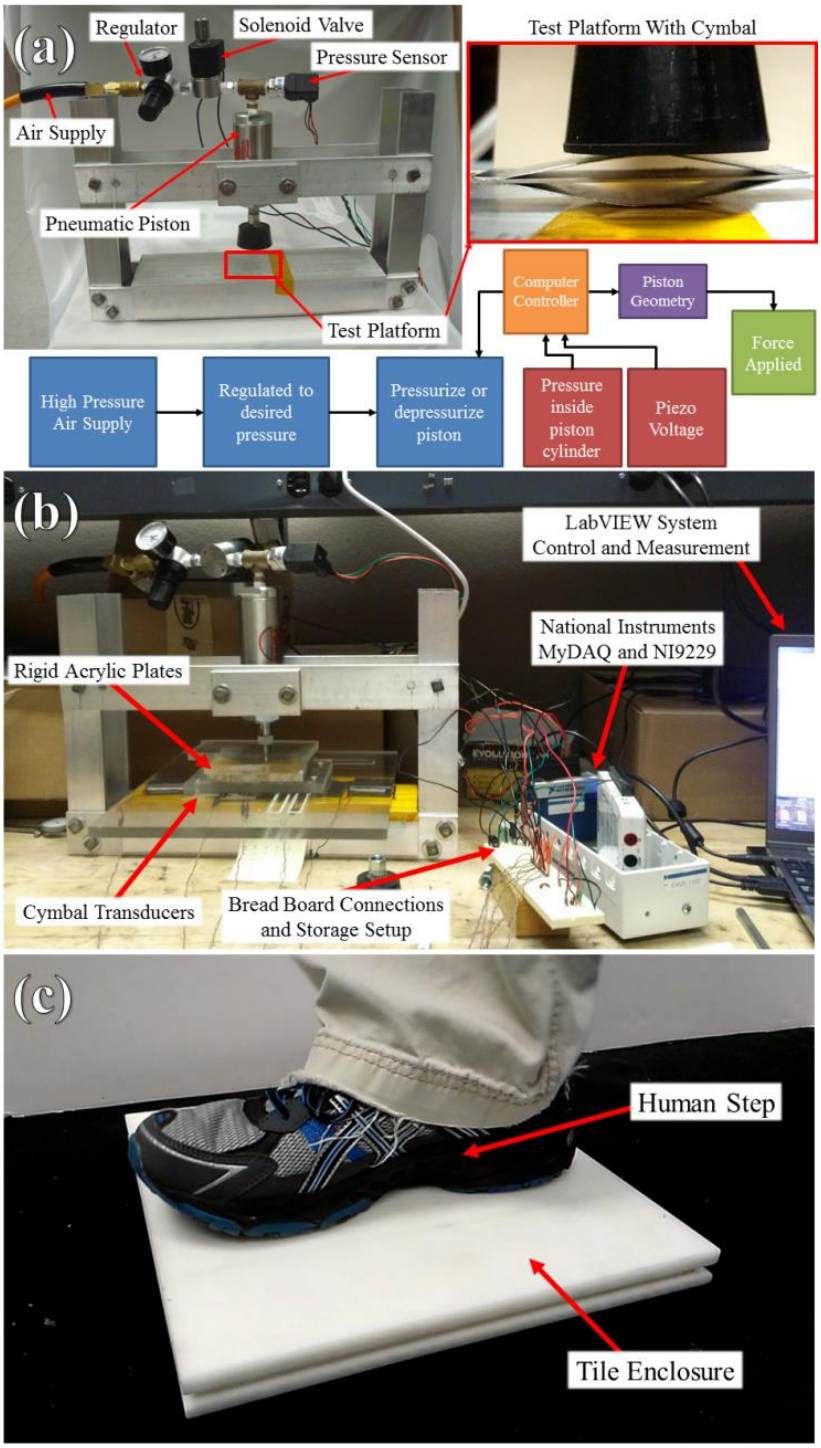

Figure 4.7 – Experimental methods, including (a) custom test stand, illustration of flow of information and testing of single transducer, (b) multiple transducer testing using custom test stand and simulated floor tile top, and (c) testing using human step inputs.

In Figure 4.7(a), force was applied to single transducers using a hard rubber (~75A Shore hardness) tip to evenly distribute the load. Multiple cymbals were tested using the test stand, as in Figure 4.7(b), by applying the load through approximately rigid acrylic plates simulating a floor tile surface. Measurements were taken using National Instruments MyDAQ and NI9229 platforms. Finally, the system was tested in a floor tile enclosure under human footstep loads, as detailed in Figure 4.7(c).

4.6 PZT Packaging

The brittle nature of lead zirconium titanate (PZT) can cause the formation of cracks over time when operating under cyclic loading conditions. Such cracks in the bulk material can reduce performance due to a complex combination of factors [202]. This effect has been shown in practice by the East Japan Railway Company when testing their "Power-Generating Floor," where they expressed the need to package the piezoelectric elements with a protective rubber structure [203]. It has been shown that PZT may be made substantially more compliant by creating a macro fiber composite [204]. It is, however, simpler and cheaper if some of the benefits realized by a fiber composite could be realized using bulk piezoelectric material. Therefore, in this study it was examined if a bulk laminate composite can be used to improve the performance of the cymbal transducer and keep the cost of ceramic at the minimal level.

To minimize the onset of brittle fracture or cracking in the PZT, it should be laminated with a more ductile material. Additionally, the laminate should have a higher Young's modulus than PZT in order to adequately transfer strain across any cracks which do form, but should be kept sufficiently thin so as to take a minimal amount of strain energy away from the PZT layer. It was thus decided to laminate the bulk PZT pieces with brass, because of its high ductility, electrical conductivity, and Young's modulus approximately 40% greater than PZT.

To examine the influence of the laminate brass layer, three cases illustrated in Figure 4.8(a) were considered, including a baseline case of unlamented (plain) PZT, a 25μm brass laminate case, and a 50μm brass laminate case. The brass was laminated at the top and bottom surfaces of the PZT using All-Spec CW2400 conductive epoxy, bonded in a kiln at 80°C for no less than two hours. For these tests, smaller scale test specimens were used to minimize the material waste during ultimate breaking strength tests. The test specimens were of similar geometry to the dimensions

shown in the drawing of Figure 4.4(a), however only 10mm in depth. The test specimens were then tested individually using the pneumatic test stand, as shown in Figure 4.7(a), in terms of energy output and ultimate breaking strength. Energy output was determined by recording the voltage in a storage capacitor when the test specimen was subjected to a force impulse of 20 N load for 0.63 seconds. The storage capacitor was a 10μF electrolytic capacitor and connected to the output from the test cymbal through a full-bridge diode (BAV21) rectifier. Energy produced was then inferred by measuring the voltage across the capacitor, by the relationship, $1/2\,CV^2$, where C is the capacitance and V is the voltage of the capacitor respectively. Ultimate breaking strength was determined by slowly increasing the load on the test cymbal until the moment of failure. Results are given as a percent increase or decrease over the unpackaged case, as it is a comparative analysis, and to avoid confusion with the reported performance of the full size cymbals.

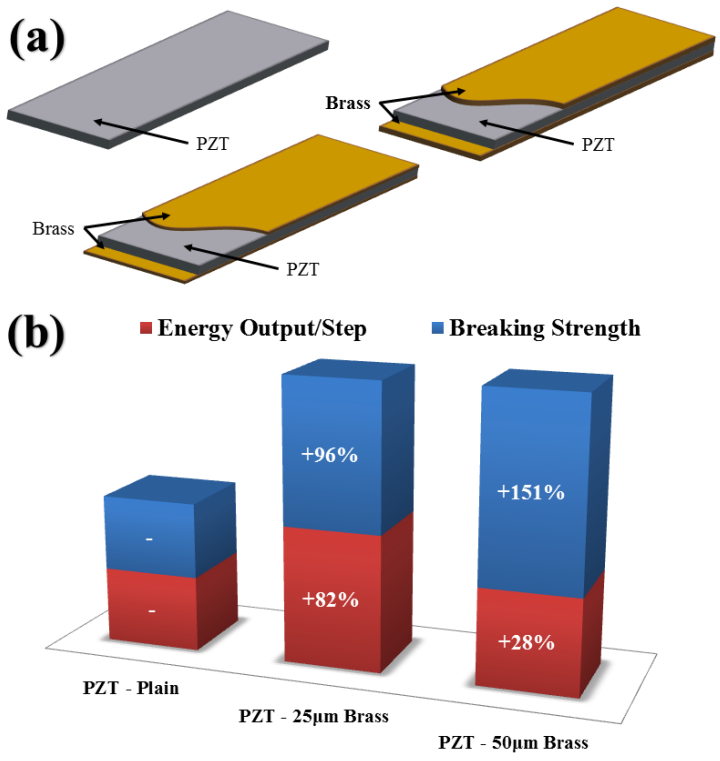

Figure 4.8 – (a) Illustration of three packaging techniques investigated including plain PZT, PZT with 25μm brass laminate, and PZT with 50μm brass laminate. (b) Results of packaging test, comparing performance in terms of ultimate breaking strength and energy output per simulated step input.

As shown in Figure 4.8(b), the addition of the brass laminate causes a dramatic increase in breaking strength, as well as an increase in energy output per simulated step input. The increase in energy production is postulated to result from a more even stress distribution in the PZT caused by the addition of the laminate. The increase in breaking strength is more intuitively caused by the additional cross-sectional area and stiffness, and subsequent reduction in stress per load. While both laminate cases offer improvements in both categories, the greatest improvement, which is defined as percent improvement in energy output per simulated step multiplied by percent improvement in ultimate breaking strength, is produced by the 25μm laminate. Therefore, this packaging scheme was used for subsequent implementation in the tile.

4.7 Optimal Number of Transducers

We now describe the selection of optimum number of cymbal transducers that should be employed within the tile enclosure. The number of cymbal transducers determines the stress each one of them will experience and subsequently the charge produced by the PZT layer. The larger the number of transducers used, the more potential there is for energy to be harvested before the cymbals become overloaded. However, the more transducers which are used, the lower the sensitivity of the tile, or the amount of energy produced per load (i.e. person's weight). Consequently, there exists an optimum number of transducers to be employed for maximum energy harvesting from a target weight. Figure 4.9 illustrates this concept by showing a qualitative comparison of energy produced per step on the tile, as a function of weight for an optimum number of transducers for the weight of an average child (8 year old) [205], average adult [205], and average NFL player [206], as examples.

The flat areas of the curves in Figure 4.9 represent condition where the transducers would become overloaded and experience failure if not for the design of the tile enclosure. A tile optimized for a child can make much more energy per step at low weights, but has a much lower maximum possible energy production compared to a tile optimized for an adult or NFL player. However, after a certain minimum weight, the floor tile will produce a constant amount of energy per step, regardless of the load. This type of performance is quite desirable as the function of tile (i.e. sending a signal when stepped upon) can be decoupled from a person's weight or gait style.

Therefore, I determined the optimal number of transducers such that the maximum possible energy harvested per step is just sufficient to power the signal transmission circuitry. For any person above a certain minimum weight the tile will function in a similar manner. For reasons discussed in later sections, this minimum weight was found to be around 36kg and an optimal number of cymbal transducers was found to be five. In this application, a minimum necessary number of transducers were used. However, if the tile was built to harvest as much energy as possible, the number of cymbal transducers would be chosen to correlate with the expected average weight of occupants that would step on the tiles most regularly.

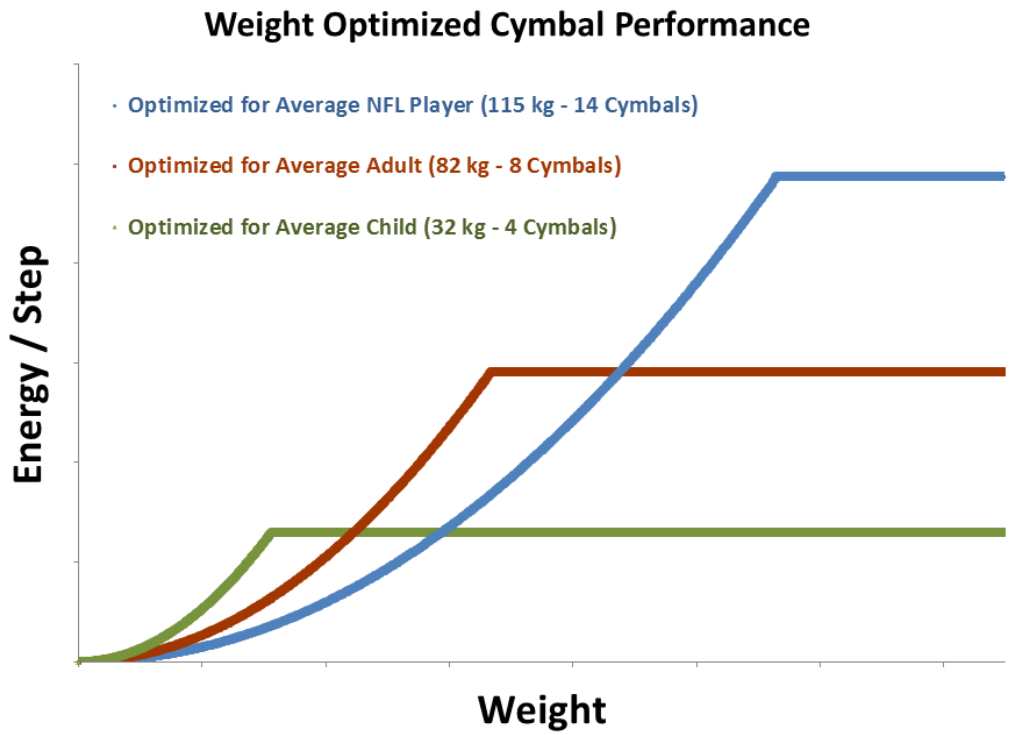

Figure 4.9 – Qualitative illustration energy production per step as a function of weight for several cases of optimal number of cymbals used for target weights of a child (8 year old)[205], average adult [205], and average NFL player [206] as examples.

4.8 Tile Enclosure Design

The main functions of the tile enclosure are to provide a flat and rigid surface to transfer force to the cymbal transducers, protect the cymbals from overstraining, and protect the cymbals

and circuitry components from the environment. To ensure a consistently flat and sufficiently rigid surface, it was chosen to construct the tile enclosure from Delrin®, a thermoplastic which exhibits high stiffness, dimensional stability, low thermal expansion, and resistance to water and other chemicals. Channels were cut (CNC Mill) into the top and bottom plates, into which the supports are fitted. The support strips were bonded only to the bottom plate, using Loctite 120HP epoxy, and were sized such that they do not come into contact with the top plate when the tile is not loaded and the top plate rests on the cymbal transducers. In Figure 4.10(a), one can see that when the tile is loaded, the cymbal transducers are compressed, although before the piezoelectric layer is strained to the point of failure, the top plate comes in contact with the supports, preventing further deflection. In this way, the cymbal transducers are protected from failure due to high loads. In addition, after a certain minimum load (i.e. person's weight), energy production is held relatively constant, as the deflection of the cymbal transducers is mechanically limited. This leads to a more consistent operation (i.e. occupancy sensing and signal transmission), as a known amount of energy is delivered to the circuitry.

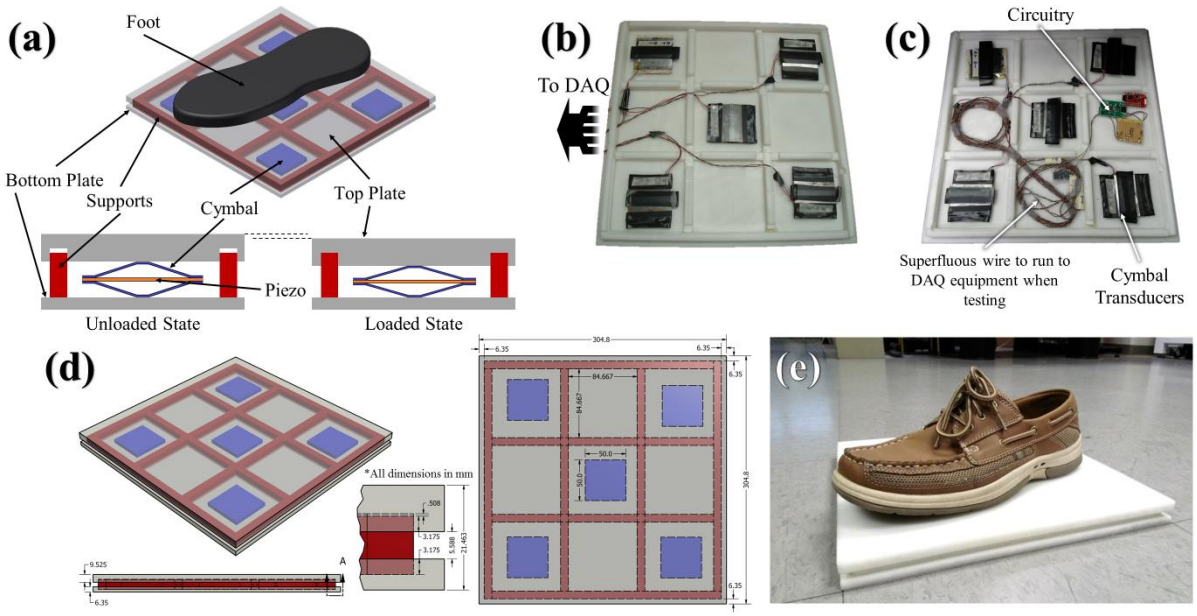

Figure 4.10 – (a) Illustration of tile enclosure parts in unloaded and loaded states, (b) fabricated enclosure (with top plate removed) used when testing with human step inputs, (c) final fabricated enclosure (with top plate removed) with all components internal to the tile, (d) dimensioned drawing of floor tile enclosure, and (e) fully assembled STEP Tech floor tile with size 9 (US) shoe for scale.

When developing the cymbal transducers and circuitry with human step loading, as shown in Figure 4.7(c), the output from the cymbal transducers was run outside the tile enclosure to the data acquisition (DAQ) modules, as shown in Figure 4.10(b), through small holes in the enclosure, which were later filled. Once the system was verified to function as anticipated, the circuitry was wired into the enclosure and superfluous wire which was used to reach the DAQ equipment in Figure 4.10(b) was wound in the extra space within the tile as shown in Figure 4.10(c). A dimensioned drawing of the tile enclosure is shown in Figure 4.10(d) with the fully assembled STEP Tech floor tile shown in Figure 4.10(e), along with a size 9 (US) shoe for scale.

4.9 Circuit Design

With the mechanics of the tile established, circuitry was designed to fulfil the target application of detection of building occupancy. The detection of human presence was achieved by transmitting a wireless signal using the energy generated by a person stepping on the tile. In this way, each time a signal was received from the tile, it would indicate that a person has stepped on it. In order to achieve this functionality, the design was examined in four stages: (i) determining the optimal electrical connection strategy for the multiple cymbals, in order to maximize the collected energy; (ii) determining a rectification method; (iii) sizing the storage capacitor; and (iv) utilizing the collected energy through an energy management section in order to power a wireless transmitter. Each of these stages will be addressed in more detail in the following sub-sections.

4.9.1 Electrical Connection Strategy

While the cymbal transducers are loaded mechanically in parallel, their electrical connection strategy must be decided in order to realize the most efficient operation of the circuitry. When a 71kg person stepped on the tile, it was seen that the output open circuit voltage of the cymbals is in range of 20V to 30V. Therefore, it can be expected that the maximum power point (MPP) will be one half of the open circuit voltage. If it’s considered connecting the cymbals in series, this would yield the maximum power point voltage of approximately 75V in the case of a tile with 5 cymbals. This was derived under the assumption that all cymbals were the same, and that their maximum power point voltage was 15V for each cymbal. In this case, the energy

management stage would be faced with the task of converting the 75V stored on the capacitor to 3V, which is the voltage typically used by sensors and wireless modules. After searching for high efficiency DC/DC converters with the required input voltage rating, it was concluded that the conversion from 75V to 3V would be very inefficient. Furthermore, integrated solutions for low power switching DC/DC converters capable of performing the task are not easily available. Therefore, connecting the cymbals in series was not an option. On the other hand, connecting the cymbals in parallel would result in approximately 15V maximum power point. At this voltage level it was possible to use off-the-shelf converters, while providing high efficiency in energy transfer from the buffer capacitor to the rest of the circuitry. It was therefore decided to connect the cymbals electrically in parallel.

4.9.2 Rectification of the AC Signal

In the literature, several different approaches have been demonstrated for piezoelectric output rectification [207-209]. These circuits have been primarily designed to operate with stable periodic oscillations that would generate a predictable output of the harvester. However, the output of the cymbals when stepped on is an irregularly shaped single pulse. Furthermore, the amount of available energy after one step is in order of one millijoule. Hence, the rectification circuit selected has to be very efficient in order to not consume more energy than the gain of using the selected rectifier circuit. Furthermore, the storage capacitor can be considered empty before each step occurs, as an indeterminate amount of time will pass between the subsequent foot falls on the tile. Advanced rectifier designs typically require stable power for the control circuitry. All these limitations made the use of the advanced rectification a very challenging task. Therefore, a standard diode bridge was selected.

4.9.3 Selection of a Storage Capacitor

As with many energy harvesting applications, in this specific tile application there is not sufficient instantaneous energy produced to power the payload device (wireless signal transmitter in this case) continuously. Therefore, an intermittent storage capacitor is necessary to accumulate energy until signal transmission can be powered. Here, there is no need for accumulating energy between transmissions, principally because occupancy has already been counted, and also because energy is only collected when the tile is being stepped upon. Therefore, the capacitor buffer size

was selected based on the value that would produce the most optimal energy output from a single step. Empirically, the value of the buffer capacitor was selected to be a 10µF ceramic X7R capacitor rated for 25V, as it stores the most energy per step, demonstrated in Figure 4.11. Note that in Figure 4.11 one simulated step input was signified by two rises in capacitor voltage, where one rise is caused by force being applied and the second rise by the force being removed. The regions of decreasing voltage in-between rises are caused by the high leakage current of the Schottky diodes used in the full bridge rectifier above 15V. Schottky diodes are thus not used in the final circuit design.

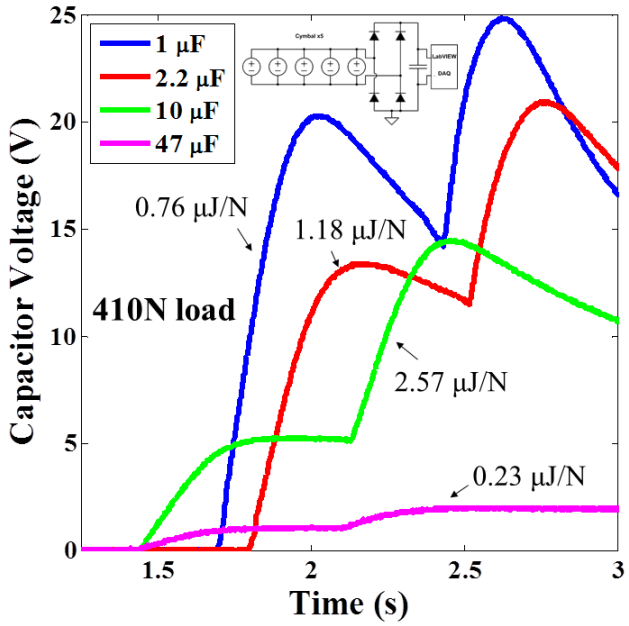

Figure 4.11 – Stored voltage for five cymbal transducers in parallel under 410N simulated step for varying storage capacitor values. Values of maximum energy stored per step per cymbal per load are noted for each capacitance value.

4.9.4 Energy Management

Wireless signal transmission was performed using the ez460-RF2500 platform by Texas Instruments [210]. The energy required for starting up the transmitter and performing a wireless transmission, based on the documentation provided by Texas Instruments, was approximately 100µJ [211]. The amount of energy harvested during the stepping onto the tile, by an approximately 71kg person, was borderline sufficient to perform the transmission. This, however,

indicates that a lighter person wouldn't generate sufficient energy, by stepping onto the tile, to perform a transmission. In order to address this issue transmission was delayed until the person steps off the tile. A similar amount of energy is generated as a person steps off the tile as when stepping on. Therefore, the minimum weight of a person necessary to power signal transmission is around 36kg. Based on the measurements, when the stepping off is completed, the voltage reached values around 15V. As a result, it was necessary to convert the voltage on the storage capacitor to the range of 1.8V to 3.6V, which is required for stable operation of the radio and MCU on the ez430-RF2500 board. The conversion is done by using a switching DC/DC regulator. Such a regulator is found in the LTC3129-1 nanowatt buck-boost DC/DC [212]. This DC/DC converter was selected firstly because the circuit is rated for the voltage range expected on the buffer capacitor, and secondly it has analog control, which can be used for selecting a threshold voltage at which the converter should activate. By applying a voltage level above 1.22V on the analog control pin, the converter would activate. Therefore, by providing the voltage from the input using a simple resistor divider it was possible to set the activation voltage at a desired input storage capacitor voltage level. However, this circuit has a narrow input hysteresis, so it is necessary to extend it in order to allow the output to use as much energy as possible before the DC/DC converter turns off. The hysteresis extension is implemented by connecting a diode and a capacitor to the RUN input, which controls the converter's operation, as shown in Figure 4.12(a).

The circuit rectifies alternating voltage input from the cymbal transducers during a step. As the voltage on the input capacitor, C8, rises, the voltage on the capacitor connected to the RUN pin, C7, also rises, at a rate defined by the voltage divider and the diode voltage drop. When the voltage on capacitor C7 reaches the threshold voltage of the converter, 1.22V, the converter starts operation. As soon as the converter starts operating, the voltage on capacitor C8 will drop, as the harvester is not capable of supplying sufficient power to prevent this, as the footstep on the tile is completed. With the drop of voltage on C8, if it weren't for the diode D5, the voltage on the RUN pin would reflect the voltage change on the input, leading to disabling the converter once the voltage on this pin reaches 1.11V. However, as the diode is preventing the discharge of the capacitor C7, the LTC3129-1 continues operation, draining the input capacitor until it reaches 1.9V, where the LTC3129-1 enters under-voltage condition and stops powering the output. This process is qualitatively illustrated in Figure 4.12(b), with measured voltages on the input and output sides of the DC/DC converter under simulated stepping loads shown in Figure 4.12(c).

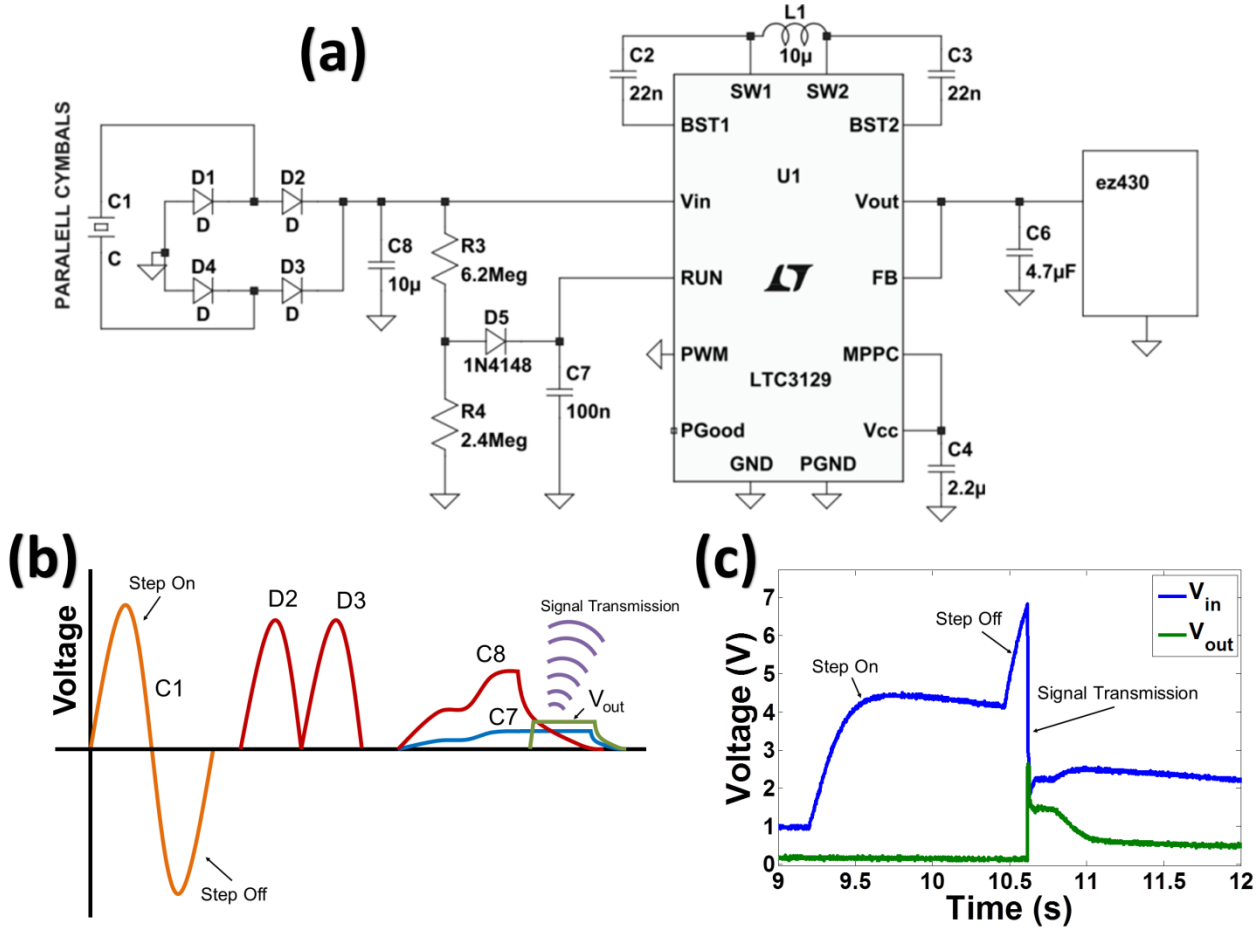

Figure 4.12 – (a) STEP Tech circuitry schematic, with (b) qualitative illustration of circuit function, and (c) measured voltage response of circuit to simulated footstep forcing input to the tile.

Introduction of the diode D5 and the capacitor C7 to the circuitry has the effect of realizing a low pass filter on the RUN pin. This in turn introduces a delay in response to the changing input. The value of the resistance divider is in megaohm range, in order to reduce the losses during charging. Therefore, the time constant of the RC network would be in the second range, depending on the values of the resistors and capacitor used. This delay could be potentially used to the advantage of the circuit. Let VTHR-DC/DC be the voltage level required for the input storage capacitor to reach in order to provide sufficient energy to perform a wireless transmission. This voltage level will be reached, as explained earlier, during the stepping off from the tile. If a person's weight is the same as the minimum weight required for the system to operate, after the

person has stepped off, the buffer would reach the required voltage VTHR-DC/DC after the delay introduced by the RC circuit. However, if a person is heavier, the voltage on the input buffer capacitor would continue to rise as the circuit is not being activated because of the said delay. In this way, more energy will be accumulated in the storage capacitor before the circuit is activated, hence providing additional energy to the circuit, increasing robustness.

4.10 Demonstration and Discussion

STEP Tech was tested in a "real world" setting at the Change the World Science & Engineering Careers Fair at Dulles Town Center in Dulles, Virginia. The event was attended by several hundred individuals, and the STEP Tech tile was stepped upon many times, by persons weighing an estimated range of 25-130kg. The demonstration showed the ability of the STEP Tech tile to harvest enough energy from a single step to transmit a wireless signal to a lamp which turned on when tile is stepped upon, and turned off when the tile was stepped upon again. A sample demonstration is shown in several frames in Figure 4.13. From this demonstration it was conceptualized how a distributed network of tiles could control not only smart building lighting but also climate control and other systems, based on real-time occupancy measurements. Additionally, the individuals stepping on the tile unanimously stated that they could not perceive any vertical deflection of the tile's top plate whilst stepping upon it. This response indicates that if the tile were embedded into a floor, it would be unperceivable to building occupants and thus not alter their normal gait patterns.

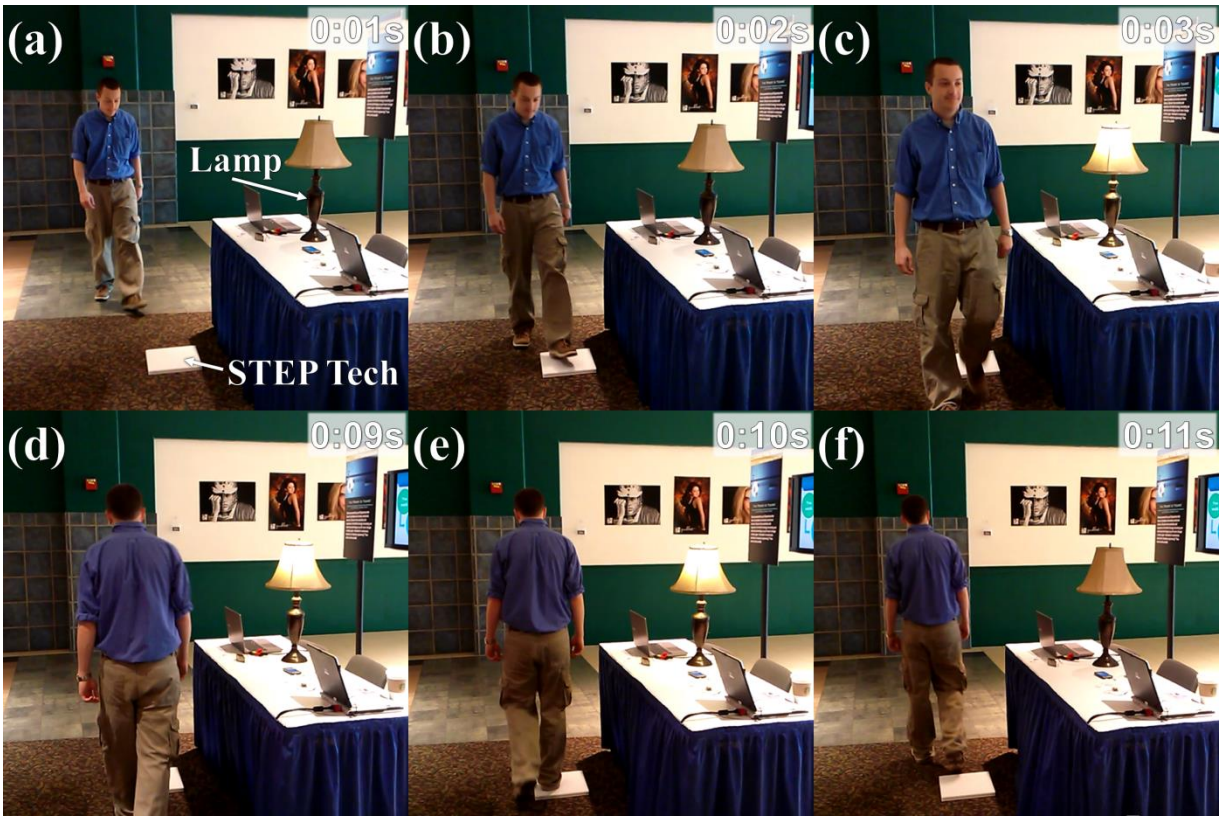

Figure 4.13 – Lighting control demonstration whereby (a) a STEP Tech tile is placed some distance away from a lamp and when (b) the tile is stepped upon, enough energy is collected to (c) transmit a signal to the lamp to turn on. When the tile is stepped upon once again (e), the same process occurs only this time (f) turning the lamp off.

The vertical deflection of the tile is unperceivable by humans because it is mechanically limited to approximately 0.5mm. By Section 1604.3.1 of the Virginia Construction Code, STEP Tech tiles would be allowed to deflect 0.85mm [191]. Therefore, the installation of STEP Tech tiles would be allowed in buildings in the state of Virginia, unlike other commercially available floor tile energy harvesters, which report an order of magnitude greater deflection [187, 188]. In addition, the level of deflection exhibited by STEP Tech tiles is not readily perceivable by persons stepping on the tile. Subsequently, STEP Tech will not disturb the gait of smart building occupants when imbedded under the floor surface (e.g. carpet, laminate, decretive tile, etc.), and thus not cause them to deviate from their normal route (i.e. avoid "soft" tiles). This then allows for accurate real-time occupancy mapping and occupancy driven smart building system control, which will lead to substantial energy savings [183-185]. Most importantly, these savings are realized without

using sensors which consume power themselves, as STEP Tech derives its energy from human motion.

The sensors currently used in the buildings are mainly motion detectors which emit radiation into a space and detect occupancy by measuring what is reflected back to the device. Infrared sensors can also be used to detect motion through a plane. Since the premise of operation of these sensors requires that they emit energy, their power consumption is in the range of hundreds of milliwatts to several watts, depending on the device range and coverage area [213]. Since these devices are constantly scanning their environment, this power consumption is persistent 24 hours a day, regardless of building occupancy. Certainly, if a room containing several hundred watts of lighting can be controlled with a one watt sensor, the advantages are obvious. However, the elimination of passive energy consumption of traditional occupancy sensors, offered by an energy harvesting solution like STEP Tech, is favorable. Naturally, the receiver for the control unit has some power consumption, but since it only needs to listen for a signal (rather than broadcast and receive), the control unit operates nearly exclusively in stand-by mode, consuming only some microwatts of power.

In addition, the control of building function through traditional occupancy sensors has proven inadequate, requiring sophisticated data analysis and redundant sensor measurements to achieve a higher certainty of occupancy detection [214]. Consequently, occupancy measurements are often left under-sampled, and rely on sensor timeouts to decide when to turn lights off, as anyone who has ever had to get up and wave their arms around to turn the lights back on in a motion detector driven lighting controlled room has experienced. STEP Tech offers the additional information about the number of people in a given area, as a signal is sent each time there is a footfall onto the tile, unlike traditional motion detectors which only see there is some level of motion in an area. Furthermore, STEP Tech tile could be arranged to capture successive footfalls, giving information about the direction of occupant motion.

Since the $Pb(Zr,Ti)O_3$ composition was discovered in the mid 1950's, many studies on developing high performance piezoelectric materials have been conducted. The commercialized piezoelectric ceramic compositions with high d_{33} value of 1000 pC/N or compositions with high g_{33} value of 40 x 10^{-3} V m N^{-1} can be found. However, compositions having high d_{33} usually show low g_{33} value while high g_{33} compositions possess low d_{33}. Thus, the achievement of high $d \cdot g$ coefficient from single piezoelectric composition is challenging. Recently, a very

different strategy for overcoming the fundamental limitations imposed by electrodynamics and thermodynamics has been proposed via designing a textured microstructure, which can result in large magnitude of $d \cdot g$ coefficient [215]. The reason for realizing high $d \cdot g$ coefficient in textured ceramics is: (1) <001> texturing (grain orientation along the <001> crystallographic direction) of piezoelectric ceramic produces engineered domain state similar to that of <001> single crystals, thus, resulting in high d values; (2) the existence of low ε templates produces a composite microstructure and suppresses the dielectric constant (ε) of piezoelectric ceramic. Thus, utilizing textured ceramics within the cymbal transducer would result in some improvement of the output power response.

Apart from the piezoelectric materials, the power density of STEP Tech could be improved by further examination of the cymbal transducer. In this study, the end caps of the cymbal were made as thin as possible to minimize energy loss in bending the end caps and maximize the stress delivered to the piezoelectric layer. Cymbal dimensions, particularly the bend angle, were then chosen to fulfill a prerequisite Factor of Safety. Since the amplification factor of the cymbal transducer follows the cotangent of the bend angle, further decreasing the bend is predicted to increase performance. However, it is difficult to produce a cymbal end cap with angles smaller than those described in this work. This is because the bends become less sharp with decreasing angle, as plastic deformation in the pressing process is not readily induced, because of the smaller applied strain. Subsequently, buckling of the end caps becomes more spontaneous, due to the imperfect small angle bends. It is postulated that the end caps could be made slightly thicker, allowing for smaller angles to be created while still guarding against buckling. Therefore, while some performance is lost by using thicker end caps, the performance gain for using smaller bend angles would still yield an overall increase in performance.

Outside the engineering challenges, occupancy sensors in general face challenges with acceptance, as it is difficult to accurately predict cost savings [216]. It is well established that cost savings are to be had by implementing occupancy sensors; however, as savings are ultimately directed by building occupancy and human tendency, they are inherently highly variant. In addition, there is also the consideration that frequent switching of lighting on/off can decrease light fixture lifetime, due to more rapid thermal cycling. In the case of fluorescent lights, it has been simulated that the calendar life of lighting (i.e. time between when lighting is replaced/required maintenance) may be decreased by frequent switching, however cost savings will nonetheless still

be realized [217]. The greatest energy (and subsequently cost) savings are ultimately determined by what is done with the building occupancy information. STEP Tech offers a more reliable method of measuring occupancy without having any passive power consumption, as well as, offering savings in simplified installation and wiring costs when compared to traditional means of occupancy sensing.

4.11 Directional Sensing

After successfully demonstrating a working technology in the previous section, it was my aim to improve the technology toward application. The principal deficiency in the previous design was that it acted like button, only knowing that it was stepped on. However, for there to be a real time occupancy count for each room of a building, the tile must infer the direction of motion, so the central receiver/controller knows to either increment or decrement the occupancy count for each room. The difficulty herein lies in that before the tile is stepped upon, it has no energy. How then can a measurement of walking direction be taken, when there is insufficient energy to run the circuitry?

The answer to this questions comes first from the strategy chosen to infer stepping direction. During stance phase of human gait, the heel of the foot strikes the ground first and then the body weight, and subsequently ground reaction force center of pressure, gradually moves in the direction of travel. In the case of the floor tile, this would mean that some parts of the tile would receive force before others, as the pressure from the foot migrates across it. Due to the fact that there are five cymbals in the design presented in this dissertation, scattered equally throughout the tile, some of the cymbal transducers would be actuated and produce voltage before others. If the circuitry were somehow able to measure and compare the voltages of the four cymbals on the periphery of the tile, at a moment soon after the step was initiated, then it could be inferred the walking direction by assuming the two cymbals producing the greatest voltage was where the heal strike is occurring.

To confirm the hypothesis of time delayed voltage output of the cymbals, in accordance with the walking direction, the tile was stepped upon in the four possible different directions. The steps occurred after steady walking speed was achieved, where the tile was simply in the path of walking. The five cymbals were measured individually for voltage output as a function of time.

The results are shown in Figure 4.14 for the individual cymbals, and illustration of walking direction over the tile.

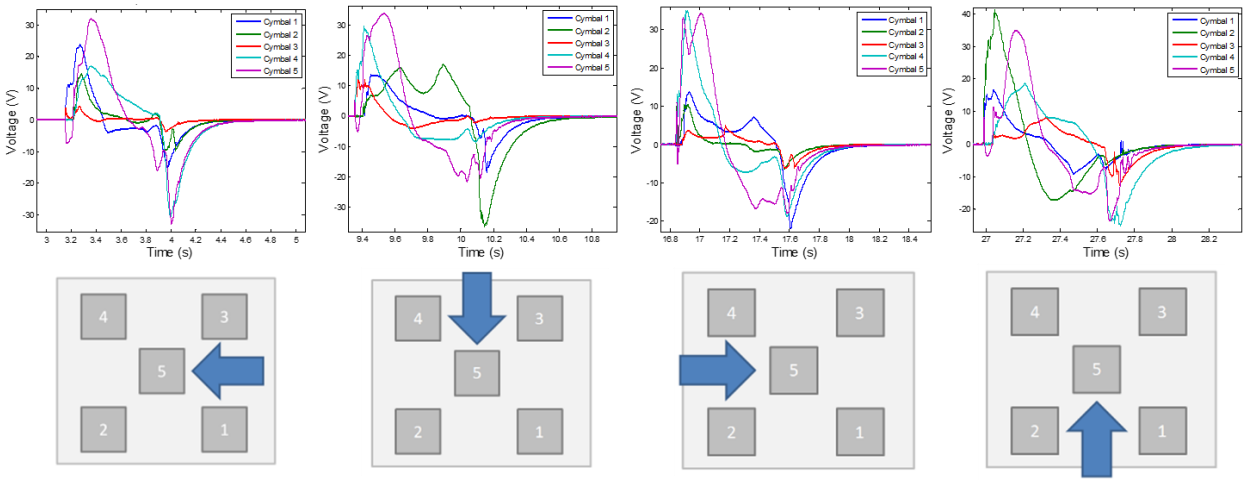

Figure 4.14 – Individual cymbal voltage output as a function of time when stepped up from the four possible different directions.

From the results of Figure 4.14, it can be seen how the cymbal transducers on the side of the tile first encountering the step produce voltage first. The direction of travel can thus be identified by comparison of cymbal voltages shortly after the step is initiated. Though the cymbals were measured individually to observe their voltage across time, the cymbals must be combined in parallel to store their energy in a capacitor to power the rest of the circuitry. This task is not as straight forward as the previous circuit connection, which was shown in Figure 4.12. Since the individual cymbal voltages must be monitored, a simple parallel connection cannot be straight way used, since this would cause the same voltage to be present across all of the cymbals. Each cymbal therefore, in the directional sensing circuit, has its own full bridge diode rectifier, storage and controller. Some of the energy from the step goes toward goes toward powering the voltage monitoring, and the rest stored in another capacitor to later power the signal transmission.

The voltage out of the individual cymbals and total voltage collected on the voltage monitoring circuit storage capacitor are shown in Figure 4.15 for a sample step across the tile of the illustrated direction. With the plot showing only the first 0.3 seconds of the step, the time delay of approximately 0.1 seconds in the cymbal voltages is apparent. The magenta line represents the voltage of the storage capacitor responsible for powering the cymbal voltage comparison circuit.

Note the ‘Total’ line goes above the other four cymbal voltages because cymbal 5 also contributes to the energy collection, and powering of the circuit, though it is not monitored like the perimeter cymbals.

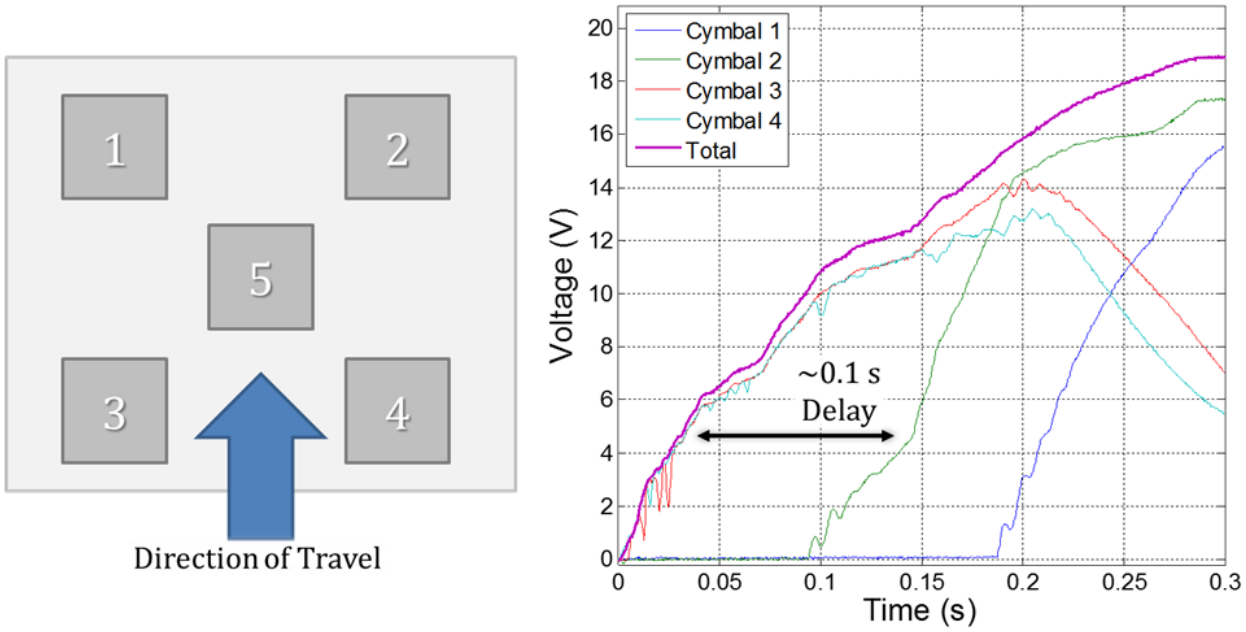

Figure 4.15 – Individual voltage output of the four perimeter cymbals, when connected to the directional sensing circuitry. Energy is stored (including cymbal 5) in a capacitor, whose voltage is labeled ‘Total’.

Since less energy, compared to the wireless signal transmission, is required to run the voltage comparison, the capacitor for the measurement circuit is smaller than the for the signal transmission. This is why voltage builds quickly, like what is shown in Figure 4.15. The observation of the capacitor powering the circuits is shown in Figure 4.16. Here a larger value of capacitance is used, thus the voltage builds more slowly, though more energy is being stored. Here, dips in the voltage signal are observed when power is consumed by the circuitry. There is first a brief dip when sufficient voltage is collected to power the voltage measurement and comparison, the results of which are briefly stored in RAM before they are transmitted when sufficient energy is collected (signaled by the voltage level) to perform the signal transmission, which is the second dip in voltage. In the configuration shown, the signal transmission occurs at a low power setting. Subsequently, excess energy is collected as the step is completed, before it decays over the next

few seconds due to the quiescent current draw of the circuit. In its final configuration, all of the available energy will be used to power the radio performing the wireless signal transmission, such that its signal strength is a large as possible, to propagate the largest possible distance. This distance should be sufficient enough that even with attenuation in the building environment that it will reach the central receiver unit controlling the automated lighting and climate control based on the occupancy.

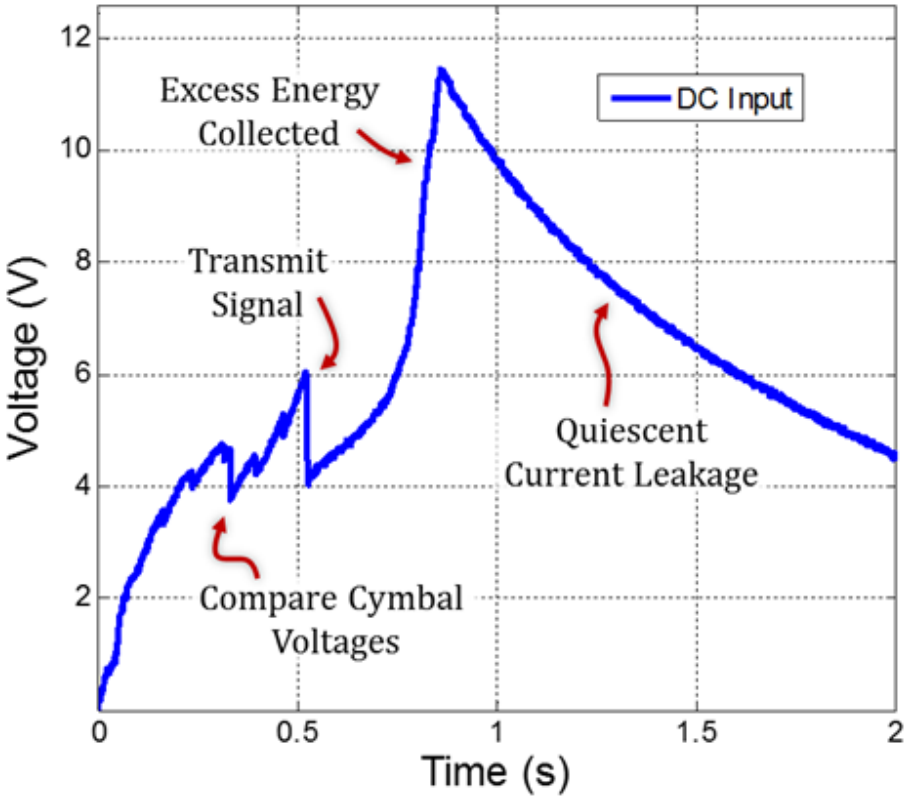

Figure 4.16 –Voltage level on the storage capacitor input to the DC/DC converter, ultimately powering the measurement and signal transmission circuitry components.

A detailed description of the circuitry responsible for realizing the functionality described above can be found in the dissertation of Dušan Vučković.[218]

4.12 Further Study of the Cymbal Transducer

After the selection of the cymbal geometry, which was guided by the analytical and finite element modeling in Section 4.3 and packaging in Section 4.6, the same cymbal design was used for all of the previous experiments. In this section, I will chronicle additional attempts to better the cymbal transducer design. These attempts will revolve around the piezoelectric layer packaging, and the cymbal geometry. Here, enhanced packaging techniques are studied, along with an experimental parametric study of cymbal geometries.

4.12.1 Enhanced PZT Packaging

In the previous PZT packaging study in Section 4.6, the energy output and breaking strength were measured for different packing laminate configurations. The packing was meant to provide resistance to brittle fracture, which it did, though also to allow functionality of the tile should brittle fracture occur. Therefore, it is also examined here how the cymbals fail in brittle fracture, and their performance after failure occurs. Figure 4.17 below shows the failure of three packaging configuration, with close up of the point of failure.

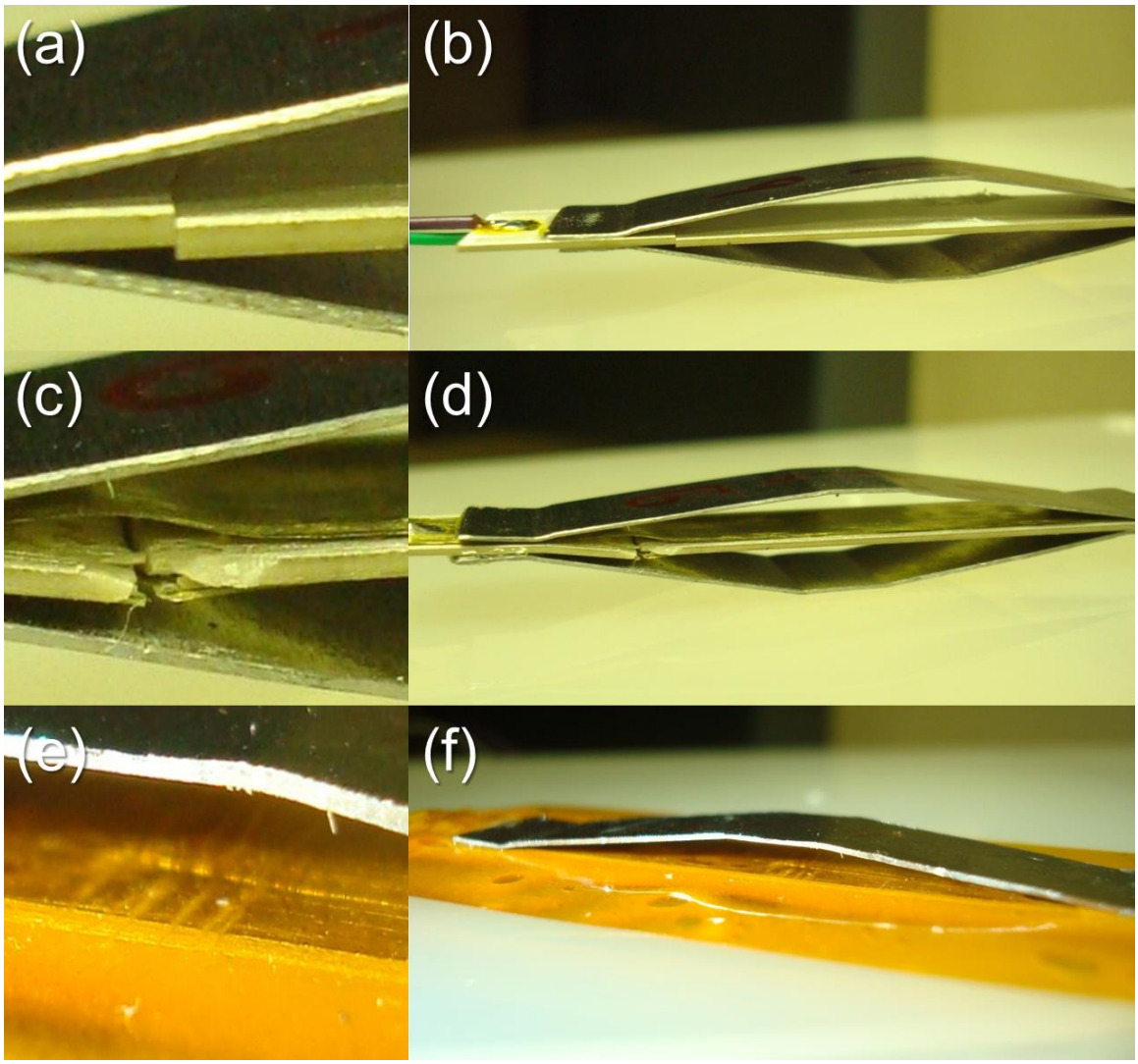

Figure 4.17 – Effects of breaking test on cymbal transducer, with (a,b) being the plain unpackaged cymbal, (c,d) the 25 µm brass laminated cymbal, and (e,f) the 25 µm brass with 25 µm Kapton laminated cymbal. (a,c,d) are close up shots of the breaking point of (b,d,f) respectively.

One can see in Figure 4.17(a,b) the plain unpackaged cymbal, with the brass laminate in Figure 4.17(c,d). Here a new packaging structure is also given, laminating Kapton film on top of the brass laminate layer, shown in Figure 4.17(e,f). When the plain PZT configuration experiences fracture, both the electrical and mechanical connection is severed. With the inclusion of the brass laminate layer, even though the piezoelectric layer fractures, electrical connection is maintained, as well as, some mechanical connection. Figure 4.18 expands on Figure 4.8, adding two new configurations, along with the energy production after breaking (brittle fracture of the PZT layer).

From Figure 4.18, it is shown that after the PZT is fractured, the inclusion of the brass layer allows some energy to be harvested, despite failure occurring. The first two brass configuration used conductive epoxy (All-Spec CW2400). It was thought, then, that a stronger epoxy would yield better results, leading two the fourth configuration using brass and Devcon 5 minute epoxy. Because of the stronger epoxy, energy output, breaking strength, and energy after breaking were all increased.

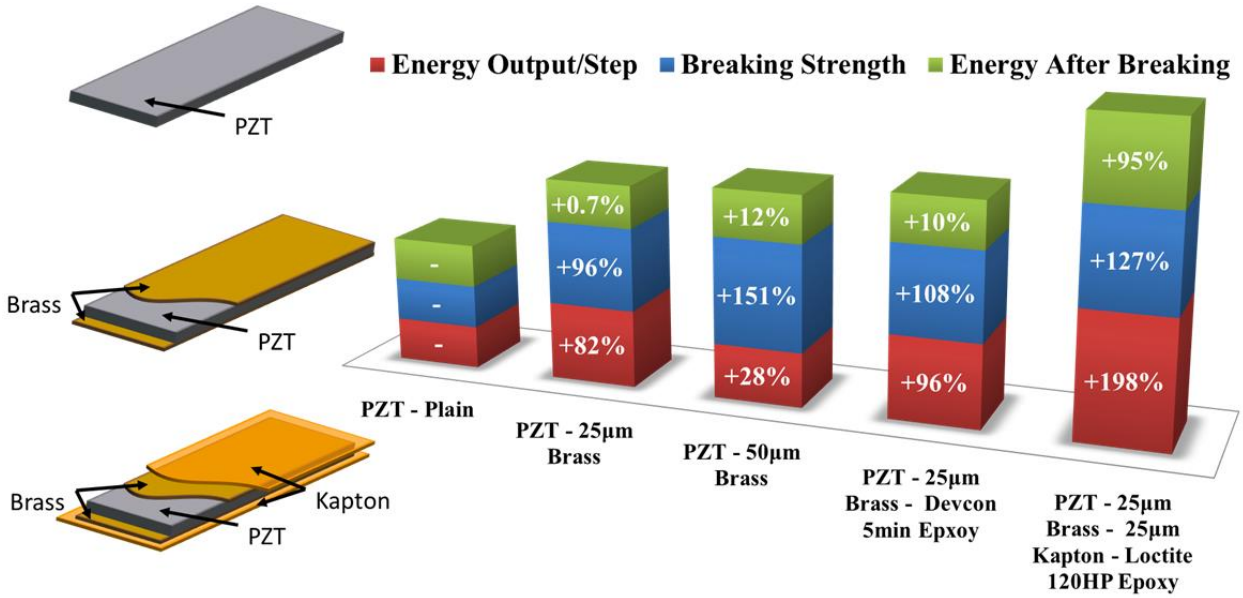

Figure 4.18 – (Left) Illustration of PZT packaging laminate structure, and (Right) stacked results of packaging improvements with respect to the unpackaged 'plain' PZT. All packaging techniques were tested with the same geometry cymbal transducer.

Examining Figure 4.17(c), the brass layer yields and delaminates locally around the fracture point. This is caused by the forces normally being supported by the PZT suddenly being applied to only the brass layer at the time of fracture. The result of the delamination is that only some 10% of the energy can be harvested, compared to the unbroken state. To deal with the delamination, it was thought that laminating a more compliant layer atop the brass would secure it in place. The compliant layer was chosen to be Kapton film, because of its lower Young's modulus compared to the brass and PZT, and it high yield strength. This new configuration is the one shown in Figure 4.17(e,f). Here Loctite 120HP epoxy is used to bond all layers. This is the same epoxy that was previously used to bond the cymbal end caps to the PZT. The fifth bar (far right) of Figure

4.18 reports the results for this configuration, where it's shown that 95% of the after figure can still be harvested. This result would indicate that the cymbals packaged in this way could yield a much longer useful lifespan, still producing most of the energy after failure occurs.

A secondary advantage to using the extra Kapton laminate layer is the electrical insulation Kapton provides. With the electrical insulation, the cymbal cannot be shorted out even if it were submerged in water, like is shown in Figure 4.19. Being waterproof is advantageous in the target application, as the tile would not be readily affected by spills on the floor, cleaning, flooding, etc.

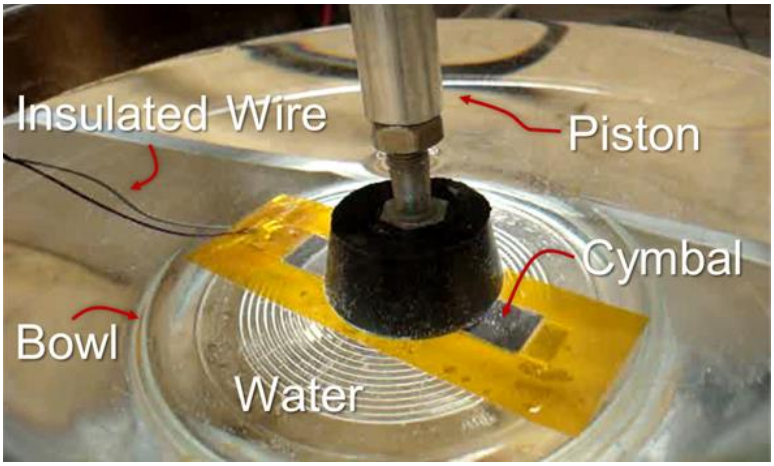

Figure 4.19 – Demonstration of waterproof cymbal transducer using brass and Kapton laminates. Underwater performance was the same as in air.

4.12.2 Cymbal Geometry

As was mentioned in the introduction to this section, previously only one geometry of cymbal was experimentally tested. Only one geometry was used because of the investment that needed be made to produce the dies used to manufacture the cymbals, pressing them under high pressure and forming the flat sheets of steel into the desired shape (Section 4.4). Furthermore, the analytical modeling made the assumption that the cymbal end caps were thing enough, that their bend could be assumed as pin connected joints, thus neglecting the energy losses due to bending. Subsequently, the end caps were made as thin as possible, up to the point of buckling failure, plus some factor of safety. In this subsection, that assumption is tested, to see at what point pin

connected joint can be assumed, and if thickener material can be used to increase the resistance to buckling.

To produce cymbals of varying thickness and at diverse geometries, a different manufacturing technique is used, to avoid the investment of making a unique set of dies for each thickness and geometry. This technique is found in air bending. The air bending technique is illustrated in Figure 4.20, along with a picture of the actual bender.

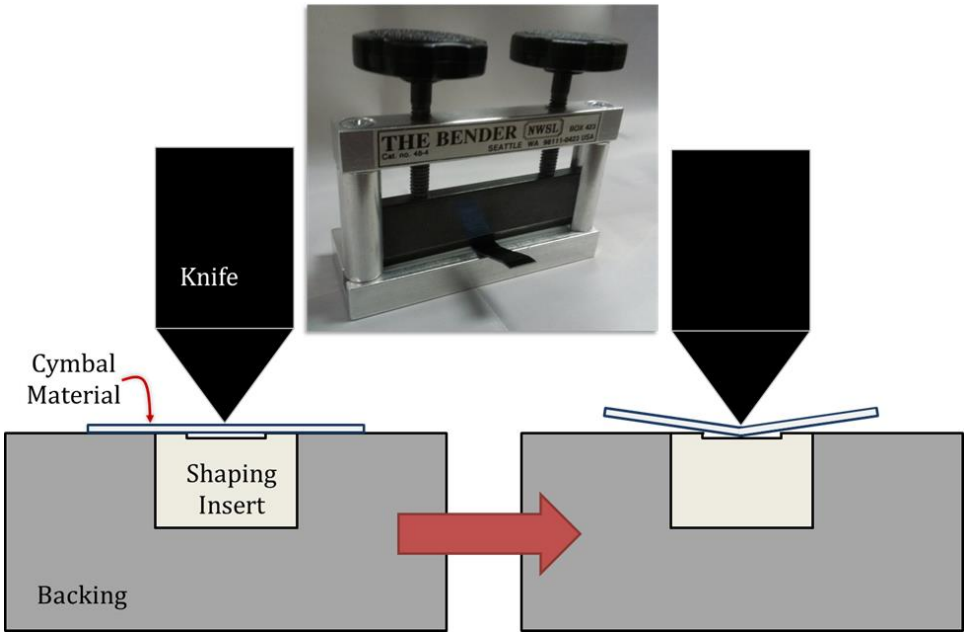

Figure 4.20 – Illustration of air bending technique (side view), with picture of actual bending device used.

Air bending forces a knife onto a flat sheet of material, forcing it into a cavity. The angle and radius of the bend are determined by the cavity dimensions, radius of the knife edge, and thickness of the material. The inside of the bend will be sharp while the outside of the bend will be curved. With this setup of air bending, each configuration of the cymbal geometry (i.e. material sheet thickness and bend angles) will only need a different insert. The inserts were design in CAD and 3D printed in VeroWhite from an Objet Eden 260v machine, with consideration from industry sources.[219, 220]

It was the goal to produce cymbals from 300, 500, and 700 μm thickness spring steel sheets, which had bend angles of 5.0, 6.5, and 8.0 degrees. The cymbal stock sheets were cut to dimension

from a larger sheet using CNC milling. Following this they were bent into shape using the appropriate shaping inserts made for each configuration. It was difficult to accurately verify the bend angles of the produced cymbals. Previously, the overall dimensions were used to geometrically calculate the bend angles, and so long as they were all the same, then tile could be made accurately. To accurately measure the bends of each of the configurations, a computer vision method was developed.

The method of optical measurement is stepped through in Figure 4.21. After the cymbals are bent, shown in part (a), they are placed on their side on a lighted table where a camera was mounted to a 3D printed stand, to shade out peripheral light sources, and ensure all photos were from the same vantage point. This setup is shown in part (b). The resulting pictures has the background saturated in white, with the cymbal profile being shaded in darkness, as seen in part (c). The edges of the cymbal were also colored with black ink to further enhance the contrast of the cymbal profile and background.

The images were filtered, using a black-white contrast filter, such that in (d) only the cymbal profile remains (white pixels). Part (e) shows how each column of pixels was averaged, such that the cymbal profile collapsed to a line. Do to pixel noise, this line is jagged. Therefore, a low pass filter of the averaged line (blue) was used to smooth the line into a more continuous profile (green). The second derivative of the smoothed line was calculated, and locations of the bend identified as spikes in second derivative. The area between the bends were treated as line segments, and the angles between the line segments were then calculated and plotted over a distorted image of the cymbal, as shown in part (f) of Figure 4.21. The bending and verification process was then repeated until all bends were ±0.2 degree of the desired angle.

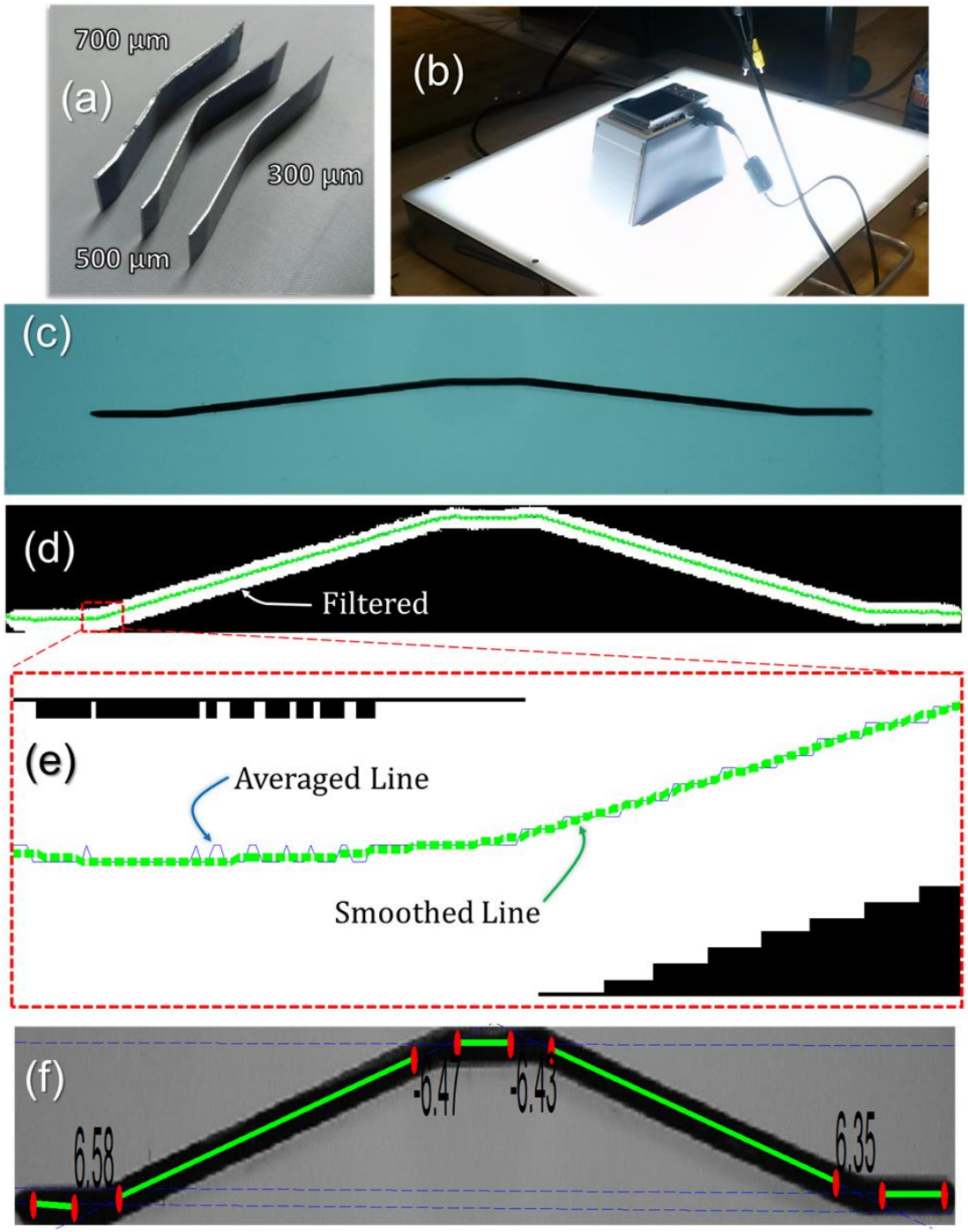

Figure 4.21 – (a) Bent cymbal profiles, which were (b) photographed on a lighted table. The photographs (c) were then digitally filtered (d) removing the background from the picture. The cymbal pictures was then (e) pixel averaged and smoothed, where (f) the bends and straight were identified automatically and bend angles calculated for accuracy, where an accurate bend was chosen to be ±0.2 degree of the desired value, in this case 6.5 degrees.

The quality controlled end caps were then bonded to the PZT using the same Loctite 120 HP epoxy and procedure as before. Not packaging of the PZT was used in this study. The nine resulting (three bend angles across three material thicknesses) cymbals were then testing using the pneumatic press described in Section 4.5. Since each cymbal had its own maximum load capacity, thanks to its geometry, a load which all the cymbal could withstand was used to test all the cymbals. Each cymbal was tested individually, subject to an 11 N impulse for 0.6 seconds. The maximum voltage from each cymbal was then recorded and averaged over several repeated impulses. The fabricated cymbals and their performance are shown in Figure 4.22 below.

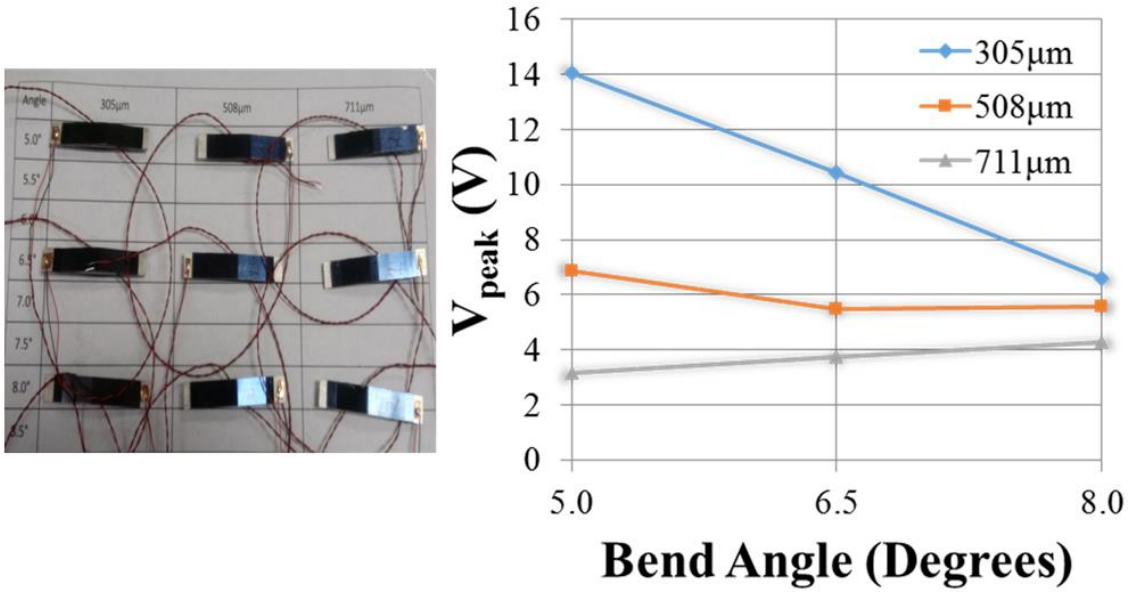

Figure 4.22 – (Left) Bent and assembled cymbal transducer used in this study. (Right) Results of cymbal peak output voltage in response to an 11 N force impulses (0.6 s).

From the figure above, it is clear that the highest voltage production is from the thinnest material, the nominally 300 micron thick spring steel. This confirms the assumption that the material needs to be as thin as possible to assume pin connected joints. Additionally, the trend of increasing voltage as a result of the increase force amplification is observed as the bend angle becomes smaller and smaller. This relationship, in theory, follows the cotangent of the bend angle.

What is ultimately learned from this study, is that there is no real optimization of the cymbal transducer. It should be made as thin and at as low of an angle as possible. Thus, the

performance capabilities of the cymbal transducer ultimately come down to the material and manufacturing quality.

4.13 Conclusion

In this chapter, a self-powered wireless occupancy sensor has been designed in order to take a major step toward practicalizing the smart building concept. The device takes the form of a floor tile, which powers the wireless signal transmission of occupancy information by deriving energy from human gait when stepped upon. This Smart Tile Energy Production Technology (STEP Tech) has demonstrated the ability to control automated process in smart buildings, in this case lighting, and can be easily extended to climate control and many other electronically controlled building systems. In realizing STEP Tech, several major challenges were addressed, including the modeling and optimization of a rectangular cymbal piezoelectric transducer, the development of a packaging technique and construction of a durable floor tile enclosure aimed at protecting and prolonging the useable life of the piezoceramic, as well as, the design of energy harvesting circuitry for optimal energy conversion and wireless signal transmission, and finally experimentation and demonstration to prove "real world" functionality. These accomplishments were made while also limiting the deflection of the tile to an unperceivable level, so the gait of the building occupants is not disturbed as they walk about, preserving the integrity of the measured occupancy.

5 CONCLUSION

In this dissertation, detailed systematic investigations were conducted on how energy harvesting solutions could be created to develop a synergy between human motion and assistive electronic devices, which could be powered by the very motions they are assisting. In this way, the assistive devices can be made more effective, by virtue of energy independence or increased longevity, ultimately increasing the quality of life for people, above and beyond what was already occurring. Solutions were examined in each of the three solution spaces possible when harvesting energy from human, which consists of Implantables (inside the body), Wearables (on the body), and Peripherials (outside the body).

The body is unique in terms of an energy harvesting source, as it is conscious of the flow of energy in its surroundings. Humans have evolved over millennia to minimize energy expenditure. Extraneous loads on the body are not well accepted and are subsequently not an acceptable design solution. Therefore, with the harvester's load placed on a source (human body) so significant, a new method of classifying energy harvesters was presented in the context of maximum power transfer theorem. In considering the classification of energy harvesters based on the load they place on the energy source, or ratio of load to source impedances, it was presented how, when harvesting energy from humans, one needs to employ either a Small Load or Decoupled type harvester. The small load type energy harvester inherently affects the source system in a small way, by virtue of the low level of power derived comparted to the potential power output level of the source. This type of interaction allows the source (body) to remain efficient, since it is hardly disturbed. Decoupled systems are those which collect and store energy in a medium of the same type in which it was collected, and then converts it into electricity at a later time. Decoupled systems are advantageous since they do not place damping on the energy source, as energy is not converted immediately. In the context of human motion, decoupled systems feel natural, since mechanical energy of motion is constantly stored and released in muscles and tendons. Energy conversion, or damping, penalizes the motions of the body, whereas energy storage only exerts a force (like a spring), which would be the most familiar interaction.

To summarize the design synergy strategy in each chapter, as well as, the classification based on load placed on the body, Figure 5.1 was created. This figure describes the studies conducted on how heartbeats can power the pacemakers regulating the heartbeat; how walking can

power the portable communication equipment guiding the path; and how movement within a smart building can power the occupancy measurement in automatic occupancy-driven lighting and climate control systems making the building habitable yet energy efficient. The mechanisms proposed in this dissertation could reach beyond the applications offered in the chapters.

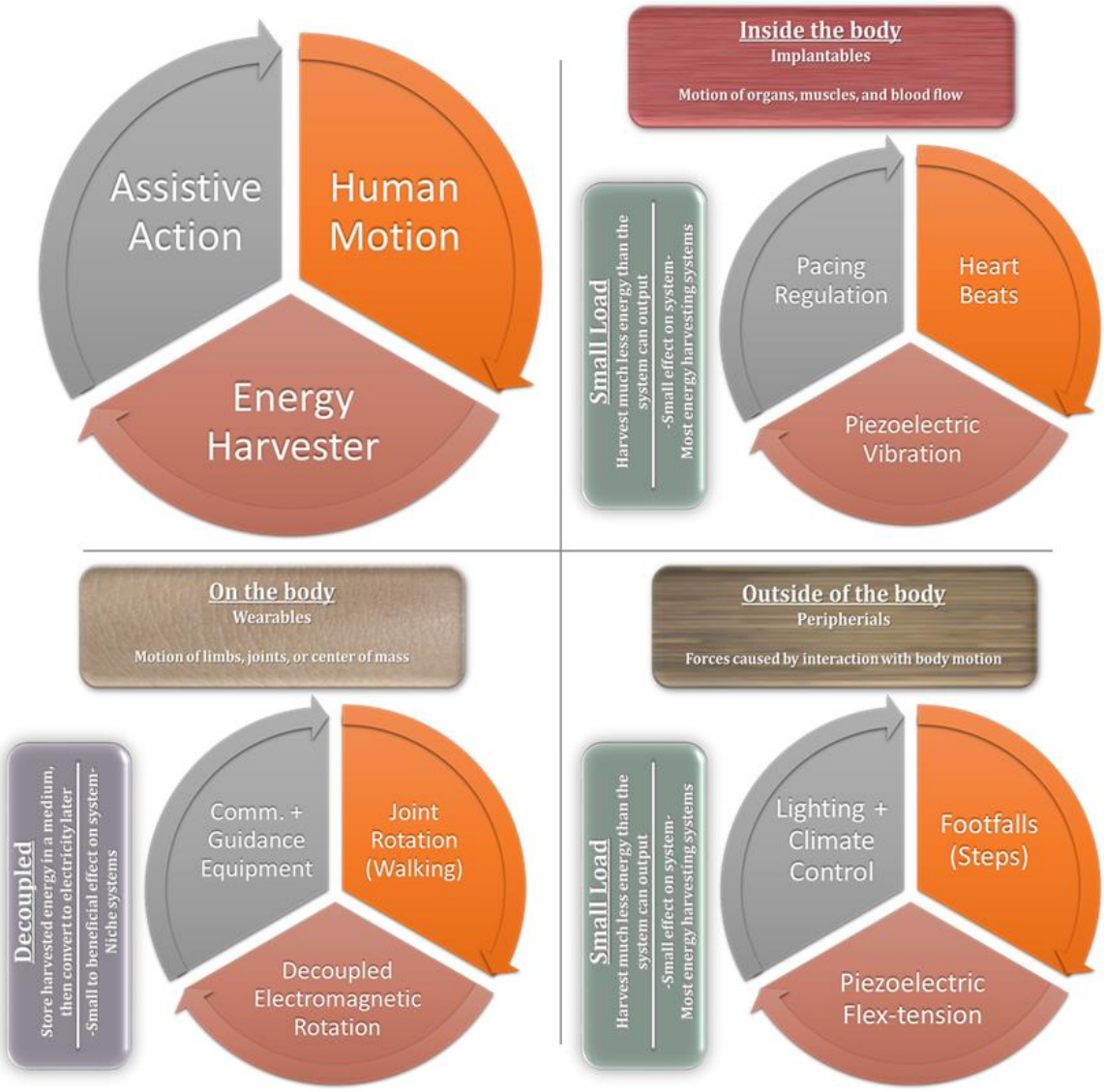

Figure 5.1 – Illustration of design methodology for each chapter of this dissertation with corresponding classification according to load placed on the body.

Chapters 2, 3, and 4 are summarized in the following sections, along with direction for future work in each area. Focus in the summaries is placed upon the novel contributions to the field.

5.1 Implantables

5.1.1 Summary

In Chapter 2, the solution space of implantable devices was explored. Due to the limited amount of energy which can be harvested from within the body, without disrupting it, stimulator type implants were chosen to attempt to power, due to their low energy consumption and extensive use in the medical field. Of the stimulator devices, cardiac defibrillators (pacemakers) were chosen as the target application. The pacemaker was introduced in terms of its function, implanted location, and device geometry, along with the key metrics associated with incorporating an energy harvester with the pacemaker. These metrics dealt with the safety and subsequently form factor, and power output.

Being an implanted device, the harvester has to be biocompatible. This is challenging for many piezoelectric-based energy harvesting materials. It was consequently proposed that the harvester could fit within the pacemaker housing, thus being sealed from the body, eliminating biocompatibility issues. With this constraint, the form factor of the harvester becomes of great importance. Since the areas of electrode connection, and sensors and electronics should not be altered, to preserve the function of the pacemaker, the harvester was proposed to occupy some of the battery area, with a smaller conformal battery (around the harvester) taking its place. Displacing battery area, the harvester must provide enough power to justify the reduction in battery, with the overall goal of increasing pacemaker longevity. To this end, the harvester must be approximately 27×27×5 mm, and produce around 100 μW. With these constraints it was determined that a vibration energy harvester would have the best chance of meeting the power requirements. A vibration energy harvester excited by the heart beats will receive vibrations of 20-30 Hz at approximately 0.1 G acceleration.

Given the relatively square area available for the harvester to occupy within pacemaker, initially a comparative analysis was performed to identify the choice between classical cantilever (one-dimensional) and zigzag (two-dimensional) piezoelectric vibration energy harvesters of the

same surface area (footprint). It was found that the zigzag harvester had approximately 3-6 times higher power density with only 55-66% of the resonance frequency of the simple cantilever. The resonance frequency is key, as the limited area available in the pacemaker housing is a hindrance to a vibration harvester reaching the soft tissue resonance frequency.

After establishing the power density merits of the zigzag harvester, next a means of increasing the vibration harvester's bandwidth or width of the resonant peak was investigated. This was done to transform the typical narrow resonant peak of a vibration harvester, to match the broader excitation peak of the soft tissue resonance. Here, the novel technique of preloaded freeplay was proposed and implemented to increase bandwidth. The harvester was shown to behaved like a single-degree-of-freedom system outside the resonant region of the clamp-screw system and as two-degree-of-freedom system within this resonant region, thereby expanding the bandwidth. The technique was applied to the cantilever and zigzag harvesters, where it was found that by using the preloaded freeplay boundary condition, a 3.9 times increase in half-power bandwidth was achieved for the 1D cantilever, and a 7.1 times increase in half-power bandwidth for the 2D zigzag harvester. Though this technique increased the bandwidth, it does not result in harvesting additional energy, in terms of peak power, since the resonant peak is spread out over wider frequency range, rather than increased as a whole.

Taking the zigzag beam shape as a control, a design study was conducted to find the optimal 2D beam shape for energy harvesting. From the thirteen different designs conceived, simulation of the stress in the first mode shape revealed that shapes with less torsion and more bending seemed to concentrate stress in the area of the piezoelectric layer, which would directly correlate with increased power output. Based upon the simulation results, three designs, the zigzag, flex, and elephant, were fabricated and thoroughly tested. Results from the experiments validated the relationship between stress concentration and increased power output in shapes with optimized bending modes. The elephant harvester showed excellent agreement when the experimental power results were compared to a single-degree-of-freedom bending model ($r^2 \sim 0.98$). For this structure, approximately 26 time increase in power output was obtained when compared to the previous state-of-the-art zigzag design. The power output of the elephant harvester was around 81 μW, which is near the goal of 100 μW.

The elephant harvester was also observed to exhibit a unique relationship between the first and second bending modes, in that they are the opposite of each other in terms of deflection. It was

hypothesized and subsequently confirmed that these two opposite modes could be merged into a combined mode shape whereby the entire beam vibrates in phase. This was accomplished through mass loading structural modification, by placing mass at measured optimal locations on the beam. While the modal frequencies of the first two bending modes never coincide, they come close enough in the frequency domain to produce the combined mode shape. This combined mode shape produced the highest power (~43 μW) of any of the considered configuration in the study of that sections, though the magnitude of harvested power was less than the power produced by operating the harvester at the first bending mode by itself (~81 μW). This is likely due to the reduction in vibration amplitude caused by the extra mass in motion. Though the combined mode shape itself is more efficient, at a fixed energy input to the system the extra mass in motion yields a decreased amplitude, and thus less stress is applied in the piezoelectric layer. Electrical performance could have also been reduced since the same harvester prototype (Elephant) was used in Section 2.7, and thus could have been fatigued.

The findings from this chapter provide a pathway towards developing a pacemaker with integrated energy harvester configuration, as illustrated in Figure 5.2. Here, the elephant vibration energy harvester occupies some of the battery area, with smaller battery sections around the harvester. The harvester would be optimized to work best in its first bending mode, tuned to between 20-30 Hz.

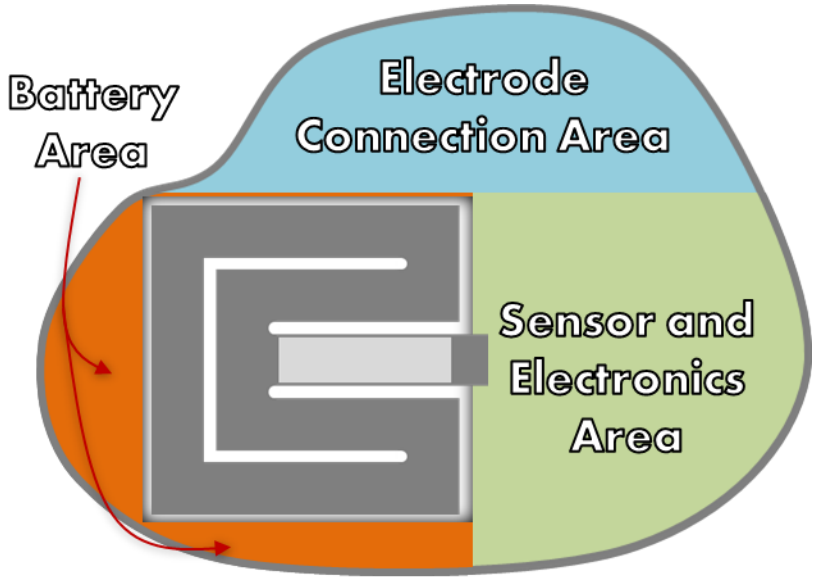

Figure 5.2 – Illustration of pacemaker internal assembly, which is split into three main (Battery, Electrode, and Senor and Electronics) areas, with the proposed inclusion of the 'Elephant' energy harvester (to scale).

5.1.2 Future Work

In Section 2.7, the design study of two-dimensional vibration energy harvesters was conducted with little regard for the fundamental frequency of the beams, so long as they were all similar, allowing for direct comparison in terms of dimensions, frequency, and power output to be made. In the future work, the harvesters (particularly the elephant, as it yielded the best performance) should be designed and tested such that the first bending resonance frequency lands within the 20-30 Hz range which matches with the excitation frequency that the pacemaker receives from heart beat vibrations. The elephant harvester, as described in this dissertation, has the first bending modal frequency around 65 Hz. To reduce the resonance frequency by 2.6 times (to make it ~25 Hz), one can modify several parameters according to Equation (1.16). Since the footprint of the harvester is somewhat fixed, due to the allowable area in the pacemaker, the effective length cannot really be changed. Thus, the thickness of the beam substrate and piezoelectric layer would have the greatest effect on the resonance frequency, since they exhibit an inverse cubic relation. This would mean reducing the thickness of the substrate from 300 μm

to about 220 μm. The thickness of the piezoelectric layer would then also be reduced in proportion, according to the relationships described in Section 1.3.1.

Improvements in materials could also be achieved to improve the energy harvesting performance. The beam substrate in the studies in this dissertation were steel to allow for configuration changes in mass load where the masses were neodymium magnets. It would most likely yield better results to use aluminum as the substrate, as aluminum has lower material damping. Thus more of the energy would go into the piezoelectric layer and less dissipated in the beam. The added masses in the final configuration integrated into a pacemaker should not be neodymium magnets as the magnetic field would most likely interfere with the pacemaker electronics. Tungsten masses are recommended to be used in the future, due to their high density. In this way, sufficient mass can be added in a low profile, which is important considering the narrow thickness of the pacemaker housing. Finally, and perhaps most significantly, either single crystal (like PMT-PT) or textured piezocermanic should be used for the piezoelectric layer. Polycrystalline PZT ceramic was used in the studies of Chapter 2, as it is the most commonly used and readily available piezoelectric material. Textured and single crystal piezoelectric are more and much more expensive, respectively, compared to polycrystalline, though they yield much higher performance, exhibiting approximately 5-10 times higher piezoelectric response.[221] Due to the high cost of pacemakers, the cost of the more exotic piezoelectric materials is justified, and compared to the total cost of the pacemaker, would hardly be noticeable.

Finally, improvement to the geometry of the elephant design is suggested. In the design study, all of the conceived beam designs had meanders of equal span width of 4.28 mm. I hypothesize that an unequal span width would yield better performance. Stress is concentrated only in the central span where the piezoelectric layer resides. All other spans act simply as a dynamic magnifier, similar to that of a whip. As illustrated in Figure 5.3, a new design is proposed which narrows the adjacent spans and increases the width of the central span, such that the total dimensions remain the same. In this way, the adjacent space could still act, or may even act better, as dynamic amplifiers, while the piezoelectric layer could be made larger with the increased area of the central span. Increasing the width of the central span would have the effect of increasing the resonance frequency, so this must be considered with all other changes. Increasing the area and decreasing the thickness of the piezoelectric layer would increase its capacitance, according to Equation (1.5).

Figure 5.3 – Illustration of possible geometry improvements to the 'Elephant' piezoelectric vibration energy harvester.

It is also proposed that lengthening the adjacent spans of the elephant could help, especially in the context of the combined bending mode studied in Section 2.8. By lengthening the adjacent spans, it would give more leverage to the mass loading, possibly allowing the combined mode shape to occur under different conditions (i.e. lower frequency, less mass). This technique is not recommended, however, for the pacemaker application, since it would increase the overall area, such that it would not fit within the pacemaker housing, unless the entire design were made proportionally smaller.

5.2 Wearables

5.2.1 Summary

In Chapter 3, the solution space of wearable devices was explored. Our society has become increasingly dependent on portable electronic devices, and the modern soldier is no exception. Going from the historical mean carried load of ~30 kg, to the modern mean carried load of ~47 kg, this abrupt change in weight carried is attributed to portable electronic devices, specifically the associated battery weight. It was proposed that by harvesting energy from a soldier's motion, specifically the torque about the ankle joint during regular gait, a primary battery could be kept charged. This eliminates the need to carry extraneous sets of spare batteries, ultimately reducing

the pack weight soldiers must carry. Reduction in pack weight would reduce fatigue and risk of injury.

A review of wearable technologies, in the form of health monitors, exoskeletons, and energy harvesters, was performed before the selection of energy harvesting strategy was explored. It was concluded that joint rotation would be the best method to pursue though center of mass motion is also a viable alternative. Next, the joint on human body conducive for harvesting energy was surveyed. With the upper body joints typically weaker than lower body joints, and soldiers frequently carrying the majority of their equipment on the upper body, it was felt that the addition of an energy harvester exoskeleton (exoskeleton needed to harvest from joint rotation) would be cumbersome. Therefore, the lower body was selected for harvesting energy.

The lower body joints were inspected based upon the published literature where it was found that the ankle produces the highest torque compared to all other joints. This is intuitive as it is the joint furthest away from the center of mass. With the highest torque, the ankle has the highest potential for energy harvesting, though the angular rotation is smaller than that of the knee, which has been targeted for energy harvesting by others. An intangible benefit to harvesting from the ankle is the fact that boots are worn by all soldiers, and if the harvester exoskeleton and mechanism could be integrated into the boot, that would satisfy the criteria of having a normal appearance and not protruding from the body. Thus, it would be more readily accepted and worn by soldiers.

There is much literature on analyzing the motion of human gait, but little has been done on understanding how gait is affected by wearing boots. A biomechanics analysis was conducted using motion tracking cameras, force plates, and pressure sensing insoles. This analysis was conducted first on myself to get a quick data set for the purpose of designing the boot mechanism. That data is given in this dissertation. Later, the biomechanics analysis was also conducted on 13 active duty military participants. This more formal experiment is described in this dissertation, though results are still under analysis. From the preliminary findings, it would appear that wearing a boot would slightly reduce the ankle angle rotation. This is to be expected as the boot supports and stiffens the ankle joint. Wearing a weighted pack (~16 kg) has the effect of increasing ankle rotation in response to the increased load.

Like any cyclic motion, in human gait there are regions of positive and negative work. In the case of the ankle joint, the positive work done is much larger than the negative work, so we can propel ourselves forward with high efficiency. The negative work comes when the foot first

hits the ground, and is stationary as the center of mass moves forward. To keep the body upright and stable, the ankle must produce a torque which is in opposition to the motion of the center of mass, which is why it is considered negative work. Based upon the information available in literature and our own studies, it is proposed that harvesting energy during the negative work phase of gait could actually reduce metabolic rate (the rate at which the body uses energy), by virtue that the harvester performs some of the negative work which is normally done through the calf muscle to perform. With this strategy, metabolic rate could not only be reduced from the reduction in battery weight associated with eliminating the need for spare batteries, but also by the harvesting action itself reducing the effort the body must put forth during certain stages of gait.

To accomplish harvesting energy only during the negative work phase of gait, a novel mechanism had to be developed. This mechanism consisted of several stages, namely, the torque input from the brace (exoskeleton), angle amplification that takes the high torque low angular displacement motion of the ankle and converts it into a lower torque but higher angular displacement motion, which winds a power spring for storing the energy, before it is converted to electricity using an induction generator. The housing of the device, which replaces the heel section of the boot to maintain a normal appearance of the boot, is also a key aspect of the design. After many design iterations, a concept was finally realized that would harvest energy during the negative work phase of gait, without encumbering the body during the positive work (push-off) or swing phases of gait.

The concept itself is quite novel and has never been attempted before. Several other aspects of the design are contributions to the field as well. Though it is not used in the final design, during the design phase, a novel pulley was developed which can transfer much more torque than a conventional round belt pulley, with minimal additional friction losses. This was designed to be part of the angle amplification section, where it was first desired to use pulleys instead of gearing to minimize noise generation. Next, a key novelty of the design was the use of planetary gears of varying configuration to virtually disconnect the mechanism during the swing phase of gait, where there is typically negligible torque on the ankle. Here a drum brake is actuated by the pressure on the sole of the boot while the foot is on the ground. This brake holds the ring gear stationary, while the planet carrier is the input, yielding an increase in rotation of the sun gear (connected to the power spring) during the negative work phase of gait. While the foot is in the air, the drum brake is released and the ring gear is free to rotate, as the planet carrier is still the input, and the sun gear

is de facto stationary thanks to the counter torque of the power spring. In this way, the boot wearer will only be rotating the ring gear of negligible mass (and also low gear ratio) during swing phase, rather than actuating the entire mechanism.

To maximize power, generators were design and built by myself, as commercial units did not fit the size requirements demanded by the boot, with all components of the mechanism having to fit within the heel section housing. The power springs were manufactured by hand for the same reason.

A model of the electrical output of the boot was developed, using the experimental data for the power springs manufactured by myself. Here, it was found that approximately 0.6 W could be expected to be produced, which is within the target goal of USB slow charging.

The design of this boot exoskeleton energy harvester, while a major step forward in harvesting energy from human motion, is not without some concerns. The weight of the mechanism should fall under scrutiny. If additional weight is added to the boot, it will most definitely increase metabolic rate. The material (high density urethane) removed from the heel is replaced with mostly plastics, so there should even be a net weight reduction from the mechanism. Though there is also the brace of the exoskeleton which runs up the leg of the boot. This weight is in addition, and could cause the boot to weigh more than without the harvesting mechanism. Though, the use of lightweight materials, like carbon fiber, would minimize the effect. Removal of heel section material to replace it with the mechanism housing, is removing shock absorbing material to replace with a rigid housing. While most shock absorption is done in the insole, the removal of midsole material may increase pressures on the foot, though it is not expected to be to a significant degree.

5.2.2 Future Work

In the future, the device as a whole should be manufactured and tested for electrical performance, and the intangible of how it feels to the boot wearer. Every consideration has been made in the design process with the wearer of the boot in mind, though actually wearing a completed boot prototype would reveal much information about its interaction with the body. To this end, the biomechanics testing should be repeated with subjects wearing the HERMES boot while metabolic rate is being measured. The goal of the biomechanics analysis will be to learn if pressure on the foot is effected, if joint rotation angles are effected, and if metabolic rate has in

fact decreased. Also, the power output of the device can be thoroughly quantified. To conduct this testing, however, many boots of different sizes would need to be manufactured, such that a broad range of persons could participate in the study and a more representative conclusion as to the performance and effect of the boot for all persons could be extrapolated.

To better the performance of the harvester mechanism, a few considerations are given here. From the beginning it was sought to maximize the size of the generator, as the thinking was a bigger generator would equal more power output, which is in general this is true. Initially, it was thought that due to the size limitation of the heel section housing, the generator would be too small. However, after several enhancements to the final heel section housing design led to a generator volume that was comparatively large. Subsequently, the inertia of the generator became greater, and through the analytical simulations it was found that the rotation speed was somewhat reduced. There seems to be optimum between the volume of the generator and the rotation speed possible when rotated operating by the power spring. The power spring should be made with more torque in mind, especially more torque at lower turns. This can be done by increasing the thickness of the spring material. Though to increase torque at lower turns, a larger arbor should be employed. In Section 3.7.4, the new designs used a smaller arbor, which allowed for more turns, but lowered the torque of the initial turns. A high number of turns is not truly desired, as to wind the spring several times would require a large gear ratio, which induce much higher frictional losses, would cause noise, and produce an unnatural feeling for the boot wearer.

5.3 Peripherals

5.3.1 Summary

In Chapter 4, the solution space of peripheral devices was explored. The interest in the Smart Building concept (or a building aware of it occupants and energy consumption) in recent decades alludes to the demand for, and recognition of, the energy savings and additional functionality brought about by measuring building occupancy. Current occupancy sensors are insufficient, as they only infer occupancy based on other measured parameters, like motion or sound produced. These technique cannot measure changes in occupancy, number of occupants, or identify the difference between an empty room and a room where the occupants are still.

To solve this problem, it was thought to use a sensor embedded in the floor between doorways or boundaries of rooms to capture footfalls as building occupants move from room to room. With this technique, a count of the number of occupants in each room could be maintained. With the number of occupants known, the control system could, for example, turn off lights when the occupancy count reaches zero, or adjust climate control air flow for rooms with more or less occupants. A simple pressure sensing mat could do this job, however, such a sensor would not solve the problem of power consumption of occupancy sensors. Occupancy sensors consume power 24 hours a day to monitor a space for perceived occupancy changes. If such a lower powered sensor successfully, for example, turns off lighting that was left on for no reason, then the advantages are obvious in terms of energy savings. Though, the use of these "always on" occupancy sensors can lead to a mitigation in energy savings, due to the constant power draw of the sensors themselves.

Therefore, it was also sought to make the sensor self-powered, by converting the pressure placed on the floor by human gait into electricity to power the occupancy measurement. Subsequently, the requirement of harvesting enough energy from a single step to power a wireless signal transmission (indicating a change in occupancy to the central receiver) was added to the requirements of the tile being imperceivable to the building occupants. As mentioned earlier, one way to implement this technology would be to embed it into the floor under the decorative layer (i.e. carpet, laminate, etc.), so it cannot be seen. The tile must then also feel like a normal floor, so that it has negligible influence on the occupants motion. This means the tile must be stiff.

Having a stiff tile while still producing sufficient power would require the use of an appropriate transduction technique. The piezoelectric cymbal transducer, a flex-tension device, typically used in high frequency applications was found to provide desired characteristics. Cymbals are used in high frequency applications because they are quite stuff structures, leading their resonance frequencies to be in the higher frequency range. In Chapter 4, however, the cymbal(s) were used in an off-resonance condition where their stiffness lends well to the criteria that the tiles as a whole must be stiff to feel like the floor.

The cymbal transducer was modeled with simplified analytical techniques. Models were validated through experimental results, and were in good agreement with finite element simulations. Analytical modeling allowed for a parametric design study to reveal the design believed to be the best tradeoff between performance, allowable deflection, and manufacturability.

Testing fixtures were also developed to mimic the force and timing of footsteps, to give repeatable test conditions across different device designs. The brittle piezoelectric material (PZT) was packaged in a bulk laminate composite configuration, which was shown to improve breaking strength and also output power due to enhanced stress distribution. The tile enclosure was made to protect the cymbals from breaking due to overloading, and it provided good collection of stepping forces. Finally, the power conditioning and signal transmission circuitry was designed and implemented for demonstration of lighting control.

In the demonstration, the tile acted as a toggle button, turning the light on if it were off, or turning it off if it were on. This happened regardless of the manner in which the tile was stressed by stepping. To function as intended in final application, the tile would need to identify and transmit the direction a person was walking, so that the receiver control system would know to increment or decrement the occupancy count for given rooms. By taking advantage of heel-toe pattern of human gait, a measurement technique was developed by comparing the instantaneous voltage produced by individual cymbals to infer the direction of motion.

The packaging technique was also enhanced to electrically isolate the piezoelectric, making it environment proof, both containing the heavy metals in the PZT and making it waterproof, which is good for the target applications. The enhanced packaging further increased breaking strength and power output.

5.3.2 Future Work

In the future, the concept should be implemented into a larger-scale demonstration of the technology. The tiles could be installed in a building where the occupancy could be counted with the tile and verified by other (traditional) means to see if the system was capable of accurately measuring the building's occupancy in real time. It has already been demonstrated in the literature how occupancy sensing can aid in the energy draw from lighting and climate control systems, the largest consumers of power in residential and commercial buildings.

While STEP Tech could be used in residential home, it would be of greatest potential in the commercial sector, where the building does not belong to the inhabitants. In this situation, there is a distribution of responsibility and apathy toward energy conservation in the building. Therefore, in commercial buildings, controlling building systems automatically would be of greater effect,

because the probability of lighting being left on, or otherwise wasting of energy, is much greater than in a residential home.

A key aspect to increasing the usefulness of the tile would be to increase the range in which it can transmit the occupancy signal. This involves using a different, lower frequency radio such that less signal attenuation in the building occurs. The radio signal itself should also be a higher power, such that even as attenuation occurs the range is still large enough that the signal can reach the central receiver. More power required for this operation could be produced using the design given below in Figure 5.4.

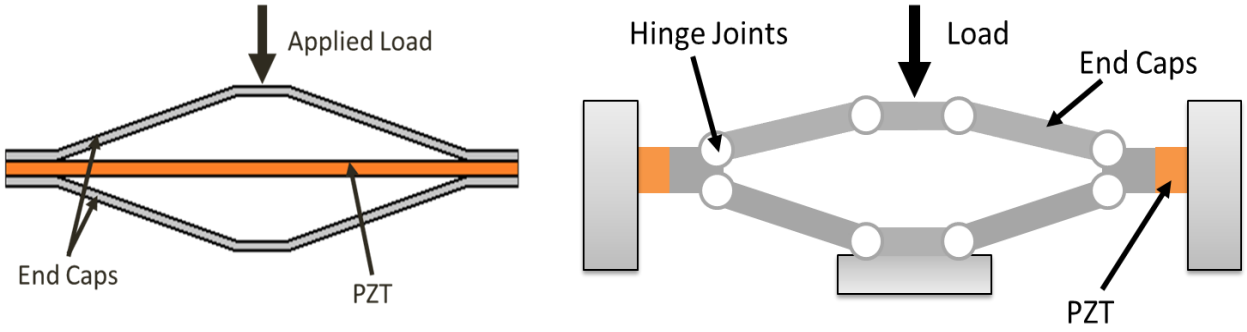

Figure 5.4 – Illustrations of (Left) cymbal transducer of the design presented in this dissertation, (Right) 'Hexpress' design proposed for increased performance under footfall loading.

As discussed in Section 4.12.2, the cymbal performs best when it becomes thinner and thinner, because the angle bends store less energy and becomes more and more like pin connected joints. I therefore hypothesize that it would simply be better to use pin connected joints. In the Hexpress design, six links are connected with pin joints to form a similar profile as the cymbal, though the piezoelectric is placed between the ends of the hexpress and the ridged walls of the floor tile housing. With this design, the piezoelectric is placed in compression and oriented in the 33 mode. The hexpress design then has several key advantages:

- Since the joints of the hexpress are pinned, the links can be made thicker to resist buckling, without compromising transducer performance.
- With the enhanced resistance to buckling, the joint angles can be made smaller, increasing stress amplification from the load to the piezoelectric layer(s).

- Joint angles can be more accurately controlled, since they are a function of the length of the individual member links, which could be machined to tight tolerance, rather than a function of less accurate bending techniques.
- Since the piezoelectric material (ceramic) is in compression, the ultimate yield strength is significantly higher than in tension. This means that more stress can be placed on the piezoceramic (thanks to the smaller joint angles), increasing voltage and current production.
- Orienting the piezoelectric in the 33 mode yield better performance in that the piezoelectric properties are approximately 2-3 times that of the 31 orientation, which is the loading case for the cymbal transducer.

Like any piezoelectric transducer, the performance of the device can be increased by simply using a better material, like those discussed in Section 5.1.2. It is thought that an encumbrance to STEP Tech would be its cost, as even readily available piezoelectric materials are somewhat expensive. The hexpress design would make better use of the piezoelectric material, producing more power per unit of piezoelectric used. It would remain to be seen if this could be translated into using ultimately less piezo, thereby reducing cost. Using a more exotic material would dramatically increase the cost, which may be acceptable in some applications. For instance, STEP Tech would be well suited for security applications where using an exotic piezoelectric material would make the tile much more sensitive, lowering the minimum weight for signal transmission substantially. In such an application, the increased performance and criticality of functionality may justify the increased cost.

The size of the tile is also crucial in its application. The current tile described in this dissertation was made to mimic the dimensions of a standard tile size (12×12 in). Though, this tile size would be insufficient for occupancy measurement. Going back to the requirement that the building occupant's motion cannot be disturbed, if the integrity of the occupancy measurement is to be maintained, the tile must be hidden beneath the decretive layer of flooring. Therefore, the occupants cannot see or perceive the tile. A one foot square tile could then be easily stepped over during normal walking or otherwise not receive a full step, even with the best of placements between a doorway. For the next iteration of the tile, it is crucial that a study be performed with subjects walking through doorways, both open and shut, while their footsteps are monitored. With

such a study, a heat map or step density plot could be drawn and the size and shape of the tile determined such that one could be nearly certain that any step through a doorway would be captured by the tile.

Such data is illustrated in Figure 5.5, along with the effect of encountering an open or closed doorways would have on the footfalls. Encountering an open doorway would do little to alter the path of individuals and the subsequent probably distribution of steps would look like a normal curve centered in the doorway. Encountering a closed door would have the effect of densifying the steps on the handle side of the door, skewing the probability of step toward that side, as shown in the figure. In such a case, it would be more difficult to measure the direction of travel of a step, since it is likely that several step would occur in close proximity, from both feet. Though, actual testing would need to be undergone to draw such conclusions with any certainty.

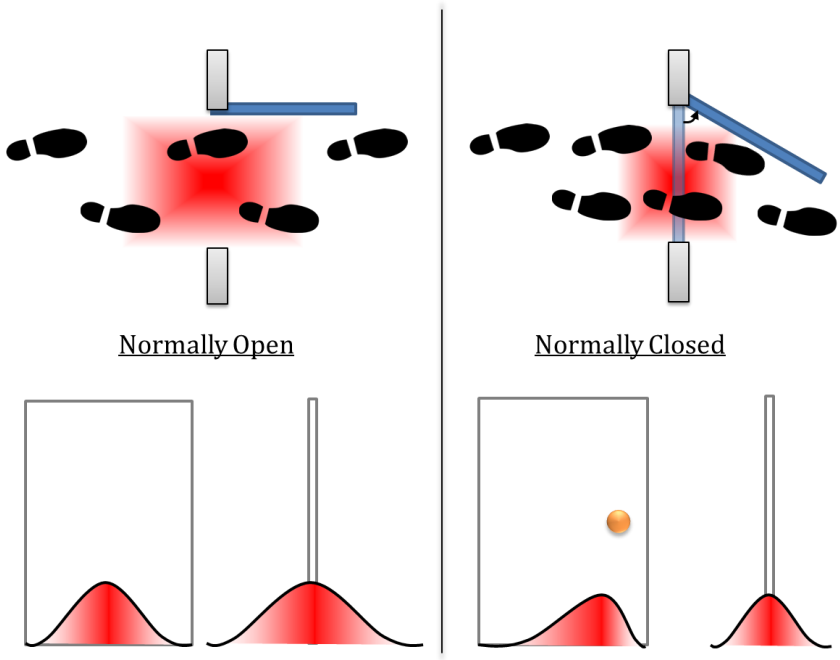

Figure 5.5 – Illustration of effect of encountering open or closed doorway and proposed probability distribution of steps. Collecting this type of data would allow the determination of the size and shape of the next generation of STEP Tech tile.

To conduct such measurements, one would need the testing space depicted in Figure 5.6. Here, study participants would start at each of the numbered spaces (orange dots) and walk to each dot on the other side of the wall, both for cases with and without a door in the opening between

the walls. In this way, locations for footfalls could be ascertained for both closed and open conditions, with subjects approaching and departing at several different angles (determined by start and end locations). This would total 100 (10×5×2) trials for each participant, which would be somewhat lengthy, though the information gathered would be of great significance.

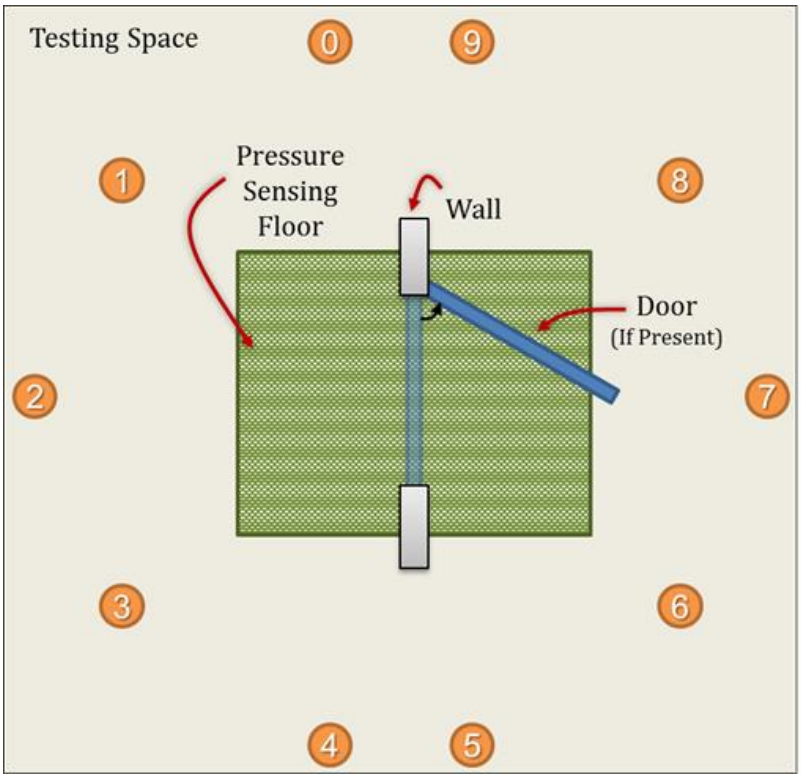

Start	Destination
0	5, 6, 7, 8, 9
1	
2	
3	
4	
5	0, 1 , 2, 3, 4
6	
7	
8	
9	

Figure 5.6 – Illustration of experimental setup for measurements described in Figure 5.5, with starting and finishing walking locations (orange numbered dots) and location of door and pressure sensing floor to track footsteps.

The experiment, shown above, should also be repeated with the tile in its final configuration, to verify if sufficient power is generated and the direction of travel can be determined. Finally, it has been asked of me several time while making presentation about my progress on STEP Tech, what would happen in a few different situations, namely:

- What if a dog (or other animal) walked across the tile?
- What if a wheel chair were rolled across the tile?

The answer to such questions could only be obtained by incorporating them into the human trials of the final design. Such cases, however, would have to be answered if a buildings lighting and

climate control were to be entrusted with autonomy to the real time occupancy measures from STEP Tech.

REFERENCES

1. Crowther, J.G., *British scientists of the 19th Century*. 1935.
2. Singleton, E., *Student Profile: Nathan Sharpes.* The CEHMS Chronicle, 2013. **1**(4): p. 6.
3. Stephen, N., *On the maximum power transfer theorem within electromechanical systems.* Proceedings of the Institution of Mechanical Engineers, Part C: Journal of Mechanical Engineering Science, 2006. **220**(8): p. 1261-1267.
4. McLaughlin, J.C. and K.L. Kaiser, *" Deglorifying" the maximum power transfer theorem and factors in impedance selection.* IEEE Transactions on Education, 2007. **50**(3): p. 251-255.
5. Radosevich, L. and A. Skinrood, *The power production operation of Solar One, the 10 MWe solar thermal central receiver pilot plant.* Journal of solar energy engineering, 1989. **111**(2): p. 144-151.
6. Chao, Y. *Autonomous underwater vehicles and sensors powered by ocean thermal energy*. in *OCEANS 2016-Shanghai*. 2016. IEEE.
7. Hodgins, D., *Implantable Medical Devices.* Medical device technology, 2004.
8. Mond, H.G. and A. Proclemer, *The 11th World Survey of Cardiac Pacing and Implantable Cardioverter-Defibrillators: Calendar Year 2009–A World Society of Arrhythmia's Project.* Pacing and clinical electrophysiology, 2011. **34**(8): p. 1013-1027.
9. Mallela, V.S., V. Ilankumaran, and S.N. Rao, *Trends in cardiac pacemaker batteries.* Indian pacing and electrophysiology journal, 2004. **4**(4): p. 201-212.
10. Austin, C. and F. Kusumoto, *Innovative pacing: Recent advances, emerging technologies, and future directions in cardiac pacing.* Trends in Cardiovascular Medicine, 2016.
11. Niu, Q., et al. *Application of a MEMS-based energy harvester for artificial heart wireless energy transmission*. in *Computing, Communication, Control, and Management, 2009. CCCM 2009. ISECS International Colloquium on*. 2009. IEEE.
12. Wang, Z., S. Mai, and C. Zhang. *Power issues on circuit design for cochlear implants*. in *Electronic Design, Test and Applications, 2008. DELTA 2008. 4th IEEE International Symposium on*. 2008. IEEE.
13. Turner, W., et al. *Nuclear magnetic resonance energy harvesting for ultra-low power biomedical implants*. in *Wireless and Microwave Technology Conference (WAMICON), 2011 IEEE 12th Annual*. 2011. IEEE.
14. Ativanichayaphong, T., et al. *An implantable batteryless wireless impedance sensor for gastroesophageal reflux diagnosis*. in *Microwave Symposium Digest (MTT), 2010 IEEE MTT-S International*. 2010. IEEE.
15. Sauer, C., et al., *Power harvesting and telemetry in CMOS for implanted devices.* Circuits and Systems I: Regular Papers, IEEE Transactions on, 2005. **52**(12): p. 2605-2613.
16. Faul, A., M. Turner, and J. Naber. *Implantable wireless microsystems for the measurement of intraocular pressure*. in *Circuits and Systems (MWSCAS), 2011 IEEE 54th International Midwest Symposium on*. 2011. IEEE.
17. Ouda, M.H., et al., *5.2-GHz RF power harvester in 0.18-/spl mu/m CMOS for implantable intraocular pressure monitoring.* Microwave Theory and Techniques, IEEE Transactions on, 2013. **61**(5): p. 2177-2184.
18. Olivo, J., et al. *Electronic implants: Power delivery and management*. in *Proceedings of the Conference on Design, Automation and Test in Europe*. 2013. EDA Consortium.

19. Kotani, K., A. Sasaki, and T. Ito, *High-efficiency differential-drive CMOS rectifier for UHF RFIDs.* Solid-State Circuits, IEEE Journal of, 2009. **44**(11): p. 3011-3018.
20. Ozeri, S. and D. Shmilovitz, *Ultrasonic transcutaneous energy transfer for powering implanted devices.* Ultrasonics, 2010. **50**(6): p. 556-566.
21. Zhu, Y., S. Moheimani, and M. Yuce. *A 2-DOF wideband electrostatic transducer for energy harvesting and implantable applications*. in *Sensors, 2009 IEEE*. 2009. IEEE.
22. Fowler, A.G., S. Moheimani, and S. Behrens. *A MEMS electromagnetic energy harvester using ultrasonic excitation*. in *Advanced Intelligent Mechatronics (AIM), 2013 IEEE/ASME International Conference on*. 2013. IEEE.
23. Olivo, J., S. Carrara, and G. De Micheli, *Energy harvesting and remote powering for implantable biosensors.* IEEE Sensors Journal, 2011. **11**(EPFL-ARTICLE-152140): p. 1573-1586.
24. Goto, K., et al., *An implantable power supply with an optically rechargeable lithium battery.* Biomedical Engineering, IEEE Transactions on, 2001. **48**(7): p. 830-833.
25. Suzuki, S.-n., et al., *Electric power-generating system using magnetic coupling for deeply implanted medical electronic devices.* Magnetics, IEEE Transactions on, 2002. **38**(5): p. 3006-3008.
26. Ay, S.U., *A CMOS energy harvesting and imaging (EHI) active pixel sensor (APS) imager for retinal prosthesis.* Biomedical Circuits and Systems, IEEE Transactions on, 2011. **5**(6): p. 535-545.
27. Beker, L., et al. *Stimulating auditory nerve with MEMS harvesters for fully implantable and self-powered cochlear implants*. in *Solid-State Sensors, Actuators and Microsystems (TRANSDUCERS & EUROSENSORS XXVII), 2013 Transducers & Eurosensors XXVII: The 17th International Conference on*. 2013. IEEE.
28. Deterre, M., et al. *Energy harvesting system for cardiac implant applications*. in *Design, Test, Integration and Packaging of MEMS/MOEMS (DTIP), 2011 Symposium on*. 2011. IEEE.
29. Zurbuchen, A., et al., *Energy harvesting from the beating heart by a mass imbalance oscillation generator.* Annals of biomedical engineering, 2013. **41**(1): p. 131-141.
30. Khaligh, A., P. Zeng, and C. Zheng, *Kinetic energy harvesting using piezoelectric and electromagnetic technologies—state of the art.* Industrial Electronics, IEEE Transactions on, 2010. **57**(3): p. 850-860.
31. Deterre, M., E. Lefeuvre, and E. Dufour-Gergam, *An active piezoelectric energy extraction method for pressure energy harvesting.* Smart Materials and Structures, 2012. **21**(8): p. 085004.
32. Potkay, J.A. and K. Brooks. *An arterial cuff energy scavenger for implanted microsystems*. in *Bioinformatics and Biomedical Engineering, 2008. ICBBE 2008. The 2nd International Conference on*. 2008. IEEE.
33. Fadhil, N., D. Saber, and P. Prabir. *Energy harvesting using nana scale dual layers PVDF film for blood artery*. in *Systems, Applications and Technology Conference (LISAT), 2013 IEEE Long Island*. 2013. IEEE.
34. Deterre, M., et al., *Micro blood pressure energy harvester for intracardiac pacemaker.* Microelectromechanical Systems, Journal of, 2014. **23**(3): p. 651-660.
35. Deterre, M., et al. *Micromachined piezoelectric spirals and ultra-compliant packaging for blood pressure energy harvesters powering medical implants*. in *Micro Electro Mechanical Systems (MEMS), 2013 IEEE 26th International Conference on*. 2013. IEEE.

36. Wang, J., et al. *Piezoelectric PDMS films for power MEMS*. in *Solid-State Sensors, Actuators and Microsystems Conference (TRANSDUCERS), 2011 16th International*. 2011. IEEE.
37. Almouahed, S., et al., *The use of piezoceramics as electrical energy harvesters within instrumented knee implant during walking.* Mechatronics, IEEE/ASME Transactions on, 2011. **16**(5): p. 799-807.
38. Lewandowski, B., K. Kilgore, and K. Gustafson, *In vivo demonstration of a self-sustaining, implantable, stimulated-muscle-powered piezoelectric generator prototype.* Annals of biomedical engineering, 2009. **37**(11): p. 2390-2401.
39. Li, Z., et al., *Muscle-driven in vivo nanogenerator.* Advanced Materials, 2010. **22**(23): p. 2534-2537.
40. Falconi, C., et al., *Studying piezoelectric nanowires and nanowalls for energy harvesting.* Sensors and Actuators B: Chemical, 2009. **139**(2): p. 511-519.
41. Kerzenmacher, S., et al., *Energy harvesting by implantable abiotically catalyzed glucose fuel cells.* Journal of Power Sources, 2008. **182**(1): p. 1-17.
42. Stetten, F., et al. *A one-compartment, direct glucose fuel cell for powering long-term medical implants*. in *Micro Electro Mechanical Systems, 2006. MEMS 2006 Istanbul. 19th IEEE International Conference on*. 2006. IEEE.
43. Kerzenmacher, S., et al. *A surface mountable glucose fuel cell for medical implants*. in *Solid-State Sensors, Actuators and Microsystems Conference, 2007. TRANSDUCERS 2007. International*. 2007. IEEE.
44. Southcott, M., et al., *A pacemaker powered by an implantable biofuel cell operating under conditions mimicking the human blood circulatory system–battery not included.* Physical chemistry chemical physics, 2013. **15**(17): p. 6278-6283.
45. Muralt, P., *Ferroelectric thin films for micro-sensors and actuators: a review.* Journal of Micromechanics and Microengineering, 2000. **10**(2): p. 136.
46. Zhou, W., W.-H. Liao, and W.J. Li. *Analysis and design of a self-powered piezoelectric microaccelerometer*. in *Smart Structures and Materials*. 2005. International Society for Optics and Photonics.
47. Karami, M.A. and D.J. Inman, *Powering pacemakers from heartbeat vibrations using linear and nonlinear energy harvesters.* Applied Physics Letters, 2012. **100**(4): p. 042901.
48. Abdelkefi, A. and M. Ghommem, *Piezoelectric energy harvesting from morphing wing motions for micro air vehicles.* Theoretical and Applied Mechanics Letters, 2013. **3**(5): p. 052004.
49. Inman, D.J. and B.L. Grisso. *Towards autonomous sensing*. in *Smart Structures and Materials*. 2006. International Society for Optics and Photonics.
50. Roundy, S. and P.K. Wright, *A piezoelectric vibration based generator for wireless electronics.* Smart Materials and structures, 2004. **13**(5): p. 1131.
51. Cook-Chennault, K., N. Thambi, and A. Sastry, *Powering MEMS portable devices—a review of non-regenerative and regenerative power supply systems with special emphasis on piezoelectric energy harvesting systems.* Smart Materials and Structures, 2008. **17**(4): p. 043001.
52. Priya, S., *Advances in energy harvesting using low profile piezoelectric transducers.* Journal of electroceramics, 2007. **19**(1): p. 167-184.
53. Ching, N.N., et al., *A laser-micromachined multi-modal resonating power transducer for wireless sensing systems.* Sensors and Actuators A: Physical, 2002. **97**: p. 685-690.

54. Sterken, T., et al. *An electret-based electrostatic/spl mu/-generator*. in *TRANSDUCERS, Solid-State Sensors, Actuators and Microsystems, 12th International Conference on, 2003*. 2003. IEEE.
55. Abdelkefi, A., *Global nonlinear analysis of piezoelectric energy harvesting from ambient and aeroelastic vibrations*. 2012, Virginia Polytechnic Institute and State University.
56. Anton, S.R. and H.A. Sodano, *A review of power harvesting using piezoelectric materials (2003–2006).* Smart materials and Structures, 2007. **16**(3): p. R1.
57. Sodano, H.A., D.J. Inman, and G. Park, *A review of power harvesting from vibration using piezoelectric materials.* Shock and Vibration Digest, 2004. **36**(3): p. 197-206.
58. Marin, A., S. Bressers, and S. Priya, *Multiple cell configuration electromagnetic vibration energy harvester.* Journal of Physics D: Applied Physics, 2011. **44**(29): p. 295501.
59. Ben Ayed, S., et al., *Design and performance of variable-shaped piezoelectric energy harvesters.* Journal of Intelligent Material Systems and Structures, 2013: p. 1045389X13489365.
60. Masana, R. and M.F. Daqaq, *Electromechanical modeling and nonlinear analysis of axially loaded energy harvesters.* Journal of Vibration and Acoustics, 2011. **133**(1): p. 011007.
61. Challa, V.R., et al., *A vibration energy harvesting device with bidirectional resonance frequency tunability.* Smart Materials and Structures, 2008. **17**(1): p. 015035.
62. Mann, B. and N. Sims, *Energy harvesting from the nonlinear oscillations of magnetic levitation.* Journal of Sound and Vibration, 2009. **319**(1): p. 515-530.
63. Shahruz, S., *Limits of performance of mechanical band-pass filters used in energy scavenging.* Journal of sound and vibration, 2006. **293**(1): p. 449-461.
64. Sari, I., T. Balkan, and H. Kulah, *An electromagnetic micro power generator for wideband environmental vibrations.* Sensors and Actuators A: Physical, 2008. **145**: p. 405-413.
65. Tang, L., Y. Yang, and C.K. Soh, *Toward broadband vibration-based energy harvesting.* Journal of Intelligent Material Systems and Structures, 2010. **21**(18): p. 1867-1897.
66. Twiefel, J. and H. Westermann, *Survey on broadband techniques for vibration energy harvesting.* Journal of Intelligent Material Systems and Structures, 2013. **24**(11): p. 1291-1302.
67. Karami, A. and D.J. Inman, *Powering pacemakers from heartbeat vibrations using linear and nonlinear energy harvesters.* Applied Physics Letters, 2012. **100**(4): p. 042901-042901-4.
68. Tang, L. and Y. Yang, *A nonlinear piezoelectric energy harvester with magnetic oscillator.* Applied Physics Letters, 2012. **101**(9): p. 094102.
69. Erturk, A., J. Hoffmann, and D.J. Inman, *A piezomagnetoelastic structure for broadband vibration energy harvesting.* Applied Physics Letters, 2009. **94**(25): p. 254102.
70. Stanton, S.C., C.C. McGehee, and B.P. Mann, *Reversible hysteresis for broadband magnetopiezoelastic energy harvesting.* Applied Physics Letters, 2009. **95**(17): p. 174103.
71. Abdelkefi, A. and N. Barsallo, *Comparative modeling of low-frequency piezomagnetoelastic energy harvesters.* Journal of Intelligent Material Systems and Structures, 2014: p. 1045389X14523860.
72. Karami, A. and D.J. Inman, *Analytical modeling and experimental verification of the vibrations of the zigzag microstructure for energy harvesting.* Journal of Vibration and Acoustics, 2011. **133**(1): p. 011002.

73. Abdelkefi, A., et al., *An energy harvester using piezoelectric cantilever beams undergoing coupled bending–torsion vibrations.* Smart Materials and Structures, 2011. **20**(11): p. 115007.
74. Karami, A. and D.J. Inman, *Parametric study of zigzag microstructure for vibrational energy harvesting.* Microelectromechanical Systems, Journal of, 2012. **21**(1): p. 145-160.
75. Arnold, D.P., *Review of microscale magnetic power generation.* Magnetics, IEEE Transactions on, 2007. **43**(11): p. 3940-3951.
76. Benasciutti, D., et al., *Vibration energy scavenging via piezoelectric bimorphs of optimized shapes.* Microsystem technologies, 2010. **16**(5): p. 657-668.
77. Ben Ayed, S., et al., *Design and performance of variable-shaped piezoelectric energy harvesters.* Journal of Intelligent Material Systems and Structures, 2014. **25**(2): p. 174-186.
78. Apo, D.J., M. Sanghadasa, and S. Priya, *Vibration Modeling of Arc-Based Cantilevers for Energy Harvesting Applications.* Energy Harvesting and Systems1 (1), 2014: p. 1-12.
79. Berdy, D.F., et al., *Low-frequency meandering piezoelectric vibration energy harvester.* Ultrasonics, Ferroelectrics and Frequency Control, IEEE Transactions on, 2012. **59**(5): p. 846-858.
80. Daqaq, M.F., *Transduction of a bistable inductive generator driven by white and exponentially correlated Gaussian noise.* Journal of Sound and Vibration, 2011. **330**(11): p. 2554-2564.
81. Shu, Y. and I. Lien, *Analysis of power output for piezoelectric energy harvesting systems.* Smart Materials and Structures, 2006. **15**(6): p. 1499.
82. Sodano, H.A., D.J. Inman, and G. Park, *Comparison of piezoelectric energy harvesting devices for recharging batteries.* Journal of Intelligent Material Systems and Structures, 2005. **16**(10): p. 799-807.
83. Mitcheson, P.D., et al., *Energy harvesting from human and machine motion for wireless electronic devices.* Proceedings of the IEEE, 2008. **96**(9): p. 1457-1486.
84. Beeby, S.P., M.J. Tudor, and N.M. White, *Energy harvesting vibration sources for microsystems applications.* Measurement science and technology, 2006. **17**(12): p. R175.
85. Najafi, K., et al. *Microsystems for energy harvesting*. in *Solid-State Sensors, Actuators and Microsystems Conference (TRANSDUCERS), 2011 16th International*. 2011. IEEE.
86. Abdelkefi, A. and N. Barsallo, *Comparative modeling of low-frequency piezomagnetoelastic energy harvesters.* Journal of Intelligent Material Systems and Structures, 2014. **25**(14): p. 1771-1785.
87. Liu, H., et al., *Investigation of a MEMS piezoelectric energy harvester system with a frequency-widened-bandwidth mechanism introduced by mechanical stoppers.* Smart Materials and Structures, 2012. **21**(3): p. 035005.
88. Liu, H., et al., *Piezoelectric MEMS-based wideband energy harvesting systems using a frequency-up-conversion cantilever stopper.* Sensors and Actuators A: Physical, 2012. **186**: p. 242-248.
89. Goldschmidtboeing, F. and P. Woias, *Characterization of different beam shapes for piezoelectric energy harvesting.* Journal of Micromechanics and Microengineering, 2008. **18**(10): p. 104013.
90. Apo, D.J., *Low Frequency Microscale Energy Harvesting.* 2014.
91. Apo, D.J., M. Sanghadasa, and S. Priya. *Low frequency arc-based MEMS structures for vibration energy harvesting*. in *Nano/Micro Engineered and Molecular Systems (NEMS), 2013 8th IEEE International Conference on*. 2013. IEEE.

92. Berdy, D., et al. *Increased-bandwidth, meandering vibration energy harvester*. in *Solid-State Sensors, Actuators and Microsystems Conference (TRANSDUCERS), 2011 16th International*. 2011. IEEE.
93. Berdy, D.F., et al., *Wide-bandwidth, meandering vibration energy harvester with distributed circuit board inertial mass.* Sensors and Actuators A: Physical, 2012. **188**: p. 148-157.
94. Brewer, J.A., *Low resonant frequency beam design for a piezoelectric energy harvesting device*. 2005, Massachusetts Institute of Technology.
95. Hu, H., H. Xue, and Y. Hu, *A spiral-shaped harvester with an improved harvesting element and an adaptive storage circuit.* Ultrasonics, Ferroelectrics and Frequency Control, IEEE Transactions on, 2007. **54**(6): p. 1177-1187.
96. Hu, Y. and Y. Xu, *A wideband vibration energy harvester based on a folded asymmetric gapped cantilever.* Applied Physics Letters, 2014. **104**(5): p. 053902.
97. Karami, A.M. and D.J. Inman, *Parametric study of zigzag microstructure for vibrational energy harvesting.* Journal of Microelectromechanical Systems, 2012. **21**(1): p. 145-160.
98. Karami, M.A. and D.J. Inman, *Electromechanical modeling of the low-frequency zigzag micro-energy harvester.* Journal of Intelligent Material Systems and Structures, 2011. **22**(3): p. 271-282.
99. Sharpes, N., A. Abdelkefi, and S. Priya, *Comparative Analysis of One-Dimensional and Two-Dimensional Cantilever Piezoelectric Energy Harvesters.* Energy Harvesting and Systems, 2014. **1**(3-4): p. 209-216.
100. Wu, H., et al., *A novel two-degrees-of-freedom piezoelectric energy harvester.* Journal of Intelligent Material Systems and Structures, 2012: p. 1045389X12457254.
101. Harb, A., *Energy harvesting: State-of-the-art.* Renewable Energy, 2011. **36**(10): p. 2641-2654.
102. Batra, A.K., et al., *Piezoelectric Power Harvesting Devices: An Overview.* Advanced Science, Engineering and Medicine, 2016. **8**(1): p. 1-12.
103. Harne, R. and K. Wang, *A review of the recent research on vibration energy harvesting via bistable systems.* Smart Materials and Structures, 2013. **22**(2): p. 023001.
104. Zhu, D., M.J. Tudor, and S.P. Beeby, *Strategies for increasing the operating frequency range of vibration energy harvesters: a review.* Measurement Science and Technology, 2010. **21**(2): p. 022001.
105. Sharpes, N., et al., *Preloaded freeplay wide-bandwidth low-frequency piezoelectric harvesters.* Applied Physics Letters, 2015. **107**(2): p. 023902.
106. Abdelkefi, A., et al., *Modeling and identification of freeplay nonlinearity.* Journal of Sound and Vibration, 2012. **331**(8): p. 1898-1907.
107. Apo, D.J., M. Sanghadasa, and S. Priya, *Vibration Modeling of Arc-Based Cantilevers for Energy Harvesting Applications.* Energy Harvesting and Systems, 2014. **1**(1-2): p. 57-68.
108. Karami, M.A., B. Yardimoglu, and D. Inman. *Coupled out of plane vibrations of spiral beams*. in *50th AIAA/ASME/ASCE/AHS/ASC Structures, Structural Dynamics, and Materials Conference*. 2009.
109. Stewart, M., P.M. Weaver, and M. Cain, *Charge redistribution in piezoelectric energy harvesters.* Applied Physics Letters, 2012. **100**(7): p. 073901.
110. Friswell, M.I. and S. Adhikari, *Sensor shape design for piezoelectric cantilever beams to harvest vibration energy.* Journal of Applied Physics, 2010. **108**(1): p. 014901.

111. Abdelkefi, A., et al., *An energy harvester using piezoelectric cantilever beams undergoing coupled bending–torsion vibrations.* Smart Materials and Structures, 2011. **20**(11): p. 115007.
112. Wu, H., et al., *A novel two-degrees-of-freedom piezoelectric energy harvester.* Journal of Intelligent Material Systems and Structures, 2013. **24**(3): p. 357-368.
113. Sharpes, N., A. Abdelkefi, and S. Priya, *Two-dimensional concentrated-stress low-frequency piezoelectric vibration energy harvesters.* Applied Physics Letters, 2015. **107**(9): p. 093901.
114. Taylor, P.J. *Review of Interests and Activities in Thermoelectrics*. in *DoE Thermoelectrics Applications Workshop*. 2011.
115. Berton, H., *Weight of War: Military struggles to lighten soldiers' load.* The Seattle Times, 2011.
116. Orr, R., *The history of the soldier's load.* Australian army journal, 2010. **7**(2): p. 67.
117. Lukowicz, P., T. Kirstein, and G. Troster, *Wearable systems for health care applications.* Methods of Information in Medicine-Methodik der Information in der Medizin, 2004. **43**(3): p. 232-238.
118. Pantelopoulos, A. and N.G. Bourbakis, *A survey on wearable sensor-based systems for health monitoring and prognosis.* Systems, Man, and Cybernetics, Part C: Applications and Reviews, IEEE Transactions on, 2010. **40**(1): p. 1-12.
119. Patel, S., et al., *A review of wearable sensors and systems with application in rehabilitation.* Journal of neuroengineering and rehabilitation, 2012. **9**(1): p. 1.
120. Mukhopadhyay, S.C., *Wearable sensors for human activity monitoring: A review.* Sensors Journal, IEEE, 2015. **15**(3): p. 1321-1330.
121. Widmer, R.J., et al., *DIGITAL HEALTH INTERVENTION DURING CARDIAC REHABILITATION ENHANCES WEIGHT LOSS.* Journal of the American College of Cardiology, 2016. **67**(13_S): p. 1844-1844.
122. Bandodkar, A.J. and J. Wang, *Non-invasive wearable electrochemical sensors: a review.* Trends in biotechnology, 2014. **32**(7): p. 363-371.
123. Lee, H., et al., *The technical trend of the exoskeleton robot system for human power assistance.* International Journal of Precision Engineering and Manufacturing, 2012. **13**(8): p. 1491-1497.
124. Yang, C., et al., *A review of exoskeleton-type systems and their key technologies.* Proceedings of the Institution of Mechanical Engineers, Part C: Journal of Mechanical Engineering Science, 2008. **222**(8): p. 1599-1612.
125. Heo, P., et al., *Current hand exoskeleton technologies for rehabilitation and assistive engineering.* International Journal of Precision Engineering and Manufacturing, 2012. **13**(5): p. 807-824.
126. Dollar, A.M. and H. Herr, *Lower extremity exoskeletons and active orthoses: challenges and state-of-the-art.* Robotics, IEEE Transactions on, 2008. **24**(1): p. 144-158.
127. Gopura, R. and K. Kiguchi. *Mechanical designs of active upper-limb exoskeleton robots: State-of-the-art and design difficulties*. in *Rehabilitation Robotics, 2009. ICORR 2009. IEEE International Conference on*. 2009. IEEE.
128. Bryant, M., M.A. Meller, and E. Garcia, *Variable recruitment fluidic artificial muscles: modeling and experiments.* Smart Materials and Structures, 2014. **23**(7): p. 074009.
129. Lima, M.D., et al., *Electrically, chemically, and photonically powered torsional and tensile actuation of hybrid carbon nanotube yarn muscles.* Science, 2012. **338**(6109): p. 928-932.

130. Mosher, R.S., *Handyman to hardiman*. 1967, SAE Technical Paper.
131. Army-Technology. *Raytheon XOS 2 Exoskeleton, Second-Generation Robotics Suit, United States of America*. [cited 2015 May 6th]; Available from: http://www.army-technology.com/projects/raytheon-xos-2-exoskeleton-us/.
132. Love, D. *South Korean Shipyard Workers Wear Robo-Suits For Super-Strength*. 2014 [cited 2015 May 6th]; Available from: http://www.businessinsider.com/daewoo-robotic-exoskeletons-2014-8.
133. Perry, J.C., J. Rosen, and S. Burns, *Upper-limb powered exoskeleton design.* Mechatronics, IEEE/ASME Transactions on, 2007. **12**(4): p. 408-417.
134. Sankai, Y., *HAL: Hybrid assistive limb based on cybernics*, in *Robotics Research*. 2011, Springer. p. 25-34.
135. Kazerooni, H., A. Chu, and R. Steger, *That which does not stabilize, will only make us stronger.* The International Journal of Robotics Research, 2007. **26**(1): p. 75-89.
136. Low, K., X. Liu, and H. Yu. *Development of NTU wearable exoskeleton system for assistive technologies*. in *Mechatronics and Automation, 2005 IEEE International Conference*. 2005. IEEE.
137. Zoss, A. and H. Kazerooni, *On the Mechanical Design of the Berkeley Lower Extemity Exoskeleton.* IEEE IROS, Edmunton Canada, 2005.
138. Zoss, A.B., H. Kazerooni, and A. Chu, *Biomechanical design of the Berkeley lower extremity exoskeleton (BLEEX).* Mechatronics, IEEE/ASME Transactions on, 2006. **11**(2): p. 128-138.
139. Cao, H., et al. *Design frame of a leg exoskeleton for load-carrying augmentation*. in *Robotics and Biomimetics (ROBIO), 2009 IEEE International Conference on*. 2009. IEEE.
140. Walsh, C.J., K. Endo, and H. Herr, *A quasi-passive leg exoskeleton for load-carrying augmentation.* International Journal of Humanoid Robotics, 2007. **4**(03): p. 487-506.
141. Martin, L. *HULC*. 2015 [cited 2015 May 6th]; Available from: http://www.lockheedmartin.com/us/products/hulc.html.
142. Bionics, E. *Rethinking Physical Limitations to Achieve the Remarkable*. 2015 [cited 2015 May 6th]; Available from: http://www.eksobionics.com/ourstory.
143. Park, Y.-L., et al., *Design and control of a bio-inspired soft wearable robotic device for ankle–foot rehabilitation.* Bioinspiration & biomimetics, 2014. **9**(1): p. 016007.
144. Wehner, M., et al. *A lightweight soft exosuit for gait assistance*. in *Robotics and Automation (ICRA), 2013 IEEE International Conference on*. 2013. IEEE.
145. Asbeck, A.T., et al., *A biologically inspired soft exosuit for walking assistance.* The International Journal of Robotics Research, 2015: p. 0278364914562476.
146. Asbeck, A.T., et al. *Biologically-inspired soft exosuit*. in *Rehabilitation Robotics (ICORR), 2013 IEEE International Conference on*. 2013. IEEE.
147. Ding, Y., et al. *Multi-joint actuation platform for lower extremity soft exosuits*. in *Robotics and Automation (ICRA), 2014 IEEE International Conference On*. 2014. IEEE.
148. Dick, G.J. and E.A. Edwards, *Human bipedal locomotion device*. 1991, Google Patents.
149. Dollar, A.M. and H. Herr. *Design of a quasi-passive knee exoskeleton to assist running*. in *Intelligent Robots and Systems, 2008. IROS 2008. IEEE/RSJ International Conference on*. 2008. IEEE.
150. Alexander, R.M., *Energy-saving mechanisms in walking and running.* Journal of Experimental Biology, 1991. **160**(1): p. 55-69.

151. Rahman, T., et al., *Passive exoskeletons for assisting limb movement.* Journal of rehabilitation research and development, 2006. **43**(5): p. 583.
152. Noonee. *Chairolution® "Bringing forth a new era of wearable ergonomic leg devices"*. 2015 [cited 2015 May 6th]; Available from: http://www.noonee.ch/index.php/technology.
153. Agrawal, S.K., et al. *A Gravity Balancing Passive Exoskeleton for the Human Leg*. in *Robotics: Science and Systems*. 2006.
154. Van den Bogert, A.J., *Exotendons for assistance of human locomotion.* Biomedical Engineering Online, 2003. **2**(17): p. 1-8.
155. van Dijk, W., H. van der Kooij, and E. Hekman. *A passive exoskeleton with artificial tendons: Design and experimental evaluation*. in *Rehabilitation Robotics (ICORR), 2011 IEEE International Conference on*. 2011. IEEE.
156. Collins, S.H., M.B. Wiggin, and G.S. Sawicki, *Reducing the energy cost of human walking using an unpowered exoskeleton.* Nature, 2015.
157. Donelan, J.M., et al., *Biomechanical energy harvesting: generating electricity during walking with minimal user effort.* Science, 2008. **319**(5864): p. 807-810.
158. SpringActive. *SPaRK*. 2012 [cited 2016 March 11th]; Available from: http://www.springactive.com/spark.php.
159. Gregory, R., et al., *Effects of a biomechanical energy harvesting ankle device on gait kinetics*, in *American Society of Biomechanics*. 2012.
160. Leemans, A., et al., *KINEMATIC EFFECTS OF BIOMECHANICAL ENERGY HARVEST AT THE ANKLE: IMPLICATIONS FOR INJURY SUSCEPTIBILITY*, in *American Society of Biomechanics*. 2012.
161. Paradiso, J.A. and T. Starner, *Energy scavenging for mobile and wireless electronics.* Pervasive Computing, IEEE, 2005. **4**(1): p. 18-27.
162. Shenck, N.S. and J.A. Paradiso, *Energy scavenging with shoe-mounted piezoelectrics.* IEEE micro, 2001(3): p. 30-42.
163. Kymissis, J., et al. *Parasitic power harvesting in shoes*. in *Wearable Computers, 1998. Digest of Papers. Second International Symposium on*. 1998. IEEE.
164. Rome, L.C., L. Flynn, and T.D. Yoo, *Biomechanics: Rubber bands reduce the cost of carrying loads.* Nature, 2006. **444**(7122): p. 1023-1024.
165. Rome, L.C., et al., *Generating electricity while walking with loads.* Science, 2005. **309**(5741): p. 1725-1728.
166. Pierrynowski, M., D. Winter, and R. Norman, *Metabolic measures to ascertain the optimal load to be carried by man.* Ergonomics, 1981. **24**(5): p. 393-399.
167. Winter, D.A., *Biomechanics and motor control of human movement*. 2009: John Wiley & Sons.
168. White, R.M. and E. Churchill, *The body size of soldiers: US army anthropometry-1966*. 1971, DTIC Document.
169. Riemer, R. and A. Shapiro, *Biomechanical energy harvesting from human motion: theory, state of the art, design guidelines, and future directions.* Journal of neuroengineering and rehabilitation, 2011. **8**(1): p. 22.
170. Chiu, H. and T. Shiang, *Effects of insoles and additional shock absorption foam on the cushioning properties of sport shoes.* Journal of applied biomechanics, 2007. **23**(2): p. 119.
171. Shigley, J.E., R.G. Budynas, and J.K. Nisbett, *Mechanical Engineering Design*. 8th ed. 2008, New York, NY: McGraw-Hill.

172. SDP/SI. *TIMING BELT DESIGN AND INSTALLATION SUGGESTIONS: GENERAL GUIDE LINES*. Timing Belt Installation and Operation General Guide Lines 2016 [cited 2014 Aug. 11]; Available from: http://sdp-si.com/resources/beltdesignsuggestions.htm.
173. Jelaska, D.T., *Gears and Gear Drives*. 2012: John Wiley & Sons.
174. Sandvik, *Spring Designer's Guide*.
175. Queener, C. and G. Wood, *Spiral power springs. Part 1—theory.* Journal of Engineering for Industry, 1971. **93**(2): p. 667-675.
176. Spring, A., *Engineering Guide to Spring Design*. 1987, Barnes Group Inc.
177. Inc., M.C.S. *About Power Springs*. Power Spring Basics 2010 3/14/2015]; Available from: http://www.spiralspring.com/about_power_springs.html.
178. Spreemann, D., B. Folkmer, and Y. Manoli, *Comparative study of electromagnetic coupling architectures for vibration energy harvesting devices.* Proceedings of PowerMems, 2008: p. 257-260.
179. Kishore, R.A., A. Marin, and S. Priya, *Efficient Direct-Drive Small-Scale Low-Speed Wind Turbine.* Energy Harvesting and Systems, 2014. **1**(1-2): p. 27-43.
180. Boca Bearing, I. *OWC307GXLZ One Way Bearings* Product Specifications 2004 [cited 2014 June 11th]; Available from: http://www.bocabearings.com/bearing-inventory/one-way-bearings/2711/3x7-2000x5-4000-owc307gxlz.
181. K&J Magnetics, I. *Neodymium Magnet Physical Properties*. Physical and Mechanical Characteristics [cited 2016 April 4th]; Available from: https://www.kjmagnetics.com/specs.asp.
182. EIA, U., *Annual energy review.* Energy Information Administration, US Department of Energy: Washington, DC www. eia. doe. gov/emeu/aer, 2011.
183. Nguyen, T.A. and M. Aiello, *Energy intelligent buildings based on user activity: A survey.* Energy and buildings, 2013. **56**: p. 244-257.
184. Weng, T. and Y. Agarwal, *From Buildings to Smart Buildings—Sensing and Actuation to Improve Energy Efficiency.* IEEE Design & Test of Computers, 2012. **29**(4): p. 36-44.
185. Agarwal, Y., et al. *Occupancy-driven energy management for smart building automation*. in *Proceedings of the 2nd ACM Workshop on Embedded Sensing Systems for Energy-Efficiency in Building*. 2010. ACM.
186. Hennig, E.M., G.A. Valiant, and Q. Liu, *Biomechanical Variables and the Perception of Cushioning for Running in Various Types of Footwear.* Journal of Applied Biomechanics, 1996. **12**(2).
187. Seow, Z.L., S.T. Chen, and N.B. Khairudin, *An investigation into energy generating tiles: Pavegen*. 2011.
188. Paulides, J., et al. *Human-powered small-scale generation system for a sustainable dance club*. in *Electric Machines and Drives Conference, 2009. IEMDC'09. IEEE International*. 2009. IEEE.
189. Kemball-Cook, L. and P. Tucker, *Energy harvesting*. 2013, Google Patents.
190. Brezet, J.C., et al., *Floor suitable for generating, converting and/or storing energy*. 2012, Google Patents.
191. International Code Council, I., *Structural Design*, in *2009 Virginia Construction Code*. 2011: 4051 West Flossmoor Road, Country Club Hills, IL 60478. p. 64.
192. Abramovich, H., et al., *Multi-layer piezoelectric generator*. 2012, Google Patents.
193. APC International, L., *Physical and Piezoelectric Properties of APC Materials*. 2013.

194. Fernandez, J., et al., *Tailoring the performance of ceramic-metal piezocomposite actuators,'cymbals'.* Sensors and Actuators A: Physical, 1998. **65**(2): p. 228-237.
195. Sun, C.-L., et al., *Displacement amplification and resonance characteristics of the cymbal transducers.* Sensors and Actuators A: Physical, 2005. **121**(1): p. 213-220.
196. Zhao, H., J. Yu, and J. Ling, *Finite element analysis of Cymbal piezoelectric transducers for harvesting energy from asphalt pavement.* Nippon seramikkusu kyokai gakujutsu ronbunshi, 2010. **118**(10): p. 909-915.
197. Kim, H.W., et al., *Energy harvesting using a piezoelectric "cymbal" transducer in dynamic environment.* Japanese Journal of Applied Physics, 2004. **43**(9R): p. 6178.
198. Kim, H.W., S. Priya, and K. Uchino, *Modeling of piezoelectric energy harvesting using cymbal transducers.* Japanese journal of applied physics, 2006. **45**(7R): p. 5836.
199. Luo, L., et al., *Displacement amplification and electric characteristics of modified rectangular cymbal transducers using electroactive materials.* Solid state communications, 2007. **143**(6): p. 321-325.
200. Rees, D.W., *Mechanics of optimal structural design: minimum weight structures*. 2009, The Atrium, Southern Gate, Chichester, West Sussex, PO19 8SQ, United Kingdom: John Wiley & Sons.
201. Martin, P.E. and A.P. Marsh, *Step length and frequency effects on ground reaction forces during walking.* Journal of biomechanics, 1992. **25**(10): p. 1237-1239.
202. Zhang, T.-Y. and C. Gao, *Fracture behaviors of piezoelectric materials.* Theoretical and applied fracture mechanics, 2004. **41**(1): p. 339-379.
203. East Japan Railway Company, *Demonstration Experiment of the "Power-Generating Floor" at Tokyo Station*. 2008. p. 3.
204. Wilkie, W.K., et al. *Low-cost piezocomposite actuator for structural control applications*. in *SPIE's 7th Annual International Symposium on Smart Structures and Materials*. 2000. International Society for Optics and Photonics.
205. Fryar, C.D., Q. Gu, and C.L. Ogden, *Anthropometric reference data for children and adults: United States, 2007–2010.* National Center for Health Statistics. Vital Health Stat, 2012. **11**(252): p. 1-40.
206. Merron, J. *The NFL Weight Rankings*. Page 2, 2004.
207. Beeby, S. and N.M. White, *Energy harvesting for autonomous systems*. 2010, Norwood, MA: Artech House.
208. Erturk, A. and D.J. Inman, *Piezoelectric energy harvesting*. 2011: John Wiley & Sons.
209. Guyomar, D., et al., *Toward energy harvesting using active materials and conversion improvement by nonlinear processing.* Ultrasonics, Ferroelectrics and Frequency Control, IEEE Transactions on, 2005. **52**(4): p. 584-595.
210. Texas Instruments, *eZ430-RF2500 development tool user's guide*, in *Texas Instruments SLAU227E*. 2009.
211. Morales, M. and Z. Shivers, *Wireless Sensor Monitor Using the eZ430-RF2500*. 2007, Texas Instruments.
212. Linear Technology Corporation, *LTC3129-1, 15V, 200mA Synchronous Buck-Boost DC/DC Converter with 1.3μA Quiescent Current*. 2013.
213. Leviton Manufacturing Co., I., *Occupancy Sensor Applications Guide*. 2011.
214. Dodier, R.H., et al., *Building occupancy detection through sensor belief networks.* Energy and buildings, 2006. **38**(9): p. 1033-1043.

215. Yan, Y., Y.U. Wang, and S. Priya, *Electromechanical behavior of [001]-textured Pb (Mg1/3Nb2/3) O3-PbTiO3 ceramics.* Applied Physics Letters, 2012. **100**(19): p. 192905.
216. Von Neida, B., D. Manicria, and A. Tweed, *An analysis of the energy and cost savings potential of occupancy sensors for commercial lighting systems.* Journal of the Illuminating Engineering Society, 2001. **30**(2): p. 111-125.
217. Maniccia, D., et al., *The effects of changing occupancy sensor time-out setting on energy savings, lamp cycling and maintenance costs.* Journal of the Illuminating Engineering Society, 2001. **30**(2): p. 97-110.
218. Vuckovic, D., *Design and Implementation of Energy Harvesting Powered Wireless Sensor Networks*. 2014, Technical Unversity of Denmark.
219. Diegel, O., *BendWorks: The fine-art of sheet metal bending*. 2002. p. 9.
220. Davis, G., *The Air Bending Process*. DSM Manufacturing Company. p. 5.
221. Cheng, K., et al. *Piezoelectric coefficients of PMN-0.33 PT single crystals*. in *Applications of Ferroelectrics, 2000. ISAF 2000. Proceedings of the 2000 12th IEEE International Symposium on*. 2000. IEEE.